

Научном већу Института за физику у Београду  
Београд, 31. децембар 2019.

ИНСТИТУТ ЗА ФИЗИКУ			
ПРИМЉЕНО: 01. 11. 2019			
Рад.јед.	б р о ј	Арх.шифра	Прилог
ДФ01	1640/1		

**ПРЕДМЕТ:**

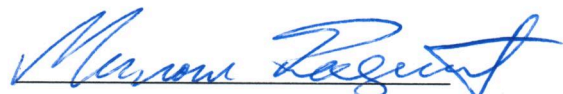
**Молба за покретање поступка за стицање звања виши научни сарадник**

Молим Научно веће Института за физику у Београду да, у складу с Правилником о поступку и начину вредновања и квантитативном исказивању научно-истраживачких резултата истраживача, покрене поступак за мој избор у звање виши научни сарадник.

У прилогу достављам:

1. Мишљење руководиоца пројекта са предлогом чланова комисије
2. Биографске податке
3. Преглед научне активности
4. Елементе за квалитативну оцену научног доприноса
5. Елементе за квантитативну оцену научног доприноса
6. Списак објављених радова и њихове копије
7. Податке о цитираности
8. Фотокопију решења о претходном избору у звање
9. Додатне прилоге

С поштовањем,



др Милош Радоњић  
научни сарадник,  
Институт за физику у Београду

ПРИМЉЕНО: 01. 11. 2019			
Рад.јед.	б р о ј	Арх.шифра	Прилог
0801	1640/2		

## Научном већу Института за физику у Београду

**Предмет: Мишљење руководиоца пројекта о избору др Милоша Радоњића у звање виши научни сарадник**

Др Милош Радоњић је запослен у Лабораторији за примену рачунара у науци, у оквиру Националног центра изузетних вредности за изучавање комплексних система Института за физику у Београду и ангажован је на пројекту основних истраживања Министарства просвете, науке и технолошког развоја Републике Србије ОН171017, под називом "Моделирање и нумеричке симулације сложених вишечестичних физичких система". На поменутом пројекту ради на проучавању електронских транспортних особина материјала, као и динамике кристалне решетке у присуству јаких корелација и неуређености. С обзиром да испуњава све предвиђене услове у складу са Правилником о поступку, начину вредновања и квантитативном исказивању научноистраживачких резултата истраживача МПНТР, сагласан сам са покретањем поступка за избор др Милоша Радоњића у звање виши научни сарадник.

За састав комисије за избор др Милоша Радоњића у звање виши научни сарадник предлажем:

- (1) др Дарко Танасковић, научни саветник, Институт за физику у Београду,
- (2) др Антун Балаж, научни саветник, Институт за физику у Београду,
- (3) академик Зоран Поповић, научни саветник, Институт за физику у Београду,
- (4) проф. др Ђорђе Спасојевић, редовни професор Физичког факултета Универзитета у Београду.

Руководилац пројекта

др Антун Балаж  
научни саветник

## 2. БИОГРАФСКИ ПОДАЦИ КАНДИДАТА

Милош Радоњић је рођен 19. 10. 1984. године у Лесковцу. Завршио је специјализовано математичко одељење у Првој крагујевачкој гимназији 2003. као ђак генерације. Након тога уписао је основне студије на Физичком факултету Универзитета у Београду, смер Теоријска и експериментална физика. Током студија је био стипендиста Фондације за развој научног и уметничког подмлатка и фондације Студеница. Дипломирао је 2008. године са просечном оценом 9.92. Дипломски рад под називом „Проводност неуређеног метала у близини Мотовог метал-изолатор прелаза” урадио је у Лабораторији за примену рачунара у науци у Институту за физику у Београду под руководством др Дарка Танасковића и за њега је добио награду „Др Љубомир Ћирковић”.

Докторске студије на смеру „Физика кондензованог стања материје” Милош Радоњић је започео 2008. године под менторством др Дарка Танасковића. Од краја 2008. до јануара 2011. године је био ангажован у Лабораторији за примену рачунара у науци као стипендиста Министарства просвете науке и технолошког развоја на пројекту основних истраживања „Моделовање и нумеричке симулације сложених физичких система” ОИ141035. Од 01. 01. 2011. Милош Радоњић је запослен у Институту за физику као истраживач сарадник на пројектима ОИ171017: „Моделирање и нумеричке симулације комплексних физичких система” и ИИИ45018: „Наноструктурни мултифункционални материјали и нанокompозити”. У том периоду је био ангажован на више билатералних пројеката са групама из Немачке и Француске. У звање научног сарадника изабран је 26. фебруара 2015. године. Од септембра 2014. до октобра 2016. године др Радоњић је радио као постдокторски истраживач у групи проф. др Дитера Фолхарда на Институту за физику универзитета у Аугсбургу у Немачкој. У том периоду је био и ангажован у настави као асистент. По повратку са постдокторског усавршавања, наставио је ангажман на пројекту ОИ171017 и наставио сарадњу са групом проф. Фолхарда, посебно са проф. др Ливијумом Киончелом. Од 2018. године др Радоњић руководи билатералним пројектом, са групом проф. Киончела под називом „Неравнотежни транспорт јакокорелисаних металних система”.

Главне научне теме кандидата су проучавање транспортних, електронских особина и динамике решетке јакокорелисаних система у равнотежном и неравнотежном режиму. У тренутку подношења овог извештаја, Милош Радоњић је коаутор укупно 31 рада и саопштења, од којих 1 у категорији М21а, 14 у категорији М21, 2 у категорији М22, 1 у категорији М32 и 13 у категорији М34. Укупан број цитата радова кандидата је 109 (100 не рачунајући самоцитате), са Хиршовим индексом 7.

Милош Радоњић је своје знање значајно проширио учешћем у великом броју престижних научних школа: *Simons Collaboration Summer School, Simons Collaboration on the Many Electron Problem, Stony Brook, NY, SAD 2016, SPICE-Workshop, On Bad Metal Behavior in Mott Systems, Mainz, Germany 2015, Autumn School on Correlated Electrons, Julich, Germany 2013, Les Houches Doctoral training, Les Houches, France 2012, Theory Winter School, NHMFL, FSU, Talahassee, USA 2012, Autumn-School Hands-on LDA+DMFT, Julich, Germany, 2011, Advanced School in High Performance and GRID Computing, ICTP, Trieste, Italy, 2009, European School on Magnetism 2009, Timisoara,*

*Romania, 2009*, као и двомесечним студијским боравком у Националној лабораторији за јака магнетна поља на Државном универзитету Флориде 2012. године.

Дана 17. јуна 2014. године, Милош Радоњић је одбранио докторску дисертацију под називом: “*Influence of disorder on charge transport in strongly correlated materials near the metal-insulator transition*”.

### 3. ПРЕГЛЕД НАУЧНЕ АКТИВНОСТИ

Научно-истраживачки рад др Милоша Радоњића је у области теоријске физике кондензо-ваног стања материје. За време докторских студија у Београду (2008-2014) кандидат се бавио проучавањем јако корелисаних електронских система, и истраживањима електронске структуре и динамике решетке пниктида и халкогенида прелазних метала. Докторирао је на теми “*Influence of disorder on charge transport in strongly correlated materials near the metal-insulator transition*”, урађеној под руководством др Дарка Танасковића. Лабораторији за примену рачунара у науци и наставља проучавање јако корелисаних материјала у близини метал-изолатор прелаза.

Научно-истраживачка активност кандидата обухвата проучавање:

- утицаја јаких електронских корелација на електронске и транспортне особине јакокорелисаних материјала у равнотежном и неравнотежном режиму,
- суперпроводних фаза елементалног бизмута,
- динамике решетке и електронске структуре пниктида, халкогенида и оксида прелазних метала,
- утицаја неуређености на транспортне особине, јако корелисаних електронских система.

У наредним одељцима укратко су приказани главни научни резултати добијени у оквиру набројаних тема.

#### 3.1 Утицај електронских корелација на електронске и транспортне особине јакокорелисаних материјала у равнотежном и неравнотежном режиму

Уочено је да велика класа материјала, попут једињења са прелазним елементима, тешким земљама, одређене класе органских материјала, често не могу бити квантитативно, па чак ни квалитативно описане теоријом функционала густине (*density functional theory - DFT*) која представља стандард и полазну тачку свих прорачуна својстава материјала из првих принципа. Јаке, локалне електронске корелације су препознате као главни недостајући ефекат који није одговарајуће урачунат у оквиру *DFT*-а. Стога је од изузетне важности испитивање утицаја ових корелација на различите особине материјала. Методе коришћене у овим истраживањима могу бити виђене као проширења *DFT* прорачуна укључивањем јаких локалних електронских корелација на нивоу динамичке теорије средњег поља. Развијеним моделима је испитиван утицај ових корелација на електронске и транспортне особине јакокорелисаних материјала.

У раду [1] (из листе радова) је развијен метод за израчунавање равнотежних и неравнотежних особина јакокорелисаних нано система на ниским температурама из првих принципа. Метод комбинује теорију функционала густине, теорију квантног транспорта, прорачуне нумеричке ренормализационе групе (*numerical renormalization group - NRG*) и ренормализовану теорију суперпертурбације (*renormalized super-perturbation theory - rSPT*). Испитиван је утицај различитих геометрија интерфејса (на атомском нивоу) између молекула и електрода, што је омогућило добро слагање израчунате и измерене Кондо температуре и

карактеристичних транспортних особина. Помоћу неравнотежних прорачуна (*rSPT*), процењена је област поузданости равнотежних прорачуна трансмисије (*DFT+NRG*) за проводност на коначном напону. Резултати показују да овај метод омогућава квалитативан увид у особине спојева молекула са металима када су ти спојеви аморфни, или недовољно одређени и да може да пружи и пун квантитативни опис експеримента када је контакт добро карактеризован.

**Рад [6]** представља проучавање ефеката јаких локалних електронских корелација, на нивоу вишеорбиталног Хабардог модела, на електронску структуру паладијума. Коришћена је комбинација (*DFT+DMFT*). Урачунавањем ових корелација је побољшано слагање експериментално измерене и теоријско израчунате константе решетке и модула стишљивости. Уочено је да јаке електронске корелације коригују само одређене делове Фермијеве сфере. Такође су разматрани нелокални ефекти поређењем са *GW* методом. Утврдили смо да за релативно мале вредности локалне Кулонове интеракције и Хундовог спрезања *DFT+DMFT* и *GW* метода не показују значајне разлике.

**У раду [7]** је предложен метод за израчунавање трансмисије кроз јакокорелисане хетероструктуре комбинујући теорију функционала густине и динамичку теорију средњег поља (*DFT+DMFT*) у неравнотежној поставци. Ова комбинација је остварена тако што је многочестична сопствена енергија израчуната у базису свих електрона и пребачена у базис локализованих електрона у облику псеудопотенцијала. Помоћу ове методе су проучавани ефекти јаке локалне интеракције електрона и коначне температуре на трансисију кроз металну хетероструктуру *Cu<sub>4</sub>CoCu<sub>4</sub>*. Показано је локалне јаке електронске корелације умањују укупну трансисију на Фермијевом нивоу (превасходно умањујући мање попуњен списнки канал), док се њена спинска поларизација увећава.

### 3.2 Проучавање суперпроводних фаза елементарног бизмута

Пратећи интензивна истраживања суперпроводности у купратима и суперпроводницима на бази гвожђа, једноставнији материјали, као елементарна једињења, или једињења са једним атомом су привукла велику пажњу. Скорашња истраживања су показала да упркос њиховој једноставности, она представљају богат полигон за откривање нових феномена и неконвенционалних особина. Једно од најзанимљивијих таквих једињења је свакако бизмут. Наиме, бизмут је компензовани полуметал, што значи да има врло дубок псеудопроеп на Фермијевом нивоу од  $10^{-6}$  носиоца наелектрисања по *eV* и да је концентрација електрона једнака концентрацији шупљина. Због тога је бизмут врло осетљив на промену спољашњих параметара, нпр. притиска, температуре, итд, а и спин-орбит интеракција значајно утиче на његове особине.

**Рад [2]** је први у низу радова који се баве истраживањем суперпроводних стања бизмута под притиском. Услед притиска бизмут пролази кроз више структурних фазних прелаза. У овом раду је истраживана природа суперпроводности у моноклиничној фази бизмута (*Bi-II*) која је присутна на  $2.80 \text{ GPa}$ . Експериментални налази су подржани и потврђени теоријским прорачунима базираним на Елиашберговој теорији полазећи од првих принципа. Приказано је одлично слагање суперпроводне критичне температуре и критичног магнетног

поља између експеримента и теорије и прорачуни су показали да бизмут у овој фази има средњу јачину суперпроводног спрезања.

### 3.3 Проучавање динамике решетке и електронске стурктуре пниктида, халкогенида и оксида прелазних метала

Трећа тема је везана за прорачуне електронске и фононске структуре (динамике решетке) разних једињења, углавном дихалкогенида и 122 суперпроводника. Прорачуни електронске структуре су вршени у оквиру теорије функционала густине, док је динамика решетке проучавана помоћу пертурбативне теорије функционала густине (*Density functional perturbation theory - DFPT*).

**Рад [3]** представља проучавање динамике решетке сулфида гвожђа. У експериментланим фононским спектрима уочене су аномалије које се огледају у појави додатних фононских мода. Порекло тих мода које се налазе у процепу између оптичких мода је утврђено детаљним прорачунима помоћу пертурбативне теорије функционала густине. Недвосмислено је показано да су двофононски процеси одговорни за њихов настанак, а као механизам њиховог испољавања у експерименту препозната је електрон-фонон интеракција.

У радовима [4, 5, 8, 9, 11, 12, 13, 17], испитивана је динамика решетке и фононске карактеристике одређених дихалкогенида и суперпроводника на бази гвожђа, помоћу пертурбативне теорије функционала густине. Представљено је добро слагање фононских фреквенција у центру Бриленове зоне, добијених помоћу прорачуна и измерених Рамановом спектроскопијом. Сви модови осциловања уочени у експерименту су правилно симетријски окарактерисани. Проучаван је и документован утицај температуре и допирања на фононске спектре и коментарисан утицај електрон-фонон интеракције. Код материјала који поседују магнетни фазни прелаз, документован је утицај магнетног уређења на фононске спектре.

**Рад [10]** представља проучавање  $S=2$  “*spin-ladder*” система  $BaFe_2Se_2O$  помоћу Раманове спектроскопије и фононских прорачуна. Анализом температурне зависности појединих модова уочено је дугодометно, антиферромагнетно уређење испод  $T=240K$ . Измерени спектри показују и постојање магнетног континуума који нестаје на температури  $T=623K$ , што представља температуру на којој се нарушава краткодометно магнетно уређење.

У сарадњи са групама са Фармацеутског и Технолошког факултета проучавани су вибрациони спектри молекула ибупрофена **рад [16]**. За кристалне структуре сачињене од великих органских молекула је карактеристично постојање јаким ковалентних веза и слабих ван дер Валсових у исто време. Оба типа веза се могу проучавати помоћу Раманове спектроскопије, што представља неопходан корак у карактеризацији главних физичко-хемијских својства и испитивању стабилности и трансформације једињења на молекуларном нивоу. Помоћу *DFPT* методе су проучавани вибрациони модови молекула, који се појављују у Рамановим спектрима на ниским енергијама.

### 3.4 Утицај неуређености на транспортне особине, јако корелисаних електронских система

Особине материјала у близини метал-изолатор прелаза су посебно интересантне због велике осетљивости на мале промене спољашњих параметара попут температуре, притиска и магнетног поља, или на допирање материјала. Мотов метал-изолатор прелаз настаје услед јаких електрон-електрон интеракција и представља пример квантног фазног прелаза. Најзагонетнији квантни критични феномени се појављују у јако корелисаним металима, као што су легуре атома ретких земаља, купрати и други оксиди прелазних метала у близини Мотовог прелаза. Електрони у овим материјалима су негде на пола пута између слободних и потпуно локализованих. Јако међуелектронско расејање доводи до некохерентних екситација које пресудно утичу на транспортне и термодинамичке особине. Како се ове особине мењају под утицајем неуређености је врло нетривијално и веома важно питање, посебно имајући у виду да су многи јако корелисани материјали нестехиометријска једињења па је неуређеност, односно одступање од идеалне периодичности, неизбежно.

Кључ у разумевању особина ових система лежи у хватању у коштац са некохерентним екситацијама. Овај задатак је недостижан ако се остане у оквирима теорије Фермијевих течности. Управо због тога је развијена динамичка теорија средњег поља (*DMFT*) и њена уопштења која укључују неуређеност – која истовремено успешно описује и некохерентне процесе на вишим температурама и Ландауове квази-честице, а која представља главни теоријски метод у радовима кандидата.

У раду [14] (M21 листа), показано је да читава фамилија експерименталних кривих отпорности у функцији температуре на *Si MOSFET*-има и *GaAs/AlGaAs* хетероструктурама може да се колапсира на једну криву, када се температура скалира са температуром кохеренције. Ова температура је процењена као температура на којој отпор достиже максимум. Утврђено је да је температура кохеренције инверзно пропорционална ефективној маси разређеног дводимензионалног електронском гаса у *Si MOSFET*-има. Слични резултати се добијају и анализом решења једноставног Хабардовог модела за Мотов метал-изолатор прелаз. Ови резултати указују да јако међуелектронско расејање, а не неуређеност, доминантно одређује особине *MOSFET*-а у широком интервалу концентрација и температура у близини *2D* метал-изолатор прелаза.

У раду [15], испитиван је утицај неуређености на особине јако интерагујућих електронских система. Неуређеност (нечистоће, допирање, дислокације) су, у већој или мањој мери, увек присутне у синтези материјала и могу да имају веома велики утицај на њихова својства. У поменутом раду се испитује међусобни утицај неуређености и јаких електронских корелација (интеракција) на метал-изолатор прелаз. Проучаван је неуређени полупопуњени Хабардов модел у оквиру динамичке теорије средњег поља и њених уопштења. Конкретно, коришћена је апроксимација кохерентног потенцијала за случај слабе до умерене неуређености. Уочено је да при константној интеракцији, неуређеност ефективно шири проводну зону и систем удаљава од Мотовог прелаза. Криве отпорности имају сличну немонотону температурну зависност у близини Мотовог прелаза као и у чистом



случају. Вредност за максималну металну отпорност прелази квази-класичну Мот-Јофе-Регел границу за ред величине. Друдеов пик у оптичкој проводности опстаје чак и када је отпорност упоредива са Мот-Јофе-Регел границом. Ова теорија је успела да опише главни ефекат неуређености уочен у експериментима, а то је да са повећањем неуређености отпорност система опада (у случају слабе до умерене неуређености).

Сви ови радови имају изражену нумеричку компоненту и за њихову реализацију су били неопходни рачунарски ресурси који су на располагању у Лабораторији за примену рачунара у науци Института за физику. Такође, овим радовима је отпочета конкретна сарадња са Лабораторијом за Раманову спектроскопију са Института за физику.

## 4. ЕЛЕМЕНТИ ЗА КВАЛИТАТИВНУ ОЦЕНУ НАУЧНОГ ДОПРИНОСА КАНДИДАТА

### 4.1 Квалитет научних резултата

#### 4.1.1 Научни ниво и значај резултата, утицај научних радова

Др Милош Радоњић је у свом досадашњем раду објавио 17 радова М20 категорије у међународним часописима са ISI листе и 14 саопштења, од којих 1 у категорији М21а, 14 у категорији М21, 2 у категорији М22, 1 у категорији М32 и 13 у категорији М34.

У периоду након одлуке Научног већа о предлогу за стицање претходног научног звања, др Милош Радоњић је објавио 17 радова у међународним часописима са ISI листе и саопштења на међународним конференцијама, од којих 1 у категорији М21а, 8 у категорији М21, 1 у категорији М32 и 7 у категорији М34.

Као пет најзначајнијих радова кандидата могу се узети:

1. **M. M. Radonjić**, D. Tanasković, V. Dobrosavljević and K. Haule, *Influence of disorder on incoherent transport near the Mott transition*, Phys. Rev. B **81**, 075118 (2010), цитиран 13 пута,
2. **M. M. Radonjić**, D. Tanasković, V. Dobrosavljević, G. Kotliar, and K. Haule, *Wigner-Mott Scaling of Transport Near the Two-dimensional Metal-insulator Transition*, Phys. Rev. B **85**, 085133 (2012), цитиран 14 пута,
3. N. Lazarević, **M. M. Radonjić**, D. Tanasković, R. Hu, C. Petrovic and Z. V. Popović, *Lattice Dynamics of FeSb<sub>2</sub>*, J. Phys. Cond. Matt. **24**, 255402 (2012),
4. W. H. Appelt, A. Droghetti, L. Chioncel, **M. M. Radonjić**, E. Munoz, S. Kirchner, D. Vollhardt, and I. Rungger: *Predicting the Conductance of Strongly Correlated Molecules: the Kondo Effect in Perchlorotriphenylmethyl/Au Junctions*, Nanoscale **10**, 17738 (2018), цитиран 1 пут,
5. R. Khasanov, **M. M. Radonjić**, H. Luetkens, E. Morenzoni, G. Simutis, S. Schoenecker, W. H. Appelt, A. Ostlin, L. Chioncel, and A. Amato: *Superconducting Nature of the Bi-II Phase of Elemental Bismuth*, Phys. Rev. B **99**, 174506 (2019), цитиран 1 пут.

Први рад је био полазна основа докторске дисертације кандидата. У њему је испитиван међусобни утицај неуређености и јаких електронских корелација (интеракција) на метал-изолатор прелаз. Помоћу нумеричких симулација, кандидат је проучавао неуређени полупопуњени Хабардов модел у оквиру динамичке теорије средњег поља и њених уопштења. Користио је апроксимацију кохерентног потенцијала за случај слабе до умерене неуређености. Утврдио је да при константној интеракцији, неуређеност ефективно шири проводну зону и систем удаљава од Мотовог прелаза. Показао је да криве отпорности имају сличну немонотону температурну зависност у близини Мотовог прелаза као и у чистом случају и да вредност за максималну металну отпорност прелази квази-класичну Мот-Јофе-Регел границу за ред величине. Друдеов пик у оптичкој проводности опстаје чак и када је отпорност упоредива са Мот-Јофе-Регел границом. Ова теорија је успела да опише главни ефекат неуређености уочен у експериментима

на одређеним јакокорелисаним органским једињењима, а то је да са повећањем неуређености отпорност система опада (у случају слабе до умерене неуређености).

Други рад се бави природом метал-изолатор прелаза у дводимензионалним електронским гасовима и документује валидност Вигнер-Мот сценарија у овим системима. Наиме, кандидат је показао да читава фамилија експерименталних кривих отпорности у функцији температуре на *Si MOSFET*-има и *GaAs/AlGaAs* хетероструктурама може да се колапсира на једну криву, када се температура скалира са температуром кохеренције. Ова температура је процењена као температура на којој отпор достиже максимум. Утврдио је да је температура кохеренције инверзно пропорционална ефективној маси разређеног дводимензионалног електронском гаса у *Si MOSFET*-има. Сличне резултате је добио и анализом решења Хабардовог модела за Мотов метал-изолатор прелаз. Анализом теоријских и експерименталних резултата утврдио је да јако међуелектронско расејање, а не неуређеност, доминантно одређује особине *MOSFET*-а у широком интервалу концентрација и температура у близини  $2D$  метал-изолатор прелаза.

Трећи рад је теоријско експериментални. Представља детаљну студију динамике решетке дихалкогенида коју је кандидат реализовао помоћу прорачуна из првих принципа и пертурбативне теорије функционала густине. Теоријски резултати су омогућили правилну асигнацију експерименталних фононских мода, као и допринели објашњењу аномалија уочених у експерименталном спектру. Истовремено је приказано одлично слагање између теоријских и експерименталних резултата.

Четврти рад уводи оквир за истраживање јакокорелисаних наносистема из првих принципа. У њему је кандидат радио на развијању метода за израчунавање равнотежних и неравнотежних особина јакокорелисаних нано система на ниским температурама из првих принципа. Метод комбинује теорију функционала густине, теорију квантног транспорта, прорачуне нумеричке ренормализационе групе и ренормализовану теорију суперпертурбације. Кандидат је осмислио и развио начин да укомбинује теорију функционала густине у неравнотежној поставци са теоријом Андерсонове нечистоће (*Anderson impurity AI*), користећи теорију квантног транспорта. Помоћу *AI* теорије је укључио многочестичне ефекте и ефекте јаких локалних корелација. Реализовао је *AI* користећи прорачуне нумеричке ренормализационе групе за равнотежне системе. То је омогућило израчунавање карактеристичних транспортних особина (измењених под утицајем јаких локалних корелација) и Кондо температуре. Водио је испитивање утицаја различитих геометрија интерфејса (на атомском нивоу) између молекула и електрода, што је довело до доброг слагања Кондо температуре и транспортних особина са експериментом. Уз минималне измене, овај метод може да се примени и на истраживање транспортних особина хетероструктура. Поредио је овако добијене резултате са неравнотежним прорачунима (*rSPT*), да би проценио област поузданости равнотежних прорачуна трансмисије (*DFT+NRG*) за проводност на коначном напону. Резултати показују да овај метод омогућава квалитативан увид у особине спојева молекула са металима када су ти спојеви аморфни, или недовољно одређени и да може да пружи и пун квантитативни опис експеримента када је контакт добро карактеризован.

Пети рад представља истраживање суперпроводних стања елементалних једињења. У конкретном случају испитивано је суперпроводно стање бизмута под притиском. Због својих особина и чињенице да је компензовани полуметал и има изражену спин-орбит интеракцију, бизмут је, у много чему, јединствен елемент и под притиском пролази кроз више структурних фазних прелаза. У овом раду кандидат је истраживао природу суперпроводности моноклиничне фазе бизмута (*Bi-II*) која се реализује под притиском од  $2.80 \text{ GPa}$ . Помоћу Елиашбергове теорије, а полазећи од првих принципа, израчунао је, поред других карактеристичних особина, критичну температуру суперпроводности и критично магнетно поље који се одлично слажу са експерименталним вредностима и тиме подржао експерименталне налазе. То је од изузетне важности, јер се ова фаза тешко реализује у експерименталним условима и постоје индиције да је метастабилна. Такође је и испитао утицај спин-орбит интеракције, за коју се испоставило да игра веома значајну улогу у овом систему.

#### 4.1.2 Позитивна цитираност научних радова кандидата

Према бази података Web of Science на дан 30. октобра 2019. године, радови кандидата су цитирани укупно 109 пута, односно 100 пута не рачунајући самоцитате. Према истој бази, Хиршов индекс кандидата је 7. Релевантни подаци о цитираности са интернет странице Web of Science базе су дати након списка свих радова (одељак 6).

#### 4.1.3 Параметри квалитета часописа

Битан елемент за процену квалитета научних резултата је и квалитет часописа у којима су радови објављени, односно њихов импакт фактор – ИФ. У категоријама M21a, M21, M22, M32 и M34 кандидат је објавио радове у следећим часописима, при чему су подвучени бројеви односе на радове објављене након одлуке Научног већа о предлогу за стицање претходног научног звања:

- 1 рад у *Nanoscale* (ИФ = 7.367),
- 6 + 4 радова у *Physical Review B* (ИФ = 3.836 за 4 рада, ИФ = 3.736 за 2 рада, ИФ = 3.767 за 2 рада, ИФ = 3.774 за 2 рада),
- 1 + 2 рада у *Journal of Physics: Condensed Matter* (ИФ = 2.346 за 1 рад, ИФ = 2.546 за 2 рада),
- 1 рад у *Journal of Nanoparticle Research* (ИФ = 2.278),
- 1 рад у *Solid State Communications* (ИФ = 1.897),
- 1 рад у *Spectrochimica Acta. Part A: Molecular and Biomolecular Spectroscopy* (ИФ = 2.353),
- 2 + 2 рада у *Symposium on Condensed Matter Physics – SFKM* (без ИФ),
- 5 рада у *DPG Spring Meeting* (без ИФ),
- 1 + 1 рад у *APS March Meeting* (без ИФ),
- 1 рад у *New Generation in Strongly-Correlated Electron Systems* (без ИФ),
- 2 рада у *HP-SEE User Forum 2012* (без ИФ),

Укупан фактор утицаја радова кандидата је 59.231, а у периоду након одлуке Научног већа о предлогу за стицање претходног научног звања тај фактор је 34.807. Часописи у којима је кандидат објављивао су по свом угледу веома цењени у областима којима припадају. Међу њима се посебно истичу: *Nanoscale*, *Physical Review B*, *Journal of Physics: Condensed Matter* и *Journal of Nanoparticle Research*.

Додатни библиометријски показатељи у вези са објављеним радовима кандидата након одлуке Научног већа о предлогу за стицање претходног научног звања дати су у доњој табели. Она садржи импакт факторе (ИФ) радова, М бодове радова по српској категоризацији научноистраживачких резултата, као и импакт фактор нормализован по импакту цитирајућег чланка (СНИП). У табели су дате укупне вредности, као и вредности свих фактора усредњених по броју чланака и по броју аутора по чланку, за радове објављене у категоријама М20.

	ИФ	М	СНИП
Укупно	34.807	74	10.301
Усредњено по чланку	3.867	8.222	1.145
Усредњено по аутору	3.852	8.161	1.132

#### 4.1.4 Степен самосталности и степен учешћа у реализацији радова у научним центрима у земљи и иностранству

Кандидат је водећи аутор 9 радова, други аутор 6 радова, трећи аутор 2 рада, четврти аутор 9 радова, пети аутор 4 рада и шести аутор 1 рада, од укупно 31 рада. На радовима који су објављени у периоду након одлуке Научног већа о предлогу за стицање претходног звања, кандидат је водећи аутор 3 рада, други аутор 2, трећи аутор 1 рада, четврти аутор 6 радова, пети аутор 4 рада и шести аутор 1 рада, од укупно 17 радова. У експериментално теоријским радовима где је кандидат други, трећи, четврти, или пети аутор је у ствари први од аутора који су били задужени за прорачуне, теоријски део рада и поређење са експериментом. Таквих радова је 7.

При изради свих публикација др Милош Радоњић је учествовао у конкретној формулацији проблема, дискусији, његовом решавању применом обимних нумеричких симулација и апроксимативних аналитичких техника, анализи добијених података (и поређењу са експериментима у одређеним случајевима), као и у самом писању.

Током израде докторске дисертације у Лабораторији за примену рачунара у науци, кандидат је дао кључан допринос разумевању утицаја неуређености у јакокорелисаним материјалима и међусобне конкуренције између јаких корелација и неуређености. Такође је показао да су јаке корелације најзначајнији механизам који у многоструко одређује транспортне особине дводимензионалних електронских гасова и подржао је слику Вигнер-Мот сценарија у овим системима. Током завршних година израде докторске тезе, кандидат је успоставио плодотворну сарадњу са Центром за физику чврстог стања и нове материјале са института за физику. У оквиру те сарадње су проучаване електронске особине и динамика решетке углавном дијалкогенида, и 122 суперпроводника. Кандидат је имао значајну улогу у вођењу дипломске тезе Наташе Белић.

Током постдокторског усавршавања у групи проф. Дитера Фолхарда и проф. Ливију Киончела, кандидат је радио на истраживањима утицаја јаких корелација на разне материјале у равнотежној и неравнотежној поставци. Коришћени методи су базирани на прорачунима из првих принципа у комбинацији са методима који урљчунавају јаке електронске корелације базиране на Динамичкој теорији средњег поља. Ово су врло актуелне теме, а теоријска истраживања система у неравнотежној поставци су раном развоју. По повратку кандидат је наставио сарадњу са групом проф. Ливиу Киончела, из Аугсбурга, Немачка са којим има билатерални пројекат. Сарадња са Центром за физику чврстог стања и нове материјале је актуелна све време од успостављања и проширена на групу проф. Руди Хакела са Валтер Мајснер института у Гархингу, Минхен, Немачка.

Кандидат има међународну сарадњу са проф. Ливију Киончелом у Аугсбургу, проф. Дитером Фолхардом у Аугсбургу, проф. Иваном Рунгером у Лондону, проф. Руди Хакелом у Минхену и др. Рустемем Кашановим са Пол Шерер института у Вилигену у Швајцарској. Скорашњи радови настали као резултат међународне сарадње су видни у листи публикација кандидата, док је неколико радова тренутно у фази припреме.

#### **4.2 Ангажовање у формирању научних кадрова**

Кандидат др Милош Радоњић је имао значајну улогу у вођењу дипломске тезе Наташе Белић што се може видети у захвалници тезе.

Прилог: дипломска теза Наташе Белић, захвалница.

За време постдокторског боравка на Универзитету у Аугсбургу, кандидат је активно учествовао у настави на основним, студијама Физичког факултета. Био је асистент-тутор на вежбама из више предмета, као и асистент који припрема материјале, испите.

#### **4.3 Нормирање броја коауторских радова, патената и техничких решења**

17 радова кандидата објављених након одлуке Научног већа о предлогу за стицање претходног научног звања, спадају у следеће категорије:

- у категорију радова са нумеричким симулацијама који се признају са пуним бројем М бодова до пет коаутора спадају радови [1, 6, 7, 20, 22, 23, 24, 25] и нормирани су у складу са Правилником,
  - у категорију експерименталних радова у природно-математичким наукама који се признају са пуним бројем М бодова до седам коаутора спадају радови [2, 3, 4, 5, 8, 9, 18, 19, 21] и нормирани су у складу са Правилником.
- Након нормирања према Правилнику, број М бодова које је кандидат остварио након одлуке Научног већа о предлогу за стицање претходног научног звања се мења са 79 на 52.42, односно и после нормирања кандидат има већи број бодова од захтеваног. Притом треба узети у обзир да је у већини радова укључено 3 или више различитих група из различитих институција.

#### **4.4 Руковођење пројектима, потпројектима и пројектним задацима**

Кандидат руководи билатералним пројектом са Немачком под називом „Неравнотежни транспорт јококорелисаних полуметаличних система“.

Прилог: Обавештење министарства о одобреном билатералном пројекту

Кандидат учествује на пројекту ON171017: „Моделирање и Нумеричке Симулације сложених вишечестичних система“.

#### **4.5 Активност у научним и научно-стручним друштвима**

Кандидат је члан Одсека за примењену и рачунарску физику Друштва физичара Србије.

Прилог: писмо члановима одсека Друштва физичара Србије.

Рецензент је за часописе *Physical Review A*, *Physical Review B* и *Physical Review E* Америчког друштва физичара.

Прилог: писма уредништва часописа рецензенту.

#### **4.6 Утицајност научних резултата**

Утицајност научних резултата кандидата је наведена у одељку 4.1 овог документа. Пун списак радова је дат у одељку 6, а подаци о цитираности са интернет странице Web of Science базе су дати након списка свих радова кандидата.

#### **4.7 Конкретан допринос кандидата у реализацији радова у научним центрима у земљи и иностранству**

Кандидат је значајно допринео сваком раду у чијој припреми је учествовао. Сви радови објављени у периоду након одлуке Научног већа Института за физику о предлогу за стицање претходног научног звања су урађени у сарадњи са колегама из земље и иностранства. Др Радоњић је имао кључни допринос публикацијама на којима је први аутор (3 рада) и други аутор (2 рада). Такође је имао кључан допринос у теоријско, експерименталним радовима у којима је трећи, четврти, или пети аутор, а у ствари је први од аутора који су били задужени за прорачуне, теоријски део рада и поређење са експериментом (7 радова). Током израде ових радова, кандидат је битно утицао на сам ток истраживања, радио на развоју и извођењу одговарајућих нумеричких симулација, анализи релевантних података и дискусији, на теоријским и аналитичким прорачунима, методима и техникама приступа проблемима, писању радова, а такође је учествовао и у комуникацији са рецензентима приликом припреме радова за објављивање.

#### **4.8 Уводна предавања на конференцијама и друга предавања**

У периоду након одлуке Научног већа о предлогу за стицање претходног звања, кандидат је одржао следеће предавање по позиву на међународном скупу, које је штампано у изводу (категорија М32):

- **Miloš M. Radonjić**, Rustem Khasanov, Liviu Chioncel and Alex Amato, *Superconducting Nature of Elemental Bismuth Under Pressure*, The 20th Symposium on Condensed Matter Physics – SFKM 2019, Belgrade, Serbia.

Прилог: позивно писмо, листа позваних предавача са интернет стране и извод из књиге апстраката са апстрактном и програмским комитетом.

Кандидат је такође одржао и предавање по позиву на Институту за Физику, Универзитета у Аугсбургу:

- **Miloš Radonjić**, *Phonon anomalies in FeS*, 11.12.2017, Institute of Physics Augsburg, University of Augsburg, Augsburg, Germany.

Остала саопштења кандидата на међународним конференцијама (категорија M34):

- **Milos Radonjic**, Ivan Rungger, and Liviu Chioncel, *Non-Equilibrium transport study in strongly correlated hetero structures*, 80th Annual Conference of the DPG and DPG Spring Meeting, Regensburg, Germany, 6 - 11 March 2016, TT – 78.59.
- **Milos Radonjic**, Darko Tanaskovic, and Vladimir Dobrosavljevic, *Influence of strong disorder on incoherent transport near the Mott transition: Statistical DMFT approach*, 79th Annual Meeting of the DPG and DPG Spring Meeting, Berlin, Germany, 15 - 20 March 2015, TT – 71.16.

Пре почетка постдока у Аугсбургу кандидат је одржао предавање на Институту за физику Универзитета у Аугсбургу:

- **Miloš Radonjić**, *Influence of disorder on charge transport in strongly correlated materials near the metal-insulator transition*, 15.10.2014, Institute of Physics Augsburg, University of Augsburg, Augsburg, Germany.



**5. ЕЛЕМЕНТИ ЗА КВАНТИТАТИВНУ ОЦЕНУ НАУЧНОГ ДОПРИНОСА  
КАНДИДАТА**

**Остварени резултати у периоду након одлуке Научног већа о предлогу за стицање претходног научног звања:**

Категорија	М бодова по раду	Број радова	Укупно М бодова	Нормирани број М бодова
M21a	10	1	10	6.25
M21	8	8	64	42.24
M32	1.5	1	1.5	1.5
M34	0.5	7	3.5	2.43

**Поређење са минималним квантитативним условима за избор у звање виши научни сарадник:**

Минимални број М бодова		Остварено, М бодова без нормирања	Остварено, нормирани број М бодова
Укупно	50	79	52.42
M10+M20+M31+M32+M33+M41+M42+M90	40	75.5	49.99
M11+M12+M21+M22+M23	30	74	48.49

Према бази података Web of Science на дан 31. октобра 2019. године, радови кандидата су цитирани укупно 109 пута, односно 100 пута не рачунајући самоцитате. Према истој бази, Хиршов индекс кандидата је 7.

## 6. СПИСАК РАДОВА ДР МИЛОША РАДОЊИЋА

### 6.1 Радови у међународним часописима изузетних вредности (M21a)

#### Радови објављени након претходног избора у звање:

- [1] W. H. Appelt, A. Droghetti, L. Chioncel, **M. M. Radonjić**, E. Munoz, S. Kirchner, D. Vollhardt, and I. Rungger: *Predicting the Conductance of Strongly Correlated Molecules: the Kondo Effect in Perchlorotriphenylmethyl/Au Junctions*, *Nanoscale* **10**, 17738 (2018) (ИФ = 7.367 за 2016. годину).

### 6.2 Радови у врхунским међународним часописима (M21)

#### Радови објављени након претходног избора у звање:

- [2] R. Khasanov, **M. M. Radonjić**, H. Luetkens, E. Morenzoni, G. Simutis, S. Schoenecker, W. H. Appelt, A. Ostlin, L. Chioncel, and A. Amato: *Superconducting Nature of the Bi-II Phase of Elemental Bismuth*, *Phys. Rev. B* **99**, 174506 (2019) (ИФ = 3.836 за 2016. годину).
- [3] A. Baum, A. Milosavljević, N. Lazarević, **M. M. Radonjić**, B. Nikolić, M. Mitschek, Z. Inanloo Maranloo, M. Scepanović, M. Grujić-Brojčin, N. Stojilović, M. Opel, Aifeng Wang, C. Petrovic, Z. V. Popović, and R. Hackl: *Phonon Anomalies in FeS*, *Phys. Rev. B* **97**, 054306 (2018) (ИФ = 3.836 за 2016. годину).
- [4] М. Опацић, N. Lazarević, D. Tanasković, **M. M. Radonjić**, A. Milosavljević, Y. Ma, C. Petrovic, and Z. V. Popović: *Small Influence of Magnetic Ordering on Lattice Dynamics in TaFe<sub>1.25</sub>Te<sub>3</sub>*, *Phys. Rev. B* **96**, 174303 (2017) (ИФ = 3.836 за 2016. годину).
- [5] М. Опацић, N. Lazarević, **M. M. Radonjić**, M. Scepanović, H. Ryu, A. Wang, D. Tanasković, C. Petrovic and Z. V. Popović: *Raman Spectroscopy of K<sub>x</sub>Co<sub>2y</sub>Se<sub>2</sub> Single Crystals Near the Ferromagnetparamagnet Transition*, *J. Phys. Cond. Matt.* **28**, 485401 (2016) (ИФ = 2.346 за 2014. годину).
- [6] A. Östlin, W. H. Appelt, I. Di Marco, W. Sun, **M. Radonjić**, M. Sekania, L. Vitos, O. Tjernberg, and L. Chioncel: *The electronic structure of Palladium in the presence of many-body effects*, *Phys. Rev. B* **93**, 155152 (2016) (ИФ = 3.836 за 2016. годину).
- [7] L. Chioncel, C. Morari, A. Ostlin, W. H. Appelt, A. Droghetti, **M. M. Radonjić**, I. Rungger, L. Vitos, U. Eckern and A. V. Postnikov: *Transmission Through Correlated Cu<sub>n</sub>CoCu<sub>n</sub> Heterostructures*, *Phys. Rev. B* **92**, 054431 (2015) (ИФ = 3.736 за 2014. годину).

- [8] Z. V. Popović, M. Šćepanović, N. Lazarević, M. Opacić, **M. M. Radonjić**, D. Tanasković, H. Lei and C. Petrovic: *Lattice Dynamics of BaFe<sub>2</sub>X<sub>3</sub> (X=S,Se) Compounds*, Phys. Rev. B **91**, 064303 (2015) (ИФ = 3.736 за 2014. годину).
- [9] Z. V. Popovic, M. Grujić-Brojcin, N. Paunovic, **M. M. Radonjić**, V. D. Araujo, M. I. B. Bernardi, M. M. de Lima and A. Cantarero: *Far-infrared Spectroscopic Study of CeO<sub>2</sub> Nanocrystals*, J. Nanopart. Res. **17**, 23 (2015) (ИФ = 2.278 за 2013. годину).

#### Радови објављени пре претходног избора у звање:

- [10] Z. V. Popović, M. Šćepanović, N. Lazarević, **M. M. Radonjić**, D. Tanasković, and C. Petrovic, *Phonon and magnetic dimer excitations in new Fe-based S=2 spin ladder compound BaFe<sub>2</sub>Se<sub>2</sub>O*, Phys. Rev. B **89**, 014301 (2014) (ИФ = 3.736 за 2014. годину).
- [11] N. Lazarević, **M. M. Radonjić**, M. Šćepanović, H. Lei, D. Tanasković, C. Petrovic, and Z. V. Popović, *Lattice dynamics of KNi<sub>2</sub>Se<sub>2</sub> single crystal*, Phys. Rev. B **87**, 144305 (2013) (ИФ = 3.767 за 2012. годину).
- [12] N. Lazarević, **M. M. Radonjić**, D. Tanasković, R. Hu, C. Petrovic and Z. V. Popović, *Lattice Dynamics of FeSb<sub>2</sub>*, J. Phys. Cond. Matt. **24**, 255402 (2012) (ИФ = 2.546 за 2011. годину).
- [13] N. Lazarević, **M. M. Radonjić**, R. Hu, D. Tanasković, C. Petrovic, and Z. V. Popović, *Phonon Properties of CoSb<sub>2</sub> Single Crystals*, J. Phys. Cond. Matt. **24**, 135402 (2012) (ИФ = 2.546 за 2011. годину).
- [14] **M. M. Radonjić**, D. Tanasković, V. Dobrosavljević, G. Kotliar, and K. Haule, *Wigner-Mott Scaling of Transport Near the Two-dimensional Metal-insulator Transition*, Phys. Rev. B **85**, 085133 (2012) (ИФ = 3.774 за 2010. годину).
- [15] **M. M. Radonjić**, D. Tanasković, V. Dobrosavljević and K. Haule, *Influence of disorder on incoherent transport near the Mott transition*, Phys. Rev. B **81**, 075118 (2010) (ИФ = 3.774 за 2010. годину).

#### 6.3 Радови у истакнутим међународним часописима (M22)

##### Радови објављени пре претходног избора у звање:

- [16] J. J. Lazarević, S. Uskoković-Marković, M. Jelikić-Stankov, **M. M. Radonjić**, D. Tanasković, N. Lazarević, and Z.V. Popović, *Intermolecular and low-frequency intramolecular Raman scattering study of racemic ibuprofen*, Spectrosc. Acta Pt. A-Molec. Biomolec. Spectr., **126**, 301 (2014) (ИФ = 2.353 за 2014. годину).
- [17] Z. V. Popović, N. Lazarević, S. Bogdanović, **M. M. Radonjić**, D. Tanasković, R. Hu, H. Lei and C. Petrovic, *Signatures of the spin-phonon coupling in Fe<sub>1+y</sub>Tel-xSex Alloys*, Solid State Comm. **193**, 51 (2014) (ИФ = 1.897 за 2014. годину).

#### 6.4 Предавања по позиву са међународних скупова штампана у изводу (M32)

##### Саопштења објављена након претходног избора у звање:

- [18] **Miloš M. Radonjić**, Rustem Khasanov, Liviu Chioncel and Alex Amato, *Superconducting Nature of Elemental Bismuth Under Pressure*, The 20th Symposium on Condensed Matter Physics – SFKM 2019, Belgrade, Serbia

#### 6.5 Саопштења са међународних скупова штампана у изводу (M34)

##### Саопштења објављена након претходног избора у звање:

- [19] A. Baum, A. Milosavljević, N. Lazarević, **M. M. Radonjić**, B. Nikolić, M. Mitschek, Z. Inanloo Maranloo, M. Šćepanović, M. Grujić –Brojčin, N. Stojilović, M. Opela, Aifeng Wang, C. Petrovic, Z.V. Popović and R. Hackl, *Lattice dynamics and phonon anomalies in FeS*, The 20th Symposium on Condensed Matter Physics – SFKM 2019, Belgrade, Serbia
- [20] Andrea Droghetti, Wilhelm Appelt, Liviu Chioncel, **Miloš Radonjić**, Enrique Muñoz, Stefan Kirchner, David Jacob, Dieter Vollhardt, Angel Rubio, and Ivan Rungger, *First-principles quantum transport simulations including strong correlation effects*, DPG Spring Meeting, Regensburg, Germany, 31 March - 5 April 2019, O – 57.1
- [21] Leander Peis, Andreas Baum, Ana Milosavljević, Nenad Lazarević, **Miloš M. Radonjić**, Božidar Nikolić, Merlin Mitscheck, Zahra Inanloo Maranloo, Maja Šćepanović, Mirjana Grujić-Brojčin, Nenad Stojilović, Matthias Opel, Aifeng Wang, Cedimir Petrovic, Zoran V. Popović, and Rudi Hackl, *Phonon anomalies in FeS*, DPG Spring Meeting, Regensburg, Germany, 31 March - 5 April 2019, TT – 49.11
- [22] **Milos Radonjic**, Ivan Rungger, and Liviu Chioncel, *Non-Equilibrium transport study in strongly correlated hetero structures*, 80th Annual Conference of the DPG and DPG Spring Meeting, Regensburg, Germany, 6 - 11 March 2016, TT – 78.59
- [23] Andreas Östlin, Wilhelm Appelt, Igor di Marco, Weiwei Sun, **Milos Radonjic**, Michael Sekania, Levente Vitos, and Liviu Chioncel, *The electronic structure of palladium in the presence of many-body effects*, 80th Annual Conference of the DPG and DPG Spring Meeting, Regensburg, Germany, 6 - 11 March 2016, TT – 47.6
- [24] Ivan Rungger, **Milos Radonjic**, Wilhelm Appelt, Liviu Chioncel, Andrea Droghetti, *First principles electron transport simulations in the Kondo regime*, APS March Meeting 2016, Baltimore, Maryland, USA
- [25] **Milos Radonjic**, Darko Tanaskovic, and Vladimir Dobrosavljevic, *Influence of strong disorder on incoherent transport near the Mott transition: Statistical DMFT*

*approach*, 79th Annual Meeting of the DPG and DPG Spring Meeting, Berlin, Germany, 15 - 20 March 2015, TT – 71.16

**Саопштења објављена пре претходног избора у звање:**

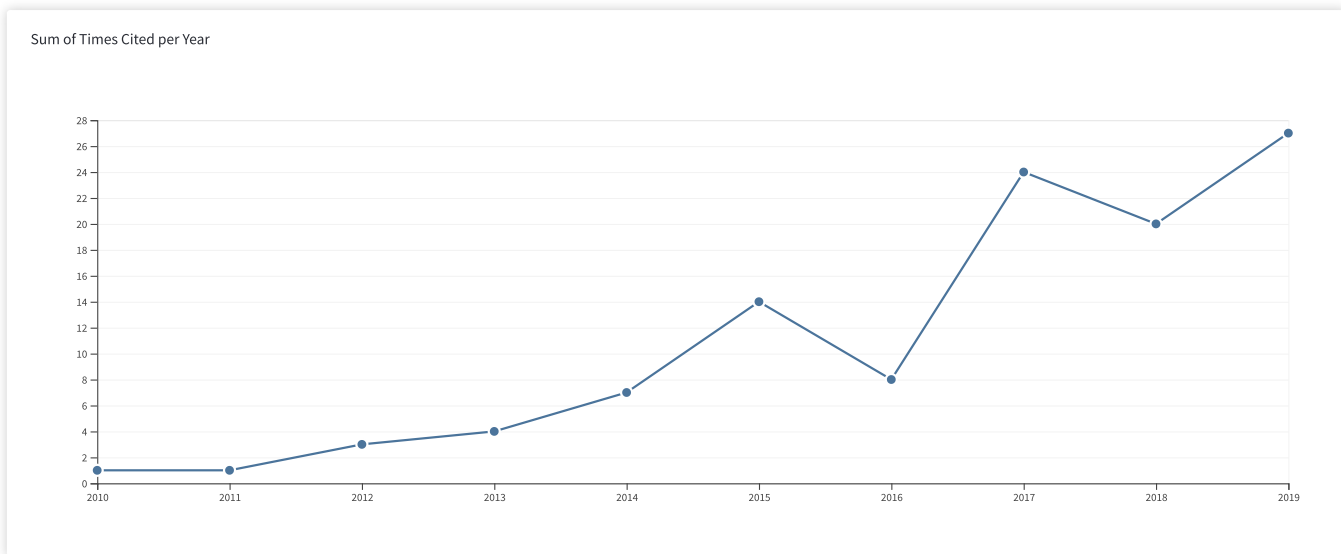
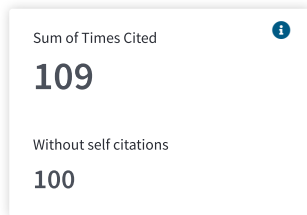
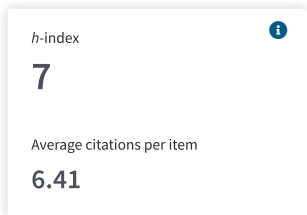
- [26] **M. M. Radonjić**, D. Tanasković, V. Dobrosavljević, G. Kotliar, and K. Haule, *Wigner-Mott Scaling of Transport Near the Two-dimensional Metal-insulator Transition*, APS March Meeting 2012, Boston, Massachusetts , USA.
- [27] **Miloš M. Radonjić**, N. Lazarević, D. Tanasković, Z. Popović, *Electronic Structure and Lattice Dynamics Calculations of FeSb<sub>2</sub> and CoSb<sub>2</sub>*, HP-SEE User Forum 2012, Belgrade, Serbia
- [28] Jaksa Vučićević, **Miloš Radonjić**, Tanasković Darko, *Iterative Perturbative Method for a Study of Disordered Strongly Correlated Systems*, HP-SEE User Forum 2012, Belgrade, Serbia
- [29] **Miloš Radonjić**, *Wigner-Mott Scaling of Transport Near the Two-dimensional Metal-insulator Transition*, New Generation in Strongly-Correlated Electron Systems, Workshop 2012, Portoroz, Slovenia, 25-29. 06. 2012.
- [30] **M. M. Radonjić**, D. Tanasković, V. Dobrosavljević, G. Kotliar, and K. Haule, *Wigner-Mott Scaling of Transport Near the Two-dimensional Metal-insulator Transition*, XVIII Symposium on Condensed Matter Physics – SFKM 2011, Belgrade, Serbia.
- [31] N. Lazarević, Z. V. Popović, **M. Radonjić**, D. Tanasković, Rongwei Hu, C. Petrovic, *Raman Scattering Study Of FeSb<sub>2</sub> Single Crystals*, XVIII Symposium on Condensed Matter Physics – SFKM 2011, Belgrade, Serbia.

Citation report for 17 results from Web of Science Core Collection between 1996 and 2020 Go

You searched for: From Marked List: ...More

This report reflects citations to source items indexed within Web of Science Core Collection. Perform a Cited Reference Search to include citations to items not indexed within Web of Science Core Collection.

Export Data: Save to Excel File



Sort by: Times Cited Date More

1 of 2

How are these totals calculated?

	2016	2017	2018	2019	2020	Total	Average Citations per Year
Use the checkboxes to remove individual items from this Citation Report							
or restrict to items published between 1996 and 2020 Go	8	24	20	27	0	109	10.90
<input type="checkbox"/> 1. <b>Lattice dynamics of KNi2Se2</b> By: Lazarevic, N.; Radonjic, M.; Scepanovic, M.; et al. PHYSICAL REVIEW B Volume: 87 Issue: 14 Article Number: 144305 Published: APR 22 2013	2	2	2	1	0	14	2.00
<input type="checkbox"/> 2. <b>Wigner-Mott scaling of transport near the two-dimensional metal-insulator transition</b> By: Radonjic, M. M.; Tanaskovic, D.; Dobrosavljevic, V.; et al. PHYSICAL REVIEW B Volume: 85 Issue: 8 Article Number: 085133 Published: FEB 29 2012	2	4	2	1	0	14	1.75
<input type="checkbox"/> 3. <b>Influence of disorder on incoherent transport near the Mott transition</b> By: Radonjic, Milos M.; Tanaskovic, D.; Dobrosavljevic, V.; et al. PHYSICAL REVIEW B Volume: 81 Issue: 7 Article Number: 075118 Published: FEB 2010	0	2	4	1	0	13	1.30
<input type="checkbox"/> 4. <b>Signatures of the spin-phonon coupling in Fe1+yTe1-xSex alloys</b> By: Popovic, Z. V.; Lazarevic, N.; Bogdanovic, S.; et al. SOLID STATE COMMUNICATIONS Volume: 193 Pages: 51-55 Published: SEP 2014	2	4	2	2	0	10	1.67
<input type="checkbox"/> 5. <b>Lattice dynamics of BaFe2X3(X = S, Se) compounds</b> By: Popovic, Z. V.; Scepanovic, M.; Lazarevic, N.; et al. PHYSICAL REVIEW B Volume: 91 Issue: 6 Article Number: 064303 Published: FEB 27 2015	1	3	2	3	0	9	1.80

<input type="checkbox"/>	6.	<b>Lattice dynamics of FeSb<sub>2</sub></b>	0	0	1	1	0	9	1.13
		By: Lazarevic, N.; Radonjic, M. M.; Tanaskovic, D.; et al. JOURNAL OF PHYSICS-CONDENSED MATTER Volume: 24 Issue: 25 Article Number: 255402 Published: JUN 27 2012							
<input type="checkbox"/>	7.	<b>Phonon anomalies in FeS</b>	0	0	2	5	0	7	3.50
		By: Baum, A.; Milosavljevic, A.; Lazarevic, N.; et al. PHYSICAL REVIEW B Volume: 97 Issue: 5 Article Number: 054306 Published: FEB 12 2018							
<input type="checkbox"/>	8.	<b>Intermolecular and low-frequency intramolecular Raman scattering study of racemic ibuprofen</b>	0	2	2	2	0	7	1.17
		By: Lazarevic, J. J.; Uskokovic-Markovic, S.; Jelikić-Stankov, M.; et al. SPECTROCHIMICA ACTA PART A-MOLECULAR AND BIOMOLECULAR SPECTROSCOPY Volume: 126 Pages: 301-305 Published: MAY 21 2014							
<input type="checkbox"/>	9.	<b>Phonon and magnetic dimer excitations in Fe-based S = 2 spin-ladder compound BaFe<sub>2</sub>Se<sub>2</sub>O</b>	0	1	0	3	0	7	1.17
		By: Popovic, Z. V.; Scepanovic, M.; Lazarevic, N.; et al. PHYSICAL REVIEW B Volume: 89 Issue: 1 Article Number: 014301 Published: JAN 3 2014							
<input type="checkbox"/>	10.	<b>Transmission through correlated CunCoCun heterostructures</b>	1	3	1	0	0	5	1.00
		By: Chioncel, L.; Morari, C.; Ostlin, A.; et al. PHYSICAL REVIEW B Volume: 92 Issue: 5 Article Number: 054431 Published: AUG 24 2015							

Select Page



Save to Excel File

Sort by: Times Cited Date More

◀ 1 of 2 ▶

17 records matched your query of the 45,842,562 in the data limits you selected.

Clarivate

Accelerating innovation

© 2019 Clarivate Copyright notice Terms of use Privacy statement Cookie policy

Sign up for the Web of Science newsletter Follow us



Citation report for 17 results from Web of Science Core Collection between 1996 and 2020 Go

You searched for: From Marked List: ...More

This report reflects citations to source items indexed within Web of Science Core Collection. Perform a Cited Reference Search to include citations to items not indexed within Web of Science Core Collection.

Sort by: Times Cited Date More

2 of 2

How are these totals calculated?

	2016	2017	2018	2019	2020	Total	Average Citations per Year
Use the checkboxes to remove individual items from this Citation Report							
or restrict to items published between 1996 and 2020 Go	8	24	20	27	0	109	10.90
<input type="checkbox"/> 11. <b>Electronic structure of palladium in the presence of many-body effects</b> By: Oestlin, A.; Appelt, W. H.; Di Marco, I.; et al. PHYSICAL REVIEW B Volume: 93 Issue: 15 Article Number: 155152 Published: APR 25 2016	0	1	2	1	0	4	1.00
<input type="checkbox"/> 12. <b>Raman spectroscopy of KxCo2-ySe2 single crystals near the ferromagnet-paramagnet transition</b> By: Opacic, M.; Lazarevic, N.; Radonjic, M. M.; et al. JOURNAL OF PHYSICS-CONDENSED MATTER Volume: 28 Issue: 48 Article Number: 485401 Published: DEC 7 2016	0	2	0	1	0	3	0.75
<input type="checkbox"/> 13. <b>Phonon properties of CoSb2 single crystals</b> By: Lazarevic, N.; Radonjic, M. M.; Hu, Rongwei; et al. JOURNAL OF PHYSICS-CONDENSED MATTER Volume: 24 Issue: 13 Article Number: 135402 Published: APR 4 2012	0	0	0	2	0	3	0.38
<input type="checkbox"/> 14. <b>Superconducting nature of the Bi-II phase of elemental bismuth</b> By: Khasanov, Rustem; Radonjic, Milos M.; Luetkens, Hubertus; et al. PHYSICAL REVIEW B Volume: 99 Issue: 17 Article Number: 174506 Published: MAY 13 2019	0	0	0	1	0	1	1.00
<input type="checkbox"/> 15. <b>Predicting the conductance of strongly correlated molecules: the Kondo effect in perchlorotriphenylmethyl/Au junctions</b> By: Appelt, W. H.; Droghetti, A.; Chioncel, L.; et al. NANOSCALE Volume: 10 Issue: 37 Pages: 17738-17750 Published: OCT 7 2018	0	0	0	1	0	1	0.50
<input type="checkbox"/> 16. <b>Small influence of magnetic ordering on lattice dynamics in TaFe1.25Te3</b> By: Opacic, M.; Lazarevic, N.; Tanaskovic, D.; et al. PHYSICAL REVIEW B Volume: 96 Issue: 17 Article Number: 174303 Published: NOV 16 2017	0	0	0	1	0	1	0.33
<input type="checkbox"/> 17. <b>Far-infrared spectroscopic study of CeO2 nanocrystals</b> By: Popovic, Z. V.; Grujic-Brojcin, M.; Paunovic, N.; et al. JOURNAL OF NANOPARTICLE RESEARCH Volume: 17 Issue: 1 Article Number: 23 Published: JAN 13 2015	0	0	0	1	0	1	0.20

Select Page | Save to Excel File

Sort by: Times Cited Date More

2 of 2

17 records matched your query of the 45,842,562 in the data limits you selected.





Република Србија  
МИНИСТАРСТВО ПРОСВЕТЕ,  
НАУКЕ И ТЕХНОЛОШКОГ РАЗВОЈА  
Комисија за стицање научних звања

Број:660-01-00042/506

26.02.2015. године

Београд

ИНСТИТУТ ЗА ФИЗИКУ			
ПРИМЉЕНО: 25-03-2015			
Ред. јед.	број	Лох. шифра	рилог
0801	361/1		

На основу члана 22. става 2. члана 70. став 5. Закона о научноистраживачкој делатности ("Службени гласник Републике Србије", број 110/05 и 50/06 – исправка и 18/10), члана 2. става 1. и 2. тачке 1 – 4.(прилози) и члана 38. Правилника о поступку и начину вредновања и квантитативном исказивању научноистраживачких резултата истраживача ("Службени гласник Републике Србије", број 38/08) и захтева који је поднео

*Инстџиџуџ за физику у Београду*

Комисија за стицање научних звања на седници одржаној 26.02.2015. године, донела је

**ОДЛУКУ  
О СТИЦАЊУ НАУЧНОГ ЗВАЊА**

***Др Милош Радоњић***

стиче научно звање

***Научни сарадник***

у области природно-математичких наука - физика

**О Б Р А З Л О Ж Е Њ Е**

*Инстџиџуџ за физику у Београду*

утврдио је предлог број 1193/1 од 23.09.2014. године на седници научног већа Института и поднео захтев Комисији за стицање научних звања број 1249/1 од 03.10.2014. године за доношење одлуке о испуњености услова за стицање научног звања ***Научни сарадник***.

Комисија за стицање научних звања је по претходно прибављеном позитивном мишљењу Матичног научног одбора за физику на седници одржаној 26.02.2015. године разматрала захтев и утврдила да именовани испуњава услове из члана 70. став 5. Закона о научноистраживачкој делатности ("Службени гласник Републике Србије", број 110/05 и 50/06 – исправка и 18/10), члана 2. става 1. и 2. тачке 1 – 4.(прилози) и члана 38. Правилника о поступку и начину вредновања и квантитативном исказивању научноистраживачких резултата истраживача ("Службени гласник Републике Србије", број 38/08) за стицање научног звања ***Научни сарадник***, па је одлучила као у изреци ове одлуке.

Доношењем ове одлуке именовани стиче сва права која му на основу ње по закону припадају.

Одлуку доставити подносиоцу захтева, именованом и архиви Министарства просвете, науке и технолошког развоја у Београду.

**ПРЕДСЕДНИК КОМИСИЈЕ**

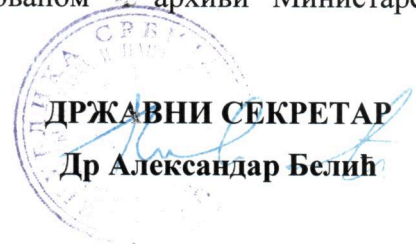
**Др Станислава Стошић-Грујичић,**

**научни саветник**

*С. Стошић-Грујичић*

**ДРЖАВНИ СЕКРЕТАР**

**Др Александар Белић**

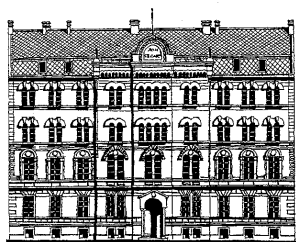


Diplomski rad

# Određivanje fononskog spektra gvožđe-telurida

Student: Nataša Belić

Mentor: Darko Tanasković



Fizički fakultet  
Univerzitet u Beogradu

*Ovaj diplomski rad urađen je u Laboratoriji za primenu računara u nauci na Institutu za fiziku u Beogradu. Posebno bih želela da se zahvalim mentoru dr Darku Tanaskoviću na rukovođenju izrade ovog rada, kolegi Milošu Radonjiću na velikoj pomoći prilikom realizacije teze, kao i kolegi Nenadu Lazareviću iz Centra za fiziku čvrstog stanja i nove materijale na Institutu za fiziku.*

*Ovaj rad posvećujem mojoj dragoj porodici i voljenom Vanji zbog njihove ljubavi, razumevanja i izuzetne podrške tokom svih ovih godina.*

*U Beogradu, Maj 2012*

*Nataša Belić*



Република Србија  
МИНИСТАРСТВО ПРОСВЕТЕ,  
НАУКЕ И ТЕХНОЛОШКОГ  
РАЗВОЈА

Број: 451-03-01732/2017-09/5

Датум: 24.01.2018.

Београд, Немањина 22-26

Институт за физику  
- Др Милош Радоњић -

ИНСТИТУТ ЗА ФИЗИКУ			
ПРИМЉЕНО: 09-02-2018			
Рад.јед.	Б р о ј	Арх.шифра	Прилог
0801	173/1		

Прегревица 118  
11 000 Београд

Поштовани господине Радоњићу,

Обавештавамо Вас да је у оквиру Програма билатералне научне и технолошке сарадње између Републике Србије и Савезне Републике Немачке, а на основу спроведених процедура оцене пројеката у обе државе, усвојена листа за финансирање пројеката у двогодишњем периоду са почетком реализације од 01. јануара 2018. године.

Са задовољством Вас обавештавамо да је Ваш пројекат *“Неравнотежни транспорт јакокорелисаних полуметаличних система”* одобрен за финансирање.

Сврха боравка истраживача у Републици Србији, односно Савезној Републици Немачкој, по овом Јавном позиву, треба да допринесе даљем унапређењу сарадње и конституисању пројектног тима, уз учешће младих истраживача, као и генерисању новог пројектног предлога којим би се конкурисало у програму HORIZON 2020 или другим програмима са међународним финансирањем.

У склопу овог Програма, Министарство просвете, науке и технолошког развоја Републике Србије, финансираће трошкове превоза српских истраживача између седишта институција које сарађују и трошкове смештаја и дневница за немачке истраживаче. На српској страни, максимална предвиђена издвајања по пројектном циклусу су у износу до 3.000 евра у динарској противвредности.

Немачка страна сносиће трошкове превоза немачких истраживача између седишта институција које сарађују и трошкове смештаја и дневница за српске истраживаче. На немачкој страни, максимална предвиђена издвајања по пројектном циклусу су у износу до 7.000 евра.

Захтеви за рефундацију трошкова путовања српских истраживача, односно трошкова боравка немачких истраживача, достављају се на обрасцу који можете преузети на интернет адреси Министарства, у огранку међународна научна сарадња, уз одговарајућу пратећу документацију.

Руководиоци одобрених пројеката за финансирање, дужни су да доставе годишњи и завршни извештај о реализацији пројекта, у року од 15 дана након завршетка пројектне године, односно након завршетка пројекта, у форми која се, такође, налази на интернет адреси Министарства. Саставни део извештаја су и прилози који садрже резултате билатералног пројекта нпр.: листа учесника заједничке радионице и агенда; апстракт са листом учесника, називом пројекта и називом потенцијалног програма или јавног позива на који се аплицира са темом која проистиче из ове сарадње; радна верзија или копија објављеног рада у међународном часопису и/или међународној конференцији, и др.

Информација о свим одобреним пројектима објављена је на интернет страници Министарства просвете, науке и технолошког развоја.

Истовремено бих желео да Вам честитам на одобреном пројекту и пожелим успешну реализацију пројектних активности.

С поштовањем,

  
МИНИСТАР  
Младен Шарчевић

**Subject:** sednica Saveta DFS za naucna istrazivanja i visoko obrazovanje

**From:** "Tatjana Vukovic" <tanja37@rcub.bg.ac.rs>

**Date:** 12/9/16, 10:28 PM

**To:** yqoq@afrodita.rcub.bg.ac.rs, ljubica.davidovic@ipb.ac.rs, igor.franovic@ipb.ac.rs, cevizd@vinca.rs, tanja37@rcub.bg.ac.rs, mpantic@df.uns.ac.rs, dugic@kg.ac.rs, nenad81@pmf.ni.ac.rs, adzic@ff.bg.ac.rs, nenad.vranjes@ipb.ac.rs, marko.vojinovic@ipb.ac.rs, ibozovic@vinca.rs, majab@ipb.ac.rs, jovana.nikolov@df.uns.ac.rs, savovic@kg.ac.rs, ddrag@pmf.ni.ac.rs, kstankovic@etf.bg.ac.rs, lpopovic@aob.bg.ac.rs, vladimir.sreckovic@ipb.ac.rs, vborka@vinca.rs, prodanvc@df.uns.ac.rs, jovana.petrovic@df.uns.ac.rs, ssimic@kg.ac.rs, dgaja@junis.ni.ac.rs, micic@aob.rs, zcvetkovic@aob.bg.ac.rs, marija.mitrovic@ipb.ac.rs, ivana.vasic@scl.rs, ivana.vidanovic@ipb.ac.rs, natasabi@vinca.rs, bradaric@vinca.rs, djordjes@ff.bg.ac.rs, knez@ff.bg.ac.rs, milica@df.uns.ac.rs, skubi@uns.ac.rs, tosa@kg.ac.rs, jovana@etf.bg.ac.rs, mancev@pmf.ni.ac.rs, jelena.maljkovic@ipb.ac.rs, sanja.tosic@ipb.ac.rs, dusborka@vinca.rs, galijas@ff.bg.ac.rs, hekata@ff.bg.ac.rs, savke@uns.ac.rs, ristic@kg.ac.rs, ljupcoh@vinca.rs, marina.lekic@ipb.ac.rs, aleksandar.krmpot@ipb.ac.rs, jovanap@vinca.rs, asimovic@kg.ac.rs, matavulj@etf.bg.ac.rs, brdrljaca@gmail.com, gsasa@pmf.ni.ac.rs, nikola.skoro@ipb.ac.rs, srdjan.marjanovic@ipb.ac.rs, ebukvic@ff.bg.ac.rs, obrat@ff.bg.ac.rs, teodora.gajo@df.uns.ac.rs, kovac@kg.ac.rs, cvetic\_j@etf.bg.ac.rs, Emilija.Zivanovic@elfak.ni.ac.rs, marko.nikolic@ipb.ac.rs, milos.radonjic@ipb.ac.rs, bobagal@vinca.rs, m.mudrinic@vinca.rs, nizoran@ff.bg.ac.rs, sstevan@ff.bg.ac.rs, zokip@pmf.ni.ac.rs, mkradovic@junis.ni.ac.rs, nstevanovic@kg.ac.rs, arsosk@etf.bg.ac.rs, kuki@ff.bg.ac.rs, zoran.mijic@ipb.ac.rs, momirm@vinca.rs, goran\_poparic@ff.bg.ac.rs, natasa.todorovic@df.uns.ac.rs, draganastrbac@uns.ac.rs, pavlovic@pmf.ni.ac.rs, dragana@kg.ac.rs, goran.istic@elfak.ni.ac.rs, ljiljana.gulan@pr.ac.rs, nesiclj@pmf.ni.ac.rs, bojan.nikolic@ipb.ac.rs, sjokic@vin.bg.ac.rs, ilijamaric1@gmail.com, mico@ff.bg.ac.rs, imre.gut@df.uns.ac.rs, sogi@uns.ac.rs, vpetrovic@kg.ac.rs

Postovane kolege,

Zakazujem sednicu Saveta DFS za naucna istrazivanja i visoko obrazovanje

za petak 16. decembar u 16h,  
na Fizickom fakultetu u Beogradu, u Fizickom amfiteatru (soba 661).

Predlazem sledeci dnevni red:

1. Izbor sekretara Odeljenja
2. Obavestenje o Kongresu fizicara Srbije
3. Predlog za promenu Pravilnika o radu Odeljenja za NIVO
4. Izbor predsednika odseka
5. Razno

U prilogu je kompletan spisak clanova Odseka u Odeljenju sa e-mail adresama. Predsednici i sekretari Odseka koji su navedeni u spisku su kolege koji su do sada obavljale te funkcije, a i dalje su clanovi odseka.

Kako bismo bili efikasni, molim clanove svakog od Odseka da se pre sednice dogovore o predlogu za Predsednika svog odseka.

Za clanove DFS koji nisu iz Beograda, DFS snosi troskove puta: uz autobusku kartu, odnosno racun za gorivo, i to fiskalni i gotovinski na

Drustvo Fizicara Srbije  
Cara Dusana 13, Beograd  
PIB 107450409

Maksimalni iznos koji pokriva DFS za gorivo je 10 din. po kilometru.

Srdacan pozdrav,

Prof. dr Tatjana Vukovic

Predsednik Odeljenja

—Attachments:—

---

SastavNIVO\_2016-tabele.doc

27 bytes

**Subject:** Review\_request RADONJIC [REDACTED]

**From:** pra@aps.org

**Date:** 3/29/19, 1:44 PM

**To:** milos.radonjic@ipb.ac.rs

Re: [REDACTED]

Dear Dr. Radonjic,

We would appreciate your review of this manuscript, which has been submitted to Physical Review A.

Comments from the editor:

Does this manuscript contain enough new and significant physics to warrant publication in the Physical Review? We append the submittal letter from the authors.

Thank you for your help.

Yours sincerely,

Franco Dalfovo  
Associate Editor  
Physical Review A

Email: [pra@aps.org](mailto:pra@aps.org)

<https://journals.aps.org/pr/>

Opening for submissions soon, Physical Review Research is a new open access, multidisciplinary journal offering the Physical Review experience and quality you value and trust. Learn more and sign up for alerts.

<https://journals.aps.org/prresearch>

@PhysRevResearch on Twitter

We ask that you download the manuscript and return your report via:

[REDACTED]

ABSTRACT:



**Subject:** Resub\_review\_request RADONJIC [REDACTED]

**From:** prb@aps.org

**Date:** 5/11/17, 3:42 PM

**To:** milos.radonjic@ipb.ac.rs

Re: [REDACTED]

Dear Dr. Radonjic,

We would appreciate your review of this manuscript, which has been submitted to Physical Review B.

Comments from the editor:

We append previous correspondence, including your report. Is the response of the authors to all the previous recommendations satisfactory?

Thank you for your help.

Yours sincerely,

Ashot Melikyan  
Associate Editor  
Physical Review B  
Email: [prb@aps.org](mailto:prb@aps.org)  
<http://journals.aps.org/prb/>

Editorial: Highlighting Impact and the Impact of Highlighting  
<http://journals.aps.org/prb/edannounce/PhysRevB.92.210001>

We ask that you download the manuscript and return your report via:

[REDACTED]

Alternatively, you may send your completed Referee Response Form by email to [prb@aps.org](mailto:prb@aps.org). If you use email, either reply to this message or give as the subject "Report RADONJIC [REDACTED]"

ABSTRACT:

[REDACTED]

**Subject:** Review\_request RADONJIC [REDACTED]

**From:** pre@aps.org

**Date:** 5/9/18, 12:12 AM

**To:** milos.radonjic@ipb.ac.rs

Re: [REDACTED]

Dear Dr. Radonjic,

We would appreciate your review of this manuscript, which has been submitted to Physical Review E.

Comments from the editor:

Physical Review editors would like your help in maintaining high standards for our journal. Is this paper important to the field? Does it significantly advance physics?

Thank you for your help.

Yours sincerely,

Serena Bradde  
Associate Editor  
Physical Review E  
Email: [pre@aps.org](mailto:pre@aps.org)  
<http://journals.aps.org/pre/>

Celebrating 125 Years of the Physical Review  
<https://journals.aps.org/125years> #PhysRev125

We ask that you download the manuscript and return your report via:

[REDACTED]

Alternatively, you may send your completed Referee Response Form by email to [pre@aps.org](mailto:pre@aps.org). If you use email, either reply to this message or give as the subject "Report RADONJIC [REDACTED]"

ABSTRACT:

**Subject:** Позивно писмо за предавање на СФКМ 2019

**From:** Zeljko Sljivancanin <zeljko@vinca.rs>

**Date:** 6/27/19, 12:46 PM

**To:** Ivana Vasic <ivana.vasic@ipb.ac.rs>, Milan Damnjanovic <yqoq@rcub.bg.ac.rs>, Nenad Lazarevic <nenad.lazarevic@ipb.ac.rs>, Zorica Konstantinovic <zorica.konstantinovic@ipb.ac.rs>, Aleksandar Matkovic <aleksandar.matkovic@ipb.ac.rs>, Ivanka Milosevic <ivag@rcub.bg.ac.rs>, Milica Milovanovic <milica.milovanovic@ipb.ac.rs>, Marija Mitrovic Dankulov <marija.mitrovic@ipb.ac.rs>, Velimir Radmilovic <vrradmilovic@lbl.gov>, Velimir Radmilovic <vrradmilovic@tmf.bg.ac.rs>, Rastko Vasilic <rastko.vasilic@ff.bg.ac.rs>, Miljko Sataric <bomisat@neobee.net>, Djordje Spasojevic <djordjes@ff.bg.ac.rs>, Mihajlo Vanevic <m\_vanevic@gmx.com>, "Zoran V. Popovic" <zoran.popovic@ipb.ac.rs>, "Zoran Š. Popovic" <zpopovic@vinca.rs>, Monika&Milan <tadic@mts.rs>, Rados Gajic <rados.gajic@ipb.ac.rs>, Marko Spasenović <spasenovic@nanosys.ihtm.bg.ac.rs>, Vladimir Djokovic <djokovic@vinca.rs>, Igor Popov <igorpopov77@yahoo.com>, Vladimir Damljanovic <vladimir.damljanovic@ipb.ac.rs>, Sanja Janicevic <sanja.janicevic@pmf.kg.ac.rs>, Ljuba Budinski Petkovic <ljupka@uns.ac.rs>, Igor Franovic <igor.franovic@ipb.ac.rs>, Jaksa Vucicevic <jaksa.vucicevic@ipb.ac.rs>, Milos Radonjic <milos.radonjic@ipb.ac.rs>, Borislav Vasic <borislav.vasic@ipb.ac.rs>, Vasil Koteski <vkotes@vinca.rs>, Antun Balaz <antun@ipb.ac.rs>, Nenad Vukmirovic <nenad.vukmirovic@ipb.ac.rs>, "Milan Rajkovic @vinca.rs" <milanr@vinca.rs>

**CC:** sfkm@ipb.ac.rs, zeljko@vinca.rs

Поштована колегинице/колега,

задовољство ми је да Вас у име научног комитета позовем да одржите предавање по позиву и представите Ваше нове научне резултате на домаћој конференцији СФКМ 2019, која ће се одржати од 7. до 11. октобра 2019. године у Београду. Резултате можете представити Ви или неко од чланова Ваше истраживачке групе за кога сматрате да је суштински допринео њиховој реализацији.

Молим Вас да се до 15. јула региструјете и пошаљете апстракт Вашег предавања.

Више информација о конференцији можете наћи на интернет адреси <http://sfkm2019.ipb.ac.rs/>.

У име програмског и организационог комитета СФКМ 2019, срдечно Вас поздрављам.

Жељко Шљиванчанин,

копредседавајући СФКМ 2019

--  
Dr. Željko Šljivančanin  
Vinča Institute of Nuclear Sciences (020)  
P.O.Box 522, 11001 Belgrade, Serbia



## Invited Speakers

### Invited Speakers at National Symposium on Condensed Matter Physics

- Marco Aprili, PS-CNRS Université Paris-Sud, France
- Stefano Baroni, Scuola Internazionale Superiore di Studi Avanzati, Italy
- Wolfgang Belzig, University of Konstanz, Germany
- Emil Božin, Brookhaven National Laboratory, USA
- Harald Brune, Ecole Polytechnique Fédérale de Lausanne, Switzerland
- Liviu Chioncel, University of Augsburg, Germany
- Gyula Eres, Oak Ridge National Laboratory, USA
- Laszlo Forro, Ecole Polytechnique Fédérale de Lausanne, Switzerland
- Rudi Hackl, Walther Meissner Institute, Germany,
- Igor Herbut, Simon Fraser University, Canada
- Kurt Hingerl, Johannes Kepler University, Linz, Austria
- Liv Hornekaer, Aarhus University, Denmark
- Zoran Ikončić, University of Leeds, UK
- Vladimir Juričić, Nordita, KTH Royal Institute of Technology and Stockholm University, Sweden
- Miloš Knezevic, Berlin Institute of Technology, Germany
- Hechang Lei, Renmin University
- Marjana Ležaić, Forschungszentrum Jülich, Germany
- Zoran Mišković, University of Waterloo, Canada
- Danilo Nikolić, Universität Konstanz, Konstanz, Germany
- Francois Peeters, University of Antwerp, Belgium
- Maria Peressi, University of Trieste, Italy
- Cedomir Petrovic, Brookhaven National Laboratory, USA
- Hyejin Ryu, Korea Institute of Science and Technology
- Milan Radović, Paul Scherrer Institute, Switzerland
- Nicolas Regnault, Ecole Normale Supérieure Paris, France
- Rastko Sknepnek, University of Dundee, UK
- Frank Steglich, MPICPFS Dresden and Zhejiang University
- Bosiljka Tadić, Jožef Štefan Institute, Slovenia
- Jack Tuszynski, University of Alberta, Canada
- Dieter Vollhardt, University of Augsburg, Germany
- Rok Zitko, Jožef Štefan Institute, Slovenia
- Qingming Zhang, Lanzhou University and Institute of Physics, Chinese Academy of Science
- Vladimir Damjanović, Institute of Physics Belgrade
- Marija Mitrović-Dankulov, Institute of Physics Belgrade
- Saša Dmitrović, Faculty of Physics, University of Belgrade
- Vladimir Đoković, Institute of Nuclear Sciences Vinca, Belgrade
- Igor Franović, Institute of Physics Belgrade
- Sanja Janičević, Institute of Physics Belgrade
- Zorica Konstantinović, Institute of Physics Belgrade
- Nenad Lazarević, Institute of Physics Belgrade
- Aleksandar Matković, Institute of Physics, Montanuniversität Leoben, Austria
- Ivana R. Milošević, Institute of Physics Belgrade
- Ivanka Milošević, Faculty of Physics, University of Belgrade
- Milica Milovanović, Institute of Physics Belgrade
- Jovan Odavić, Institut für Theoretischer Statistischer Physik, RWTH Aachen University
- Marko Petrović, Department of Physics & Astronomy, University of Delaware
- Igor Popov, Institute for Multidisciplinary Research, Belgrade
- Miloš Radonjić, Institute of Physics Belgrade
- Milan Rajković, Institute of Nuclear Sciences Vinca, Belgrade
- Marko Spasenović, Institute of Chemistry, Technology and Metallurgy (IHTM),
- Đorđe Spasojević, Faculty of Physics, University of Belgrade
- Borislav Vasić, Institute of Physics Belgrade
- Jakša Vučićević, Institute of Physics Belgrade

## Conference photo



## Latest news

### Conference photo

October 8, 2019

Please join us at Wednesday at 13.30h in front of the SASA building for conference photo.

### Changes in the program

October 6, 2019

Please note changes in the program for Monday morning session and Tuesday afternoon session.

### Book of Abstracts is online

October 2, 2019

Book of abstracts is online!

### PROGRAM IN ONLINE!

September 20, 2019

Preliminary schedule for SCMP conference is online!

### Participation fee in cash

August 15, 2019

Everyone having issues with payment from abroad can pay participation fee in cash at conference opening (payment confirmation will be provided on-site).

## Conference Poster



7-11th October 2019  
Belgrade, Serbia



<http://www.sfkm.ac.rs/>

# The 20th Symposium on Condensed Matter Physics

---

## BOOK OF ABSTRACTS

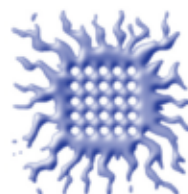
---



University of Belgrade,  
Faculty of Physics



Institute of Physics Belgrade



Vinca Institute  
of Nuclear Sciences



Serbian Academy  
of Sciences and Arts



Ministry of Education, Science and  
Technological Development,  
Republic of Serbia

## Conference Chair

Cedomir Petrovic, *Brookhaven National Laboratory, USA*

Željko Šljivančanin, *Vinča Institute of Nuclear Sciences Serbia*

## Organizing Committee

Jelena Pešić, *Institute of Physics Belgrade*

Andrijana Šolajić, *Institute of Physics Belgrade*

Petar Mali, *Faculty of Sciences, University of Novi Sad*

Jelena Pajović, *Faculty of Physics, University of Belgrade, Serbia*

Srđan Stavrčić, *Vinča Institute of Nuclear Sciences*

Svetislav Mijatović, *Faculty of Physics, University of Belgrade, Serbia*

Božidar Nikolić, *Faculty of Physics, University of Belgrade, Serbia – chair*

## Organized by

Institute of Physics Belgrade

Faculty of Physics, University of Belgrade

Vinča Institute of Nuclear Sciences

Serbian Academy of Sciences and Arts

## Program Committee

Ivan Božović, *Brookhaven National Laboratory, USA*

Vladimir Dobrosavljević, *Florida State University, USA*

Milan Damnjanović, *Faculty of Physics, University of Belgrade, Serbia*

Vladimir Djoković, *Vinča Institute, University of Belgrade, Serbia*

Gyula Eres, *Oak Ridge National Laboratory, USA*

Laszló Forró, *Ecole Polytechnique Fédérale de Lausanne, Switzerland*

Radoš Gajić, *Institute of Physics Belgrade, University of Belgrade, Serbia*

Igor Herbut, *Simon Fraser University, Canada*

Zoran Ikonić, *University of Leeds, UK*

Ivanka Milošević, *Faculty of Physics, University of Belgrade, Serbia*

Branislav Nikolić, *University of Delaware, USA*

Cedomir Petrovic, *Brookhaven National Laboratory, USA*

Dragana Popović, *National High Magnetic Field Laboratory USA*

Zoran S. Popović, *Vinča Institute, University of Belgrade, Serbia*

Zoran V. Popović, *Institute of Physics, University of Belgrade, Serbia*

Zoran Radović, *Faculty of Physics, University of Belgrade, Serbia*

Miljko Satarić, *Faculty of Technical Sciences, University of Novi Sad, Serbia*

Vojislav Stamenković, *Argonne National Laboratory, USA*

Željko Šljivančanin, *Vinča Institute, University of Belgrade, Serbia*

Bosiljka Tadić, *Jožef Štefan Institute, Slovenia*

Milan Tadić, *School of Electrical Engineering, University of Belgrade, Serbia*

Darko Tanasković, *Institute of Physics, University of Belgrade, Serbia*

# Superconducting Nature of Elemental Bismuth Under Pressure

Miloš M. Radonjić<sup>a</sup>, Rustem Khasanov<sup>b</sup>, Liviu Chioncel<sup>c</sup> and Alex Amato<sup>b</sup>

<sup>a</sup>Scientific Computing Laboratory, Center for the Study of Complex Systems, Institute of Physics Belgrade, University of Belgrade, Pregrevica 118, 11080 Belgrade, Serbia

<sup>b</sup>Laboratory for Muon Spin Spectroscopy, Paul Scherrer Institute, CH-5232 Villigen, Switzerland

<sup>c</sup>Augsburg Center for Innovative Technologies, and Center for Electronic Correlations and Magnetism, Theoretical Physics III, Institute of Physics, University of Augsburg, D-86135 Augsburg, Germany

**Abstract.** Elemental bismuth has a very rich pressure-dependent phase diagram. At room temperature, it undergoes a series of structural transitions. Upon cooling all phases become superconducting, but the superconducting nature between phases is very different. We report the superconductivity in the Bi-II phase of elemental bismuth (transition temperature  $T_c \simeq 3.94$  K at  $p \simeq 2.80$  GPa). It was studied experimentally by means of muon-spin rotation as well as theoretically using the Eliashberg theory in combination with Density Functional calculations. Experiments reveal that Bi-II is the type-I superconductor with the zero temperature thermodynamic critical field  $B_c(0) = 32.07(2)$  mT. The Eliashberg theory provides an excellent agreement with the experimental critical temperature and magnetic field and the estimated value for the strong coupling parameter  $T_c/\omega_{\text{ph}}$  suggests that Bi-II is an intermediately-coupled superconductor. We also address the superconducting nature of Bi-I phase. We report the negligible electron-phonon interaction and possible signatures of exciton-mediated superconductivity.

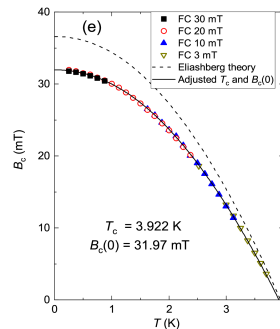


**FIGURE 1.** The temperature dependence of the thermodynamical critical field  $B_c$  for Bi-II phase obtained in  $\mu$ SR experiments and within the framework of *ab-initio* Eliashberg calculations using Density Functional Theory.

## REFERENCES

1. R. Khasanov, M. M. Radonjić, H. Luetkens, E. Morenzoni, G. Simutis, S. Schoenecker, W. H. Appelt, A. Östlin, L. Chioncel, and A. Amato, *Phys. Rev. B* **99**, 174506 (2019).



Cite this: *Nanoscale*, 2018, **10**, 17738

## Predicting the conductance of strongly correlated molecules: the Kondo effect in perchlorotriphenylmethyl/Au junctions†

W. H. Appelt,<sup>‡a,b</sup> A. Droghetti,<sup>‡c</sup> L. Chioncel,<sup>id b,d</sup> M. M. Radonjić,<sup>e</sup> E. Muñoz,<sup>id f</sup> S. Kirchner,<sup>g</sup> D. Vollhardt<sup>d</sup> and I. Rungger<sup>id h</sup>

Stable organic radicals integrated into molecular junctions represent a practical realization of the single-orbital Anderson impurity model. Motivated by recent experiments for perchlorotriphenylmethyl (PTM) molecules contacted to gold electrodes, we develop a method that combines density functional theory (DFT), quantum transport theory, numerical renormalization group (NRG) calculations and renormalized super-perturbation theory (rSPT) to compute both equilibrium and non-equilibrium properties of strongly correlated nanoscale systems at low temperatures effectively from first principles. We determine the possible atomic structures of the interfaces between the molecule and the electrodes, which allow us to estimate the Kondo temperature and the characteristic transport properties, which compare well with experiments. By using the non-equilibrium rSPT results we assess the range of validity of equilibrium DFT + NRG-based transmission calculations for the evaluation of the finite voltage conductance. The results demonstrate that our method can provide qualitative insights into the properties of molecular junctions when the molecule–metal contacts are amorphous or generally ill-defined, and that it can further give a fully quantitative description when the experimental contact structures are well characterized.

Received 17th May 2018,  
Accepted 9th August 2018

DOI: 10.1039/c8nr03991g

rsc.li/nanoscale

### 1. Introduction

Molecular electronics holds great promise for future applications in computing, sensing, clean-energy, and even data-storage technologies.<sup>1–3</sup> However, a general difficulty so far has

been the poor characterization of the device structures and their relationship with the measured conductances and functionalities. For this problem, *ab initio* simulations based on density functional theory (DFT)<sup>4</sup> have proven very successful in supporting experiments, and they have played a key role in advancing the field during the last decade.<sup>5–9</sup> Yet, standard DFT-based transport schemes for simulations of experimental molecular junctions have several limitations. The most prominent of these is the failure to account for the strong electron correlations leading to the Kondo effect in devices comprising magnetic molecules, and rigorous treatments and extensions overcoming this problem are currently under active development.<sup>10–15</sup>

In this article, we establish a suitable combination of DFT and many-body techniques to achieve an unprecedented quantitative description of the equilibrium and non-equilibrium conductance of molecular devices showing Kondo effect. By using gold/perchlorotriphenylmethyl (PTM)/gold junctions as a specific example we relate the Kondo temperature to the electrode–molecule contact geometries, thus matching the range of variability of the experimental results.<sup>16</sup> Furthermore we address the dependence of the conductance at finite temperature and extend the method to finite bias.

Our multi-scale approach combines DFT, non-equilibrium Green's functions (NEGF),<sup>17</sup> numerical renormalization group

<sup>a</sup>Theoretical Physics II, Institute of Physics, University of Augsburg, D-86135 Augsburg, Germany

<sup>b</sup>Augsburg Center for Innovative Technologies, University of Augsburg, D-86135 Augsburg, Germany

<sup>c</sup>Nano-Bio Spectroscopy Group and European Theoretical Spectroscopy Facility (ETSF), Centro de Física de Materiales, Universidad del País Vasco, Avenida Tolosa 72, 20018 San Sebastian, Spain

<sup>d</sup>Theoretical Physics III, Center for Electronic Correlations and Magnetism, Institute of Physics, University of Augsburg, D-86135 Augsburg, Germany

<sup>e</sup>Scientific Computing Laboratory, Center for the Study of Complex Systems, Institute of Physics Belgrade, University of Belgrade, Pregrevica 118, 11080 Belgrade, Serbia

<sup>f</sup>Facultad de Física, Pontificia Universidad Católica de Chile, Casilla 306, Santiago 22, Chile

<sup>g</sup>Zhejiang Institute of Modern Physics, Zhejiang University, Hangzhou, Zhejiang 310027, China

<sup>h</sup>National Physical Laboratory, Teddington, TW11 0LW, UK

E-mail: ivan.rungger@npl.co.uk

†Electronic supplementary information (ESI) available: DETAILS. See DOI: 10.1039/C8NR03991G

‡These authors contributed equally to this work.





(NRG) methods,<sup>18–21</sup> and renormalized superperturbation theory (rSPT).<sup>22,23</sup> First the contact geometry and electronic structure of molecular junctions are obtained by DFT + NEGF. Then the DFT Kohn–Sham (KS) states are projected onto an effective Anderson impurity model,<sup>24–33</sup> which is solved exactly to obtain the Kondo temperature and the equilibrium zero-temperature conductance *via* NRG. Based on these results we finally compute the non-equilibrium rSPT transport coefficients, which encode the behavior of the junctions at low temperature, finite magnetic field, and finite bias voltage.<sup>22</sup>

Stable organic radicals contacted to metal electrodes, such as the PTM molecule on Au, form a practical realization of the prototypical single-orbital Anderson impurity model,<sup>16,31,34,35</sup> and are therefore ideally suited to study the fundamental aspects of the interaction of magnetic impurities with metallic surfaces. These aspects include the interplay between the binding geometry and the energy level alignment with respect to the surface Fermi energy, as well as the electron correlations leading to the Kondo effect.

In recent experiments<sup>16,36</sup> PTM-radicals were functionalized with thiophene linkers producing the PTM-bis-thiophene radical (called PTM-BT in the following to distinguish it from the bare PTM; see also Fig. 1 for their atomic structures). These molecules were then integrated into gold mechanically-controlled break-junctions (MCBJs) and gold electromigrated break-junctions (EMBJs) to measure their transport properties. While at room temperature very low conductance values were reported,<sup>36</sup> at low temperature a zero-bias conductance resonance was observed in many of the junctions, and its Kondo character verified by temperature- and magnetic field-dependent measurements.<sup>16</sup> The low-temperature results indicate that the PTM radical can preserve the unpaired spin in a solid state three-terminal configuration, and that it is stable under mechanical stretching of the electrodes. One of the remarkable features is the rather high Kondo temperature of about 3 K, which is largely constant upon stretching of the junction. This implies that for the junctions that exhibiting Kondo behavior the contact of the molecule to one of the electrodes is very strong, and is not affected by the elongation of the junction in the MCBJ process. In contrast, the background conductance shows large variations. This can happen upon stretching when the contact to the second electrode varies significantly, or else when one of the two electrodes changes its Au–Au bond

conformation significantly.<sup>37,38</sup> Overall the low-temperature experimental results point to a structure with highly asymmetric coupling to the electrodes. In the following we will show that this hypothesis is indeed confirmed by our calculations, thus providing a detailed understanding of the electronic and transport properties of the PTM/gold junctions at the atomic scale.

The paper is organized as follows. We first discuss the equilibrium DFT results for a number of possible junction structures (section 2), and then provide estimates for the Kondo temperature for these geometries (section 3). For a set of geometries we then present the linear response transport properties including the strong electron–electron correlations obtained by DFT + NEGF + NRG (section 4) and finally extend the results to finite temperature and finite bias *via* rSPT (section 5).

## 2. DFT calculations

PTM has a propeller-like structure with a central carbon atom coordinated by the three phenyl rings. In the gas phase, it has the typical electronic structure of a radical.<sup>39–41</sup> The energy spectrum has doubly occupied electronic states filled up to the highest occupied molecular orbital (HOMO). Above the HOMO there is a further well-separated, singly occupied molecular orbital (SOMO) with an unpaired electron, giving a total molecular spin quantum number of 1/2. In the PTM, the charge iso-surface indicates that the SOMO is mainly confined to the central carbon, while the HOMO and the lowest unoccupied molecular orbital (LUMO) are largely located on the rest of the molecule. This is presented more extensively in the ESI section S2,† while the computational details of our DFT calculations are given in the ESI section S1.† The difference between the ionization potential and electron affinity of the molecule defines the fundamental gap and corresponds to the charging energy  $U$ . In the absence of any experimental results, we calculate  $U$  *via* total energy differences<sup>42</sup> to be about 4 eV. PTM-BT has a very similar electronic structure to that of the bare PTM, although the SOMO is slightly delocalized over the thiophene ligands,<sup>16</sup> and this results in a charging energy smaller by about 0.4 eV. Note that when the molecule is placed between Au electrodes there is a significant renormalization of the energy levels and consequently a reduction of the charging energy, which we discuss in section S2 of the ESI as well as in section 3.2.†

In order to understand the electronic structure of the molecule/Au contact and how this determines the key parameters affecting the Kondo temperature, we consider a number of qualitatively different model structures, which are shown in Fig. 2.

To start, we look at the ideal case of a bare PTM molecule on a flat Au(111) surface, which we denote as configuration (CFG) B1 in Fig. 2. The 3-atom Au tip is placed at a rather large distance, so that the electronic coupling between the molecule and the tip is negligible with respect to that to the substrate. Since in MCBJ and EMBJ experiments the Au stretched surface

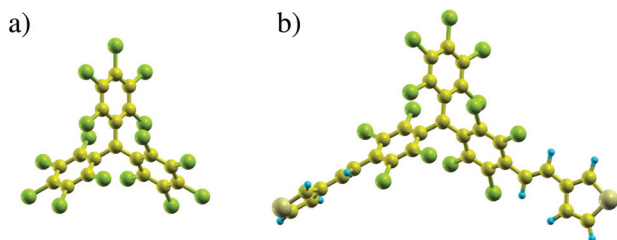


**Fig. 1** Relaxed atomic structures of the bare PTM molecule (a) and of PTM-bis-thiophene (b) (green spheres represent Cl atoms, blue spheres H, large yellow spheres S, and smaller dark yellow spheres represent C).



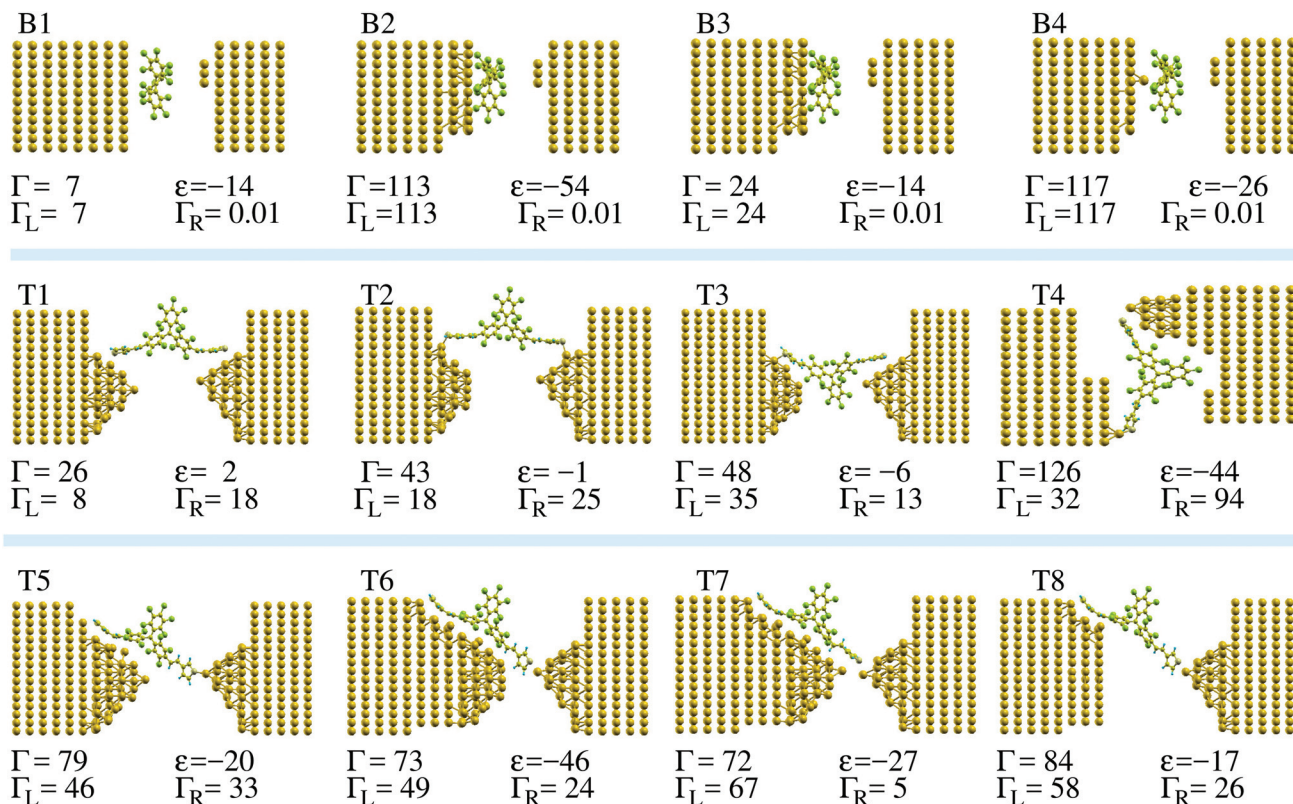


Fig. 2 Junction geometries for bare-PTM on an Au surface (B1–B4), and for PTM-BT between two Au electrodes (T1–T8), investigated in this paper. For each junction we specify the broadening of the singly occupied molecular orbital induced by the coupling to the electrodes ( $\Gamma$ ), its position with respect to  $E_F$  ( $\epsilon$ ), and the coupling to the left and right electrodes ( $\Gamma_L$  and  $\Gamma_R$ , respectively;  $\Gamma = \Gamma_L + \Gamma_R$ ). All units of the specified quantities are meV.

is expected to be highly corrugated rather than perfectly flat,<sup>37,38</sup> we then model a rough Au surface by removing a number of Au atoms from the perfect Au(111) surface (CFGs B2 to B4). Finally, we consider a number of break-junction setups comprising PTM-BT (CFGs T1 to T8). The detailed contact structure is expected to be different for each individual experimental conductance trace measurement. The model junctions considered here include cases with both symmetric and asymmetric molecule–electrodes coupling. For some structures the PTM central core is located inside the junction’s empty gap, whereas for other structures it is physisorbed on one of the electrodes. Furthermore, the thiophene linkers can be connected to the electrodes either non-covalently or covalently *via* a sulfur–Au adatom direct bond.

A representative DFT projected density of states (PDOS) is shown in Fig. 3 (see ESI section S1† for the computational details). When the molecule is in contact with the Au electrodes, the SOMO DOS can be modeled approximately by a half-filled Lorentzian-like peak close to the Fermi energy,  $E_F$ . Note that while we refer to the state as SOMO also when the molecule is on the Au substrate for consistency, its occupation can generally deviate from one in this case. The full width at half maximum (FWHM) of the SOMO peak corresponds to its electronic coupling to the Au substrate,  $\Gamma$ ,<sup>24</sup> which can be calculated by using the projection scheme recently developed in

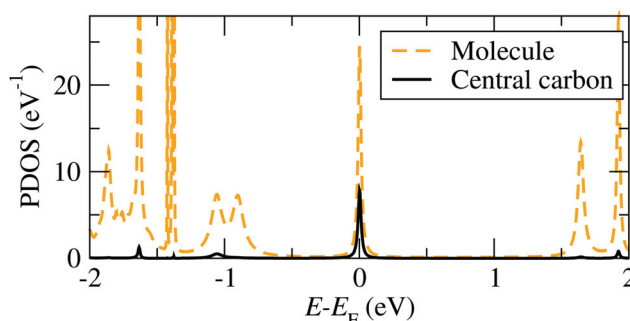


Fig. 3 LDA projected density of states (PDOS) for the configuration T1. The peak at the Fermi energy corresponds to the singly occupied molecular orbital, which defines our Anderson impurity, and is located mainly on the central carbon atom of the PTM.

ref. 24. The results for each model geometry considered are indicated in Fig. 2 along with the DFT SOMO on-site energy,  $\epsilon$ , relative to  $E_F$ . These values are the parameters required for the evaluation of the Kondo temperature.

As a matter of notation we label the structures with the propeller-like PTM parallel (perpendicular) to the surface, as “parallel” (“perpendicular”) configurations. For the idealized case of a bare PTM on a flat Au(111) surface, we find that the



molecule is physisorbed with an energy difference between the “parallel” configuration (B1) and the “perpendicular” configuration (not shown) of about 335 meV, favoring the “parallel” configuration. The equilibrium position of the central C atom is located at about 5.18 Å from the top Au layer. For this configuration there is a negligible charge-transfer from the surface to the molecule, and the PTM preserves its unpaired electron, with  $\Gamma \approx 7$  meV and therefore very small.

On the corrugated surface (CFG B2) the molecule can bind better to the Au, since part of its phenyl rings can move into regions where the Au surface has a dip. In CFG B2 an Au atom is located below the central C atom of the bare-PTM. This atom is then removed in the CFG B3, while it is kept as the only atom from the top-most Au surface in the CFG B4. Comparing the  $\Gamma$ -values for these structures allows us to estimate the effect of Au atoms directly in contact with the central C atom of the PTM. For CFG B2 we find the occupation of the SOMO to be 1.40 electrons, indicating that a partial electron transfer between the gold and the molecule has occurred. In fact, the SOMO DOS peak lies below  $E_F$  ( $\epsilon = -54$  meV). The increased charge transfer indicates an increased screening of the transferred electrons by the Au surface atoms, which is due to the molecule moving closer to the Au surface, in particular to the Au atom closest to the core of the PTM molecule. In general an increase in the screening also leads to a reduction of  $U$  (see the discussion in the ESI section S2†). We note that the results for the charge transfer obtained for non-spin-polarized calculations are approximately the same as those obtained in spin-polarized calculations in the ESI section S2.† The electronic coupling of 114 meV for CFG B2 is much larger than the one for the PTM on flat Au(111). An analysis of the origin of such a large coupling shows that it is mainly due to the Au atom underneath the central C atom of the PTM. In fact, for CFG B3, where this central Au adatom is removed, the coupling drops to 23 meV, while it remains large for CFG B4, where only this Au adatom is kept of the top Au surface layer.

Finally, we consider the model break-junctions (CFGs T1 to T8). In these cases, we use only the “perpendicular” configuration, since the “parallel” PTM-BT configuration would require very large simulation cells, which are beyond our current computing resources. The results allow us to infer the general trends for the electronic coupling of the radical center to the Au electrodes through the thiophene linkers (see Fig. 2). As can be seen the computed values of  $\Gamma$  vary over almost one order of magnitude, from 26 to 126 meV. We note that in break-junctions  $\Gamma$  is the sum of two contributions,  $\Gamma_L$  and  $\Gamma_R$ , representing the electronic coupling to the left and right lead, which we calculate individually with the method outlined in ref. 24. In general we find that  $\Gamma_L$  or  $\Gamma_R$  are large when there are Au atoms close to the thiophene linkers, such as for  $\Gamma_L$  in CFG T7. A bond between the sulfur atoms and a protruding Au atom also increases the coupling. On the other hand, the coupling is low when such a bond is absent, and when the angle between the thiophene and the Au is larger, such as for  $\Gamma_L$  in CFG T1.

### 3. Kondo effect

#### 3.1. Formulation of the single impurity Anderson problem

The PTM in contact with the leads is modeled by a single impurity Anderson Model (SIAM), which has the Hamiltonian<sup>43</sup>

$$H_{\text{SIAM}} = H_d + H_c + H_{\text{hyb}}, \quad (1)$$

$$H_d = \sum_{\sigma} \epsilon_d n_{d\sigma} + U n_{d\uparrow} n_{d\downarrow},$$

$$H_c = \sum_{k,\sigma} \epsilon_k n_{k,\sigma},$$

$$H_{\text{hyb}} = \sum_{k,\sigma} V_k \left( d_{\sigma}^{\dagger} c_{k,\sigma} + c_{k,\sigma}^{\dagger} d_{\sigma} \right),$$

where  $H_d$  describes the electrons of spin  $\sigma$  localized at the impurity site, which are created (annihilated) by the operator  $d_{\sigma}^{\dagger}$  ( $d_{\sigma}$ ), with  $n_{d\sigma} = d_{\sigma}^{\dagger} d_{\sigma}$  being the corresponding number operator;  $\epsilon_d$  is the orbital energy,  $U$  the charging energy, and  $\langle n_d \rangle = \sum_{\sigma} \langle d_{\sigma}^{\dagger} d_{\sigma} \rangle$  the occupation, where the bracket  $\langle \dots \rangle$

denotes the thermal expectation value. For the PTM molecule the impurity site is the SOMO. Note that  $\epsilon_d$  does not coincide with  $\epsilon$  in Fig. 3, since the on-site Coulomb interaction is already partially accounted for in KS-DFT, and this contribution has to be subtracted, so that  $\epsilon_d = \epsilon - \epsilon_{\text{dc}}$ .<sup>24,44</sup> Here  $\epsilon_{\text{dc}}$  is the so-called double counting correction, whose exact expression is not known except for certain limiting cases, and several approximations have been introduced in the literature.<sup>45</sup> In general  $\epsilon_{\text{dc}}$  depends on  $U$ , and in the commonly used “fully localized limit” it is given by  $\epsilon_{\text{dc}} = U(n_{\text{d}}^{\text{DFT}} - 1/2)$ ,<sup>12</sup> where  $n_{\text{d}}^{\text{DFT}}$  is the DFT occupation of the impurity. A comprehensive discussion of the difficulties arising when combining DFT with such an Anderson impurity model and more generally the dynamical mean field theory is given in ref. 45 and 46. Note that instead of the Anderson impurity model one can also use other methods to treat the highly correlated subsystem, such as for example embedded correlated wavefunction schemes.<sup>47,48</sup> A review of the advantages and limitations of various embedding schemes that link many-body calculations for a subsystem to an environment treated at the DFT level is given in ref. 49.

Since in an experimental setting the occupation can be set by applying a gate voltage, here we treat  $\epsilon_d$  as an adjustable parameter, independent of the DFT results, and choose its value to ensure a specified occupation of the impurity orbital. We will also investigate how the results depend on the charging energy  $U$ , and will provide estimates of possible values of  $U$  for PTM/Au geometries.

In eqn (1)  $H_c$  describes the effective bath of electrons with momentum  $k$  and spin  $\sigma$ , which are created (annihilated) by the operator  $c_{k,\sigma}^{\dagger}$  ( $c_{k,\sigma}$ ) and with number operator  $n_{k,\sigma} = c_{k,\sigma}^{\dagger} c_{k,\sigma}$ . The effective bath includes the electrons in the Au leads, as well as those in the molecular orbitals, except for the SOMO. We note that the chemical potential in the Hamiltonian eqn (1) is set to zero by shifting both the bath and impurity



energies  $\varepsilon_d$  and  $\varepsilon_k$  by an additive constant. This does not affect the properties of the system. Furthermore, in zero-temperature calculations we will refer to the chemical potential  $\mu = 0$  as the Fermi energy  $E_F = 0$ , which is most commonly used in first principles calculations.

Finally,  $H_{\text{hyb}}$  accounts for the hybridization between the bath and the impurity, with  $V_k$  corresponding to the hybridization matrix element. Accordingly, we can define the hybridization function  $\Delta(E) = \text{Re}\Delta(E) + i\text{Im}\Delta(E)$ , with

$$\text{Im}\Delta(E) = -\pi \sum_k |V_k|^2 \delta(E - \varepsilon_k), \quad (2)$$

$$\text{Re}\Delta(E) = \frac{1}{\pi} P \int dE' \frac{\text{Im}\Delta(E')}{E' - E}, \quad (3)$$

and the coupling strength  $\Gamma(E) = -2\text{Im}\Delta(E)$ . The DFT results for  $\Gamma(E_F = 0)$  for several PTM/Au contacts are presented in the previous section, and the results are shown in Fig. 2.

### 3.2. Estimation of the Kondo temperature

In order to obtain a first estimate of the Kondo temperature for different junctions presented in Fig. 2, we assume a constant (energy independent) coupling  $\Gamma = \Gamma(E_F = 0)$ . The Anderson model then maps onto the Kondo model while approaching the so-called local moment limit, where  $|\varepsilon_d| \gg \Gamma$  and  $|\varepsilon_d + U| \gg \Gamma$ , ( $n_d \approx 1$ )<sup>50</sup> (see ESI section S3† for details), and the Kondo temperature is given by the Haldane equation<sup>51,52</sup>

$$k_B\theta_L = \frac{1}{2} \sqrt{\Gamma U} e^{-\frac{\pi|\varepsilon_d||\varepsilon_d+U|}{U\Gamma}}, \quad (4)$$

with  $-U \leq \varepsilon_d \leq 0$ . The results obtained with this expression are shown in Fig. 4, and are compared with the NRG calculations in the next subsection. The experiments in ref. 16 show that the SOMO of the PTM is close to half-filling and that it can be brought to exact half-filling by applying a gate voltage to the system. Here we therefore consider only this half-filled case, and the effects of small deviations from half filling are presented in section 5. We note that if the molecule is partially charged, then in general  $\theta_L$  increases compared to the charge

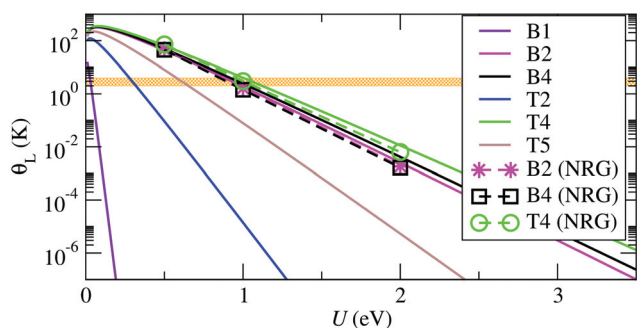


**Fig. 4** Kondo temperature,  $\theta_L$ , as function of the charging energy,  $U$ , obtained using eqn (4) with  $\varepsilon_d = -U/2$ , and NRG solutions for the exact system- and energy-dependent hybridization function. The corresponding electrodes–molecule configurations are illustrated in Fig. 2. The horizontal orange region illustrates the experimental range of Kondo temperatures of about 1–3 K.<sup>16</sup>

neutral state,<sup>24</sup> so that the values for half filling represent a lower limit for the theoretical results. The values of  $\Gamma$  for each structure are taken from Fig. 2, and at half-filling for a particle-hole symmetric SIAM we have  $\varepsilon_d = -U/2$ . For large enough  $U$  all curves in Fig. 4 decay exponentially with  $U$ , and the slope of the exponential decay is inversely proportional to  $\Gamma$ , so that the configurations with the largest  $\Gamma$  have the slowest decay, and therefore the highest  $\theta_L$ , for a given value of  $U$ .

Experimentally it is found that  $\theta_L$  is approximately constant upon stretching of the junction, which indicates a highly asymmetric coupling, where the molecule preserves the contact geometry to one electrode, while the contact with the other electrode is elongated. In other words, the molecule is strongly bound to one of the electrodes, which may correspond to the core of the PTM-BT lying flat on a rough Au surface with the thiophene linkers bridging both sides of the junction.

This conclusion is supported by calculations for the CFGs B2, B4 and T4 structures, which have the largest values of  $\Gamma$ , and which all show asymmetric couplings. The calculated  $\theta_L$  values lie in the experimental range if  $U$  is equal to about 1 eV. This charging energy is considerably smaller than the gas phase value of about 4 eV, and we ascribe this reduction of  $U$  to the charge screening by the electrons in the Au surface (see ESI section S2†). A value for the change of  $U$  due to screening can be calculated using a number of methods,<sup>53</sup> for molecules on general corrugated and irregular metal surfaces constrained DFT (cDFT) has been shown to give good results.<sup>54,55</sup> Alternatively, here we estimate it by approximating the metal surface as a plane, and by using a classical image charge model with a molecule between two metal electrodes<sup>54</sup> to capture this effect. In this way we calculate that a gap reduction of about 3 eV corresponds to ideal planar Au electrodes at a distance of about 2.7 Å from the center of the molecule. This number is similar to the distance of 3.4 Å for the CFG B2 structure. The remaining difference can be due to either an overestimated theoretical gas phase gap, or due to the experimental atomic structures having an even stronger binding between molecule and electrodes than CFG B2.

For the structures with small  $\Gamma$  the value of  $U$  that brings  $\theta_L$  in the experimental range is very small, and goes below the expected possible range. Such junctions are therefore expected to exhibit a  $\theta_L$  well below the experimentally accessible temperatures. This is consistent with the experimental evidence that only a fraction of the molecular junctions, which we attribute to those with the largest  $\Gamma$ , exhibit a Kondo state at an experimentally accessible temperature. Overall our results confirm that the molecule lies flat on a rough Au surface when it exhibits Kondo behavior, since only such structures allow for small binding distances and strong electronic coupling.

### 3.3. NRG calculations

In order to confirm the trends for  $\theta_L$  obtained with the simplified model eqn (4), and to evaluate the conductance in the presence of electronic correlations, we integrate NRG calculations in the method. We consider the SIAM representing the PTM/Au structures with the largest  $\Gamma$  (CFGs B2, B4 and T4), for



which in the previous subsection have estimated the Kondo temperatures to lie in the experimental range. For each junction we calculate  $\text{Im}\Delta(E)$  in eqn (2) by using DFT + NEGF with the method presented in ref. 24, and the results are shown in Fig. 5. While the value around  $E_F$  is similar for all cases, there are pronounced differences in the energy dependence. The NRG calculations then allow us to verify whether the approximation of a constant  $\Gamma$  used so far is applicable for these realistic atomic structures. The real part is obtained with the Kramers–Kronig relation, eqn (3). Further details about the NRG calculations are presented in the ESI section S4.† The many-body self-energy calculated with NRG is then used to evaluate the zero-bias and zero-temperature transmission in the presence of strong correlations in the next section.

The Kondo temperature is extracted from the impurity contribution to the magnetic susceptibility  $\chi_s(\theta)$ <sup>19</sup> (see ESI section S5†). In Fig. 6 we present  $\chi_s(\theta)$  for the B4 geometry, where the

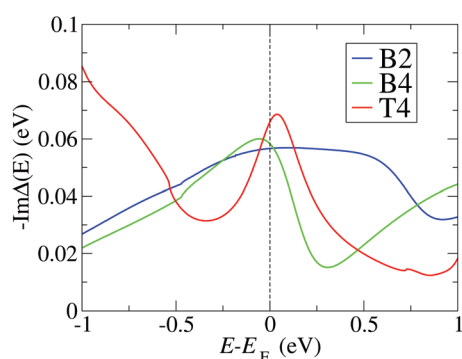


**Fig. 5** Negative imaginary part of the hybridization function calculated using the DFT + NEGF method, and used as input for the NRG calculation, for the three configurations with the largest hybridizations (B2, B4, T4) (see Fig. 2). High energy contributions are truncated as outlined in the ESI section S4.†

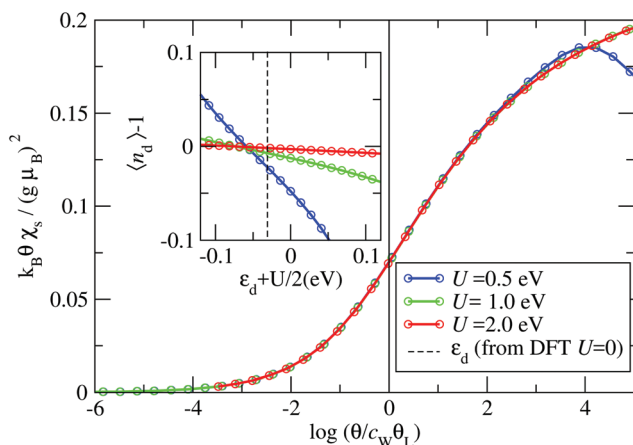


**Fig. 6** Main graph: The universal function displaying the temperature dependent scaling function  $(g\mu_B)^2 F(\theta/c_W\theta_L) = k_B\theta\chi_s$  against  $\log(\theta/c_W\theta_L)$ . Inset: The impurity occupation as a function of the rescaled on-site energy  $\varepsilon_d + U/2$ . The on-site energy obtained within DFT is indicated as the vertical dashed line.

inset shows the small deviation of the impurity occupation  $n_d$  from the half-filled case ( $n_d = 1$ ). We find that  $\chi_s(\theta)$  always follows the same universal behavior as long as the interaction strength is large enough ( $U > 0.5$  eV). A crossover is observed from the high  $\theta$  local moment regime, where  $k_B\theta\chi_s/(g\mu_B)^2 = 1/4$ , to the low  $\theta$  strong correlation limit, where  $k_B\theta\chi_s/(g\mu_B)^2 = 0$ ; here  $g$  is the Landè-factor and  $\mu_B$  the Bohr magneton.<sup>19</sup> We find that for  $U$  values above  $U = 0.5$  eV the curves can be collapsed onto a single universal function. Note that for  $U = 0.5$  eV one can already recognize the deviation from the universal behavior as a dip in the high  $\theta$  susceptibility.

The collapse of the susceptibilities is interpreted as a universality due to the formation of a Kondo-singlet. In the local moment regime the static spin-susceptibility scaled by the Kondo-temperature follows the same universal curve,<sup>20</sup> where the scaling function  $F(x)$  is defined by<sup>51</sup>

$$\frac{k_B\theta\chi_s}{(g\mu_B)^2} = F\left(\frac{\theta}{c_W\theta_L}\right), \quad (5)$$

and where  $c_W$  is the so called Wilson number, which is a model-dependent constant (see ESI section S3†). Here, the Kondo temperature  $\theta_L$  plays the role of a scale invariant in the renormalization group (RG) language. This means that systems with different initial parameters end up in the same low temperature fixed point after mode elimination (RG-flow towards the same fixed point).<sup>51</sup> This gives rise to the universal behavior in Fig. 6 at low  $\theta$ . The value for  $\theta_L$  is obtained in the standard way from the condition that the universal function at  $\theta = c_W\theta_L$  is  $F(1) = 0.07$ .<sup>43</sup> In Fig. 4 the values of  $\theta_L$  calculated in this way are displayed as dashed lines. Importantly, they agree rather well with those obtained using the approximate eqn (4), showing that the approximation of a constant  $\Gamma$  is valid for this system. The NRG results therefore also confirm the conclusion that for the three structures with large  $\Gamma$  the value of  $\theta_L$  is in the experimental range for  $U \approx 1$  eV.

## 4. Electron transmission

To evaluate the transport properties of this system we add the zero-temperature NRG self-energy,  $\Sigma(E, \theta = 0)$ , to the DFT + NEGF Green's function *via* the Dyson equation and compute the resulting energy-dependent transmission function,  $T_t(E, \theta = 0)$ , in the presence of many-body correlations not captured at the standard DFT-KS level.<sup>24,29,30</sup> As outlined in the ESI sections S7 and S8,† the linear response zero-temperature conductance,  $G_0 = G(V = 0, \theta = 0) = dI(V, \theta = 0)/dV|_{V=0}$ , is given by:

$$G_0 = \frac{2e^2}{h} T_t(E_F, \theta = 0), \quad (6)$$

where  $e$  is the electron charge,  $h$  the Planck constant and  $2e^2/h$  the quantum of conductance. Note that we have also implicitly assumed that there is no external magnetic field, whose effect will be considered in the next section. When  $\Gamma_L \gg \Gamma_R$  ( $\Gamma_L \ll \Gamma_R$ ) this can be extended to finite  $V$  as  $G(V, 0) \approx (2e^2/h) T_t(-eV, 0)$  ( $G(V, 0) \approx (2e^2/h) T_t(+eV, 0)$ ). As discussed in the



previous sections, we expect the Au/PTM/Au system exhibiting Kondo behavior to have such a highly asymmetric coupling. This condition is indeed fulfilled for CFGs B2 and B4, and to a minor extent also for CFG T4, so that the energy dependence of the transmission approximately corresponds to the voltage dependence of the conductance. Note that for such highly asymmetric coupling the dominant effect of the voltage is a shift of the molecular energies due to its induced local electric field, while for the case of approximately symmetric coupling ( $\Gamma_L \approx \Gamma_R$ ) the current induced non-equilibrium change of occupation gives an additional important contribution and therefore needs to be taken into account. In the next section we will therefore generalize these relations and provide the non-equilibrium relations for the conductance that are also valid for arbitrary values of  $\Gamma_L$  and  $\Gamma_R$ .

As outlined in ref. 24 and in the ESI section S7,† the total transmission function is the sum of the elastic transmission,  $T$ , and of the inelastic impurity transmission,  $T_{R,Al}$ , so that  $T_t = T + T_{R,Al}$ . The elastic transmission has contributions from electrons flowing through the impurity,  $T_{Al}$ , from the background transmission,  $T_B$ , and from interference terms,  $T_I$  ( $T = T_{Al} + T_B + T_I$ ). Notably, at zero-temperature, for a system in the Kondo regime one has  $T_{R,Al}(E_F) = 0$ , because the imaginary part of the impurity many-body self-energy vanishes at  $E_F$  in accordance with the Fermi-liquid picture.<sup>51</sup>

The calculated low energy transmissions for the B2, B4 and T4 configurations are presented in Fig. 7. Here  $U$  is set to 1 eV, since this is the charging energy that provides a Kondo temperature in the experimental range. The results for different values of  $U$  are shown in the ESI section S7.† One can clearly identify the Kondo peak around  $E_F$ , which has a width of the order of 1 meV, in good agreement with the experiments.<sup>16</sup>

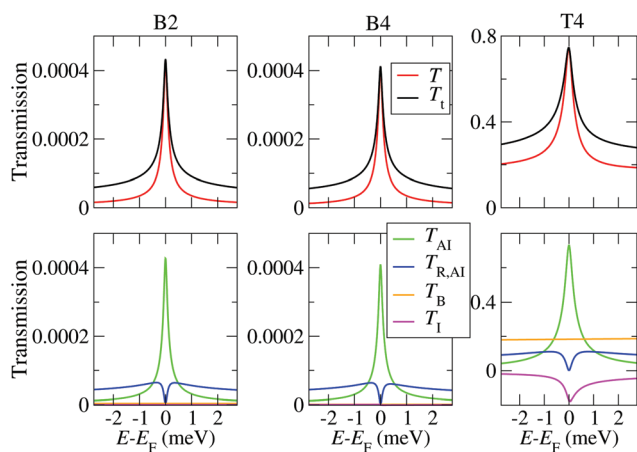


**Fig. 7** Zero-bias transmission including the zero-temperature NRG self-energy for the B2, B4 and T4 structures, and for  $U = 1.0$  eV. Here  $T$  is the total coherent transmission,  $T_t$  is the total transmission including incoherent effects,  $T_{Al}$  is the coherent transmission component of the Al itself,  $T_B$  is the coherent background transmission,  $T_I$  is the interference term, and  $T_{R,Al}$  is the incoherent transmission. The total transmission is then  $T_t = T + T_{R,Al}$ , with  $T = T_{Al} + T_B + T_I$ . Note the different scales of the transmission-axis for B2, B4 and T4.

The overall dominant contribution comes from  $T_{Al}$  for all cases. While the background transmission and interference terms are negligible in the highly asymmetric setups (CFGs B2 and B4), they are rather large in the break-junction geometry T4. Importantly, while in the B2 and B4 geometry the transmission values are very small, for the T4 break-junction configuration they can reach values up to 0.8, and such variations are indeed found in experiments.<sup>16</sup> In the present case the magnitude of both the background transmission and of the Kondo peak become large for symmetric coupling ( $\Gamma_L \approx \Gamma_R$ ), while they progressively decrease as the coupling becomes more asymmetric. However, we point out that the background transmission may generally be very large if the overlap between the Au electrodes is large or if the electrodes are very broad. In that case one may still have  $\Gamma_L \gg \Gamma_R$  for the molecule itself, but the background current will be much larger than that flowing through the molecule. Therefore, for a comparison between theory and experiments for the Kondo conductance itself ideally one needs to separate out the background conductance. While this is difficult to do in experiment, our simulation scheme allows to perform this separation for each atomic configuration. In Fig. 7 we also plot the incoherent transmission  $T_{R,Al}$  and  $T_t = T + T_{R,Al}$ , which determines the measured conductance. As stated above,  $T_{R,Al}$  vanishes at  $E_F$ , while it leads to a further overall enhancement of the transmission spectrum away from it. It therefore does not affect the zero-bias and zero-temperature conductance, but it plays an important role at finite bias and finite temperatures, as discussed below.

Although the results shown so far are obtained for zero temperature, we can obtain an estimate of the temperature dependence of the full width at half maximum (FWHM,  $W$ ) of the Kondo peak in the DOS by performing a low energy expansion of the SIAM DOS. For the system investigated here we consider the half-filled particle-hole symmetric case, and moreover, since  $\Gamma \ll U$ , we are in the so-called strong correlation regime.<sup>56</sup> As shown in the ESI section S6,† in such a regime the dependence of the FWHM on temperature for a SIAM with energy-independent hybridization  $\Delta = \Gamma/2$  is approximately given by:

$$W(\theta, \tilde{\Delta}) = \tilde{\Delta} 2\sqrt{2} \sqrt{\sqrt{1 + \left(\frac{\pi^2 k_B^2 \theta^2}{2\tilde{\Delta}^2} + 1\right)^2} - 1}. \quad (7)$$

Here  $\tilde{\Delta}$  is the renormalized quasi-particle spectral width,  $\tilde{\Delta} = z\Delta$ , and  $z = [1 - \partial_E \Re(\Sigma(E, \theta = 0))_{E=E_F}]^{-1}$  is the so called wave-function renormalization factor.<sup>22,56</sup> Note that here we use the zero temperature limit of  $\Sigma(E, \theta)$ , since we perform the perturbation expansion around  $\theta = 0$ , but in general  $z$  can also be evaluated at finite temperature by using the finite-temperature  $\Sigma(E, \theta)$  in its definition above. Furthermore, in the particle-hole symmetric regime  $\tilde{\Delta}$  is related to the Kondo temperature as<sup>56</sup>

$$k_B \theta_L = \frac{\pi}{4} \tilde{\Delta}. \quad (8)$$

Note that the relation in eqn (7) is different from the widely used form given in ref. 57, since in that reference the energy



dependence of the real part of the many-body self-energy is neglected. In the ESI section S6† we show that  $W(\theta, \tilde{\Delta})$  from eqn (7) reproduces rather well the NRG results up to temperatures of about  $2\theta_L$ .

In experiments,  $\theta_L$  can be obtained by fitting eqn (7) and (8) to the measured temperature dependent data for the FWHM of the conductance peak. Note that this is somewhat larger than the FWHM of the DOS due to the additional temperature induced broadening of the Fermi distribution of the electrons (see ESI section S8†).

From our NRG calculations we can extract effective values of  $\tilde{\Delta}$  for the three configurations B2, B4 and T4, which take into account the energy-dependent hybridization at an average level (see ESI section S6†). The resulting values, together with the corresponding Kondo temperatures, are shown in Table 1. Note that the values for  $\theta_L$  calculated in this way are in good agreement with the values calculated directly from the NRG susceptibility (Fig. 4). In Fig. 8(a) we present the resulting temperature dependent FWHM for all three systems calculated using eqn (7) and the parameters in Table 1.

Finally, within the approximation considered in this section we also estimate the temperature dependence of the normalized conductance of the Anderson impurity at zero bias. If one neglects the interference terms ( $T_I \approx 0$ ), then one can write  $G(V, \theta) \approx G_{AI}(V, \theta) + G_B(V, \theta)$ , where  $G_B$  is the background conductance originating from  $T_B$ , and  $G_{AI}$  is the conductance due to  $T_{AI} + T_{R,AI}$ . The temperature dependence of  $G_B$  is usually small, and for small  $V$  also the voltage dependence can be neglected, so that we set  $G_B$  to be a constant background conductance. Within the approximations used in this section, the temperature dependence of  $G_{AI}$  is derived in the ESI section S8 (eqn (S29) of the ESI†) to be

$$\frac{G_{AI}(0, \theta)}{G_0} \approx 1 - \frac{\pi^4}{16} \left( \frac{\theta}{\theta_L} \right)^2 = 1 - \pi^2 \left( \frac{k_B \theta}{\tilde{\Delta}} \right)^2, \quad (9)$$

where  $G_0 = G_{AI}(0, 0)$ . If accurate experimental data are available at low  $\theta$ , then the mapping of the measured temperature dependent conductance profile to this equation allows to determine the experimental  $\theta_L$ . However, in many experiments including also those for Au/PTM/Au junctions in ref. 16, the low temperature conductance data is too noisy, so that  $\theta_L$  is estimated from the high temperature data. Since no analytic

**Table 1** Renormalized quasi-particle spectral width,  $\tilde{\Delta}$ , and corresponding Kondo temperature  $\theta_L$  calculated with eqn (8), as well as wavefunction renormalization factor,  $z$ , for the configurations B2, B4, T4 (note that  $\tilde{\Delta}$  and  $z$  given here are denoted as  $\tilde{\Delta}_\Sigma$  and  $z_\Sigma$  in the ESI section S6 and in Table S1). For  $U = 1$  eV we also give the value of  $U/\pi\Delta$ , with the values of  $\Delta = \Gamma/2$  taken from Fig. 2

	B2	B4	T4
$\theta_L$ (K)	1.91	1.96	4.09
$\tilde{\Delta}$ (meV)	0.210	0.215	0.449
$z$	0.00315	0.00326	0.00598
$U/\pi\Delta$	5.63	5.44	5.05

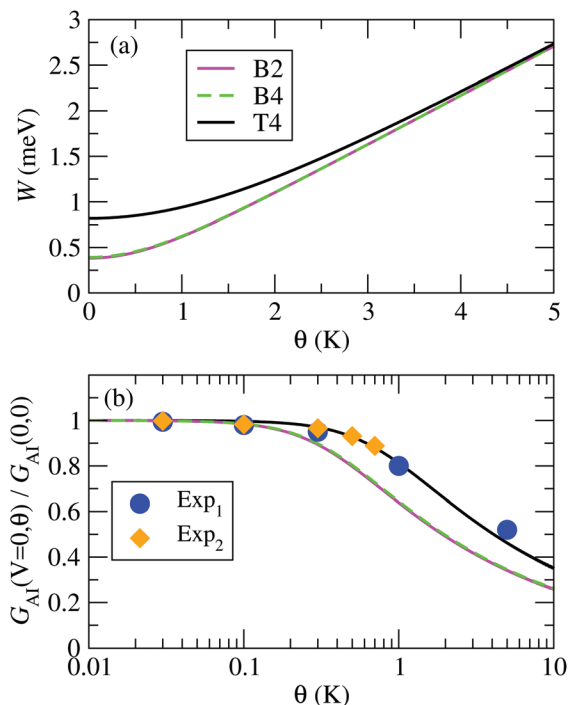


**Fig. 8** (a) Full width at half maximum of the Kondo peak in the DOS,  $W$ , calculated with the model eqn (7); (b) normalized impurity conductance as function of temperature using the function in eqn (10), for the B2, B4 and T4 configurations. The results are compared to experimental data from ref. 16, denoted as “Exp<sub>1</sub>” and “Exp<sub>2</sub>”.

expression is available for the whole temperature range, in ref. 58 a functional form is introduced in order to fit calculated NRG results in ref. 59. The proposed fitting curve is:

$$\frac{G_{AI}(0, \theta)}{G_0} = \left( \frac{1}{1 + (\theta/\tilde{\theta}_K)^2} \right)^s, \quad (10)$$

where  $\tilde{\theta}_K = (2^{1/s} - 1)^{-1/2} \theta_K$ , and  $\theta_K$  and  $s$  are phenomenological parameters. The value of  $\theta_K$  sets the temperature at which the conductance is reduced by a factor 2 ( $G_{AI}(0, \theta_K) = G_{AI}(0, 0)/2$ ). The second order expansion of this relation leads to  $G_{AI}(0, \theta)/G_{AI}(0, 0) \approx 1 - s(2^{1/s} - 1) \left( \frac{\theta}{\theta_K} \right)^2$ . As outlined in the ESI section S8,† for the particle-hole symmetric SIAM one can approximate  $\theta_K \approx \theta_L$ . Furthermore, the condition that the second order expansion needs to be equal to the form given in eqn (9) then sets the value of  $s$  to be  $s \approx 0.20$ .

A comparison of the temperature dependent conductance obtained using eqn (10) for the B2, B4 and T4 structures with the experimental data in ref. 16 is plotted in Fig. 8(b). The experimental normalized conductance agrees rather well with the calculated curves, in particular with the one for T4, which has the highest Kondo temperature of all the calculated structures. We denote as “Exp<sub>1</sub>” and “Exp<sub>2</sub>” the data for the two sets of experiments presented in Fig. 3c and d of ref. 16, respectively. When extracting the experimental Anderson Impurity



conductance one has to first subtract the background conductance,  $G_B$ . Our calculations show that the background conductance depends significantly on the detailed atomic structure, as shown by the values of  $T_B$  in Fig. 7. However, in experiments only the total conductance is accessible. One can approximate the background conductance by the conductance at zero bias for a very large applied magnetic field, which can be extracted from Fig. 3g–h of ref. 16. In this way we extract the ratio of background conductance to the total conductance at zero bias and zero temperature to be about 0.29 for Exp<sub>1</sub>, and 0.34 for Exp<sub>2</sub>.

While the results presented in this section show good agreement with the experiments in ref. 16, the limitation is that the equations are all based on the assumption of a particle-hole symmetric system, which is not generally the case. Indeed, in ref. 16 it is also shown that by applying a gate voltage the occupation of the SIAM can be systematically changed. At particle-hole symmetry the system is characterized by a single energy scale,  $k_B\theta_L$ , and eqn (7)–(10) reflect this property. Away from particle-hole symmetry, however, this no longer holds and corrections to these formulas enter. Furthermore, the condition that  $\Gamma_L$  is very different from  $\Gamma_R$  does not apply for a general system. In the next section we will therefore extend the method to the general non-equilibrium case, and also to the case away from particle-hole symmetry within a perturbative approach.

## 5. Non-equilibrium relations: renormalized super-perturbation theory

In this section we account for finite-temperature ( $\theta > 0$ ) and general finite-bias ( $V \neq 0$ ) effects by using the renormalized super perturbation theory (rSPT) described in ref. 22, 23 and 60. The rSPT corresponds to a perturbative method organized around the particle-hole symmetric strong coupling fixed point considered in the previous sections. While for the PTM/Au system considered here we always have  $U \gg \Delta$ , the rSPT relations are in principle valid for arbitrary values of  $U$ , and account for deviations from the particle-hole symmetry at a perturbative level. It is based on the insight that at the strong-coupling fixed point the equations have the form of an Anderson model, albeit with renormalized parameters.<sup>56</sup> These parameters are the renormalized hybridization,  $\tilde{\Delta}$ , which has been introduced in the previous section ( $\tilde{\Delta} = z\Delta$ ), the renormalized energy level,  $\tilde{\epsilon}_d$ , which is given by  $\tilde{\epsilon}_d = (\epsilon_d + U/2)/\Delta$ , and the renormalized interaction energy,  $\tilde{U}$ , defined in the ESI section S9.† We introduce the rescaled renormalized interaction  $\tilde{u} = \tilde{U}/\pi\tilde{\Delta}$ , which lies in the range from 0 for small  $U$  to 1 for very large  $U$  (see Fig. S9†). In this section we present results as function of  $\tilde{\epsilon}_d$ , which determines the deviation from the particle-hole symmetric case, and which can be tuned experimentally by applying a gate voltage.<sup>16</sup>

The Kondo temperature  $\theta_L$  near the strong coupling fixed point is obtained as  $k_B\theta_L = ((g\mu_B)^2/4) \lim_{\theta \rightarrow 0} (\chi_s)^{-1}$ ,<sup>60</sup> with the  $\theta = 0$  limit of the static spin susceptibility<sup>56</sup>

$$\lim_{\theta \rightarrow 0} \chi_s = \frac{(g\mu_B)^2}{2} \tilde{A}_{\text{AI}}(0, 0) (1 + \tilde{U} \tilde{A}_{\text{AI}}(0, 0)), \quad (11)$$

and where  $\tilde{A}_{\text{AI}}(E = 0, \theta = 0) = z^{-1} A_{\text{AI}}(E = 0, \theta = 0)$  denotes the equilibrium quasi-particle renormalized spectral density at the Fermi energy. Note that for the particle-hole symmetric reference system this definition of  $\theta_L$  is equivalent to the one presented in section 3 (see also ESI section S3†). Up to second order in  $\tilde{u}\tilde{\epsilon}_d$  we have

$$\tilde{A}_{\text{AI}}(0, 0) \approx [\pi\tilde{\Delta}(1 + (1 - \tilde{u})^2 \tilde{\epsilon}_d^2)]^{-1}. \quad (12)$$

Inserting this into eqn (11) yields the Kondo temperature

$$k_B\theta_L = \frac{2 + 2(1 - \tilde{u})^2 \tilde{\epsilon}_d^2}{1 + \frac{\tilde{u}}{1 + (1 - \tilde{u})^2 \tilde{\epsilon}_d^2}} \frac{\pi\tilde{\Delta}}{4}, \quad (13)$$

which is a generalization to finite  $\tilde{\epsilon}_d$  and to arbitrary  $U$  of the result for the symmetric SIAM in the strong coupling limit given in eqn (8).

A central issue is the relation between renormalized and bare parameters, which is encoded in the wave-function renormalization factor  $z$ . The renormalization factor  $z = \tilde{\Delta}/\Delta$  can be obtained from NRG for a general energy-dependent hybridization function, and from Bethe ansatz for the case of a constant energy-independent hybridization function.<sup>56</sup> A comparison between  $z$  calculated for a constant hybridization function  $\Delta(E) = \Delta(E_F) = \Gamma/2$  using Bethe ansatz and the NRG is shown as function of the interaction energy in Fig. 9, and demonstrates

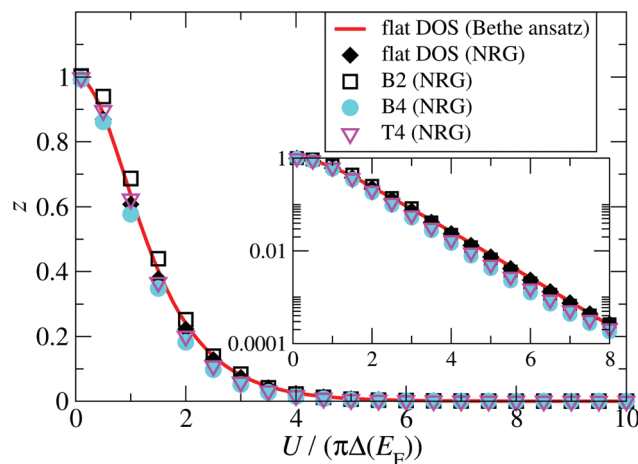


**Fig. 9** (Main graph) Comparison between the wave-function renormalization factor,  $z$ , calculated using NRG, for a constant hybridization function (black diamonds), and for the three configurations B2 (turquoise filled disks), B4 (pink open triangles), and T4 (white open rectangles). The Bethe ansatz solution for the same constant hybridization used in the NRG calculation is shown as the red solid line. Inset: Wave-function renormalization factor from the main graph plotted on a semi-logarithmic scale.





that they agree well. To address the question of the effect of an energy-dependent hybridization function on  $z$ , we also calculate  $z$  using NRG and with the full energy-dependent  $\Delta(E)$  for the B2, B4, and T4 structures (Fig. 5). Importantly, we find that they also agree rather well with the results for constant hybridization, showing that the low energy SIAM is largely dominated by the hybridization function around the Fermi energy. Based on these results we therefore calculate  $z$  and  $\tilde{u}$  for the rSPT expansion using the Bethe ansatz for the particle-hole symmetric SIAM with constant hybridization  $\Delta(E_F) = \Gamma/2$  (see Fig. S9 in the ESI section S9†), where the values of  $\Gamma$  for each configuration are given in Fig. 2.

In order to generalize the relations for the conductance, we first evaluate the equilibrium conductance,  $G_0 = G_{\text{AI}}(V = 0, \theta = 0, B = 0)$ , defined in eqn (6) and (S18) of the ESI,† away from the particle-hole symmetry. Here we have explicitly noted that we consider the reference case with zero magnetic field ( $B$ ). This results to

$$G_0 = \frac{2e^2}{h} \frac{4\Gamma_L\Gamma_R}{\Gamma_L + \Gamma_R} 2\pi A_{\text{AI}}(0, 0). \quad (14)$$

Then the extension of rSPT to current-carrying steady states allows us to evaluate the non-linear low-voltage conductance for finite temperatures and also magnetic fields, which has the form:<sup>22,23,60</sup>

$$\begin{aligned} \frac{G_0 - G_{\text{AI}}(V, \theta, B)}{G_0} = & c_\theta \left( \frac{k_B\theta}{\Delta} \right)^2 + c_B \left( \frac{g\mu_B B}{\Delta} \right)^2 \\ & + c_V \left( \frac{eV}{\Delta} \right)^2 - c_{VE_d} \left( \frac{eV}{\Delta} \right) \\ & - c_{\theta V} \left( \frac{eV}{\Delta} \right)^2 \left( \frac{\theta}{\Delta} \right)^2 + c_{\theta VE_d} \left( \frac{eV}{\Delta} \right) \left( \frac{\theta}{\Delta} \right)^2. \end{aligned} \quad (15)$$

This result can be obtained by expanding  $G_{\text{AI}}(\theta, V, B)$  up to second order in  $eV/\Delta$ ,  $k_B\theta/\Delta$ , and  $g\mu_B B/\Delta$ . The relations for the expansion coefficients are presented in the ESI section S9,† and extend the second order coefficients in  $U$  given in ref. 22 to arbitrarily large values of  $U$ . Note that the equilibrium transmission calculations, presented in the previous section and in the ESI section S8,† allow to extract the values of  $c_\theta = \pi^2$  and also  $c_V = 3/2$  in the strong coupling limit ( $\tilde{u} = 1$ ) and at particle-hole symmetry ( $\tilde{\epsilon}_d = 0$ ), and for highly asymmetric coupling to the electrodes (eqn (S29) in the ESI†). Using the general rSPT relations given in the ESI section S9† one can see that as long as  $\tilde{u} = 1$  and  $\tilde{\epsilon}_d = 0$  these values are valid for arbitrary  $\Gamma_L$  and  $\Gamma_R$ , so that they are independent of the level of asymmetry in the electronic coupling to the electrodes. Note that an important advantage of the rSPT approach is that it is not restricted to these limiting cases, and it is valid for arbitrary values of the parameters, which is a consequence of the fact that it is a truly non-equilibrium method.

The rSPT expansion coefficients calculated for the B2, B4, and T4 structures are displayed in Fig. 10 as a function of the local level energy  $\tilde{\epsilon}_d = (\epsilon_d + U/2)/\Delta$ . As noted above, in an experiment this can be modified by applying a gate voltage. We use the Bethe ansatz  $\tilde{\epsilon}_d = 0$  for the values of  $U/\pi\Delta$  given in Table 1,

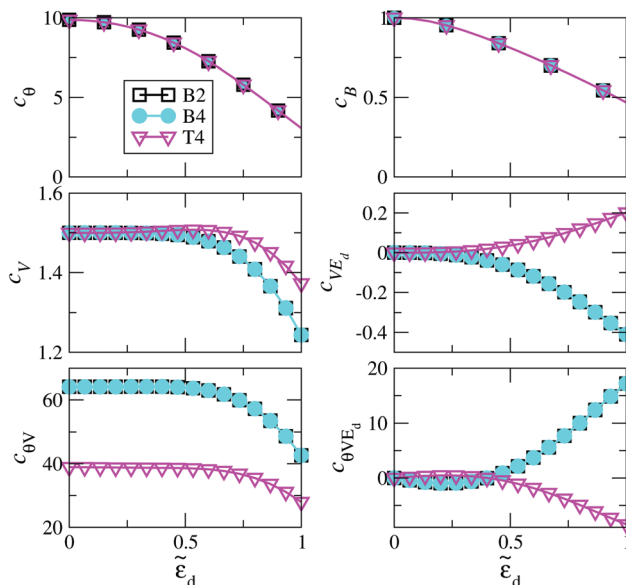


**Fig. 10** The dependence of the conductance coefficients in eqn (15) on the deviation from particle-hole symmetry, determined by  $\tilde{\epsilon}_d = (\epsilon_d + U/2)/\Delta(E_F)$ , for the configurations B2, B4 and T4. The mathematical relations for the coefficients are given in the ESI section S9,† and the parameter  $\zeta = 3(\Gamma_L/\Gamma_R)/(1 + \Gamma_L/\Gamma_R)^2$  in those equations, which determines the asymmetry of the electronic coupling to the left and right electrodes, follows from the values of  $\Gamma_R$  and  $\Gamma_L$  in Fig. 2 as  $\zeta_{\text{B2}} = 2.6 \times 10^{-4}$ ,  $\zeta_{\text{B4}} = 2.6 \times 10^{-4}$ , and  $\zeta_{\text{T4}} = 0.568$ . The dimensionless Coulomb repulsion  $U/(\pi\Delta(E_F))$  for the effective Anderson model applicable to each system is presented in Table 1.

which then result to  $\tilde{u} = 0.99999418$  for the B2 structure,  $\tilde{u} = 0.99999088$  for B4, and  $\tilde{u} = 0.99997705$  for T4. These values are all very close to 1, and indeed replacing them with 1 leads to essentially the same results, confirming that the Au-PTM system is in the strong coupling limit. The coefficients therefore differ only due to the changes in  $\Gamma_L/\Gamma_R$ , for which we use the DFT values given in Fig. 2. Since  $c_\theta$  and  $c_B$  are linear-response properties and do not depend on  $\Gamma_L/\Gamma_R$ , they are identical for all configurations. Consequently,  $c_\theta$  and  $c_B$  can also be calculated *via* NRG. A comparison for these two quantities between rSPT and NRG is given in ref. 23, where a rather good agreement is found up to moderate values of  $\tilde{\epsilon}_d$ .

The effect of the contact asymmetry, as captured by the ratio  $\Gamma_L/\Gamma_R$ , affects the value of the finite voltage coefficients, as clearly seen in the lower part of Fig. 10. At particle hole symmetry ( $\tilde{\epsilon}_d = 0$ ) the influence of the contact asymmetry vanishes, except for  $c_{\theta V}$ . A more detailed analysis of this effect is presented in Fig. 11, where we show  $c_V$  as function of  $\Gamma_L/\Gamma_R$  for different value of  $\tilde{\epsilon}_d$  and  $U$ . It can be seen that the overall variations of  $c_V$  are rather large, and only as the system goes into the strongly interacting regime (large  $U$ ) the effect of contact asymmetry becomes small, and it completely vanishes for very large  $U$  and  $\tilde{\epsilon}_d = 0$ , where it reaches the limiting value of 3/2 discussed above. Note that around  $\Gamma_L/\Gamma_R = 1$  (symmetric coupling)  $c_V$  varies quadratically for small variations of  $\Gamma_L/\Gamma_R$  around 1 (see also ESI section S9†).



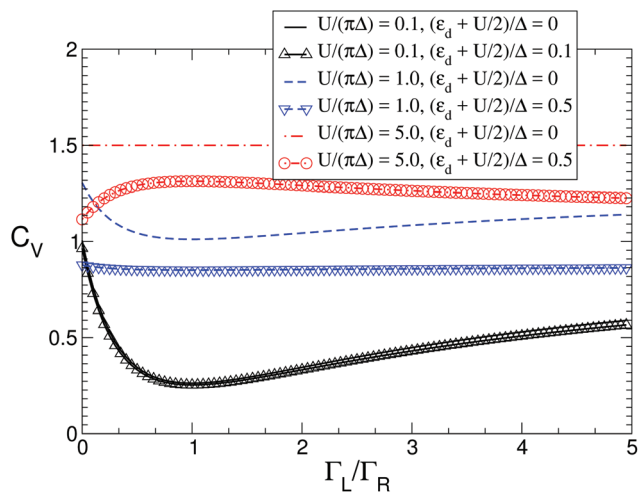


**Fig. 11** The dependence of the transport coefficient  $c_V$ , obtained from the rSPT, is displayed as a function of the asymmetry in the contacts  $\Gamma_L/\Gamma_R$ , for different values of the dimensionless Coulomb repulsion  $U/(\pi\Delta)$  and local level energy  $(\epsilon_d + U/2)/\Delta$ .

The rSPT provides a consistent description of the low-temperature, low-field, low-bias transport properties of the Anderson model. When the parameters are calculated from DFT + NEGF, and combined with NRG and/or Bethe ansatz, the method allows for an effectively first principles calculation of all the transport parameters. If the atomic structure is well defined, as is the case in STM experiment of molecules or other adsorbates on flat surfaces,<sup>24</sup> the approach is predictive on a quantitative level. When the structure is not known, as is the case for the PTM/Au system considered here, the approach allows to estimate ranges of possible electronic coupling coefficients, interactions energies and deviations from the particle-hole asymmetry. In this case the results give a qualitative guidance to experiments as to which atomic structures are expected to lead to Kondo physics in a measurement.

## 6. Conclusions

The theoretical modeling of Kondo physics in nanoscale devices is usually limited to fitting the parameters of a SIAM to conductivity measurements. Due to this adjustment of the parameters to the experiment such an approach is therefore not predictive, and the question whether it captures the right physics for a given experiment is therefore open. Moreover, it does not provide any information on the relationship between the device structure and its conductance as well as its electronic interactions. In order to overcome this limitation and provide a predictive model here we present a scheme that obtains the required parameters of the SIAM from DFT calculations for realistic atomic structures. Importantly, conductance measurements are inherently a non-equilibrium process, and our novel scheme combining DFT, NEGF, NRG and rSPT is designed to capture such effects. We derive the equations

that relate the equilibrium density of states to the non-equilibrium conductance *versus* voltage curves, which is necessary to interpret experimental conductance measurements in terms of the electronic and atomic structure of the system. With this approach it is therefore possible to calculate the electronic and non-equilibrium transport properties of strongly correlated molecular junctions in a systematic and predictive way effectively from first principles.

We employ the method for the description of the recently measured Au/PTM/Au break-junctions. The main limitation of break-junction experiments is that the statistical nature of the measurements does not allow a direct understanding of the atomic structures responsible for the conductance and its variations. First-principles calculations are therefore essential to gain a full atomistic insight on the system properties. While state of the art DFT + NEGF can only be applied to weakly correlated systems, the method presented here is proven to overcome this limitation. In fact, for the Au/PTM/Au break-junction we show how the molecule–electrode contacts affect the energy level alignment, charge transfer, hybridization and, ultimately, the Kondo temperature and conductance. Importantly, we show that while the Kondo temperature depends only on the total hybridization of the molecules with the electrodes, the experimental conductance depends also on the relative coupling to left and right electrodes, since those determine the current flow. Our projection scheme allows us to obtain these required individual electronic couplings from DFT, and with these we are able to evaluate the low bias conductance *versus* voltage curves by means of the rSPT. For PTM molecules weakly coupled to the electrodes, as is the case for a molecule on an idealized perfectly flat Au surface, we predict the Kondo temperature to lie below the experimentally accessible limit. In contrast, for asymmetric junctions with molecules on a corrugated Au surface, where the central carbon atom has a good electronic contact with the Au, the calculated Kondo temperature is in good agreement with experiments. These results are consistent with the experimental finding, where only a limited number of junctions exhibit Kondo features in the conductance at the accessible low temperatures.

Finally, we note that for experimental setups, where the atomic structure is well characterized, such as for certain adsorbates or defects on flat metal surfaces, the method will enable quantitative comparisons with low-noise experiments. By eliminating free parameters it can therefore lead to a systematic understanding of the non-equilibrium Kondo physics of molecular systems. The inclusion of the rSPT allows to predict systematic changes in non-linear transport at low voltage, temperature and magnetic field, which cannot be addressed directly from state of the art calculations of the transmission coefficient alone. Such changes can be induced experimentally, for example by varying the scanning tip height, which modifies the asymmetry in the electronic coupling to the electrodes, and these can then be calculated effectively from first principles with the approach presented here. Our method therefore paves the way toward the rational design of Kondo systems, and the possibility of performing systematic



comparisons with unprecedented accuracy between theory and experiments.

## Conflicts of interest

There are no conflicts to declare.

## Acknowledgements

A. D. and I. R. would like to thank E. Burzuri and A. V. Rudnev for useful discussions about transport experiments in Au/PTM/Au junctions, and C. Weber for insightful discussions on the Kondo physics. A. D. and I. R. acknowledge the financial support from the EU project ACMOL (FET Young Explorers, No. 618082). A. D. received additional support from EU Marie Skłodowska-Curie project SPINMAN (No. SEP-210189940) and from the Ministerio de Economía y Competitividad de España (No. FPGI-2013-16641). I. R. acknowledges additional financial support from the EU H2020 programme PETMEM project (Grant No. 688282). I. R. thanks the Cambridge CSD3 HPC centre for providing part of the computing resources. W. H. A., L. C. and D. V. acknowledge the financial support from the Deutsche Forschungsgemeinschaft through TRR80/F6, TRR80/G7 and the FOR1346/P3. E. Muñoz acknowledges financial support by Fondecyt (Chile) No. 1141146. M. M. Radonjić acknowledges the support from Ministry of Education, Science, and Technological Development of the Republic of Serbia under project ON171017. S. Kirchner acknowledges support by the National Key R&D Program of the MOST of China, grant No. 2016YFA0300202, the National Science Foundation of China, grant No. 11774307 and No. 11474250, and the U.S. Army RDECOM – Atlantic Grant No. W911NF-17-1-0108.

## References

- S. V. Aradhya and L. Venkataraman, *Nat. Nanotechnol.*, 2013, **8**, 399.
- L. Bogani and W. Wernsdorfer, *Nat. Mater.*, 2008, **7**, 179.
- D. Xiang, X. Wang, C. Jia, T. Lee and X. Guo, *Chem. Rev.*, 2016, **116**, 4318.
- W. Kohn, *Rev. Mod. Phys.*, 1999, **71**, 1253.
- J. Taylor, H. Guo and J. Wang, *Phys. Rev. B: Condens. Matter Mater. Phys.*, 2001, **63**, 245407.
- M. Brandbyge, J.-L. Mozos, P. Ordejón, J. Taylor and K. Stokbro, *Phys. Rev. B: Condens. Matter Mater. Phys.*, 2002, **65**, 165401.
- A. R. Rocha, V. M. García-Suárez, S. Bailey, C. Lambert, J. Ferrer and S. Sanvito, *Phys. Rev. B: Condens. Matter Mater. Phys.*, 2006, **73**, 085414.
- J. J. Palacios, A. J. Pérez-Jiménez, E. Louis, E. SanFabián and J. A. Vergés, *Phys. Rev. B: Condens. Matter Mater. Phys.*, 2002, **66**, 035322.
- A. Pecchia and A. di Carlo, *Rep. Prog. Phys.*, 2004, **67**, 1497.
- G. Stefanucci and S. Kurth, *Phys. Rev. Lett.*, 2011, **107**, 216401.
- P. Tröster, P. Schmitteckert and F. Evers, *Phys. Rev. B: Condens. Matter Mater. Phys.*, 2012, **85**, 115409.
- J. P. Bergfield, Z.-F. Liu, K. Burke and C. A. Stafford, *Phys. Rev. Lett.*, 2012, **108**, 066801.
- G. Stefanucci and S. Kurth, *Nano Lett.*, 2015, **15**, 8020–8025.
- S. Kurth and G. Stefanucci, *Phys. Rev. B: Condens. Matter Mater. Phys.*, 2016, **94**, 241103.
- D. Jacob and S. Kurth, *Nano Lett.*, 2018, **18**, 2086–2090.
- R. Frisenda, R. Gaudenzi, C. Franco, M. Mas-Torrent, C. Rovira, J. Veciana, I. Alcon, S. T. Bromley, E. Burzuri and H. S. Van der Zant, *Nano Lett.*, 2015, **15**, 3109–3114.
- S. Datta, *Electronic Transport in Mesoscopic Systems*, Cambridge University Press, Cambridge, UK, 1995.
- K. G. Wilson, *Rev. Mod. Phys.*, 1975, **47**, 773–840.
- H. R. Krishna-murthy, J. W. Wilkins and K. G. Wilson, *Phys. Rev. B: Condens. Matter Mater. Phys.*, 1980, **21**, 1003–1043.
- H. R. Krishna-murthy, J. W. Wilkins and K. G. Wilson, *Phys. Rev. B: Condens. Matter Mater. Phys.*, 1980, **21**, 1044–1083.
- R. Bulla, T. A. Costi and T. Pruschke, *Rev. Mod. Phys.*, 2008, **80**, 395–450.
- E. Muñoz, C. J. Bolech and S. Kirchner, *Phys. Rev. Lett.*, 2013, **110**, 016601.
- E. Muñoz, F. Zamani, L. Merker, T. A. Costi and S. Kirchner, *J. Phys.: Conf. Ser.*, 2017, **807**, 092001.
- A. Droghetti and I. Rungger, *Phys. Rev. B: Condens. Matter Mater. Phys.*, 2017, **95**, 085131.
- D. Jacob, K. Haule and G. Kotliar, *Phys. Rev. Lett.*, 2009, **103**, 016803.
- D. Jacob, K. Haule and G. Kotliar, *Phys. Rev. B: Condens. Matter Mater. Phys.*, 2010, **82**, 195115.
- M. Karolak, D. Jacob and A. I. Lichtenstein, *Phys. Rev. Lett.*, 2011, **107**, 146604.
- D. Jacob, M. Soriano and J. J. Palacios, *Phys. Rev. B: Condens. Matter Mater. Phys.*, 2013, **88**, 134417.
- D. Jacob, *J. Phys.: Condens. Matter*, 2015, **27**, 245606.
- L. Chioncel, C. Morari, A. Östlin, W. H. Appelt, A. Droghetti, M. M. Radonjić, I. Rungger, L. Vitos, U. Eckern and A. V. Postnikov, *Phys. Rev. B: Condens. Matter Mater. Phys.*, 2015, **92**, 054431.
- R. Requist, S. Modesti, P. P. Baruselli, A. Smogunov, M. Fabrizio and E. Tosatti, *Proc. Natl. Acad. Sci. U. S. A.*, 2014, **111**, 69.
- P. Lucignano, R. Mazzarello, A. Smogunov, M. Fabrizio and E. Tosatti, *Nat. Mater.*, 2009, **8**, 563.
- P. P. Baruselli, A. Smogunov, M. Fabrizio and E. Tosatti, *Phys. Rev. Lett.*, 2012, **108**, 206807.
- J. Liu, H. Isshiki, K. Katoh, T. Morita, B. K. Breedlove, M. Yamashita and T. Komeda, *J. Am. Chem. Soc.*, 2013, **135**, 651.



- 35 Y.-h. Zhang, S. Kahle, T. Herden, C. Stroh, M. Mayor, U. Schlickum, M. Ternes, P. Wahl and K. Kern, *Nat. Commun.*, 2013, **4**, 2110.
- 36 F. Bejarano, I. J. Olavarria-Contreras, A. Droghetti, I. Rungger, A. Rudnev, D. Gutiérrez, M. Mas-Torrent, J. Veciana, H. S. J. van der Zant, C. Rovira, E. Burzurí and N. Crivillers, *J. Am. Chem. Soc.*, 2018, **140**, 1691–1696.
- 37 W. R. French, C. R. Iacovella, I. Rungger, A. M. Souza, S. Sanvito and P. T. Cummings, *Nanoscale*, 2013, **5**, 3654.
- 38 W. R. French, C. R. Iacovella, I. Rungger, A. M. Souza, S. Sanvito and P. T. Cummings, *J. Phys. Chem. Lett.*, 2013, **4**, 887.
- 39 N. Crivillers, C. Munuera, M. Mas-Torrent, C. Simao, S. T. Bromley, C. Ocal, C. Rovira and J. Veciana, *Adv. Mater.*, 2009, **21**, 1177.
- 40 N. Crivillers, M. Paradinas, M. Mas-Torrent, S. T. Bromley, C. Rovira, C. Ocal and J. Veciana, *Chem. Commun.*, 2011, **47**, 4664.
- 41 G. Seber, A. V. Rudnev, A. Droghetti, I. Rungger, J. Veciana, M. Mas-Torrent, C. Rovira and N. Crivillers, *Chem. – Eur. J.*, 2017, **23**, 1415.
- 42 A. Droghetti, I. Rungger, C. Das Pemmaraju and S. Sanvito, *Phys. Rev. B: Condens. Matter Mater. Phys.*, 2016, **93**, 195208.
- 43 P. W. Anderson, *Phys. Rev.*, 1961, **124**, 41–53.
- 44 G. Kotliar, S. Y. Savrasov, K. Haule, V. S. Oudovenko, O. Parcollet and C. A. Marianetti, *Rev. Mod. Phys.*, 2006, **78**, 865–951.
- 45 A. G. Petukhov, I. I. Mazin, L. Chioncel and A. I. Lichtenstein, *Phys. Rev. B: Condens. Matter Mater. Phys.*, 2003, **67**, 153106.
- 46 M. I. Katsnelson, V. Y. Irkhin, L. Chioncel, A. I. Lichtenstein and R. A. de Groot, *Rev. Mod. Phys.*, 2008, **80**(315), 315–378.
- 47 P. Huang and E. A. Carter, *Nano Lett.*, 2006, **6**, 1146.
- 48 F. Libisch, C. Huang and E. A. Carter, *Acc. Chem. Res.*, 2014, **47**, 2768.
- 49 Q. Sun and G. K.-L. Chan, *Acc. Chem. Res.*, 2705, **49**, 2705.
- 50 J. Schrieffer and P. Wolff, *Phys. Rev.*, 1966, **149**, 491.
- 51 A. Hewson, *The Kondo Problem to Heavy Fermions*, Cambridge Univ. Press, Cambridge, UK, 1993.
- 52 F. D. M. Haldane, *J. Phys. C: Solid State Phys.*, 1978, **11**, 5015.
- 53 B. Himmetoglu, A. Floris, S. de Gironcoli and M. Cococcioni, *Int. J. Quantum Chem.*, 2014, **114**, 14.
- 54 A. M. Souza, I. Rungger, C. D. Pemmaraju, U. Schwingenschlögl and S. Sanvito, *Phys. Rev. B: Condens. Matter Mater. Phys.*, 2013, **88**, 165112.
- 55 A. M. Souza, I. Rungger, R. B. Pontes, A. R. Rocha, A. J. Roque da Silva, U. Schwingenschlögl and S. Sanvito, *Nanoscale*, 2014, **6**, 14495.
- 56 A. C. Hewson, *Phys. Rev. Lett.*, 1993, **70**, 4007.
- 57 K. Nagaoka, T. Jamneala, M. Grobis and M. F. Crommie, *Phys. Rev. Lett.*, 2002, **88**, 077205.
- 58 D. Goldhaber-Gordon, J. Gores, M. A. Kastner, H. Shtrikman, D. Mahalu and U. Meirav, *Phys. Rev. Lett.*, 1998, **81**, 5225.
- 59 T. A. Costi, A. C. Hewson and V. Zlatić, *J. Phys.: Condens. Matter*, 1994, **6**, 2519.
- 60 L. Merker, S. Kirchner, E. Muñoz and T. A. Costi, *Phys. Rev. B: Condens. Matter Mater. Phys.*, 2013, **87**, 165132.



## Superconducting nature of the Bi-II phase of elemental bismuth

Rustem Khasanov,<sup>1,\*</sup> Miloš M. Radonjić,<sup>2</sup> Hubertus Luetkens,<sup>1</sup> Elvezio Morenzoni,<sup>1</sup> Gediminas Simutis,<sup>1</sup> Stephan Schönecker,<sup>3</sup> Wilhelm H. Appelt,<sup>4</sup> Andreas Östlin,<sup>4</sup> Liviu Chioncel,<sup>4</sup> and Alex Amato<sup>1</sup>

<sup>1</sup>Laboratory for Muon Spin Spectroscopy, Paul Scherrer Institute, CH-5232 Villigen PSI, Switzerland

<sup>2</sup>Scientific Computing Laboratory, Center for the Study of Complex Systems, Institute of Physics Belgrade, University of Belgrade, Pregrevica 118, 11080 Belgrade, Serbia

<sup>3</sup>Applied Materials Physics, Department of Materials Science and Engineering, KTH Royal Institute of Technology, SE-10044 Stockholm, Sweden

<sup>4</sup>Augsburg Center for Innovative Technologies, and Center for Electronic Correlations and Magnetism, Theoretical Physics III, Institute of Physics, University of Augsburg, D-86135 Augsburg, Germany



(Received 25 February 2019; revised manuscript received 18 April 2019; published 13 May 2019)

The superconductivity in the Bi-II phase of elemental bismuth (transition temperature  $T_c \simeq 3.92$  K at pressure  $p \simeq 2.80$  GPa) was studied experimentally by means of the muon-spin rotation as well as theoretically by using the Eliashberg theory in combination with density functional theory calculations. Experiments reveal that Bi-II is a type-I superconductor with a zero temperature value of the thermodynamic critical field  $B_c(0) \simeq 31.97$  mT. The Eliashberg theory approach provides a good agreement with the experimental  $T_c$  and the temperature evolution of  $B_c$ . The estimated value for the retardation (coupling) parameter  $k_B T_c / \omega_{\text{ln}} \approx 0.07$  ( $\omega_{\text{ln}}$  is the logarithmically averaged phonon frequency) suggests that Bi-II is an intermediately coupled superconductor.

DOI: [10.1103/PhysRevB.99.174506](https://doi.org/10.1103/PhysRevB.99.174506)

### I. INTRODUCTION

Bismuth is element 83 in the periodic table. It is a brittle metal with a silvery white color. Its complex and tunable electronic structure exhibits many fascinating properties that often defy the expectations of conventional theories of metals. Most notably, measurements on bismuth provided the first evidence of quantum oscillations and the existence of the Fermi surface, thereby experimentally confirming the underlying paradigm of all modern solid state physics [1,2].

At ambient pressure bismuth is a compensated semimetal with an exceptionally low carrier concentration of one free charge carrier per about  $10^5$  atoms [3]. The Fermi surface consists of tiny electron- and hole-like pockets giving rise to a highly anisotropic effective mass, which can become as low as  $\sim 10^{-3}$  that of the electron mass in some directions [4]. Such properties lead to the highest Hall coefficient, the largest diamagnetism, and an exceptionally small thermal conductivity which sets bismuth to be quite different compared to other metals [5].

Upon application of pressure at room temperature, Bi undergoes a series of structural transitions [6]:



Upon cooling, all the above phases become superconducting with the transition temperature ( $T_c$ ) of  $T_c \simeq 0.53$  mK for Bi-I,  $T_c \simeq 3.9$  K for Bi-II,  $T_c \simeq 7$  K for Bi-III, and  $T_c \simeq 8.5$  K for Bi-V, respectively [7–16]. The superconductivity in Bi-I and Bi-III phases were found to be of type I and type II, respectively [12–16]. Much less information is known for

other Bi phases. In particular, the Bi-I to Bi-II and Bi-II to Bi-III transitions are well established at room temperature, while their low temperature behavior leads to contradicting results. References [17–22] suggest that the Bi-III phase forms at 2.7 GPa at room temperature, while the Bi-II to Bi-III (or possibly Bi-I to Bi-III) phase boundary occurs at pressures  $p \gtrsim 3.0$  GPa at 0 K. The Bi-II phase likely extends down to 200 K only, where the Bi-I-II-III triple point may occur [20,22]. On the other hand, the superconducting Bi-III phase was observed at pressures of  $\simeq 2.7$  GPa by several other research groups, as well as by us [13–16]. Some groups have also reported superconductivity in Bi-II phase at pressures of  $\simeq 2.5$  GPa with  $T_c \simeq 4$  K [7,10,22]. It is worth to note here, that a pure Bi-II phase has never been observed alone, but always appeared as an admixture to the Bi-I or Bi-III phases [10,13,15]. It seems, therefore, likely that the Bi-II phase becomes metastable at low temperatures.

This paper presents the results of an experimental and theoretical study of the Bi-II superconductor. The bulk Bi-II phase ( $T_c \simeq 3.92$  K at  $p \simeq 2.80$  GPa) was stabilized by approaching it from the preformed Bi-III one ( $T_c \simeq 7.05$  K at  $p \simeq 2.72$  GPa, Ref. [16]). Muon-spin-rotation ( $\mu$ SR) measurement reveal that the magnetic induction ( $B$ ) in a cylindrical Bi-II sample (with the magnetic field applied perpendicular to the cylinder axis) is separated between normal state ( $B_N = B_c$ ,  $B_c$  is the thermodynamical critical field) and superconducting ( $B_S = 0$ ) domains thus indicating that Bi-II is a superconductor of type I. The zero temperature thermodynamic critical field was found to be  $B_c(0) \simeq 31.97$  mT. The Eliashberg theory provides a good agreement with the experimental critical temperature ( $\simeq 3.95$  K), the zero temperature critical field ( $\simeq 36.6$  mT), and the temperature evolution of  $B_c(T)$ . The estimated value for the retardation parameter

\*rustem.khasanov@psi.ch

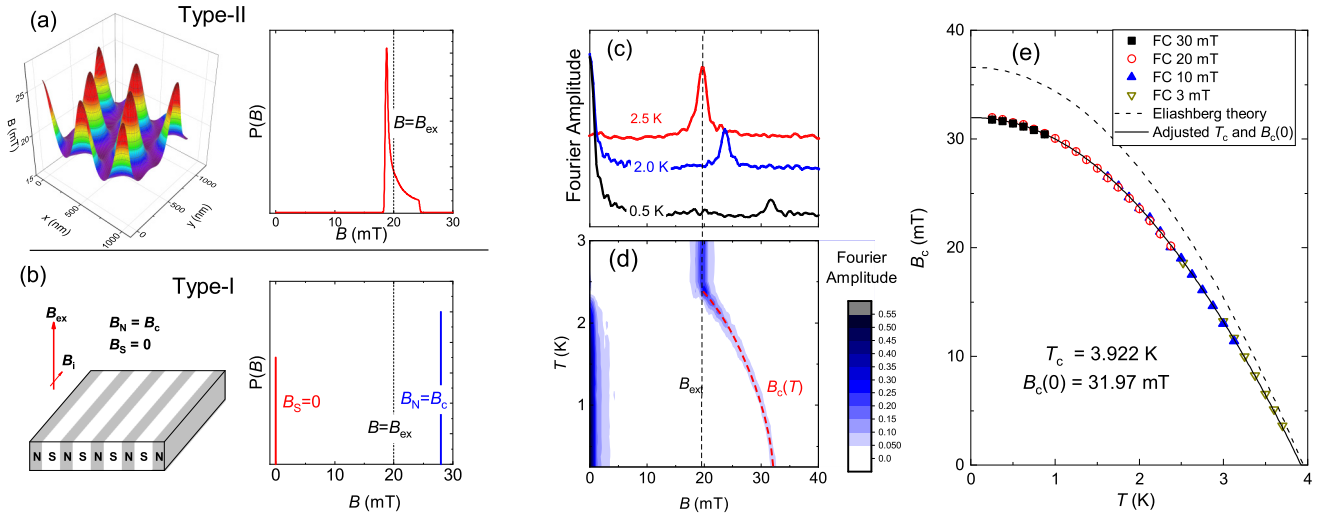


FIG. 1. (a) The distribution of fields in a type-II superconductor in the vortex state (left panel) and the corresponding magnetic field distribution function  $P(B)$  (right panel). (b) The schematic representation of nucleation of a plate-like type-I superconductor in normal state ( $B_N = B_c$ ) and superconducting ( $B_S = 0$ ) domains (left panel). An ordered laminar structure is formed with an additional in-plane component  $B_i$ , after Refs. [23,24]. The right panel is the  $P(B)$  distribution in type-I superconductor. (c) Fourier transform of TF- $\mu$ SR time spectra measured at external field  $B_{\text{ex}} \simeq 20$  mT reflecting the  $P(B)$  distribution in the Bi-II sample above ( $T = 2.5$  K) and below ( $T = 0.5$  and  $2.0$  K) the superconducting transition temperature [ $T_c(20 \text{ mT}) \simeq 2.3$  K]. (d) The contour plot of the  $P(B)$  distribution measured at  $B_{\text{ex}} \simeq 20$  mT. (e) The temperature dependence of the thermodynamical critical field  $B_c$  for the Bi-II sample obtained in  $\mu$ SR experiments with the applied field  $B_{\text{ex}} = 3, 10, 20,$  and  $30$  mT. The dashed line is the temperature evolution of the “theoretical”  $B_{c,T}$  obtained within the framework of *ab initio* Eliashberg calculations using density functional theory. The solid line is the same  $B_{c,T}(T)$  curve with  $T_c = 3.922$  K and  $B_c(0) = 31.97$  mT adjusted from the fit (see text for details).

$k_B T_c / \omega_{\text{in}} \approx 0.07$  ( $\omega_{\text{in}}$  is the logarithmically averaged phonon frequency) suggests that Bi-II is an intermediately coupled superconductor.

## II. EXPERIMENT

The Bi sample and the pressure cell were the same as used in our previous experiments for studying Bi-III superconductivity (Ref. [16]). The transformation of the Bi sample from the Bi-III to Bi-II phase was made by allowing the sample volume to increase inside the pressure cell [25], and ac susceptibility (ACS) measurements reveal the presence of a sharp superconducting transition at  $T_c \simeq 3.92$  K at  $p \simeq 2.80$  GPa. The amount of Bi-III phase admixture, obtained in the ACS experiments, does not exceed 10%–15% (see the Supplemental Material, Ref. [25]). The transverse-field (TF)  $\mu$ SR experiments were carried out at the  $\mu$ E1 beam line by using the dedicated General Purpose Decay (GPD) spectrometer (Paul Scherrer Institute, Switzerland). The details of TF- $\mu$ SR experiments performed under pressure are provided in the Supplemental Material, Ref. [25], and in Refs. [26–28].

Due to its microscopic nature, the  $\mu$ SR technique allows one to directly distinguish between type-I and type-II superconductors, since both superconductivity types are characterized by very different magnetic field distributions [ $P(B)$ ’s] inside the specimen. An ordered flux-line lattice (FLL) of the type-II superconductor has the field distribution and the corresponding  $P(B)$  which are shown schematically in the left and right panels of Fig. 1(a). The calculations were performed within the framework of the London model with the Gaussian cutoff for a triangular FLL ( $B_{\text{ex}} = 20$  mT, the

magnetic penetration depth  $\lambda = 200$  nm, and the coherence length  $\xi = 50$  nm; see the Supplemental Material, Ref. [25]). The asymmetric magnetic field distribution function  $P(B)$  centers in the vicinity of  $B_{\text{ex}}$ . It is characterized by two cutoffs fields and by the peak shifted below  $B_{\text{ex}}$  [see the right panel at Fig. 1(a), and, e.g., Refs. [31,32] and references therein]. A type-I superconductor expels a magnetic field completely, apart from a layer at the surface of thickness  $\lambda$ . However, in samples with a finite demagnetization factor  $n$ , a separation between superconducting domains (with  $B_S = 0$ ) and normal state domains (with  $B_N = B_c > B_{\text{ex}}$ ) can occur [see the left panel at Fig. 1(b) showing schematically the nucleation of a platelike sample on S/N domains, and, e.g., Refs. [33–36] and references therein]. In this case,  $P(B)$  consists of two,  $B = 0$  and  $B = B_c$ , lines [right panel of Fig. 1(b)]. Such distributions (without, however, the  $B = 0$  line) were reported in earlier  $\mu$ SR measurements on type-I superconductors Sn, Pb, and In [37–40], and in recent experiments on BeAu [41,42].

Figure 1(c) shows the Fourier transform of few representative TF- $\mu$ SR time spectra (the pressure cell background subtracted) measured at  $B_{\text{ex}} = 20$  mT. Figure 1(d) represents the contour plot of the corresponding Fourier intensities. The overall behavior shown in Figs. 1(c) and 1(d) corresponds to the response of a type-I superconductor with a nonzero demagnetization factor  $n$  in an applied field  $B_{\text{ex}}$  of  $B_c(1 - n) \leq B_{\text{ex}} \leq B_c$  [see the discussion above, Fig. 1(b) and Refs. [37–42]]. Indeed, the  $P(B)$  distributions at  $T \simeq 0.5$  and  $2.0$  K split into two peaks with the first one at  $B = 0$  and the second one  $\simeq 12$  and  $\simeq 5$  mT higher than the applied field  $B_{\text{ex}}$ , respectively. With increasing temperature, the intensity of the  $B = 0$  peak decreases until it vanishes at  $T \simeq 2.3$  K, while the

TABLE I. Experimental and calculated material parameters for various bismuth phases.  $T_c$  is the superconducting transition temperature,  $B_c$  is the thermodynamical critical field,  $B_{c2}$  is the upper critical field,  $\lambda_{\text{el-ph}}$  is the electron-phonon coupling constant,  $\gamma_N$  is the normal state electronic specific heat coefficient [25],  $\omega_{\text{ln}}$  is the characteristic phonon frequency, and  $k_B T_c / \omega_{\text{ln}}$  is the retardation (coupling) parameter. n/a means the parameter is not available.

Superconductivity		$T_c$ (K)	$B_c$ (mT)	$B_{c2}$ (T)	$\lambda_{\text{el-ph}}$	$\gamma_N$ (erg cm <sup>-3</sup> K <sup>-2</sup> )	$\omega_{\text{ln}}$	$k_B T_c / \omega_{\text{ln}}$ (meV)	References
Bi-I	type-I	0.00053	0.0052	–	0.236	399	n/a	n/a	[12,29,30]
Bi-II	type-I	3.92	31.97	–	–	–	–	–	This work, experiment
Bi-II	type-I	3.95	36.6	–	1.02	2206	4.69	0.072	This work, theory
Bi-III	type-II	7.05	73.6	2.6	2.75	n/a	5.51	0.110	[14–16]
Bi-V	n/a	8.50	n/a	n/a	n/a	n/a	n/a	n/a	[10,15]

intensity of the  $B \geq B_{\text{ex}}$  peak increases by approaching  $T \simeq 2.3$  K and saturates above it [Figs. 1(c) and 1(d)]. The position of the  $B \geq B_{\text{ex}}$  peak shifts in the direction of  $B_{\text{ex}}$  all the way up to  $\simeq 2.3$  K and coincides with  $B_{\text{ex}}$  for higher temperatures. The intensities of the  $B = 0$  and  $B \geq B_{\text{ex}}$  peaks are proportional to the volume fractions of the superconducting ( $B_S = 0$ ) and the normal state ( $B_N = B_c$ ) domains. The disappearance of the  $B = 0$  peak above 2.3 K corresponds to the transition of the sample into the normal state [ $T_c(B = 20 \text{ mT}) \simeq 2.3$  K]. The position of the  $B > B_{\text{ex}}$  peak represents the temperature evolution of the thermodynamical critical field  $B_c$  [red dashed line in Fig. 1(d)].

Note that our  $\mu$ SR data exclude the possibility of type-II superconductivity in Bi-II. Additionally, the zero temperature critical field was found to be half the value of  $B_c(0) \simeq 73$  mT reported in Ref. [13]. Field scans at  $T = 0.25, 2.1,$  and  $3.0$  K with 1-mT steps (from 0.3 to 35 mT) and temperature scans at  $B_{\text{ex}} = 3, 10, 20, 30,$  and  $35$  mT with 0.125 K steps (from 0.25 to 8.0 K) do not show any FLL-type  $\mu$ SR response. No superconductivity was detected at  $B_{\text{ex}} = 35$  mT down to the lowest temperature of the experiment ( $\simeq 0.25$  K) and for all applied fields at  $T \geq 4$  K. The fact that no FLL signal was observed above 4.0 K, suggests also that the admixture of the Bi-III phase ( $T_c \simeq 7$  K as is detected in the ACS experiment; see the Supplemental Material, Ref. [25]) is minimal in the sample volume. Our results imply, therefore, that within the full range of temperatures ( $0.25 \leq T \leq 8.0$  K) and fields ( $0.3 \leq B_{\text{ex}} \leq 0.35$  mT) studied, the Bi-II phase of elemental bismuth behaves as a typical *type-I superconductor*.

The temperature dependence of the thermodynamical critical field  $B_c$ , as determined from the measured field value in the normal-state domain [ $B_c = B_N$ , see Figs. 1(b), 1(c) and 1(d)], is shown in Fig. 1(e). The points are obtained with several applied fields ( $B_{\text{ex}} = 3, 10, 20,$  and  $30$  mT) and they overlap within certain temperature and field regions. The reason for such overlapping is caused by the intermediate state formation condition:  $B_c(T) (1 - n) \leq B_{\text{ex}} \leq B_c(T)$ , showing that *similar*  $B_c(T)$  can be obtained for different  $B_{\text{ex}}$ 's [37–40].

### III. THEORY

The obtained experimental data were compared with quantitative predictions based on *ab initio* Eliashberg calculations using density functional theory (DFT). The details of calculations are given in the Supplemental Material, Ref. [25]. The

experimental and calculated material parameters for the Bi-II phase are summarized in Table I.

Figures 2(a) and 2(b) display the phonon density of states (DOS), the Eliashberg electron-phonon spectral function [ $\alpha^2 F(\omega)$ ], and the integrated electron-phonon coupling constant:  $\lambda_{\text{el-ph}}(\omega) = 2 \int_0^\omega \frac{d\omega'}{\omega'} \alpha^2 F(\omega')$ . In the high frequency limit  $\lambda_{\text{el-ph}}$  was estimated to be  $\lambda_{\text{el-ph}}(\omega \rightarrow \infty) \simeq 1.02$ . The logarithmically averaged phonon frequency  $\omega_{\text{ln}}$ , representing a characteristic phonon energy mediating the pairing [43], was calculated via

$$\omega_{\text{ln}} = \exp \left( \frac{2}{\lambda_{\text{el-ph}}} \int_0^\infty \frac{d\omega}{\omega} \alpha^2 F(\omega) \ln \omega \right), \quad (1)$$

and found to be  $\omega_{\text{ln}} = 4.69$  meV.

The dashed line in Fig. 1(e) represents the temperature evolution of  $B_{c,T}(T)$  computed from the free energy difference between the normal and superconducting states ( $\Delta F$ ) via  $B_{c,T}(T) = \sqrt{-8\pi \Delta F}$  (hereafter the index ‘‘T’’ accounts for the parameter obtained from the theory).  $\Delta F$  was calculated within the strong-coupling Eliashberg theory following the approach developed by Bardeen and Stephen [44]. The transition temperature  $T_{c,T} = 3.95$  K and the zero temperature value of the thermodynamical field  $B_{c,T}(0) = 36.6$  mT are found. Scaling the  $B_c(T)$  curve further allows direct comparison with the experimental data. The adjusted curve with  $T_c \simeq 3.922$  K and  $B_c(0) \simeq 31.97$  mT is shown by the solid line in Fig. 1(e).

In order to better visualize the difference between the theory and the experiment, the deviation function  $D(T/T_c) = B_c(T)/B_c(0) - (1 - [T/T_c]^2)$  is plotted in Fig. 2(c). For comparison, the weak coupling BCS results are also shown. Obviously, the BCS theory underestimates the experimental  $D(T/T_c)$  and a significant improvement is obtained using the Eliashberg theory. Although some quantitative discrepancies remain, the main features are captured.

Many thermodynamic quantities, like the condensation energy or the specific heat jump  $\Delta C(T_c)/\gamma_N T_c = C_{\text{es}}(T_c)/\gamma_N T_c - 1$ , can be expressed directly by using the derivative of  $D(T/T_c)$  as follows [45]:

$$\frac{\Delta C(T_c)}{\gamma_N T_c} = \frac{B_c(0)^2}{2\pi \gamma_N T_c^2} \left[ \frac{\partial D(T/T_c)}{\partial ([T/T_c]^2)} \Big|_{(T/T_c)^2=1} - 1 \right]^2. \quad (2)$$

Here  $\gamma_N$  is the electronic specific heat coefficient in the normal state (see the Supplemental Material, Ref. [25], for the  $\gamma_N$  estimate) and  $C_{\text{es}}(T)/\gamma_N T_c$  is the electronic specific heat in the

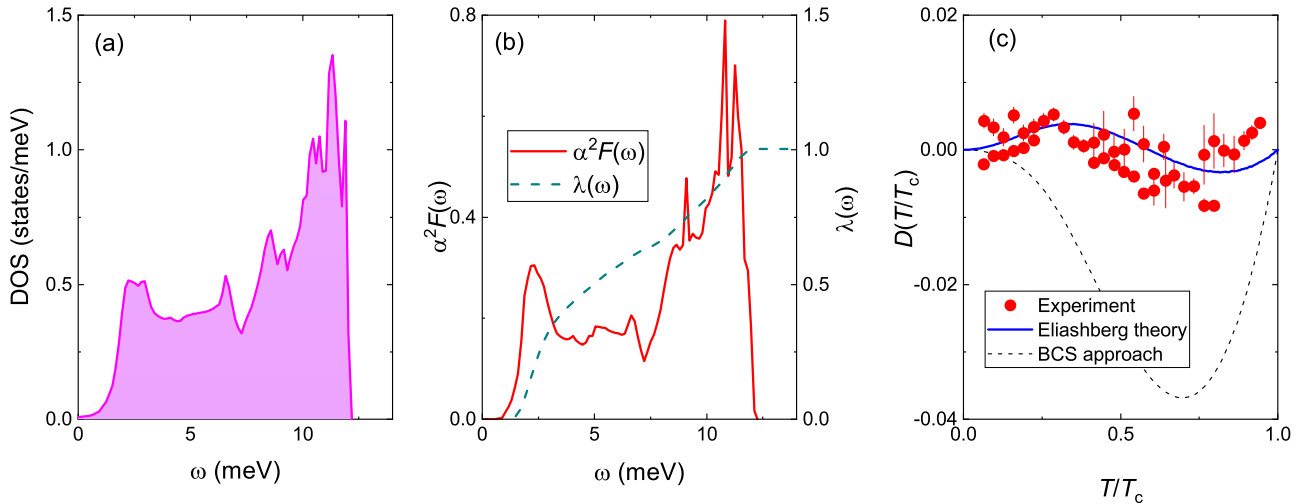


FIG. 2. (a) Calculated phonon density of states. (b) Calculated Eliashberg electron-phonon spectral function (red solid line) and integrated electron-phonon coupling strength  $\lambda_{\text{el-ph}}$  (green dashed line). (c) The deviation function  $D(T/T_c) = B_c(T)/B_c(0) - (1 - [T/T_c]^2)$ . The solid blue and dashed lines correspond to the Eliashberg and the BCS approach, respectively.

superconducting state. We proceed with the direct numerical calculation of  $C_{\text{eS}}(T)$  within the Eliashberg theory (see the Supplemental Material, Ref. [25]). The heat capacity jump  $\Delta C(T_c)/\gamma_N T_c \simeq 2.40$  was found, which is large in comparison with the universal BCS value of 1.43. Such a large jump in the specific heat for Bi-II is certainly accessible for calorimetric measurements.

#### IV. CONCLUSIONS

To conclude, the superconductivity in the Bi-II phase of elemental bismuth was studied experimentally by means of muon-spin rotation, as well as theoretically using the Eliashberg theory in combination with density functional theory calculations. Experiments reveal that the magnetic induction in the cylindrical Bi-II sample is separated into the normal state and superconducting domains thus suggesting that Bi-II is a superconductor of type I. The transition temperature and the zero temperature thermodynamic critical field were found to be  $T_c \simeq 3.92$  K and  $B_c(0) \simeq 31.97$  mT, respectively. The electronic and the superconducting properties of Bi-II were computed from first principles. Following the phenomenological approach of Carbotte [46], the strong coupling corrections were embodied via the retardation parameter  $k_B T_c / \omega_{\text{in}}$ . Including retardation effects, the Eliashberg theory provides better agreement with the experimental data than the weak coupling BCS approach. The theory values for the critical temperature ( $T_{c,T} \simeq 3.95$  K) and the zero temperature critical field  $B_{c,T}(0) = 36.6$  mT, as well as the temperature evolution of  $B_c(T)$  are in agreement with the experiment. The specific heat jump, as estimated from the deviation function  $D(T/T_c)$ , was found to be  $\Delta C(T_c)/\gamma_N T_c = 2.40$ , which is large in comparison with the universal BCS value of 1.43. The *ab initio* calculations result in the value of the retardation parameter  $k_B T_c / \omega_{\text{in}} \approx 0.07$  and put Bi-II in the category of intermediate

coupling superconductors, being away from the very strong coupling limit  $k_B T_c / \omega_{\text{in}} \approx 0.25$ . Finally, our analysis reveals that the Cooper pairing in Bi-II is a consequence of balance between the electron-phonon attraction and a significant direct Coulomb repulsion. Compared to our previous study of Bi-III [16], the retardation effects in Bi-II were found to be less efficient than in Bi-III. While Bi-III is a type-II strong-coupled superconductor [14–16], the Bi-II and Bi-I are type-I superconductors with the intermediate (present study) and weak-coupling (Ref. [30]) strength, respectively (see also Table I summarizing experimental and calculated material parameters for various bismuth phases). In this respect the high pressure  $\mu$ SR experiments, as those presented here and in Ref. [16] on elemental Bi, are essential tools to elucidate the nature of the interplay between structural and superconducting phases in conventional superconductors.

#### ACKNOWLEDGMENTS

This work was performed at the Swiss Muon Source ( $S\mu S$ ), Paul Scherrer Institute (PSI, Switzerland). The work of GS is supported by the Swiss National Science Foundation, Grants No. 200021\_149486 and No. 200021\_175935. M.M.R. acknowledges the support from the Ministry of Education, Science, and Technological Development of the Republic of Serbia under Project No. ON171017. Numerical simulations were run on the PARADOX supercomputing facility at the Scientific Computing Laboratory of the Institute of Physics Belgrade. L.C. and A.Ö acknowledge DFG for financial support through the TRR80/F6 project. S.S. acknowledges financial support from the Swedish Research Council and computational facilities provided by the Swedish National Infrastructure for Computing at the National Supercomputer Centers in Linköping and Umeå.

[1] L. Shubnikov and W. J. de Haas, *Nature (London)* **126**, 500 (1930).

[2] W. J. de Haas and P. M. van Alphen, *Proc. Neth. Roy. Acad. Sci.* **33**, 1106 (1930).



- [3] F. Y. Yang, K. Liu, K. Hong, D. H. Reich, P. C. Searson, C. L. Chien, Y. Leprince-Wang, K. Yu-Zhang, and K. Han, *Phys. Rev. B* **61**, 6631 (2000).
- [4] P. Hofmann, *Prog. Surf. Sci.* **81**, 191 (2006).
- [5] N. C. Norman, *Chemistry of Arsenic, Antimony and Bismuth* (Springer Science+Business Media, Berlin, Heidelberg, 1998).
- [6] O. Degtyareva, M. I. MCMahon, and R. J. Nelmes, *High Press. Res.* **24**, 319 (2004).
- [7] N. B. Brandt and N. I. Ginzburg, *Sov. Phys. JETP* **17**, 326 (1963).
- [8] W. Buckel and J. Wittig, *Phys. Lett.* **17**, 187 (1965).
- [9] M. A. Il'ina and E. S. Itskevich, *Sov. Phys. JETP Lett.* **11**, 218 (1970).
- [10] N. Lotter and J. Wittig, *Europhys. Lett.* **6**, 659 (1988).
- [11] X. Du, S. W. Tsai, D. L. Maslov, and A. F. Hebard, *Phys. Rev. Lett.* **94**, 166601 (2005).
- [12] O. Prakash, A. Kumar, A. Thamizhavel, and S. Ramakrishnan, *Science* **355**, 52 (2017).
- [13] Y. Li, E. Wang, X. Zhu, and H.-H. Wen, *Phys. Rev. B* **95**, 024510 (2017).
- [14] P. Brown, K. Semeniuk, D. Wang, B. Monserrat, C. J. Pickard, and F. M. Grosche, *Sci. Adv.* **4**, eaao4793 (2018).
- [15] P. Brown, Ph.D thesis, Dept. of Physics, University of Cambridge, 2017.
- [16] R. Khasanov, H. Luetkens, E. Morenzoni, G. Simutis, S. Schönecker, A. Östlin, L. Chioncel, and A. Amato, *Phys. Rev. B* **98**, 140504(R) (2018).
- [17] F. Bundy, *Phys. Rev.* **110**, 314 (1958).
- [18] W. Klement, A. Jayaraman, and G. C. Kennedy, *Phys. Rev.* **131**, 632 (1963).
- [19] M. A. Il'ina and E. S. Itskevich, *Sov. Phys.-Solid State* **8**, 1873 (1967).
- [20] E. M. Compy, *J. Appl. Phys.* **41**, 2014 (1970).
- [21] S. Yomo, N. Mari, and T. Mitsui, *J. Phys. Soc. Jpn.* **32**, 667 (1972).
- [22] C. G. Homan, *J. Phys. Chem. Solids* **36**, 1249 (1975).
- [23] I. V. Sharvin, *Sov. Phys. JETP* **6**, 1031 (1958).
- [24] A. T. Dorsey and R. E. Goldstein, *Phys. Rev. B* **57**, 3058 (1998).
- [25] See Supplemental Material at <http://link.aps.org/supplemental/10.1103/PhysRevB.99.174506> for a description of the experimental techniques, the data analysis procedure, and the details of the density functional theory calculations. The Supplemental Material includes Refs. [47–62].
- [26] R. Khasanov, S. Sanna, G. Prando, Z. Shermadini, M. Bendele, A. Amato, P. Carretta, R. De Renzi, J. Karpinski, S. Katrych, H. Luetkens, and N. D. Zhigadlo, *Phys. Rev. B* **84**, 100501(R) (2011).
- [27] R. Khasanov, Z. Guguchia, A. Maisuradze, D. Andreica, M. Elender, A. Raselli, Z. Shermadini, T. Goko, E. Morenzoni, and A. Amato, *High Press. Res.* **36**, 140 (2016).
- [28] Z. Shermadini, R. Khasanov, M. Elender, G. Simutis, Z. Guguchia, K. V. Kamenev, and A. Amato, *High Press. Res.* **37**, 449 (2017).
- [29] H. K. Collan, M. Krusius, and G. R. Pickett, *Phys. Rev. Lett.* **23**, 11 (1969).
- [30] Z. Mata-Pinzón, A. A. Valladares, R. M. Valladares, and A. Valladares, *PLoS ONE* **11**, e0147645 (2016).
- [31] A. Maisuradze, R. Khasanov, A. Shengelaya, and H. Keller, *J. Phys.: Condens. Matter* **21**, 075701 (2009).
- [32] R. Khasanov, H. Zhou, A. Amato, Z. Guguchia, E. Morenzoni, X. Dong, G. Zhang, and Z.-X. Zhao, *Phys. Rev. B* **93**, 224512 (2016).
- [33] M. Tinkham, *Introduction to Superconductivity* (Krieger Publishing, Malabar, 1975).
- [34] R. P. Huebener, *Magnetic Flux Structures in Superconductors* (Springer-Verlag, New York, 1979).
- [35] R. Prozorov, *Phys. Rev. Lett.* **98**, 257001 (2007).
- [36] R. Prozorov, A. F. Fidler, J. R. Hoberg, and P. C. Canfield, *Nat. Phys.* **4**, 327 (2008).
- [37] M. Gladisch, D. Herlach, H. Metz, H. Orth, G. zu Putlitz, A. Seeger, H. Teichler, W. Wahl, and W. Wigand, *Hyperfine Interact.* **6**, 109 (1979).
- [38] V. G. Grebinnik, I. I. Gurevich, V. A. Zhukov, A. I. Klimov, L. A. Levina, V. N. Maiorov, A. P. Manych, E. V. Mel'nikov, B. A. Nikol'skii, A. V. Pirogov, A. N. Ponomarev, V. S. Roganov, V. I. Selivanov, and V. A. Suetin, *Sov. Phys. JETP* **52**, 261 (1980).
- [39] V. S. Egorov, G. Solt, C. Baines, D. Herlach, and U. Zimmermann, *Physica B* **289-290**, 393 (2000).
- [40] V. S. Egorov, G. Solt, C. Baines, D. Herlach, and U. Zimmermann, *Phys. Rev. B* **64**, 024524 (2001).
- [41] D. Singh, A. D. Hillier, and R. P. Singh, *Phys. Rev. B* **99**, 134509 (2019).
- [42] J. Beare, M. Nugent, M. N. Wilson, Y. Cai, T. J. S. Munsie, A. Amon, A. Leithe-Jasper, Z. Gong, S. L. Guo, Z. Guguchia, Y. Grin, Y. J. Uemura, E. Svanidze, and G. M. Luke, *Phys. Rev. B* **99**, 134510 (2019).
- [43] P. B. Allen and R. C. Dynes, *Phys. Rev. B* **12**, 905 (1975).
- [44] J. Bardeen and M. Stephen, *Phys. Rev.* **136**, A1485 (1964).
- [45] H. Padamsee, J. E. Neighbor, and C. A. Shiffman, *J. Low Temp. Phys.* **12**, 387 (1973).
- [46] J. P. Carbotte, *Rev. Mod. Phys.* **62**, 1027 (1990).
- [47] K. Murata, H. Yoshino, H. O. Yadev, Y. Honda, and N. Shirakawa, *Rev. Sci. Instrum.* **68**, 2490 (1997).
- [48] A. Eiling and J. C. Schilling, *J. Phys. F: Met. Phys.* **11**, 623 (1981).
- [49] A. Suter and B. M. Wojek, *Phys. Procedia* **30**, 69 (2012).
- [50] R. Khasanov, M. Bendele, A. Amato, K. Conder, H. Keller, H.-H. Klauss, H. Luetkens, and E. Pomjakushina, *Phys. Rev. Lett.* **104**, 087004 (2010).
- [51] A. Yaouanc, and P. D. de Réotier, *Muon Spin Rotation, Relaxation and Resonance: Applications to Condensed Matter* (Oxford University Press, Oxford, 2011).
- [52] E. H. Brandt, *J. Low Temp. Phys.* **26**, 709 (1977).
- [53] E. H. Brandt, *J. Low Temp. Phys.* **73**, 355 (1988).
- [54] E. H. Brandt, *Phys. Rev. B* **37**, 2349(R) (1988).
- [55] J. Rammer, *Physica C* **177**, 421 (1991).
- [56] E. H. Brandt, *Phys. Rev. B* **68**, 054506 (2003).
- [57] M. Laulajainen, F. D. Callaghan, C. V. Kaiser, and J. E. Sonier, *Phys. Rev. B* **74**, 054511 (2006).
- [58] P. Giannozzi *et al.*, *J. Phys.: Condens. Matter* **21**, 395502 (2009).
- [59] S. Baroni, S. de Gironcoli, A. Dal Corso, and P. Giannozzi, *Rev. Mod. Phys.* **73**, 515 (2001).
- [60] W. E. Pickett, *Phys. Rev. B* **26**, 1186 (1982).
- [61] F. Marsiglio, M. Schossmann, and J. P. Carbotte, *Phys. Rev. B* **37**, 4965 (1988).
- [62] A. E. Karakozov, E. G. Maksimov, and S. A. Mashkov, *Sov. Phys. JETP* **41**, 971 (1976).

## Phonon anomalies in FeS

A. Baum,<sup>1,2</sup> A. Milosavljević,<sup>3</sup> N. Lazarević,<sup>3</sup> M. M. Radonjić,<sup>4</sup> B. Nikolić,<sup>5</sup> M. Mitschek,<sup>1,2,\*</sup> Z. Inanloo Maranloo,<sup>1,†</sup> M. Šćepanović,<sup>3</sup> M. Grujić-Brojčin,<sup>3</sup> N. Stojilović,<sup>3,6</sup> M. Opel,<sup>1</sup> Aifeng Wang (王爱峰),<sup>7</sup> C. Petrović,<sup>7</sup> Z. V. Popović,<sup>3,8</sup> and R. Hackl<sup>1</sup>

<sup>1</sup>Walther Meissner Institut, Bayerische Akademie der Wissenschaften, 85748 Garching, Germany

<sup>2</sup>Fakultät für Physik E23, Technische Universität München, 85748 Garching, Germany

<sup>3</sup>Center for Solid State Physics and New Materials, Institute of Physics Belgrade, University of Belgrade, Pregrevica 118, 11080 Belgrade, Serbia

<sup>4</sup>Scientific Computing Laboratory, Center for the Study of Complex Systems, Institute of Physics Belgrade, University of Belgrade, Pregrevica 118, 11080 Belgrade, Serbia

<sup>5</sup>Faculty of Physics, University of Belgrade, Studentski trg 12, Belgrade, Serbia

<sup>6</sup>Department of Physics and Astronomy, University of Wisconsin Oshkosh, Oshkosh, Wisconsin 54901, USA

<sup>7</sup>Condensed Matter Physics and Materials Science Department, Brookhaven National Laboratory, Upton, New York 11973-5000, USA

<sup>8</sup>Serbian Academy of Sciences and Arts, Knez Mihailova 35, 11000 Belgrade, Serbia



(Received 12 December 2017; published 12 February 2018)

We present results from light scattering experiments on tetragonal FeS with the focus placed on lattice dynamics. We identify the Raman active  $A_{1g}$  and  $B_{1g}$  phonon modes, a second order scattering process involving two acoustic phonons, and contributions from potentially defect-induced scattering. The temperature dependence between 300 and 20 K of all observed phonon energies is governed by the lattice contraction. Below 20 K the phonon energies increase by  $0.5\text{--}1\text{ cm}^{-1}$ , thus indicating putative short range magnetic order. Along with the experiments we performed lattice-dynamical simulations and a symmetry analysis for the phonons and potential overtones and find good agreement with the experiments. In particular, we argue that the two-phonon excitation observed in a gap between the optical branches becomes observable due to significant electron-phonon interaction.

DOI: [10.1103/PhysRevB.97.054306](https://doi.org/10.1103/PhysRevB.97.054306)

### I. INTRODUCTION

In the iron based superconductors (IBS) magnetic order, structure, nematicity, and superconductivity are closely inter-related. Upon substituting atoms in the parent compounds the properties change in a way that the shape of the Fermi surface is generally believed to play a crucial role. Yet, the magnetic properties were found recently to be more complex and to depend also on the degree of correlation in the individual  $d$  orbitals contributing to the density of states close to the Fermi surface [1–3].

The influence of correlation effects seems to increase from the 122 systems such as  $\text{BaFe}_2\text{As}_2$  to the 11 chalcogenides  $\text{FeTe}$ ,  $\text{FeSe}$ , and  $\text{FeS}$  [4,5]. Surprisingly, the properties of the 11 class members differ substantially although they are isostructural and isoelectronic [3,6]:  $\text{FeSe}$  undergoes a structural transition at  $T_s \sim 90\text{ K}$  and displays electronic nematicity [7]. While long-range magnetic order cannot be observed down to the lowest temperatures [7–10] the thermodynamic properties and the Raman spectra strongly support the presence of short-ranged magnetism [11,12]. Below  $T_c \sim 9\text{ K}$  superconductivity is observed [13] in pristine  $\text{FeSe}$ . In mono-layer  $\text{FeSe}$   $T_c$  can reach values close to  $100\text{ K}$  [14,15].

The replacement of Se by Te leads to slightly off-stoichiometric  $\text{Fe}_{1+y}\text{Te}$  which exhibits a simultaneous magnetostructural transition near  $67\text{ K}$  [16] but is not superconducting [17,18]. Finally,  $\text{FeS}$  having a superconducting transition at  $T_c \sim 5\text{ K}$  [19] remains tetragonal down to the lowest temperatures [20]. It is still an open question whether tetragonal  $\text{FeS}$  hosts magnetic order. Obviously, the iron-chalcogenides are at the verge of various neighboring phases and very susceptible to small changes in the lattice and electronic structure. Yet direct access to the competing phases is still very difficult in  $\text{FeTe}$  and  $\text{FeS}$  because of the variation of the crystal quality across the families.

Here, we choose a slightly different approach and do not look directly at the electronic but rather at the lattice properties in  $\text{FeS}$  close to potential instabilities and use the Raman-active phonons as probes. We identify the  $A_{1g}$  and  $B_{1g}$  modes, a two-phonon scattering process, and a fourth mode from either defect-induced scattering or second-order scattering as well. These results are in good agreement with numerical calculations. Furthermore the temperature dependence of all phononic modes supports the results reported in Refs. [21,22], where emerging short range magnetic order at approximately  $20\text{ K}$  was reported.

### II. EXPERIMENT

Single crystals of  $\text{FeS}$  were synthesized as described elsewhere [23]. Before the experiment the samples were cleaved in air.

\*Present address: Physikalisches Institut, Goethe Universität, 60438 Frankfurt am Main, Germany.

†Present address: Fakultät für Physik E21, Technische Universität München, 85748 Garching, Germany.

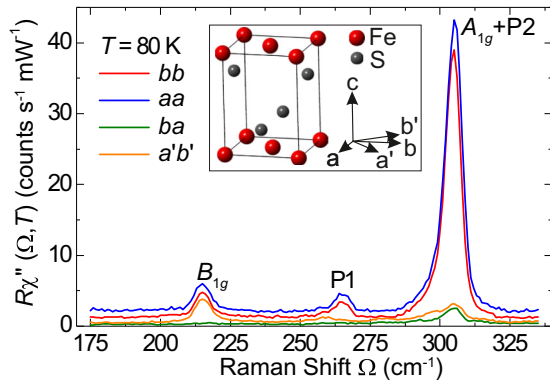


FIG. 1. Raman spectra of FeS at  $T = 80$  K measured with light polarizations as indicated. The inset shows the crystal structure of FeS and the polarization directions with respect to the crystal orientation.

Calibrated customized Raman scattering equipment was used for the experiment. The samples were attached to the cold finger of a He-flow cryostat having a vacuum of approximately  $5 \times 10^{-5}$  Pa. For excitation we used a diode-pumped solid state laser emitting at 575 nm (Coherent GENESIS). Polarization and power of the incoming light were adjusted in a way that the light inside the sample had the proper polarization state and, respectively, a power of typically  $P_a = 3$  mW independent of polarization. The samples were mounted as shown in the inset of Fig. 1. The crystallographic axes are  $a$  and  $b$  with  $|a| = |b|$ . The  $c$  axis is parallel to the optical axis.  $a'$  and  $b'$  are rotated by  $45^\circ$  with respect to  $a$  and  $b$ . The laser beam reached the sample at an angle of incidence of  $66^\circ$  and was focused to a spot of approximately  $50 \mu\text{m}$  diameter. The plane of incidence is the  $bc$  plane. By choosing proper in-plane polarizations of the incident and scattered light the four symmetry channels  $A_{1g}$ ,  $A_{2g}$ ,  $B_{1g}$ , and  $B_{2g}$  of the  $D_{4h}$  space group can be accessed. Additionally, for the large angle of incidence, exciting photons being polarized along the  $b$  axis have a finite  $c$ -axis projection and the  $E_g$  symmetry can also be accessed. For the symmetry assignment we use the 2 Fe unit cell (crystallographic unit cell).

The observed phonon lines were analyzed quantitatively. Since the phonon lines are symmetric and  $\Gamma_L(T) \ll \omega(T)$  the intrinsic line shape can be described by a Lorentz function with a central temperature dependent energy  $\omega(T)$  and a width  $\Gamma_L(T)$  (FWHM). The widths turn out to be comparable to the resolution  $\sigma$  of the spectrometer. Therefore, the Lorentzian needs to be convoluted with a Gaussian having width  $\Gamma_G \equiv \sigma$ .

### III. THEORY

The electronic structure and the phonon dispersion were calculated using density functional theory (DFT) and density functional perturbation theory (DFPT), respectively, [24] within the QUANTUM ESPRESSO package [25]. The calculations were performed with the experimental unit cell parameters  $a = 3.6735 \text{ \AA}$ ,  $c = 5.0328 \text{ \AA}$ , and  $z = 0.2602$ , where  $z$  is the height of the sulfur atoms above the Fe plane in units of the  $c$  axis [26]. We used the Vanderbilt ultrasoft pseudopotentials with the Becke-Lee-Yang-Parr (BLYP) exchange-correlation functional and  $s$  and  $p$  semicore states included in the valence for iron. The electron-wave-function and density energy cut-

offs were 70 Ry and 560 Ry, respectively, chosen to ensure stable convergence of the phonon modes. We used a Gaussian smearing of 0.01 Ry. The Brillouin zone was sampled with a  $16 \times 16 \times 16$  Monkhorst-Pack  $k$ -space mesh. Our electronic structure and phonon calculations are in agreement with previously reported results [27,28].

The experimental positions of the S atoms entail a nonzero  $z$  component of the force of  $6 \times 10^{-2} \text{ Ry}/a_B$  acting on them with  $a_B$  the Bohr radius. However, the relaxation of the  $z$  positions of the S atoms would result in a large discrepancy between the calculated and experimental energies of the optical branches [28], whereas the phonon frequencies calculated from experimental structure parameters are in good agreement with the experiment (see Table II). When using the measured lattice parameters, including atomic positions, some of the acoustic phonons are unstable and do not have a linear dispersion at small  $k$ . Upon relaxing the atomic positions the acoustic dispersion becomes linear and the energies at the zone boundary decrease slightly. The energies of the optical branches, on the other hand, increase by some 10%. Having all this in mind, we choose to use the experimental lattice parameters stated above. In this sense our calculations should be understood as a compromise.

The phonon dispersion and the density of states were calculated on a  $6 \times 6 \times 6$  Monkhorst-Pack  $k$ -point mesh, and the dispersion is interpolated along the chosen line. The calculated phonon dispersions of the experimental and relaxed structures qualitatively coincide and display similar shapes and a gap. Discrepancies only appear in the absolute energies.

The selection rules for two-phonon processes were calculated using the modified group projector technique (MGPT) [29], which avoids summing over an infinite set of space group elements.

## IV. RESULTS AND DISCUSSION

### A. Polarization dependence

Raman spectra of FeS for four linear polarization configurations at a sample temperature of  $T = 80$  K are shown in Fig. 1. Three peaks can be identified at 215, 265, and 305  $\text{cm}^{-1}$ . The symmetric peak at 215  $\text{cm}^{-1}$  shows up for  $aa$ ,  $bb$ , and  $a'b'$  polarizations, but vanishes for  $ba$  polarization. Hence the excitation obeys  $B_{1g}$  selection rules and can be identified as the out-of-phase vibration of iron atoms along the  $c$  axis. The strongest slightly asymmetric peak at 305  $\text{cm}^{-1}$  obeys  $A_{1g}$  selection rules with contributions of order 5% in  $ba$  and  $a'b'$  polarizations from either leakage or defect-induced scattering. An asymmetric Fano-type line shape can be acquired by coupling a phonon to an electronic continuum. However, as shown in Fig. 6 in the Appendixes, we find that the superposition of two symmetric, yet spectrally unresolved peaks gives a better agreement with the data than the description in terms of a Fano function. The stronger peak at 305  $\text{cm}^{-1}$  has  $A_{1g}$  symmetry with some remaining leakage. We therefore identify this mode with the in-phase vibration of sulfur atoms along the  $c$  axis. The second peak, labeled P2, appears in spectra with parallel light polarizations and vanishes in  $ba$ , but has some contribution in  $a'b'$  polarizations, suggesting mixed  $A_{1g}$  and  $B_{1g}$  symmetry. The third peak, labeled P1, is symmetric and appears only in

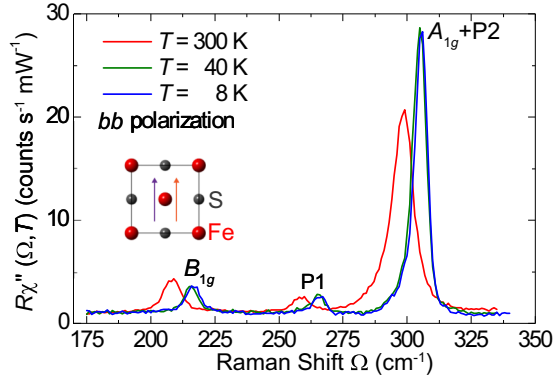


FIG. 2. Raman spectra of FeS in  $bb$  polarization projecting  $A_{1g} + B_{1g} + E_g$  symmetries measured at temperatures given in the legend. The inset shows the light polarizations with respect to the crystal orientation.

spectra with parallel light polarizations and thus has pure  $A_{1g}$  symmetry.

### B. Temperature dependence

For properly assigning all observed modes and for getting access to putative phase transitions we studied the temperature dependence. Figure 2 shows Raman spectra in  $bb$  polarization at 8, 40, and 300 K. The three peaks shift to higher energies upon cooling. The fourth peak P2 cannot be resolved in the raw data and can only be analyzed after a fitting procedure (see Appendix B). The peak energies  $\omega(T)$  and the (intrinsic) linewidths  $\Gamma_L(T)$  were determined as described at the end of Sec. II. All four modes show a monotonous increase in energy and decrease in linewidth upon cooling as shown in Fig. 3. Below 20 K the increase in the energies accelerates. We first address this overall behavior and disregard the anomaly around 50 K for the moment.

The shift and narrowing of all modes can be explained in terms of lattice contraction using a constant Grüneisen parameter  $\gamma$  and anharmonic decay into other phonon modes, respectively. The change in the (Lorentzian) linewidth  $\Gamma_L(T)$  is given by [30]

$$\Gamma_L(T) = \Gamma_{L,0} \left( 1 + \frac{2\lambda_{\text{ph-ph}}}{\exp\left(\frac{\hbar\omega_0}{2k_B T}\right) - 1} \right). \quad (1)$$

The zero temperature limits  $\Gamma_{L,0}$  and  $\omega_0$  were obtained by extrapolating the respective experimental points of  $\Gamma_L(T)$  and  $\omega(T)$  in the range  $20 \leq T \leq 50$  K to  $T = 0$  (Fig. 3). With the phonon-phonon coupling  $\lambda_{\text{ph-ph}}$  being the only free parameter the temperature dependence of  $\Gamma_L(T)$  can be described as shown by red dashed lines in Fig. 3. The phonon energy  $\omega(T)$  contains contributions from both the anharmonic decay and the lattice contraction, which depends essentially on the thermal occupation of the phonons, and can be written as [31]

$$\omega(T) = \omega_0 \left[ 1 - \gamma \frac{V(T) - V_0}{V_0} - \left( \frac{\Gamma_{L,0}}{\sqrt{2}\omega_0} \right)^2 \left( 1 + \frac{4\lambda_{\text{ph-ph}}}{\exp\left(\frac{\hbar\omega_0}{2k_B T}\right) - 1} \right) \right]. \quad (2)$$

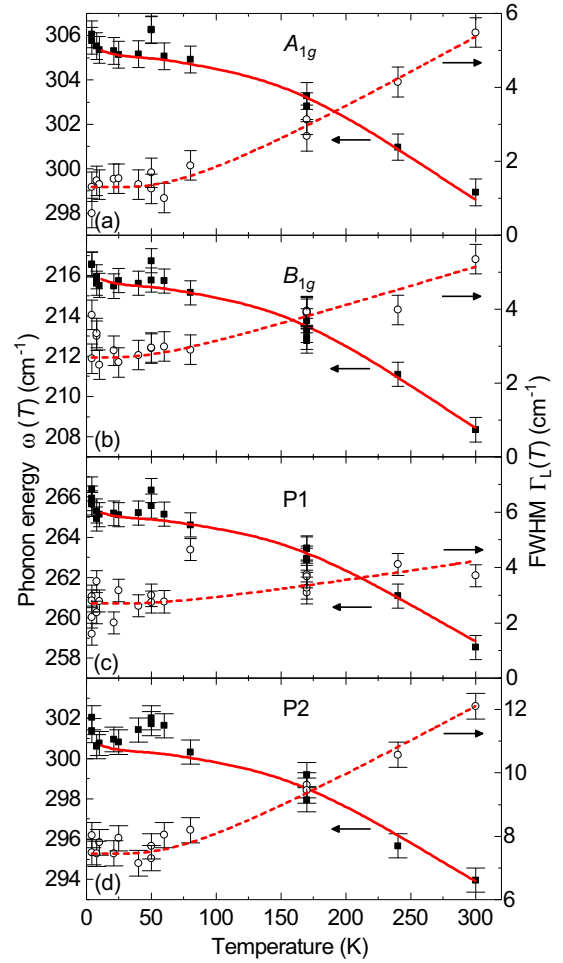


FIG. 3. Temperature dependence of energy and width of the four observed phonon modes in FeS. Black squares show the phonon energies  $\omega$ ; open circles denote the phonon linewidths  $\Gamma_L$ . The red dashed and solid lines represent the temperature dependencies of the phonon linewidths and energies according to Eqs. (1) and (2), respectively. For better visualizing the low-temperature part, the data of this figure are plotted on a logarithmic temperature scale in Fig. 8 of Appendix D.

$V(T)$  and  $V_0$  are the volumes of the unit cell at temperatures  $T$  and  $T \rightarrow 0$ , respectively. The numbers for the calculations are taken from Ref. [20]. The second term describes the effect of phonon damping on the line position in the harmonic approximation. Using  $\lambda_{\text{ph-ph}}$  from Eq. (1), the Grüneisen parameter  $\gamma$  is the only free parameter and is assumed to be constant. The temperature dependencies  $\omega(T)$  resulting from the fits are plotted in Fig. 3 as solid red lines. The numerical values for parameters  $\gamma$  and  $\lambda_{\text{ph-ph}}$  obtained from the  $T$ -dependent energy and linewidth are compiled in Table I.

Below 20 K and around 50 K anomalies are found in the experimental data as follows:

(i) At 50 K the peak energies of all four modes deviate significantly from the otherwise smooth temperature dependence. The nearly discontinuous increase in energy could be reproduced for the  $A_{1g}$  phonon and peak P2 in multiple measurements. For the  $B_{1g}$  phonon and mode P1 the anomaly is not as clearly reproducible. The energy anomalies do not

TABLE I. Symmetry, Grüneisen constant  $\gamma$ , and phonon-phonon coupling parameter  $\lambda_{\text{ph-ph}}$  of the four experimentally observed modes.

Mode	Symmetry	$\gamma$	$\lambda_{\text{ph-ph}}$
S	$A_{1g}$	2.2	1.68
Fe	$B_{1g}$	3.4	0.31
P1	$A_{1g}$	2.4	0.25
P2	$A_{1g} + B_{1g}$	2.2	0.31

have a correspondence in the linewidth. As there is neither an abrupt change in the lattice constants [20] nor any other known phase transition close to 50 K the origin of this anomaly remains unexplained although we consider it significant.

(ii) Upon cooling from 20 K to 4 K all four modes exhibit sudden, yet small, increases in energy. The changes in width are heterogeneous in that the  $A_{1g}$  mode narrows and the  $B_{1g}$  mode broadens. No clear tendencies can be derived for modes P1 and P2. Sudden changes in the temperature dependence typically indicate phase transitions. Yet, no phase transition has been identified so far. However, the anomaly at 20 K coincides with the emergence of short range magnetic order as inferred from two  $\mu\text{SR}$  studies [21,22]. Susceptibility measurements on a sample from the same batch were inconclusive. On the other hand, the XRD data show a small anomaly in the lattice parameters and the unit cell volume does not saturate at low temperature but rather decreases faster between 20 K and 10 K than above 20 K [20]. This volume contraction by and large reproduces the change in the phonon energies as can be seen by closely inspecting the low-temperature parts of Fig. 3 (see also Fig. 8). Hence the indications of short-range magnetism in FeS found by  $\mu\text{SR}$  have a correspondence in the temperature dependence of the volume and the phonon energies.

Clear phonon anomalies were observed at the onset of the spin density wave (SDW) phases in 122 systems [32–34] and of the more localized magnetic phase in FeTe [35], whereas continuous temperature dependence of the phonons was found in systems without long-range magnetism [36,37]. Upon entering the SDW state in the 122 systems the  $A_{1g}$  (As) mode softens abruptly and narrows by a factor of 3, whereas the  $B_{1g}$  (Fe) mode stays pinned and narrows only slightly [32]. The strong coupling of the As mode to magnetism was traced back to the interaction of the Fe magnetic moment with the Fe-As tetrahedra angle [38], which goes along with a change of the  $c$ -axis parameter. In  $\text{Fe}_{1+y}\text{Te}$  the roles of the  $B_{1g}$  and  $A_{1g}$  modes are interchanged [35,39,40]. In contrast, all four modes observed here in FeS harden below  $T^* \approx 20$  K being indicative of a type of magnetic ordering apparently different from that in the other Fe-based systems.

Very recently, commensurate magnetic order with a wave vector of  $\mathbf{q} = (0.25, 0.25, 0)$  was found in FeS below  $T_N = 116$  K using neutron powder diffraction [41]. In the Raman spectra no anomalies can be seen around 120 K even if the range is studied with fine temperature increments of 10 K as shown in Appendix C. However, a small change in the temperature dependence of the  $c$ -axis parameter is observed around 100 K by XRD [20], which could be related to this type of magnetic order. Since the influence on the volume is small there is no detectable impact on the phonons.

TABLE II. Raman active phonon modes in t-FeS. Shown are the symmetries, the theoretical predictions for the experimental lattice parameters at  $T = 0$ , and the atoms involved in the respective vibrations. The experimental energies in the third column are extrapolations to  $T = 0$  of the points measured between 20 K and 50 K.

Symmetry	Phonon energy ( $\text{cm}^{-1}$ )		Atomic displacement
	Calculation	Experiment	
$A_{1g}$	316.1	305.3	S
$B_{1g}$	220.4	215.8	Fe
$E_g$	231.6		Fe, S
$E_g$	324.8		Fe, S

### C. Analysis of the modes P1 and P2

Based on the energies, the selection rules, and the temperature dependence we first clarify the phononic nature of the two lines P1 and P2, which cannot as straightforwardly be identified as lattice vibrations as the in-phase sulfur and out-of-phase iron vibrations at 305.3 and 215.8  $\text{cm}^{-1}$ . Second we derive their origin from the phonon density of states (PDOS) calculated for the zero-temperature limit.

All experimental energies for  $T \rightarrow 0$  were derived from the points at low temperature as described in Sec. IV B (see also Fig. 3). The results for the modes at the  $\Gamma$  point are summarized in Table II and can be directly compared to the results of the calculations. The discrepancies between the experimental and theoretical energies for the Raman-active phonons are smaller than 4%. The price for this accuracy in the optical energies is an instability and possibly too high energies in the acoustical branches at small and, respectively, large momentum (see Sec. III).

The unidentified peaks P1 and P2 appear in the spectra measured with  $aa$  polarization, where none of the electric fields has a projection on the  $c$  axis. Thus they cannot have  $E_g$  symmetry obeying  $ca$  and  $cb$  selection rules. In addition, the observed energies would be relatively far off of the calculated energies (see Table II). Both peaks exhibit temperature dependencies similar to those of the two Raman-active phonons and the Grüneisen parameters are close to the typical value [42] of 2 and similar to those of the Raman-active phonons. The phonon-phonon coupling parameters  $\lambda_{\text{ph-ph}}$  derived from the temperature dependence of the linewidths are close to 0.3 similar to that of the  $B_{1g}$  phonon.  $\lambda_{\text{ph-ph}}$  of the  $A_{1g}$  phonon is roughly five times bigger for reasons we address later. Yet, because of the small prefactor  $(\Gamma_{L,0}/\sqrt{2}\omega_0)^2 = O(10^{-3})$ , the contribution of phonon-phonon coupling to the temperature dependence of  $\omega(T)$  remains negligible in all cases and the phonon energies are essentially governed by the lattice contraction. These considerations demonstrate the phononic origin of the peaks P1 and P2.

In the second step we try to identify the phonon branches to which P1 and P2 can be related. To this end the full phonon dispersion and density of states (PDOS) were derived as described in Sec. III and are plotted in Fig. 4.

Independent of using the relaxed or experimental structure, P1 is located in the gap of the (theoretical) PDOS and cannot result from first order defect-induced Raman scattering. What

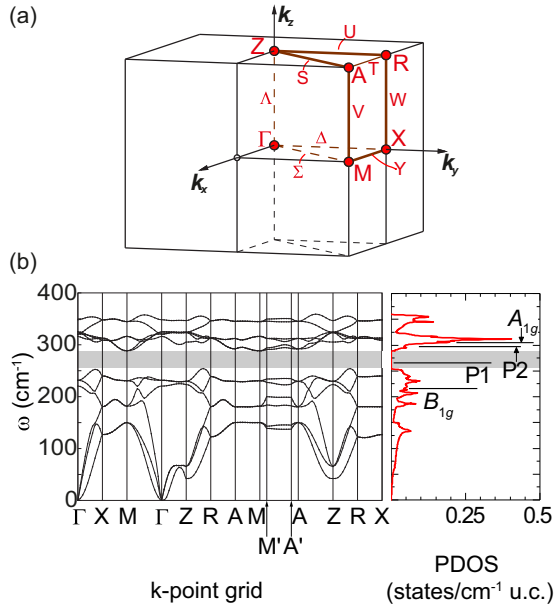


FIG. 4. Phonon dispersion of t-FeS. (a) Brillouin zone with high symmetry points and lines [43]. (b) Phonon dispersion along the directions as indicated and phonon density of states (PDOS). The gray-shaded area marks the gap in the phonon dispersion. The dispersion shown here is derived using experimental lattice parameters. For this reason some of the acoustic phonons are unstable and do not have a linear dispersion around the  $\Gamma$  point. Upon relaxing the structure the acoustic dispersion becomes linear at  $\Gamma$ , and the energies at the zone boundary decrease slightly. The energies of the optical branches, on the other hand, increase by some 10%.  $M' = (0.4, 0.4, 0.0)$  and  $A' = (0.4, 0.4, 0.5)$ . The experimental energies of the four observed modes are shown as black lines.

alternatives exist for explaining P1? If we exclude exotic explanations such as a collective mode for the reasons given above the energy of  $\omega_{P1} = 265 \text{ cm}^{-1}$  can only be obtained by the sum of two phonon modes having equal energy  $\omega_{P1}/2$  and momenta  $\mathbf{k}$  and  $-\mathbf{k}$  (for maintaining the  $q \approx 0$  selection rule). As shown for various transition metal compounds including TiN, ZrN, or NbC second-order phonon Raman scattering can occur in the presence of defects [44]. Then first-order scattering being proportional to the PDOS (modulo energy and symmetry dependent weighting factors) is expected to be also substantial if not stronger. Although our crystals are slightly disordered there is no indication of substantial intensity at energies with high PDOS as can be seen by directly comparing Figs. 1 and 4(b). Alternatively, second-order scattering can originate in enhanced electron-phonon coupling [45]. In either case the energies of two phonons add up as they get excited in a single scattering process. Generally, no selection rules apply for second order Raman scattering and the resulting peak would appear in all symmetry channels [46]. Exceptions exist if the phonon wave vectors coincide with high-symmetry points or lines of the Brillouin zone.

From the phonon dispersion alone several phonon branches having  $\mathbf{k}$  and  $-\mathbf{k}$  and energies in the range around  $\omega_{P1}/2$  could add up to yield  $265 \text{ cm}^{-1}$  (see Fig. 4). However, as explained in Appendix F and shown in Table III for the space group P4/nmm

of t-FeS, the  $A_{1g}$  selection rules of P1 exclude all nonsymmetric combinations of branches (right column of Table III). On the other hand, all symmetric combinations include  $A_{1g}$  selection rules for the two-phonon peak (left column of Table III) and one has to look essentially for a high PDOS in the range  $\omega_{P1}/2$ . As shown in Fig. 4(b) the PDOS has a maximum in the right energy range. Since the maximum results from momenta away from the high-symmetry points or lines (see Fig. 4) which alone lead to pure  $A_{1g}$  symmetry one expects also intensity in  $B_{1g}$  and  $E_g$  symmetry as opposed to the experiment. For exclusive  $A_{1g}$  selection rules only seven possibilities exist. Since phase space arguments favor modes having a flat dispersion in extended regions of the Brillouin zone the  $\Gamma$ ,  $M$ , and/or  $A$  points are unlikely to give rise to P1, and only the lines  $S = A - Z$ ,  $\Sigma = \Gamma - M$ , and  $V = A - M$  remain. The dispersion along the  $S$  or  $\Sigma$  branch contributes very little to the PDOS. On the high-symmetry line  $V$  a doubly degenerate branch would have a flat dispersion [see Fig. 4(b)] and contributes substantially to the PDOS but the energy of  $150 \text{ cm}^{-1}$  differs by 13% from the expected energy of  $132.5 \text{ cm}^{-1}$ . Instead of arguing about the accuracy of the theoretical phonon energies (see Sec. III) we looked at the dispersion close to but not strictly on  $V$  where the contribution to  $B_{1g}$  and  $E_g$  symmetries is expected to be still very small, e.g., along  $M' - A'$  [Fig. 4(b)]. A detailed inspection shows that the maximum of the PDOS between  $130$  and  $140 \text{ cm}^{-1}$  comes from there. This explains both the selection rules and the energy of P1 to within a few percent.

Peak P2 cannot be explained in terms of one of the two  $E_g$  phonons either. As opposed to P1 it is not inside the gap of the PDOS and thus can originate from either first or second order scattering. If P2 originates in second order scattering in the same fashion as P1 there are five possibilities yielding  $A_{1g} + B_{1g}$  but not  $E_g$  selection rules. As explained in the last paragraph only the branches  $\Delta = \Gamma - X$  and  $U = Z - R$  may contribute. For the low PDOS there we consider also first order defect-induced scattering for P2 to originate from. In fact, the PDOS possesses its strongest maximum  $5 \text{ cm}^{-1}$  below the (theoretical)  $A_{1g}$  phonon exactly where P2 is found. In spite of the very high PDOS here, the peak is weak explaining the negligible contributions from first order defect-induced scattering at lower energies. The high PDOS between  $300$  and  $325 \text{ cm}^{-1}$  may also be an alternative yet less likely explanation for the weak contributions in crossed polarizations in the energy range of the  $A_{1g}$  phonon (Fig. 1).

Finally, we wish to clarify whether the large phonon-phonon coupling  $\lambda_{\text{ph-ph}}^{A_{1g}}$  found for the  $A_{1g}$  Raman-active mode (see Table I) is related to the appearance of P1. Due to the close proximity of the energies the  $A_{1g}$  mode apparently decays into states close to those adding up to yield P1. The decay is less restricted by symmetry leaving more options. For both processes the phonon-phonon coupling has to be substantial with the order of magnitude given by  $\lambda_{\text{ph-ph}}^{A_{1g}} \approx 1.7$ . Phonon-phonon coupling is present in any type of material because of the anharmonic potential. Defects enhance this effect [44]. Since FeS is a metal the phonon-phonon coupling goes at least partially through electronic states and may be indicative of enhanced electron-phonon coupling,  $\lambda_{\text{el-ph}}$ , as described, e.g., in Ref. [45]. The related contribution to  $\lambda_{\text{ph-ph}}$  is then expected

TABLE III. Two-phonon processes in FeS. The symmetry group of the FeS system is the space group  $P4/nmm$ . For products of irreducible representations (IRs) in the left column Raman active modes (RM) in decomposition are given in the right one. Raman active modes of FeS are  $\Gamma_1^+$  ( $A_{1g}$ ),  $\Gamma_2^+$  ( $B_{1g}$ ), and two double degenerate  $\Gamma_5^+$  ( $E_g$ ).  $\Gamma_1^+$  comes from vibrations of S atoms,  $\Gamma_2^+$  from Fe ones, and both atom types contribute with one pair of  $\Gamma_5^+$  modes. For complex representations ( $V_{1,2,3,4}$  and all  $W$ ) the double index indicates that the real representation is used, for example,  $V_{13} = V_1 \oplus V_1^* = V_1 \oplus V_3$ . Irreducible representations of the space group given in Ref. [53] are used.

Overtones		Combinations	
IR products (phonon states)	RM in decomposition	IR products (phonon states)	RM in decomposition
$[(\Gamma_i^\pm)^2]$ ( $i = 1, 2, 3, 4$ )	$A_{1g}$	$\Gamma_1^h \otimes \Gamma_2^h, \Gamma_3^h \otimes \Gamma_4^h$ ( $h = \pm$ )	$B_{1g}$
$[(\Gamma_5^\pm)^2]$	$A_{1g}, B_{1g}$	$\Gamma_i^h \otimes \Gamma_5^h$ ( $i = 1, 2, 3, 4, h = \pm$ )	$E_g$
$[(X_i)^2]$ ( $i = 1, 2$ )	$A_{1g}, B_{1g}, E_g$	$X_1 \otimes X_2$	$E_g$
$[(M_i)^2]$ ( $i = 1, 2, 3, 4$ )	$A_{1g}$	$M_1 \otimes M_2, M_3 \otimes M_4$	$B_{1g}$
$[(\Sigma_i)^2]$ ( $i = 1, 2, 3, 4$ )	$A_{1g}$	$M_1 \otimes M_3, M_1 \otimes M_4, M_2 \otimes M_3, M_2 \otimes M_4$	$E_g$
$[(\Delta_i)^2]$ ( $i = 1, 2, 3, 4$ )	$A_{1g}, B_{1g}$	$\Sigma_1 \otimes \Sigma_2, \Sigma_3 \otimes \Sigma_4$	$B_{1g}$
$[(V_{13})^2], [(V_{24})^2], [(V_5)^2]$	$A_{1g}$	$\Sigma_1 \otimes \Sigma_3, \Sigma_1 \otimes \Sigma_4, \Sigma_2 \otimes \Sigma_3, \Sigma_2 \otimes \Sigma_4$	$E_g$
$[(W_{13})^2], [(W_{24})^2]$	$A_{1g}, B_{1g}, E_g$	$\Delta_1 \otimes \Delta_2, \Delta_1 \otimes \Delta_3, \Delta_2 \otimes \Delta_4, \Delta_3 \otimes \Delta_4$	$E_g$
$[(Y_1)^2]$	$A_{1g}, B_{1g}, E_g$	$V_{13} \otimes V_{24}$	$\Gamma_2^+$
$[(Z_i^\pm)^2]$ ( $i = 1, 2, 3, 4$ )	$A_{1g}$	$V_{13} \otimes V_5, V_{24} \otimes V_5$	$\Gamma_5^+$
$[(Z_5^\pm)^2]$	$A_{1g}, B_{1g}$	$W_{13} \otimes W_{24}$	$\Gamma_5^+$
$[(A_i)^2]$ ( $i = 1, 2, 3, 4$ )	$A_{1g}$	$Z_1^h \otimes Z_2^h, Z_3^h \otimes Z_4^h$ ( $h = \pm$ )	$B_{1g}$
$[(R_i)^2]$ ( $i = 1, 2$ )	$A_{1g}, B_{1g}, E_g$	$Z_i^h \otimes Z_5^h$ ( $i = 1, 2, 3, 4, h = \pm$ )	$E_g$
$[(S_i)^2]$ ( $i = 1, 2, 3, 4$ )	$A_{1g}$	$A_1 \otimes A_2, A_3 \otimes A_4$	$B_{1g}$
$[(U_i)^2]$ ( $i = 1, 2, 3, 4$ )	$A_{1g}, B_{1g}$	$A_1 \otimes A_3, A_1 \otimes A_4, A_2 \otimes A_3, A_2 \otimes A_4$	$E_g$
$[(\Lambda_i)^2]$ ( $i = 1, 2, 3, 4$ )	$A_{1g}$	$R_1 \otimes R_2$	$E_g$
$[(\Lambda_5)^2]$	$A_{1g}, B_{1g}$	$S_1 \otimes S_2, S_3 \otimes S_4$	$B_{1g}$
$[(T_1)^2]$	$A_{1g}, B_{1g}, E_g$	$S_1 \otimes S_3, S_1 \otimes S_4, S_2 \otimes S_3, S_2 \otimes S_4$	$E_g$
		$U_1 \otimes U_2, U_1 \otimes U_3, U_2 \otimes U_4, U_3 \otimes U_4$	$E_g$
		$\Lambda_1 \otimes \Lambda_2, \Lambda_3 \otimes \Lambda_4$	$B_{1g}$
		$\Lambda_i \otimes \Lambda_5$ ( $i = 1, 2, 3, 4$ )	$E_g$

to be proportional to  $\lambda_{\text{el-ph}}^2$ . This conclusion is compatible with early results on the branch-dependent electron-phonon coupling in LaFeAsOF, where the strongest effects are reported for some  $\Gamma$ -point modes and the acoustic branches with intermediate to large momenta [47].  $\lambda_{\text{ph-ph}}^{A_{1g}} > 1$  and the two-phonon peak P1 indicate that the electron-phonon coupling is possibly larger than in the other Fe-based systems and reaches values up to unity. In BaFe<sub>2</sub>As<sub>2</sub>, as an example from the pnictide family,  $\lambda_{\text{el-ph}}^2 \approx (1-4) \times 10^{-2} < \lambda_{\text{ph-ph}} \approx 0.1$  is reported [32,48,49]. On the other hand, one finds  $\lambda_{\text{el-ph}}^2 \approx 0.4 < \lambda_{\text{ph-ph}} \approx 0.9$  for the  $E_g$  phonon in MgB<sub>2</sub>, being generally believed to be a conventional superconductor [50,51]. Thus one may speculate whether  $\lambda_{\text{el-ph}}$  might be even large enough in FeS to account for a  $T_c$  in the 5 K range.

## V. CONCLUSION

We have studied and identified phonons in tetragonal FeS by Raman scattering. For the  $A_{1g}$  sulfur and  $B_{1g}$  iron mode the DFT and DFPT calculations agree to within a few percent with the experiment. A third observed peak within a gap in the theoretical phonon density of states can be identified as a second order scattering process involving two phonons. Both the selection rules, based on the modified group projector tech-

nique, and the energy are in agreement with the experiment. A fourth mode identified close to the  $A_{1g}$  sulfur phonon can be traced back to the biggest maximum of the PDOS and is most likely activated by a small amount of defects.

The temperature dependence of all four modes is governed by the contraction of the lattice, but shows anomalies at 50 K and below 20 K. The anomaly observed at 20 K has a correspondence in the thermal expansion [20] and  $\mu$ SR experiments [21,22], which indicate short-range magnetic order. The long-range magnetic order observed recently by neutron diffraction experiments [41] below  $T_N = 116$  K has no correspondence in the Raman spectra.

The appearance of two-phonon scattering indicates strong phonon-phonon scattering, which is likely to originate from an electron-phonon interaction being enhanced in comparison to other pnictides and chalcogenides. We argue that in FeS the  $T_c$  can in principle entirely result from electron-phonon interaction.

## ACKNOWLEDGMENTS

We acknowledge valuable discussions with T. Böhm and D. Jost. The work was supported by the German Research Foundation (DFG) via the Priority Program SPP 1458 (Grant No. Ha2071/7) and the Serbian Ministry of Education, Science

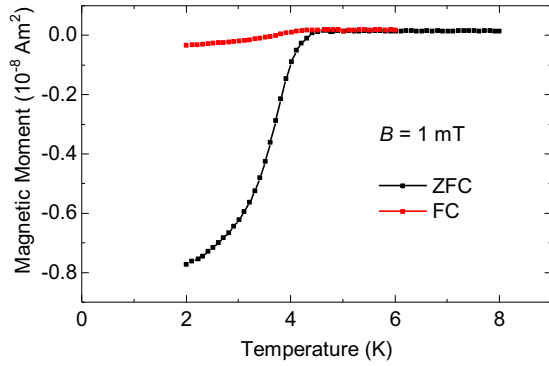


FIG. 5. Magnetization measurements of t-FeS at an applied field of  $B = 1$  mT cooled to 2 K with (red curve) and without applied field (black curve).

and Technological Development under Projects No. III45018 and No. ON171017. Numerical simulations were run on the PARADOX supercomputing facility at the Scientific Computing Laboratory of the Institute of Physics Belgrade. We acknowledge support by the DAAD through the bilateral project between Serbia and Germany (Grants No. 56267076 and No. 57142964). Work carried out at the Brookhaven National Laboratory was primarily supported by the Center for Emergent Superconductivity, an Energy Frontier Research Center funded by the U.S. DOE, Office of Basic Energy Sciences (A.W. and C.P.). N.S. was supported by UW Oshkosh FDS498 grant.

A.B. and A.M. have contributed equally to this work.

APPENDIX A: MAGNETIZATION MEASUREMENTS

Figure 5 shows magnetization measurements on a t-FeS sample from the batch studied in small applied fields. Measurements were done on a Quantum Design MPMS XL-7 SQUID magnetometer by cooling the sample to 2 K and sweeping

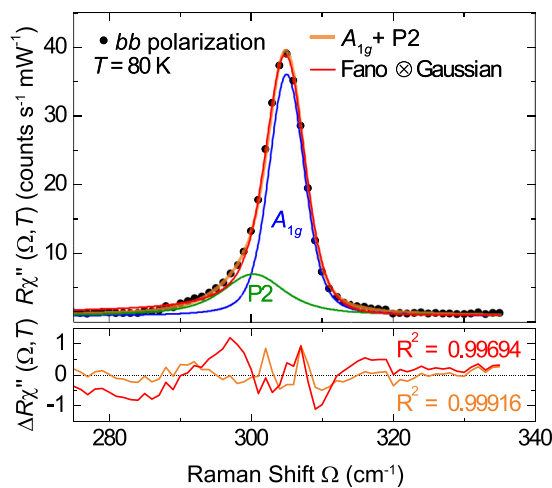


FIG. 6. Decomposition of the asymmetric phonon peak at  $305 \text{ cm}^{-1}$ . Measured data are shown as black dots. The orange line shows the sum of two Voigt profiles shown as blue and green lines, respectively. The convolution of Fano and Gaussian (red line) deviates in the peak flanks and the nearby continuum.

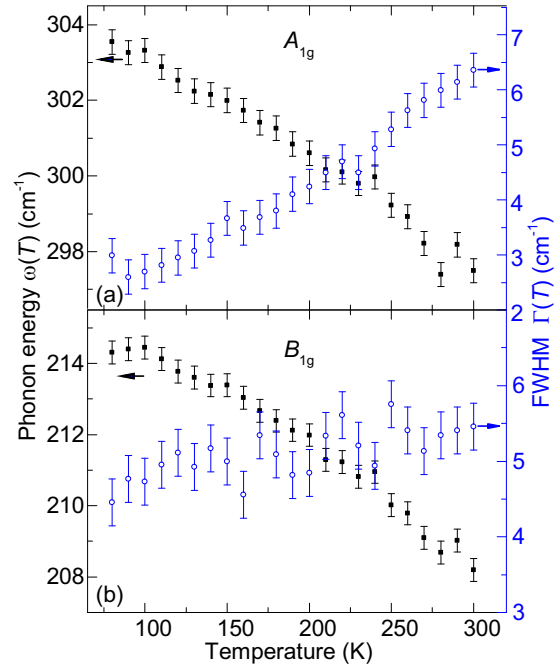


FIG. 7. Temperature dependence of  $A_{1g}$  and  $B_{1g}$  phonon modes in the temperature range between 80 K and 300 K. Black squares denote the phonon energies; open circles denote the phonon linewidths.

the temperature at 0.1 K/min. When cooled without applied field (ZFC, black curve) the sample shows a superconducting transition with onset at 4.5 K and a center of the transition at 3.6 K. When cooled in an applied field the magnetization decreases only weakly in the superconducting state indicating strong pinning.

APPENDIX B: DECOMPOSITION OF THE LINE AT  $305 \text{ cm}^{-1}$

The peak at  $305 \text{ cm}^{-1}$  at low temperatures shows a significant asymmetry towards lower energies (see also Fig. 1). Coupling of the  $A_{1g}$  phonon mode to an electronic continuum by strong electron-phonon coupling would result in a line shape given by the convolution of a Fano function and a Gaussian, the latter representing the resolution of the spectrometer. We find, however, that this does not yield a satisfactory description of the measured line shape as can be seen from the red curve in Fig. 6, and thus conclude that the asymmetry of the peak stems from the overlap of two peaks which cannot be resolved separately. The corresponding line shape is the sum of two Lorentzians convoluted with a Gaussian which governs the resolution of the setup. Due to the distributivity of the convolution this is identical to the sum of two Voigt functions sharing the same width  $\Gamma_G$  of the Gaussian part. The overall spectral shape is shown in Fig. 6 as an orange line and agrees excellently with the data. The two contributing lines are shown in blue and green. From the selection rules (see Fig. 1) we identify the blue curve as the in-phase vibration of sulfur atoms in  $A_{1g}$  symmetry. The green line denotes a second mode P2, the origin of which is discussed in the main text.



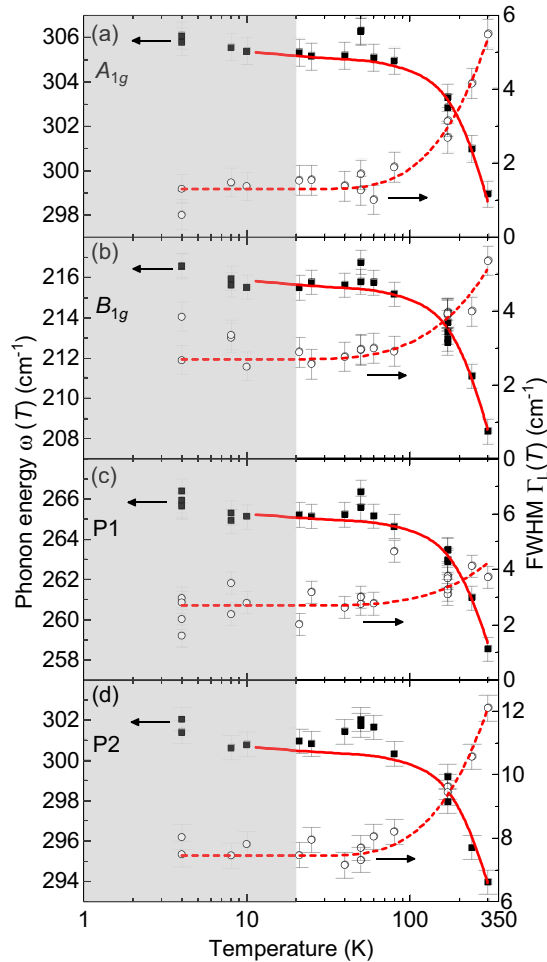


FIG. 8. Temperature dependence of energy and width of the four observed phonon modes in FeS on a logarithmic scale. The data is identical to Fig. 3 of the main text. Black squares show the phonon energies  $\omega$ ; open circles denote the phonon linewidths  $\Gamma_L$ . The red dashed and full lines represent the temperature dependence of the phonon linewidths and energies according to Eqs. (1) and (2), respectively. The region below 20 K is shaded light gray. Since the data for the volume are limited to the range above 10 K the theoretical curves for the phonon energies (full red lines) end at 10 K.

### APPENDIX C: DETAILED TEMPERATURE DEPENDENCE FOR $80 \leq T \leq 300$ K

Figure 7 shows the temperature dependence of the energies  $\omega$  and linewidths  $\Gamma(T)$  (FWHM) from 80 K to 300 K measured in temperature increments of 10 K. Raman scattering measurements were performed using a Jobin Yvon T64000 Raman system in micro-Raman configuration. A solid state laser with 532 nm line was used as an excitation source. Measurements were performed in high vacuum ( $10^{-6}$  mbar) using a KONTI CryoVac continuous helium flow cryostat with 0.5 mm thick window. Laser beam focusing was accomplished using a microscope objective with  $\times 50$  magnification. The samples were cleaved right before being placed in the vacuum. As can be seen from Fig. 7, there is no deviation from the standard temperature behavior around 120 K.

### APPENDIX D: TEMPERATURE DEPENDENCE ON A LOGARITHMIC SCALE

To better illustrate the behavior of the phonons at low temperatures Fig. 8 shows the experimental data and the theoretical curves from Fig. 3 of the main text on a logarithmic temperature scale. The region below 20 K is shaded light gray. As explained in Sec. IV B all four modes show an increase in energy below 20 K instead of the expected saturation, indicative of the putative onset of short range magnetic order. This effect manifests itself also in an incipient decrease of the unit cell volume [20] and is visible in the theoretical results for the phonon energies (full red lines). No clear tendency can be seen for the linewidths. The energy anomaly found around 50 K is discussed in the same section.

### APPENDIX E: SECOND SAMPLE BATCH

Figure 9 shows Raman spectra on a t-FeS sample from a different batch (E256) taken at  $T = 310$  K. The sample was oriented the same way as described in the main text. All three modes are visible for parallel light polarizations (*bb*), but vanish for crossed polarizations (*ba*), confirming the selection rules observed in the sample described in the main text. The inset shows magnetization measurements on a sample from batch E256 similar to the ones described in Appendix A. The superconducting transition sets in at 4.1 K.

### APPENDIX F: SELECTION RULES FOR TWO-PHONON PROCESSES AND MGPT

In the multiphonon scattering process the system goes from an initial vibrational state (ground vibrational state)  $|0,0,\dots\rangle$  to a final multiphonon state  $|n_\mu, n_{\mu'}, \dots\rangle$ , where  $n_\mu$  is the number of phonons in the same state  $\mu$  and  $\mu$  stands for the entire set of quantum numbers (quasimomentum  $k$ , angular momentum quantum number  $m$ , etc.). For two-phonon processes the final vibrational state is the state with two phonons in the same quantum state (double-phonon or the first overtone state) or with two phonons in different states (combination state). The corresponding matrix element for

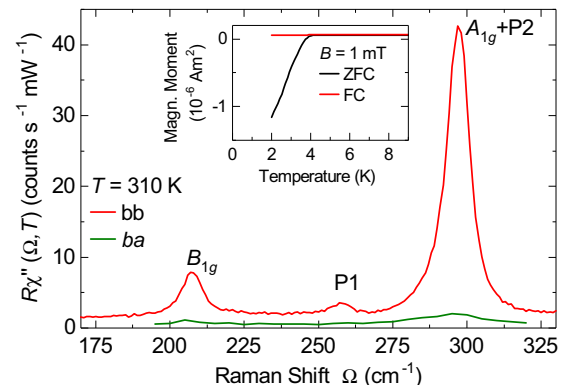


FIG. 9. Raman spectra of a t-FeS sample from a different batch taken at  $T = 310$  K in polarizations as given in the legend. The inset shows magnetization measurements on a sample from this batch similar to Appendix A.

two-phonon Raman scattering is

$$\begin{aligned} &\langle 0, \dots, n_\mu, 0, \dots | \mathcal{R} | 0, 0, \dots \rangle, n_\mu = 2, \text{overtones,} \\ &\langle 0, \dots, n_\mu, 0, \dots, n_{\mu'}, \dots | \mathcal{R} | 0, 0, \dots \rangle, \\ &n_\mu = n_{\mu'} = 1, \text{combinations,} \end{aligned} \quad (\text{F1})$$

where  $\mathcal{R}$  is the Raman tensor. This matrix element should be a scalar or should transform as unit representation of the system space group  $\mathcal{S}$ . The standard approximation for the Raman tensor in infinite wavelength-light approximation for the non-resonant case is the polarizability tensor, which transforms as the (symmetrized) square of the vector representation,  $D^{\mathcal{R}}(\mathcal{S})$ . Decomposition of  $D^{\mathcal{R}}(\mathcal{S})$  gives irreducible representations of the Raman active modes. The ground vibrational state transforms as unit representation, whereas the final two-phonon state transforms as symmetrized square,  $[(D^\mu(\mathcal{S}))^2]$ , of the corresponding irreducible representation  $D^\mu(\mathcal{S})$  (overtones) or the direct product of two irreducible representations  $D^\mu(\mathcal{S}) \otimes D^{\mu'}(\mathcal{S})$  (combinations). Symmetrization in the case of overtones comes from the bosonic nature of phonons. The matrix element [Eq. (F1)] transforms as reducible representation

$$\begin{aligned} &[(D^\mu(\mathcal{S}))^2] \otimes D^{\mathcal{R}}(\mathcal{S}), \text{ for overtones, or} \\ &D^\mu(\mathcal{S}) \otimes D^{\mu'}(\mathcal{S}) \otimes D^{\mathcal{R}}(\mathcal{S}), \text{ for combinations.} \end{aligned} \quad (\text{F2})$$

It is a scalar if the decomposition of the representations shown above contains the unit representation or, equivalently, if the intersection of decompositions of  $[(D^\mu(\mathcal{S}))^2]$  or  $D^\mu(\mathcal{S}) \otimes D^{\mu'}(\mathcal{S})$  and  $D^{\mathcal{R}}(\mathcal{S})$  is a nonempty set. To obtain selection rules for two-phonon processes, following Birman's original method [52], it is enough to find the decomposition of  $[(D^\mu(\mathcal{S}))^2]$  (for overtones) and  $D^\mu(\mathcal{S}) \otimes D^{\mu'}(\mathcal{S})$  (for combinations) for all irreducible representations. If there is any representation

of the Raman active mode in those decompositions then that overtone or two-phonon combination is symmetrically allowed in the Raman scattering process. The decomposition of the (symmetrized) square of the vector representation is straightforward and is actually a finite dimensional point group problem. On the other hand, decomposition of  $[(D^\mu(\mathcal{S}))^2]$  or  $D^\mu(\mathcal{S}) \otimes D^{\mu'}(\mathcal{S})$  for any irreducible representation could be a difficult task because space groups are infinite. In the standard method based on character theory summation over all group elements is used and it is a problem in the infinite case. Therefore, it is necessary to apply a method which avoids summation over group elements. As is proven in Ref. [29] the modified group projector technique (MGPT) uses only group generators and finite dimensional matrices. Actually, the decomposition  $D(\mathcal{S}) = \oplus_\mu f_D^\mu D^{(\mu)}(\mathcal{S})$  of the arbitrary reducible representation  $D(\mathcal{S})$  into irreducible representations is effectively a determination of the frequency numbers  $f_D^\mu$ . The MGPT expression for frequency numbers involves group generators  $s_i$  only:

$$f_D^\mu = \text{Tr} F \left( \prod_{i=1}^S F(D(s_i) \otimes D^{(\mu)*}(s_i)) \right). \quad (\text{F3})$$

Here  $S$  is the number of group generators,  $F(X)$  is the projector on the subspace of the fixed points of the operator  $X$ , and  $\text{Tr}$  is the matrix trace (sum of the diagonal matrix elements). Consequently, the problem is reduced to calculation of the  $S + 1$  projector to the fixed points. Technically, one looks for the eigenspaces for the eigenvalue 1 of each of the operators  $D(s_i) \otimes D^{(\mu)*}(s_i)$ , finding projectors on them, then multiplies the corresponding projectors, and repeats the procedure for the whole product from Eq. (F3). The trace of the final projector gives the corresponding frequency number.

- 
- [1] Z. P. Yin, K. Haule, and G. Kotliar, Magnetism and charge dynamics in iron pnictides, *Nat. Phys.* **7**, 294 (2011).
- [2] Q. Si, R. Yu, and E. Abrahams, High-temperature superconductivity in iron pnictides and chalcogenides, *Nat. Rev. Mater.* **1**, 16017 (2016).
- [3] I. Leonov, S. L. Skornyakov, V. I. Anisimov, and D. Vollhardt, Correlation-Driven Topological Fermi Surface Transition in FeSe, *Phys. Rev. Lett.* **115**, 106402 (2015).
- [4] C. Tresca, G. Giovannetti, M. Capone, and G. Profeta, Electronic properties of superconducting FeS, *Phys. Rev. B* **95**, 205117 (2017).
- [5] J. Miao, X. H. Niu, D. F. Xu, Q. Yao, Q. Y. Chen, T. P. Ying, S. Y. Li, Y. F. Fang, J. C. Zhang, S. Ideta, K. Tanaka, B. P. Xie, D. L. Feng, and F. Chen, Electronic structure of FeS, *Phys. Rev. B* **95**, 205127 (2017).
- [6] S. L. Skornyakov, V. I. Anisimov, D. Vollhardt, and I. Leonov, Effect of electron correlations on the electronic structure and phase stability of FeSe upon lattice expansion, *Phys. Rev. B* **96**, 035137 (2017).
- [7] T. M. McQueen, A. J. Williams, P. W. Stephens, J. Tao, Y. Zhu, V. Ksenofontov, F. Casper, C. Felser, and R. J. Cava, Tetragonal-to-Orthorhombic Structural Phase Transition at 90 K in the Superconductor Fe<sub>1.01</sub>Se, *Phys. Rev. Lett.* **103**, 057002 (2009).
- [8] Y. Mizuguchi, T. Furubayashi, K. Deguchi, S. Tsuda, T. Yamaguchi, and Y. Takano, Mössbauer studies on FeSe and FeTe, *Physica C (Amsterdam)* **470**, S338 (2010).
- [9] M. Bendele, A. Amato, K. Conder, M. Elender, H. Keller, H.-H. Klauss, H. Luetkens, E. Pomjakushina, A. Raselli, and R. Khasanov, Pressure Induced Static Magnetic Order in Superconducting FeSe<sub>1-x</sub>, *Phys. Rev. Lett.* **104**, 087003 (2010).
- [10] S.-H. Baek, D. V. Efremov, J. M. Ok, J. S. Kim, J. van den Brink, and B. Büchner, Orbital-driven nematicity in FeSe, *Nat. Mater.* **14**, 210 (2015).
- [11] M. He, L. Wang, F. Hardy, L. Xu, T. Wolf, P. Adelmann, and C. Meingast, Evidence for short-range magnetic order in the nematic phase of FeSe from anisotropic in-plane magnetotstriction and susceptibility measurements, [arXiv:1709.03861](https://arxiv.org/abs/1709.03861) [cond-mat.supr-con].
- [12] A. Baum, H. N. Ruiz, N. Lazarević, Y. Wang, T. Böhm, R. Hosseinian Ahangharnejhad, P. Adelmann, T. Wolf, Z. V. Popović, B. Moritz, T. P. Devereaux, and R. Hackl, Frustrated spin order and stripe fluctuations in FeSe, [arXiv:1709.08998](https://arxiv.org/abs/1709.08998) [cond-mat.str-el].
- [13] F.-C. Hsu, J.-Y. Luo, K.-W. Yeh, T.-K. Chen, T.-W. Huang, P. M. Wu, Y.-C. Lee, Y.-L. Huang, Y.-Y. Chu, D.-C. Yan, and M.-K.

- Wu, Superconductivity in the PbO-type structure  $\alpha$ -FeSe, *Proc. Natl. Acad. Sci. U.S.A.* **105**, 14262 (2008).
- [14] S. He, J. He, W. Zhang, L. Zhao, D. Liu, X. Liu, D. Mou, Y.-B. Ou, Q.-Y. Wang, Z. Li, L. Wang, Y. Peng, Y. Liu, C. Chen, L. Yu, G. Liu, X. Dong, J. Zhang, C. Chen, Z. Xu, X. Chen, X. Ma, Q. Xue, and X. J. Zhou, Phase diagram and electronic indication of high-temperature superconductivity at 65 K in single-layer FeSe films, *Nat. Mater.* **12**, 605 (2013).
- [15] J.-F. Ge, Z.-L. Liu, C. Liu, C.-L. Gao, D. Qian, Q.-K. Xue, Y. Liu, and J.-F. Jia, Superconductivity above 100 K in single-layer FeSe films on doped SrTiO<sub>3</sub>, *Nat. Mater.* **14**, 285 (2014).
- [16] S. Li, C. de la Cruz, Q. Huang, Y. Chen, J. W. Lynn, J. Hu, Y.-L. Huang, F.-C. Hsu, K.-W. Yeh, M.-K. Wu, and P. Dai, First-order magnetic and structural phase transitions in Fe<sub>1+y</sub>Se<sub>x</sub>Te<sub>1-x</sub>, *Phys. Rev. B* **79**, 054503 (2009).
- [17] M. H. Fang, H. M. Pham, B. Qian, T. J. Liu, E. K. Vehstedt, Y. Liu, L. Spinu, and Z. Q. Mao, Superconductivity close to magnetic instability in Fe(Se<sub>1-x</sub>Te<sub>x</sub>)<sub>0.82</sub>, *Phys. Rev. B* **78**, 224503 (2008).
- [18] K.-W. Yeh, T.-W. Huang, Y.-I. Huang, T.-K. Chen, F.-C. Hsu, P. M. Wu, Y.-C. Lee, Y.-Y. Chu, C.-L. Chen, J.-Y. Luo, D.-C. Yan, and M.-K. Wu, Tellurium substitution effect on superconductivity of the  $\alpha$ -phase iron selenide, *Europhys. Lett.* **84**, 37002 (2008).
- [19] X. Lai, H. Zhang, Y. Wang, X. Wang, X. Zhang, J. Lin, and F. Huang, Observation of superconductivity in tetragonal FeS, *J. Am. Chem. Soc.* **137**, 10148 (2015).
- [20] U. Pachmayr, N. Fehn, and D. Johrendt, Structural transition and superconductivity in hydrothermally synthesized FeX (X = S, Se), *Chem. Commun.* **52**, 194 (2016).
- [21] S. Hohenstein, U. Pachmayr, Z. Guguchia, S. Kamusella, R. Khasanov, A. Amato, C. Baines, H.-H. Klauss, E. Morenzoni, D. Johrendt, and H. Luetkens, Coexistence of low-moment magnetism and superconductivity in tetragonal FeS and suppression of T<sub>c</sub> under pressure, *Phys. Rev. B* **93**, 140506 (2016).
- [22] F. K. K. Kirschner, F. Lang, C. V. Topping, P. J. Baker, F. L. Pratt, S. E. Wright, D. N. Woodruff, S. J. Clarke, and S. J. Blundell, Robustness of superconductivity to competing magnetic phases in tetragonal FeS, *Phys. Rev. B* **94**, 134509 (2016).
- [23] A. Wang, L. Wu, V. N. Ivanovski, J. B. Warren, J. Tian, Y. Zhu, and C. Petrovic, Critical current density and vortex pinning in tetragonal FeS<sub>1-x</sub>Se<sub>x</sub> (x = 0, 0.06), *Phys. Rev. B* **94**, 094506 (2016).
- [24] S. Baroni, S. de Gironcoli, A. Dal Corso, and P. Giannozzi, Phonons and related crystal properties from density-functional perturbation theory, *Rev. Mod. Phys.* **73**, 515 (2001).
- [25] P. Giannozzi, S. Baroni, N. Bonini, M. Calandra, R. Car, C. Cavazzoni, D. Ceresoli, G. L. Chiarotti, M. Cococcioni, I. Dabo, A. D. Corso, S. de Gironcoli, S. Fabris, G. Fratesi, R. Gebauer, U. Gerstmann, C. Gougoussis, A. Kokalj, M. Lazzeri, L. Martin-Samos, N. Marzari, F. Mauri, R. Mazzarello, S. Paolini, A. Pasquarello, L. Paulatto, C. Sbraccia, S. Scandolo, G. Sclauzero, A. P. Seitsonen, A. Smogunov, P. Umari, and R. M. Wentzcovitch, QUANTUM ESPRESSO: a modular and open-source software project for quantum simulations of materials, *J. Phys.: Condens. Matter* **21**, 395502 (2009).
- [26] A. R. Lennie, S. A. T. Redfern, P. F. Schofield, and D. J. Vaughan, Synthesis and Rietveld crystal structure refinement of mackinawite, tetragonal FeS, *Mineral. Mag.* **59**, 677 (1995).
- [27] A. Subedi, L. Zhang, D. J. Singh, and M. H. Du, Density functional study of FeS, FeSe, and FeTe: Electronic structure, magnetism, phonons, and superconductivity, *Phys. Rev. B* **78**, 134514 (2008).
- [28] Y. El Mendili, B. Minisini, A. Abdelouas, and J.-F. Bardeau, Assignment of Raman-active vibrational modes of tetragonal mackinawite: Raman investigations and *ab initio* calculations, *RSC Adv.* **4**, 25827 (2014).
- [29] M. Damnjanović and I. Milošević, Full symmetry implementation in condensed matter and molecular physics—Modified group projector technique, *Phys. Rep.* **581**, 1 (2015).
- [30] P. G. Klemens, Anharmonic decay of optical phonons, *Phys. Rev.* **148**, 845 (1966).
- [31] H.-M. Eiter, P. Jaschke, R. Hackl, A. Bauer, M. Gangl, and C. Pfleiderer, Raman study of the temperature and magnetic-field dependence of the electronic and lattice properties of MnSi, *Phys. Rev. B* **90**, 024411 (2014).
- [32] M. Rahlenbeck, G. L. Sun, D. L. Sun, C. T. Lin, B. Keimer, and C. Ulrich, Phonon anomalies in pure and underdoped R<sub>1-x</sub>K<sub>x</sub>Fe<sub>2</sub>As<sub>2</sub> (R = Ba, Sr) investigated by Raman light scattering, *Phys. Rev. B* **80**, 064509 (2009).
- [33] L. Chauvière, Y. Gallais, M. Cazayous, A. Sacuto, M. A. Measson, D. Colson, and A. Forget, Doping dependence of the lattice dynamics in Ba(Fe<sub>1-x</sub>Co<sub>x</sub>)<sub>2</sub>As<sub>2</sub> studied by Raman spectroscopy, *Phys. Rev. B* **80**, 094504 (2009).
- [34] L. Chauvière, Y. Gallais, M. Cazayous, M. A. Méasson, A. Sacuto, D. Colson, and A. Forget, Raman scattering study of spin-density-wave order and electron-phonon coupling in Ba(Fe<sub>1-x</sub>Co<sub>x</sub>)<sub>2</sub>As<sub>2</sub>, *Phys. Rev. B* **84**, 104508 (2011).
- [35] Y. J. Um, A. Subedi, P. Toulemonde, A. Y. Ganin, L. Boeri, M. Rahlenbeck, Y. Liu, C. T. Lin, S. J. E. Carlsson, A. Sulpice, M. J. Rosseinsky, B. Keimer, and M. Le Tacon, Anomalous dependence of *c*-axis polarized Fe B<sub>1g</sub> phonon mode with Fe and Se concentrations in Fe<sub>1+y</sub>Te<sub>1-x</sub>Se<sub>x</sub>, *Phys. Rev. B* **85**, 064519 (2012).
- [36] Y. J. Um, J. T. Park, B. H. Min, Y. J. Song, Y. S. Kwon, B. Keimer, and M. Le Tacon, Raman scattering study of the lattice dynamics of superconducting LiFeAs, *Phys. Rev. B* **85**, 012501 (2012).
- [37] V. Gnezdilov, Y. G. Pashkevich, P. Lemmens, D. Wulferding, T. Shevtsova, A. Gusev, D. Chareev, and A. Vasiliev, Interplay between lattice and spin states degree of freedom in the FeSe superconductor: Dynamic spin state instabilities, *Phys. Rev. B* **87**, 144508 (2013).
- [38] T. Yildirim, Strong Coupling of the Fe-Spin State and the As-As Hybridization in Iron-Pnictide Superconductors from First-Principle Calculations, *Phys. Rev. Lett.* **102**, 037003 (2009).
- [39] V. Gnezdilov, Yu. Pashkevich, P. Lemmens, A. Gusev, K. Lamonova, T. Shevtsova, I. Vitebskiy, O. Afanasiev, S. Gnatchenko, V. Tsurkan, J. Deisenhofer, and A. Loidl, Anomalous optical phonons in FeTe chalcogenides: Spin state, magnetic order, and lattice anharmonicity, *Phys. Rev. B* **83**, 245127 (2011).
- [40] Z. V. Popović, N. Lazarević, S. Bogdanović, M. M. Radonjić, D. Tanasković, R. Hu, H. Lei, and C. Petrovic, Signatures of the spin-phonon coupling in Fe<sub>1+y</sub>Te<sub>1-x</sub>Se<sub>x</sub> alloys, *Solid State Commun.* **193**, 51 (2014).
- [41] S. J. Kuhn, M. K. Kidder, D. S. Parker, C. dela Cruz, M. A. McGuire, W. M. Chance, L. Li, L. Debeer-Schmitt, J. Ermen-trout, K. C. Littrell, M. R. Eskildsen, and A. S. Sefat, Structure and property correlations in FeS, *Physica C (Amsterdam)* **534**, 29 (2017).

- [42] R. A. MacDonald and W. M. MacDonald, Thermodynamic properties of fcc metals at high temperatures, *Phys. Rev. B* **24**, 1715 (1981).
- [43] M. I. Aroyo, D. Orobengoa, G. de la Flor, E. S. Tasci, J. M. Perez-Mato, and H. Wondratschek, Brillouin-zone database on the *Bilbao Crystallographic Server*, *Acta Crystallogr. A* **70**, 126 (2014).
- [44] W. Spengler and R. Kaiser, First and second order Raman scattering in transition metal compounds, *Solid State Commun.* **18**, 881 (1976).
- [45] W. Spengler, R. Kaiser, A. N. Christensen, and G. Müller-Vogt, Raman scattering, superconductivity, and phonon density of states of stoichiometric and nonstoichiometric TiN, *Phys. Rev. B* **17**, 1095 (1978).
- [46] W. Hayes and R. Loudon, *Scattering of Light by Crystals* (John Wiley and Sons, New York, 1978).
- [47] L. Boeri, O. V. Dolgov, and A. A. Golubov, Is LaFeAsO<sub>1-x</sub>F<sub>x</sub> an Electron-Phonon Superconductor? *Phys. Rev. Lett.* **101**, 026403 (2008).
- [48] B. Mansart, D. Boschetto, A. Savoia, F. Rullier-Albenque, F. Bouquet, E. Papalazarou, A. Forget, D. Colson, A. Rousse, and M. Marsi, Ultrafast transient response and electron-phonon coupling in the iron-pnictide superconductor Ba(Fe<sub>1-x</sub>Co<sub>x</sub>)<sub>2</sub>As<sub>2</sub>, *Phys. Rev. B* **82**, 024513 (2010).
- [49] L. Rettig, R. Cortés, H. S. Jeevan, P. Gegenwart, T. Wolf, J. Fink, and U. Bovensiepen, Electron-phonon coupling in 122 Fe pnictides analyzed by femtosecond time-resolved photoemission, *New J. Phys.* **15**, 083023 (2013).
- [50] H. Martinho, C. Rettori, P. G. Pagliuso, A. A. Martin, N. O. Moreno, and J. L. Sarrao, Role of the E<sub>2g</sub> phonon in the superconductivity of MgB<sub>2</sub>: a Raman scattering study, *Solid State Commun.* **125**, 499 (2003).
- [51] Y. Wang, T. Plackowski, and A. Junod, Specific heat in the superconducting and normal state (2–300 K, 0–16 T), and magnetic susceptibility of the 38 K superconductor MgB<sub>2</sub>: evidence for a multicomponent gap, *Physica C (Amsterdam)* **355**, 179 (2001).
- [52] J. L. Birman, Theory of infrared and Raman processes in crystals: Selection rules in diamond and zinblende, *Phys. Rev.* **131**, 1489 (1963).
- [53] M. I. Aroyo, A. Kirov, C. Capillas, J. M. Perez-Mato, and H. Wondratschek, Bilbao Crystallographic Server. II. Representations of crystallographic point groups and space groups, *Acta Crystallogr. A* **62**, 115 (2006).

**Small influence of magnetic ordering on lattice dynamics in TaFe<sub>1.25</sub>Te<sub>3</sub>**M. Opačić,<sup>1</sup> N. Lazarević,<sup>1</sup> D. Tanasković,<sup>2</sup> M. M. Radonjić,<sup>2</sup> A. Milosavljević,<sup>1</sup> Yongchang Ma,<sup>3,4</sup>  
C. Petrović,<sup>3</sup> and Z. V. Popović<sup>1,5</sup><sup>1</sup>*Center for Solid State Physics and New Materials, Institute of Physics Belgrade, University of Belgrade, Pregrevaica 118,  
11080 Belgrade, Serbia*<sup>2</sup>*Scientific Computing Laboratory, Center for the Study of Complex Systems, Institute of Physics Belgrade, University of Belgrade,  
Pregrevaica 118, 11080 Belgrade, Serbia*<sup>3</sup>*Condensed Matter Physics and Materials Science Department, Brookhaven National Laboratory, Upton, New York 11973-5000, USA*<sup>4</sup>*School of Materials Science and Engineering, Tianjin University of Technology, Tianjin 300384, People's Republic of China*<sup>5</sup>*Serbian Academy of Sciences and Arts, Knez Mihailova 35, 11000 Belgrade, Serbia*

(Received 12 September 2017; published 16 November 2017)

Raman scattering spectra of zigzag spin chain TaFe<sub>1.25</sub>Te<sub>3</sub> single crystal are presented in a temperature range from 80 to 300 K. Nine Raman active modes of  $A_g$  and  $B_g$  symmetry are clearly observed and assigned by probing different scattering channels, which is confirmed by lattice dynamics calculations. Temperature dependence of the Raman modes linewidth is mainly governed by the lattice anharmonicity. The only deviation from the conventional behavior is observed for  $A_g$  symmetry modes in a vicinity of the magnetic phase transition at  $T_N \approx 200$  K. This implies that the electron-phonon interaction weakly changes with temperature and magnetic ordering, whereas small changes in the spectra near the critical temperature can be ascribed to spin fluctuations.

DOI: [10.1103/PhysRevB.96.174303](https://doi.org/10.1103/PhysRevB.96.174303)**I. INTRODUCTION**

The discovery of superconductivity in La(O<sub>1-x</sub>F<sub>x</sub>)FeAs in 2008 [1] initiated an intensive search for new iron-based superconducting materials, in order to obtain better understanding of their physical properties and the mechanism of high- $T_c$  superconductivity [2–4]. Novel iron-based materials, however, are not only superconducting, but can also exhibit various types of magnetic ordering. In some cases the magnetic phase transition is continuous [5–8], whereas in others it is accompanied by structural changes [9–15], or even by a nanoscale coexistence of antiferromagnetic (AFM) and superconducting domains [16–18].

TaFe<sub>1+y</sub>Te<sub>3</sub> was synthesized and characterized about 25 years ago [19,20]. It is a layered system consisting of FeTe chains, along the  $b$  axis, separated by a Ta/Te network in between; see Fig. 1. These layers are parallel to the natural cleavage plane. There are also additional Fe ions, Fe2, randomly occupying interstitial sites [21–23]. TaFe<sub>1+y</sub>Te<sub>3</sub> features anisotropic charge transport with metallic resistivity within the plane and insulating in the direction normal to the FeTe layers [23]. The first study of magnetic structure implies that TaFe<sub>1+y</sub>Te<sub>3</sub> is composed of double zigzag spin chains with antiferromagnetic ordering of Fe1 spins [22]. The newest neutron diffraction measurements suggest that spin ordering within zigzag chains is ferromagnetic, whereas these zigzag chains couple antiferromagnetically [23], as shown in Fig. 1(b). However, the exact interaction mechanism is not clearly resolved.

There is a similarity between TaFe<sub>1+y</sub>Te<sub>3</sub> and the extensively studied Fe<sub>1+y</sub>Te compound since they are correlated bad metals which order antiferromagnetically below  $T_N \approx 200$  K and 70 K, respectively [10,23], both having rather large magnetic moments on Fe ions,  $\approx 2 \mu_B/\text{Fe}$ . TaFe<sub>1+y</sub>Te<sub>3</sub>, however, forms ferromagnetic (FM) zigzag spin chains which couple antiferromagnetically between the layers, whereas the Fe spins in Fe<sub>1+y</sub>Te form a bicollinear AFM structure. The magnetic phase transition in Fe<sub>1+y</sub>Te is accompanied by the

structural change from a tetragonal to a monoclinic, as opposed to TaFe<sub>1+y</sub>Te<sub>3</sub> where a continuous transition to the AFM phase is observed in thermodynamic and transport measurements [22]. Just like in Fe<sub>1+y</sub>Te, interest in spin chain and ladder materials [24] stems not only from their block-AFM states similar to parent compounds of iron-based superconductors [25], but also from superconductivity. It is worth noting that spin 1/2 copper oxide ladder structures host a spin gap and superconductivity upon doping [26–28]. In contrast to superconductivity in copper oxide ladder materials that was rather rare and with critical temperatures rather small when compared to highest achieved in copper square lattices [29,30], iron-ladder materials feature  $T_c$ 's similar to the highest found in Fe-based superconductors [31].

Raman spectra provide additional information on magnetic ordering and electron-phonon coupling. There exist several Raman studies of the phonon spectra of iron based materials near the superconducting or magnetic phase transition [32,33]. While no anomalies were observed in 1111 compounds [34,35], the Raman spectra show anomalous behavior near the spin density wave (SDW) transition in some of the 122 and 11 compounds [15,36–38], which was ascribed to the phonon renormalization due to the opening of the SDW or superconducting gap, or to the structural transition. Large anomalies were observed also in ferromagnetic K<sub>x</sub>Co<sub>2-y</sub>Se<sub>2</sub> [5], which was ascribed to the effect of electron-phonon coupling and spin fluctuations. Fe<sub>1+y</sub>Te phonon spectra feature unusually large anomalies near the magnetic phase transition, as seen in sudden changes in the phonon frequencies and linewidths, due to the phonon modulation of magnetic interactions and structural phase transition [11–13]. Therefore, it is of interest to examine lattice dynamics in the normal state of iron-spin chain and ladder materials and compare it to materials like Fe<sub>1+y</sub>Te. To the best of our knowledge, there are no published data on lattice dynamics of TaFe<sub>1+y</sub>Te<sub>3</sub>.

In this paper we present polarized Raman scattering spectra of TaFe<sub>1.25</sub>Te<sub>3</sub> single crystal measured in a temperature range from 80 to 300 K. Nine out of 15 Raman active modes are

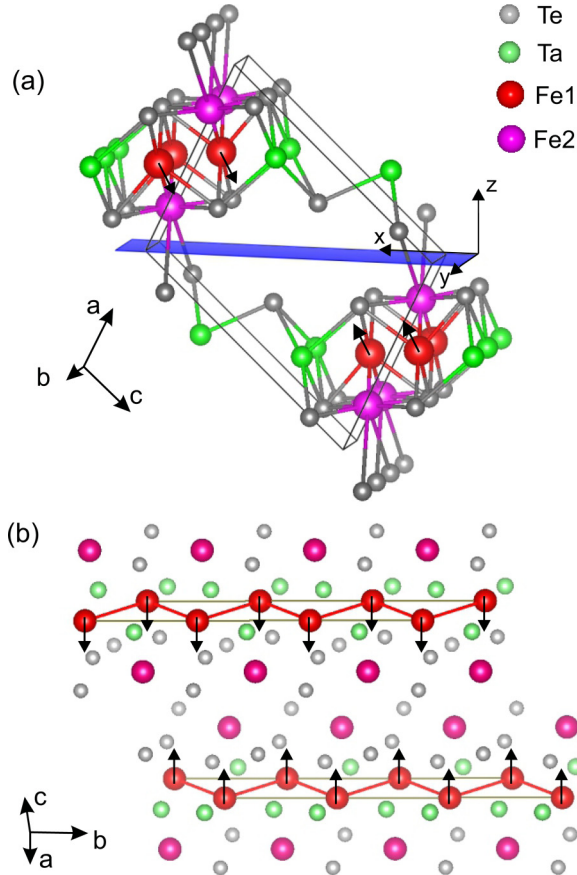


FIG. 1. (a) Structure of the  $\text{TaFe}_{1.25}\text{Te}_3$  single crystal together with the natural cleavage plane  $[\bar{1}01]$ .  $\mathbf{x} = 1/\sqrt{2}(\bar{1}0\bar{1})$  and  $\mathbf{y} = (010)$  correspond to our laboratory system. (b) A view of the  $\text{TaFe}_{1.25}\text{Te}_3$  structure along the  $b$  axis. Two neighboring chains of Fe1 spins point in a parallel direction, forming a ferromagnetic zigzag chain, whereas spins of neighboring zigzag chains order antiferromagnetically. One should note that Fe2 is present with occupancy of 0.25.

observed and assigned using the selection rules for different polarization configurations and lattice dynamics calculations. In a sharp contrast to the related FeTe compound,  $\text{TaFe}_{1.25}\text{Te}_3$  Raman spectra do not show significant changes near  $T_N \approx 200$  K, which clearly indicates that the phase transition is continuous. Temperature dependence of the frequency and linewidth is conventional, driven by the anharmonicity effects, except very near  $T_N$  where some of phonon lines slightly broaden which should be the consequence of spin fluctuations near the critical temperature. These results indicate very small changes in the electron-phonon coupling and in the Fermi surface in the measured temperature range.

## II. EXPERIMENT AND NUMERICAL METHOD

Single crystals were grown using the self-flux method, as described elsewhere [19]. Raman scattering measurements were performed on freshly cleaved  $(\bar{1}01)$ -oriented samples, using Jobin Yvon T64000 Raman system, equipped with a nitrogen-cooled CCD detector, in the backscattering micro-Raman configuration. The 532 nm line of a solid state laser was used as an excitation source. A microscope objective with

$50\times$  magnification was used for focusing the laser beam. All measurements were performed at low laser power, to reduce local heating of the sample. For low temperature measurements KONTI CryoVac continuous flow cryostat with 0.5 mm thick window was used. All spectra were corrected for the Bose factor. For extracting the data from the Raman spectra, phonon modes were fitted with a Lorentzian profile.

The electronic structure is calculated for stoichiometric  $\text{TaFeTe}_3$  in the paramagnetic phase within the density functional theory (DFT), and the phonon frequencies at the  $\Gamma$ -point are obtained within the density functional perturbation theory (DFPT) [39], using the QUANTUM ESPRESSO package [40]. We have used projector augmented wave (PAW) pseudopotentials with Perdew-Burke-Ernzerhof (PBE) exchange-correlation functional with nonlinear core correction and Gaussian smearing of 0.01 Ry. The electron wave function and the density energy cutoffs were 64 Ry and 782 Ry, respectively. The Brillouin zone is sampled with  $8 \times 8 \times 8$  Monkhorst-Pack  $k$ -space mesh. The phonon frequencies were calculated with the unit cell size taken from the experiments and the relaxed positions of atoms within the unit cell. The forces acting on individual atoms in the relaxed configuration were smaller than  $10^{-4}$  Ry/a.u.

## III. RESULTS AND DISCUSSION

$\text{TaFe}_{1+y}\text{Te}_3$  crystallizes in the monoclinic crystal structure, which is shown in Fig. 1. The space group is  $P2_1/m$  (unique axis  $b$ ), with two formula units per unit cell [19,20]. The experimental values of the unit cell parameters are  $a = 7.436$  Å,  $b = 3.638$  Å,  $c = 10.008$  Å, and  $\beta = 109.17^\circ$ . All atoms (including the excess Fe), are at  $2e$  Wyckoff positions, with fractional coordinates given in Table I.

The factor group analysis (FGA) for  $P2_1/m$  space group yields the following normal mode distribution at the  $\Gamma$  point:

$$\Gamma_{\text{Raman}} = 10A_g + 5B_g,$$

$$\Gamma_{\text{IR}} = 4A_u + 8B_u,$$

$$\Gamma_{\text{acoustic}} = A_u + 2B_u.$$

The Raman spectra were measured from the  $(\bar{1}01)$  plane of the sample, which is the natural cleavage plane [23,42]. From the Raman tensors given in Table II, the  $A_g$  phonon modes are expected to be observable in the  $(xx)$  and  $(yy)$  scattering configurations. The  $B_g$  modes can be observed only in  $(xy)$  polarization configuration.

TABLE I. Experimental fractional coordinates of  $\text{TaFe}_{1.25}\text{Te}_3$  taken from Ref. [19]. In the parentheses are the calculated values for  $\text{TaFeTe}_3$ .

Atom type	$x$	$y$	$z$
Ta	0.8340 (0.8331)	0.25	0.3007 (0.2987)
Fe1	0.6147 (0.6223)	-0.25	0.0890 (0.0988)
Fe2	0.7686	0.25	-0.0047
Te1	0.4392 (0.4326)	0.25	0.1860 (0.1637)
Te2	0.9835 (0.9842)	-0.25	0.1589 (0.1584)
Te3	0.2179 (0.2192)	0.25	0.4970 (0.5028)

TABLE II. Upper panel: atomic species (all of them are at  $2e$  Wyckoff positions) and the contribution of each atom to the  $\Gamma$ -point phonons, the corresponding Raman tensors for the TaFeTe<sub>3</sub> single crystal ( $P2_1/m$  space group) [41]. Lower panel: the calculated (for the stoichiometric TaFeTe<sub>3</sub>) and experimental phonon energies at 100 K (for the TaFe<sub>1.25</sub>Te<sub>3</sub> single crystal).

Atoms			Irreducible representations		
Ta, Fe1, Te1, Te2, Te3			$2A_g + A_u + B_g + 2B_u$		
$\hat{R}_{A_g} = \begin{pmatrix} a & 0 & d \\ 0 & b & 0 \\ d & 0 & c \end{pmatrix}$			$\hat{R}_{B_g} = \begin{pmatrix} 0 & e & 0 \\ e & 0 & f \\ 0 & f & 0 \end{pmatrix}$		
Raman active			Infrared active		
Symmetry	Calc. (cm <sup>-1</sup> )	Expt. (cm <sup>-1</sup> )	Symmetry	Calc. (cm <sup>-1</sup> )	Expt. (cm <sup>-1</sup> )
$A_g^1$	36.2		$A_u^1$	42.8	
$B_g^1$	43.8		$B_u^1$	54.9	
$B_g^2$	57.9	61.6	$B_u^2$	94.4	
$A_g^2$	63.8	62.3	$A_u^2$	101.4	
$A_g^3$	75.3	68.5	$B_u^3$	111.3	
$A_g^4$	104.4	90	$A_u^3$	131.1	
$B_g^3$	105.1		$B_u^4$	143.2	
$A_g^5$	124.6		$B_u^5$	160.4	
$B_g^4$	127.2	130.4	$B_u^6$	188.6	
$A_g^6$	149.8	155	$B_u^7$	227.9	
$A_g^7$	164.9	165	$A_u^4$	231.1	
$A_g^8$	191		$B_u^8$	289.4	
$B_g^5$	217.1	222.3			
$A_g^9$	241.9	223.9			
$A_g^{10}$	276.22				

Raman scattering spectra of TaFe<sub>1.25</sub>Te<sub>3</sub> single crystals, measured at 100 K in three different polarization configurations, are presented in Fig. 2. By using the selection rules, we assign the Raman peaks appearing in the ( $xx$ ) and ( $yy$ ) polarization configuration as the  $A_g$  ones. This conclusion is supported by the lattice dynamics calculations, given in Table II. By comparing the calculated values of  $A_g$  mode energies with those of the peaks appearing in the ( $xx$ ) and ( $yy$ ) spectra, we can unambiguously assign four Raman modes ( $A_g^4$ ,  $A_g^6$ ,  $A_g^7$ , and  $A_g^9$ ). The broad structure around 65 cm<sup>-1</sup> probably originates from the  $A_g^2$  and  $A_g^3$  modes, although the contribution of the  $A_g^1$  mode (with calculated energy of 42.7 cm<sup>-1</sup>) cannot be excluded. The peaks at 57.9 cm<sup>-1</sup> and 130 cm<sup>-1</sup> that are clearly visible in ( $xy$ ) but absent in ( $yy$ ) configuration are assigned as  $B_g^2$  and  $B_g^4$  modes, respectively. The low intensity peak at  $\approx 220$  cm<sup>-1</sup>, that becomes clearly observable at low temperatures, is tentatively assigned as  $B_g^5$  mode, although the contribution from the leakage of  $A_g^9$  mode cannot be excluded. The origin of the two very broad structures at about 70 cm<sup>-1</sup> and 160 cm<sup>-1</sup>, which are pronounced in the ( $xy$ ) configuration, is not completely clear. Aside from providing additional charge, Fe2 atoms may contribute to momentum transfer scattering, in line with the pronounced quasielastic continuum, present in all the scattering configurations. Consequently, contribution from single-phonon scattering away from  $\Gamma$  point becomes observable, which is theoretically predicted [43,44] and experimentally observed

[45,46]. Although we cannot exclude the possibility of two- and, in particular, double-phonon contributions, we believe it is less likely due to the nature of the processes and since they usually have more pronounced contribution to  $A$  channel (for arbitrary irreducible symmetry  $\mu$  of  $C_{2h}$  holds  $\mu \otimes \mu \ni A$ ).

The normal modes of the selected  $A_g$  and  $B_g$  vibrations, as obtained by the lattice dynamics calculations, are shown in Fig. 3. The low energy  $B_g^2$  mode represents vibrations of Te and Ta atoms which tend to elongate the (Ta,Fe)Te tetrahedra in the  $xy$  plane.  $B_g^4$  phonon originates mainly from Ta and Te atom vibrations in directions opposite to each other, whereas  $A_g^4$  mode represents dominantly vibrations of another Te atom in the  $xy$  plane.  $A_g^7$  and  $A_g^9$  modes originate from the vibrations of Fe and Te atoms which tend to rotate the tetrahedra around the  $x$  axis.

The DFT calculations are in very good agreement with the measured Raman spectra, specially having in mind the strength of electronic correlations in iron based compounds and the presence of additional Fe2 atoms in the measured sample. We restricted to the nonmagnetic DFT calculations. This is because small changes in the phonon energies due to the magnetic ordering cannot be reliably captured since the DFT does not treat strong correlation and spin-fluctuations effects. Our DFT calculations for the electronic band structure agree with the results from Ref. [42]. The calculated electronic dispersions are in rather good agreement with the ARPES measurements [42], which indicates that the main effect of the interstitial Fe2 ion is to provide additional charge and shift

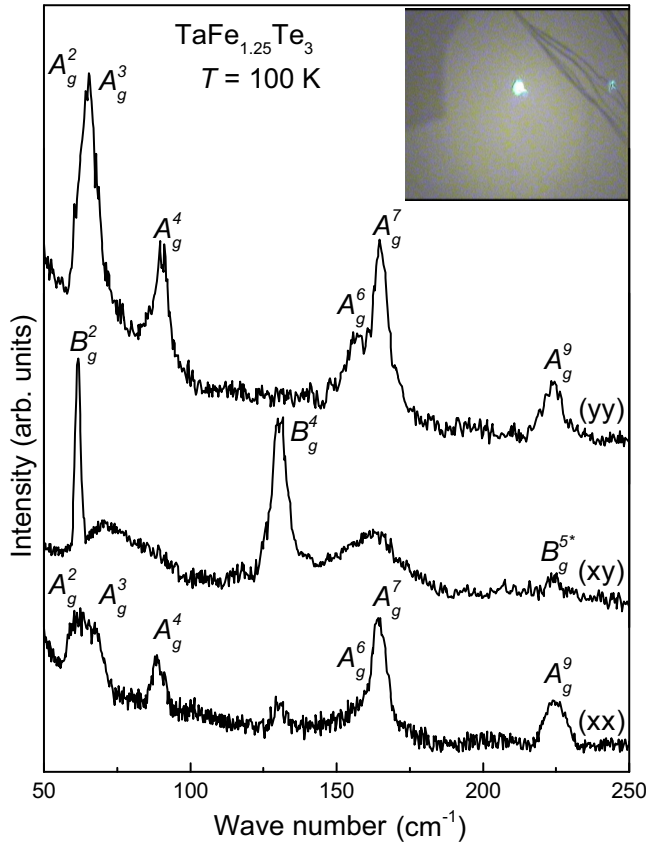


FIG. 2. Polarized Raman scattering spectra of  $\text{TaFe}_{1.25}\text{Te}_3$  single crystal measured at 100 K in various polarizations. The notation in parentheses indicates the polarization directions of the incident and scattered light according to Fig. 1(a). Inset: surface of the probed  $\text{TaFe}_{1.25}\text{Te}_3$  single crystal.

the Fermi level. This conclusion is supported with a small difference between the relaxed and experimental fractional coordinates; see Table I.

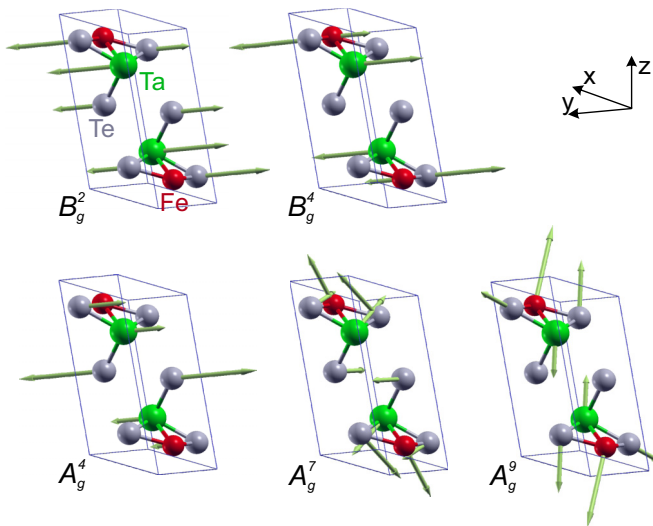


FIG. 3. Unit cell of  $\text{TaFeTe}_3$  single crystal with the displacement patterns of several  $A_g$  and  $B_g$  Raman modes. Arrow lengths are proportional to the square root of the interatomic forces.

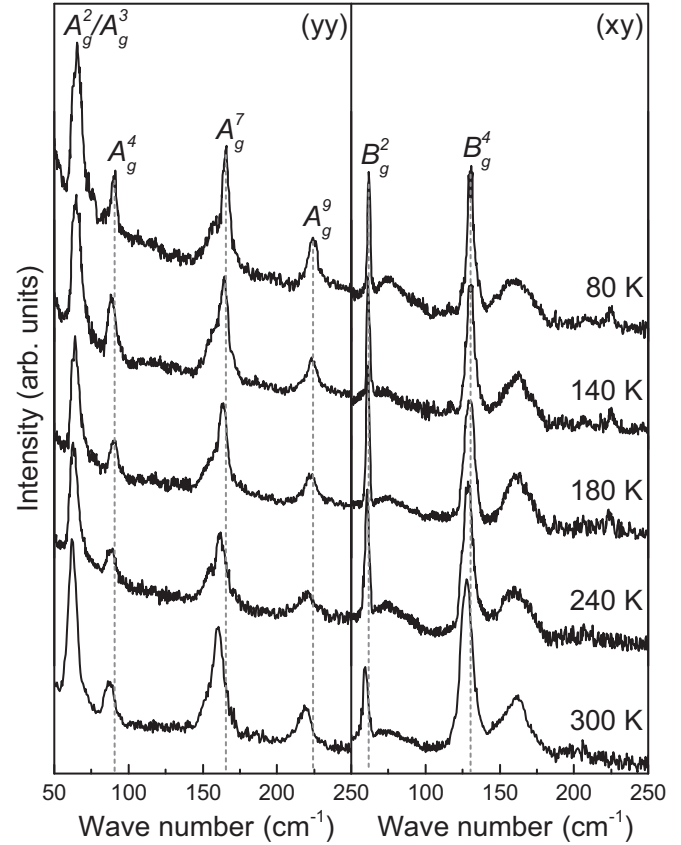


FIG. 4. Temperature dependent Raman scattering spectra of  $\text{TaFe}_{1.25}\text{Te}_3$  single crystal in the (yy) (left panel) and (xy) (right panel) polarization.

In order to analyze the changes of the Raman spectra near the AFM transition at  $T_N \approx 200$  K, we have performed measurements in a temperature range from 80 K up to 300 K. Raman spectra of  $\text{TaFe}_{1.25}\text{Te}_3$  single crystal, measured at different temperatures in the (yy) and (xy) scattering configurations, are given in Fig. 4. In the following, we perform the temperature analysis of the energy and the linewidth for five most clearly observed modes.

The temperature dependence of the Raman mode energy is usually described with [47,48]

$$\omega_i(T) = \omega_{0,i} + \Delta_i^V(\gamma_i, \alpha_i(T)) + \Delta_i^A(C_i), \quad (1)$$

where  $\omega_{0,i}$  is a temperature independent contribution to the Raman mode energy. The second term represents a change of the phonon energy induced by the lattice thermal expansion and depends on the Grüneisen parameter  $\gamma_i$  and the thermal expansion coefficient  $\alpha_i(T)$ . The term  $\Delta_i^A$  describes the anharmonicity induced change of the Raman mode energy which is a function of the anharmonic constant  $C_i$ . Both  $\Delta_i^V$  and  $\Delta_i^A$  have qualitatively the same temperature dependence. Since there are no reported experimental data on the temperature dependence of the lattice parameters for  $\text{TaFe}_{1+y}\text{Te}_3$ , we didn't attempt to fit the data, and the black dotted lines in Figs. 5 and 6 are guides to the eye. The  $\omega_i(T)$  curves follow the “standard” [5,15,37,49,50] continuous decrease in energy with temperature, with very small anomalies near  $T_N$  except for the  $A_g^4$  mode.



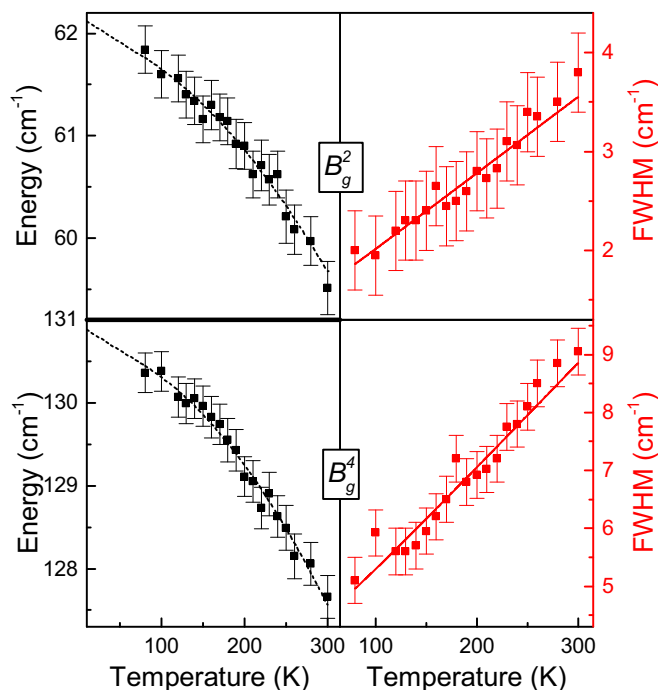


FIG. 5. Temperature dependence of the energy and linewidth for the  $B_g^2$  and  $B_g^4$  Raman modes of the  $\text{TaFe}_{1.25}\text{Te}_3$  single crystal. The red lines are fitted according to Eq. (2), whereas black lines are guides to the eye.

The temperature dependences of the linewidth of selected  $B_g$  and  $A_g$  modes are given in the right panels of Figs. 5 and 6, respectively. While the  $B_g^2$  and  $B_g^4$  phonon modes do not show significant deviation from the usual behavior due to the anharmonicity effects, with gradual broadening with increasing temperature, the  $A_g^4$ ,  $A_g^7$ , and  $A_g^9$  modes exhibit moderate additional broadening above 200 K. The red lines present a fit to the standard formula for the temperature dependent linewidth due to the anharmonicity [11,47,51]:

$$\Gamma_i(T) = \Gamma_{0,i} \left( 1 + \frac{2}{e^{\hbar\omega_{0,i}/2k_B T} - 1} \right) + A_i, \quad (2)$$

where  $\Gamma_{0,i}$  is the anharmonic constant and  $A_i$  is the constant term due to the disorder and electron-phonon interaction [52]. The deviation from these anharmonicity curves is most pronounced around  $T_N$  (see the insets of Fig. 6).

We can observe that all Raman modes have moderate linewidth and exhibit small anomalies near  $T_N$ . This shows that the phase transition is continuous, in agreement with the thermodynamic and transport measurements [22]. Small anomalies in the phonon spectra, which are restricted only to the vicinity of the phase transition, imply that the electron-phonon interaction of Raman active modes does not change with temperature. This is in agreement with the recent ARPES measurements which show negligible change of the Fermi surface across the AFM transition [42], indicating that the magnetic transition is not driven by the Fermi surface instability. The anomalies in the linewidth of some phonon modes near  $T_N$  are likely the signature of the increased scattering by spin fluctuations near the phase transition [51,53].

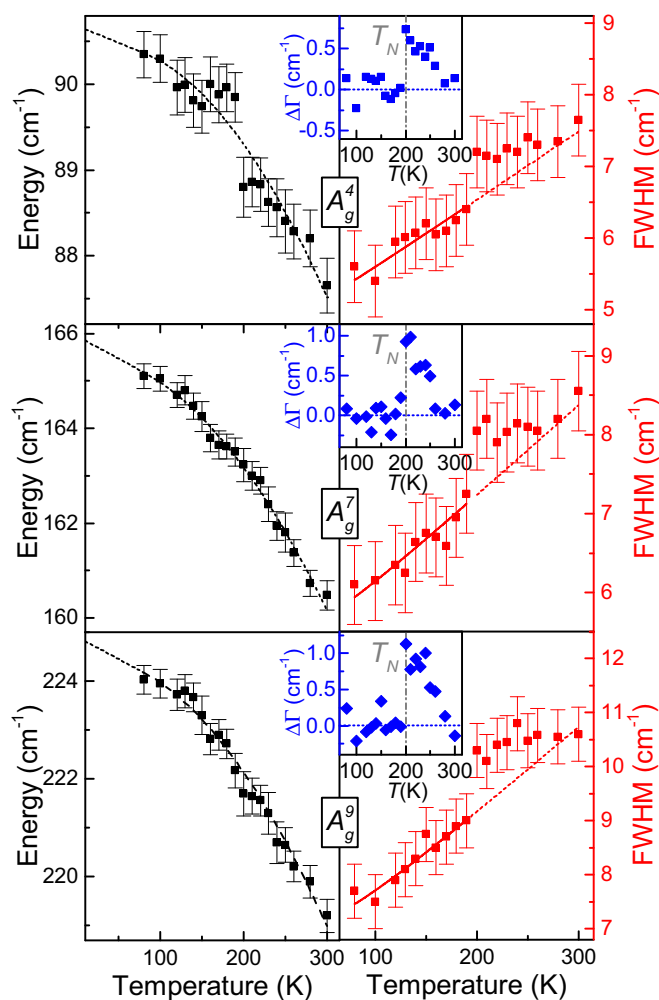


FIG. 6. Energy and linewidth of the  $A_g^4$ ,  $A_g^7$ , and  $A_g^9$  Raman modes of the  $\text{TaFe}_{1.25}\text{Te}_3$  single crystal as a function of temperature. The red lines are plotted according to Eq. (2), and the black dotted lines are guides to the eye. The insets represent deviations of the Raman mode linewidth from the anharmonic form.

The density of states (DOS) at the Fermi level is not large. This can be concluded from the ARPES experiments [42] which have shown three bands crossing the Fermi level but with strong dispersion, while several relatively flat bands are found only well below the Fermi level. The DFT calculations also give moderate values for the DOS,  $N(E_F) \approx 1 \text{ eV}^{-1}/\text{f.u.}$ , after the Fermi level is shifted due to the additional charge provided by the Fe2 atoms. This value for the DOS also suggests that the electron-phonon coupling is not strong in  $\text{TaFe}_{1.25}\text{Te}_3$ , since it is proportional to  $N(E_F)$ .

$\text{TaFe}_{1.25}\text{Te}_3$  has a similar moment size as  $\text{Fe}_{1+y}\text{Te}$ ,  $\approx 2\mu_B/\text{Fe}$ . However, the differences in the magnetic ordering and crystal structure cause different phonon properties of these two compounds. Namely, the phonon lines in the Raman spectra of  $\text{Fe}_{1+y}\text{Te}$  have very large linewidth and pronounced anomalies both in the frequency and in the linewidth near the first order phase transition [11,13]. Small anomalies in the Raman spectra of  $\text{TaFe}_{1.25}\text{Te}_3$  as compared to  $\text{Fe}_{1+y}\text{Te}$  can be ascribed to the continuous, second order nature of the AFM transition and smaller electron-phonon coupling due to lower DOS at the

Fermi level. Also, the monoclinic angle  $\beta$  in the  $\text{TaFe}_{1.25}\text{Te}_3$  unit cell significantly differs from  $90^\circ$  and therefore the form of the vibrational modes is different.

#### IV. CONCLUSION

In summary, we have performed the Raman scattering study of the zigzag spin chain  $\text{TaFe}_{1.25}\text{Te}_3$  single crystal, together with the lattice dynamics calculations of  $\text{TaFeTe}_3$ . By analyzing the Raman spectra in different polarization configurations and using numerical calculations we have assigned nine Raman active modes predicted by the FGA. Very good agreement between the experimental frequencies and those calculated for the stoichiometric compound shows that the excess iron atoms weakly influence the phonon energies but provide momentum conservation for the phonon scattering away from  $\Gamma$  point. The temperature dependence of the frequency and the linewidth of the  $B_g$  Raman modes looks conventional, governed by the anharmonicity effects. While in a broad temperature range the behavior of the  $A_g$  modes is also conventional, there are clear anomalies near

the AFM transition. The anomalies in the frequency and the linewidth are in the form of small kinks near  $T_N$ . This implies that the electron-phonon interaction and the DOS at the Fermi level are approximately constant in the measured temperature range. The increase in the linewidth near  $T_N$  is likely due to the coupling of spin fluctuations and vibration near the second order phase transition.

#### ACKNOWLEDGMENTS

We thank D. Stepanenko for useful discussions. This work was supported by the Serbian Ministry of Education, Science and Technological Development under Projects No. ON171032, No. III45018, and No. ON171017, and by the European Commission under H2020 project VI-SEEM, Grant No. 675121. Work at Brookhaven is supported by the Center for Emergent Superconductivity, an Energy Frontier Research Center funded by the U.S. DOE, Office for Basic Energy Science (C.P. and Y.M.). Numerical calculations were performed on the PARADOX supercomputing facility at the Scientific Computing Laboratory of the Institute of Physics Belgrade.

- 
- [1] Y. Kamihara, T. Watanabe, M. Hirano, and H. Hosono, *J. Am. Chem. Soc.* **130**, 3296 (2008).
- [2] L. Ma, G. F. Ji, J. Dai, X. R. Lu, M. J. Eom, J. S. Kim, B. Normand, and W. Yu, *Phys. Rev. Lett.* **109**, 197002 (2012).
- [3] B. Wei, H. Qing-Zhen, C. Gen-Fu, M. A. Green, W. Du-Ming, H. Jun-Bao, and Q. Yi-Ming, *Chin. Phys. Lett.* **28**, 086104 (2011).
- [4] G. R. Stewart, *Rev. Mod. Phys.* **83**, 1589 (2011).
- [5] M. Opačić, N. Lazarević, M. M. Radonjić, M. Šćepanović, H. Ryu, A. Wang, D. Tanasković, C. Petrovic, and Z. V. Popović, *J. Phys.: Condens. Matter* **28**, 485401 (2016).
- [6] Z. S. Gönen, P. Fournier, V. Smolyaninova, R. Greene, F. M. Araujo-Moreira, and B. Eichhorn, *Chem. Mater.* **12**, 3331 (2000).
- [7] H. Lei, H. Ryu, A. I. Frenkel, and C. Petrovic, *Phys. Rev. B* **84**, 214511 (2011).
- [8] F. Han, X. Wan, B. Shen, and H.-H. Wen, *Phys. Rev. B* **86**, 014411 (2012).
- [9] M. H. Fang, H. M. Pham, B. Qian, T. J. Liu, E. K. Vehstedt, Y. Liu, L. Spinu, and Z. Q. Mao, *Phys. Rev. B* **78**, 224503 (2008).
- [10] S. Li, C. de la Cruz, Q. Huang, Y. Chen, J. W. Lynn, J. Hu, Y.-L. Huang, F.-C. Hsu, K.-W. Yeh, M.-K. Wu, and P. Dai, *Phys. Rev. B* **79**, 054503 (2009).
- [11] V. Gnezdilov, Y. Pashkevich, P. Lemmens, A. Gusev, K. Lam-onova, T. Shevtsova, I. Vitebskiy, O. Afanasiev, S. Gnatchenko, V. Tsurkan, J. Deisenhofer, and A. Loidl, *Phys. Rev. B* **83**, 245127 (2011).
- [12] Y. J. Um, A. Subedi, P. Toulemonde, A. Y. Ganin, L. Boeri, M. Rahlenbeck, Y. Liu, C. T. Lin, S. J. E. Carlsson, A. Sulpice, M. J. Rosseinsky, B. Keimer, and M. Le Tacon, *Phys. Rev. B* **85**, 064519 (2012).
- [13] Z. V. Popović, N. Lazarević, S. Bogdanović, M. M. Radonjić, D. Tanasković, R. Hu, H. Lei, and C. Petrovic, *Solid State Commun.* **193**, 51 (2014).
- [14] K.-Y. Choi, D. Wulferding, P. Lemmens, N. Ni, S. L. Bud'ko, and P. C. Canfield, *Phys. Rev. B* **78**, 212503 (2008).
- [15] M. Rahlenbeck, G. L. Sun, D. L. Sun, C. T. Lin, B. Keimer, and C. Ulrich, *Phys. Rev. B* **80**, 064509 (2009).
- [16] F. Chen, M. Xu, Q. Q. Ge, Y. Zhang, Z. R. Ye, L. X. Yang, J. Jiang, B. P. Xie, R. C. Che, M. Zhang, A. F. Wang, X. H. Chen, D. W. Shen, J. P. Hu, and D. L. Feng, *Phys. Rev. X* **1**, 021020 (2011).
- [17] W. Li, H. Ding, P. Deng, K. Chang, C. Song, K. He, L. Wang, X. Ma, J.-P. Hu, P. Chen, and Q.-K. Xue, *Nat. Phys.* **8**, 126 (2012).
- [18] N. Lazarević, M. Abeykoon, P. W. Stephens, H. Lei, E. S. Bozin, C. Petrovic, and Z. V. Popović, *Phys. Rev. B* **86**, 054503 (2012).
- [19] M. Badding, J. Li, F. DiSalvo, W. Zhou, and P. Edwards, *J. Solid State Chem.* **100**, 313 (1992).
- [20] J. Neuhausen, E. Potthoff, W. Tremel, J. Enslin, P. Gütlich, and R. Kremer, *Z. Naturforsch. B* **48**, 797 (1993).
- [21] C. Perez Vicente, M. Womes, J. C. Jumas, L. Sanchez, and J. L. Tirado, *J. Phys. Chem. B* **102**, 8712 (1998).
- [22] R. H. Liu, M. Zhang, P. Cheng, Y. J. Yan, Z. J. Xiang, J. J. Ying, X. F. Wang, A. F. Wang, G. J. Ye, X. G. Luo, and X. H. Chen, *Phys. Rev. B* **84**, 184432 (2011).
- [23] X. Ke, B. Qian, H. Cao, J. Hu, G. C. Wang, and Z. Q. Mao, *Phys. Rev. B* **85**, 214404 (2012).
- [24] E. Dagotto, *Rev. Mod. Phys.* **85**, 849 (2013).
- [25] W. Li, C. Setty, X. H. Chen, and J. Hu, *Front. Phys.* **9**, 465 (2014).
- [26] E. Dagotto, J. Riera, and D. Scalapino, *Phys. Rev. B* **45**, 5744 (1992).
- [27] E. Dagotto and T. M. Rice, *Science* **271**, 618 (1996).
- [28] E. Dagotto, *Rep. Prog. Phys.* **62**, 1525 (1999).
- [29] M. Uehara, T. Nagata, J. Akimitsu, H. Takahashi, N. Môri, and K. Kinoshita, *J. Phys. Soc. Jpn.* **65**, 2764 (1996).
- [30] A. Hisada, K. Matsubayashi, Y. Uwatoko, N. Fujiwara, G. Deng, E. Pomjakushina, K. Conder, D. M. Radheep, R. Thiyagarajan, S. Esakkimuthu, and S. Arumugam, *J. Phys. Soc. Jpn.* **83**, 073703 (2014).

- [31] H. Takahashi, A. Sugimoto, Y. Nambu, T. Yamauchi, Y. Hirata, T. Kawakami, M. Avdeev, K. Matsubayashi, F. Du, C. Kawashima, H. Soeda, S. Nakano, Y. Uwatoko, Y. Ueda, T. J. Sato, and K. Ohgushi, *Nat. Mater.* **14**, 1008 (2014).
- [32] A.-M. Zhang and Q.-M. Zhang, *Chin. Phys. B* **22**, 087103 (2013).
- [33] M. Opačić and N. Lazarević, *J. Serb. Chem. Soc.* **82**, 957 (2017).
- [34] L. Zhang, T. Fujita, F. Chen, D. L. Feng, S. Maekawa, and M. W. Chen, *Phys. Rev. B* **79**, 052507 (2009).
- [35] Y. Gallais, A. Sacuto, M. Cazayous, P. Cheng, L. Fang, and H. H. Wen, *Phys. Rev. B* **78**, 132509 (2008).
- [36] V. Gnezdilov, Y. G. Pashkevich, P. Lemmens, D. Wulferding, T. Shevtsova, A. Gusev, D. Chareev, and A. Vasiliev, *Phys. Rev. B* **87**, 144508 (2013).
- [37] A. P. Litvinchuk, B. Lv, and C. W. Chu, *Phys. Rev. B* **84**, 092504 (2011).
- [38] K.-Y. Choi, P. Lemmens, I. Eremin, G. Zwirner, H. Berger, G. L. Sun, D. L. Sun, and C. T. Lin, *J. Phys.: Condens. Matter* **22**, 115802 (2010).
- [39] S. Baroni, S. de Gironcoli, A. Dal Corso, and P. Giannozzi, *Rev. Mod. Phys.* **73**, 515 (2001).
- [40] P. Giannozzi, S. Baroni, N. Bonini, M. Calandra, R. Car, C. Cavazzoni, D. Ceresoli, G. L. Chiarotti, M. Cococcioni, I. Dabo, A. D. Corso, S. de Gironcoli, S. Fabris, G. Fratesi, R. Gebauer, U. Gerstmann, C. Gougoussis, A. Kokalj, M. Lazzeri, L. Martin-Samos, N. Marzari, F. Mauri, R. Mazzarello, S. Paolini, A. Pasquarello, L. Paulatto, C. Sbraccia, S. Scandolo, G. Sclauzero, A. P. Seitsonen, A. Smogunov, P. Umari, and R. M. Wentzcovitch, *J. Phys.: Condens. Matter* **21**, 395502 (2009).
- [41] D. L. Rousseau, R. P. Bauman, and S. P. S. Porto, *J. Raman Spectrosc.* **10**, 253 (1981).
- [42] X. Min, W. Li-Min, P. Rui, G. Qing-Qin, C. Fei, Y. Zi-Rong, Z. Yan, C. Su-Di, X. Miao, L. Rong-Hua, M. Arita, K. Shimada, H. Namatame, M. Taniguchi, M. Matsunami, S. Kimura, S. Ming, C. Xian-Hui, Y. Wei-Guo, K. Wei, X. Bin-Ping, and F. Dong-Lai, *Chin. Phys. Lett.* **32**, 027401 (2015).
- [43] R. Shuker and R. W. Gammon, *Phys. Rev. Lett.* **25**, 222 (1970).
- [44] P. Benassi, O. Pilla, V. Mazzacurati, M. Montagna, G. Ruocco, and G. Signorelli, *Phys. Rev. B* **44**, 11734 (1991).
- [45] H. Ryu, M. Abeykoon, K. Wang, H. Lei, N. Lazarevic, J. B. Warren, E. S. Bozin, Z. V. Popovic, and C. Petrovic, *Phys. Rev. B* **91**, 184503 (2015).
- [46] B.-B. Zhang, N. Zhang, S.-T. Dong, Y. Lv, Y. B. Chen, S. Yao, S.-T. Zhang, Z.-B. Gu, J. Zhou, I. Guedes, D. Yu, and Y.-F. Chen, *AIP Adv.* **5**, 087111 (2015).
- [47] J. Menéndez and M. Cardona, *Phys. Rev. B* **29**, 2051 (1984).
- [48] H.-M. Eiter, P. Jaschke, R. Hackl, A. Bauer, M. Gangl, and C. Pfleiderer, *Phys. Rev. B* **90**, 024411 (2014).
- [49] N. Lazarević, M. Radonjić, M. Šćepanović, H. Lei, D. Tanasković, C. Petrovic, and Z. V. Popović, *Phys. Rev. B* **87**, 144305 (2013).
- [50] M. Opačić, N. Lazarević, M. Šćepanović, H. Ryu, H. Lei, C. Petrovic, and Z. V. Popović, *J. Phys.: Condens. Matter* **27**, 485701 (2015).
- [51] M. N. Iliev, A. P. Litvinchuk, H.-G. Lee, C. W. Chu, A. Barry, and J. M. D. Coey, *Phys. Rev. B* **60**, 33 (1999).
- [52] N. Lazarević, Z. V. Popović, R. Hu, and C. Petrovic, *Phys. Rev. B* **81**, 144302 (2010).
- [53] M. N. Iliev, A. P. Litvinchuk, H.-G. Lee, C. L. Chen, M. L. Dezaneti, C. W. Chu, V. G. Ivanov, M. V. Abrashev, and V. N. Popov, *Phys. Rev. B* **59**, 364 (1999).

# Raman spectroscopy of $K_x\text{Co}_{2-y}\text{Se}_2$ single crystals near the ferromagnet–paramagnet transition

M Opačić<sup>1</sup>, N Lazarević<sup>1</sup>, M M Radonjić<sup>2,3</sup>, M Šćepanović<sup>1</sup>, Hyejin Ryu<sup>4,5,6</sup>, Aifeng Wang<sup>4</sup>, D Tanasković<sup>3</sup>, C Petrović<sup>4,5</sup> and Z V Popović<sup>1</sup>

<sup>1</sup> Center for Solid State Physics and New Materials, Institute of Physics Belgrade, University of Belgrade, Pregrevica 118, 11080 Belgrade, Serbia

<sup>2</sup> Center for Electronic Correlations and Magnetism, Theoretical Physics III, Institute of Physics, University of Augsburg, D-86135 Augsburg, Germany

<sup>3</sup> Scientific Computing Laboratory, Institute of Physics Belgrade, University of Belgrade, Pregrevica 118, 11080 Belgrade, Serbia

<sup>4</sup> Condensed Matter Physics and Materials Science Department, Brookhaven National Laboratory, Upton, NY 11973-5000, USA

<sup>5</sup> Department of Physics and Astronomy, Stony Brook University, Stony Brook, NY 11794-3800, USA

E-mail: [nenad.lazarevic@ipb.ac.rs](mailto:nenad.lazarevic@ipb.ac.rs)

Received 1 July 2016, revised 24 August 2016

Accepted for publication 6 September 2016

Published 5 October 2016



## Abstract

Polarized Raman scattering spectra of the  $K_x\text{Co}_{2-y}\text{Se}_2$  single crystals reveal the presence of two phonon modes, assigned as of the  $A_{1g}$  and  $B_{1g}$  symmetry. The absence of additional modes excludes the possibility of vacancy ordering, unlike in  $K_x\text{Fe}_{2-y}\text{Se}_2$ . The ferromagnetic (FM) phase transition at  $T_c \approx 74$  K leaves a clear fingerprint on the temperature dependence of the Raman mode energy and linewidth. For  $T > T_c$  the temperature dependence looks conventional, driven by the thermal expansion and anharmonicity. The Raman modes are rather broad due to the electron–phonon coupling increased by the disorder and spin fluctuation effects. In the FM phase the phonon frequency of both modes increases, while an opposite trend is seen in their linewidth: the  $A_{1g}$  mode narrows in the FM phase, whereas the  $B_{1g}$  mode broadens. We argue that the large asymmetry and anomalous frequency shift of the  $B_{1g}$  mode is due to the coupling of spin fluctuations and vibration. Our density functional theory (DFT) calculations for the phonon frequencies agree rather well with the Raman measurements, with some discrepancy being expected since the DFT calculations neglect the spin fluctuations.

Keywords: Raman spectroscopy, electron–phonon, lattice dynamics

(Some figures may appear in colour only in the online journal)

## 1. Introduction

In the last few years considerable attention was focused on the iron-based superconductors in an effort to gain deeper insight into their physical properties and to determine the origin of high- $T_c$  superconductivity [1–4]. Discovery of superconductivity in alkali-doped iron chalcogenides, together with its

uniqueness among the iron based superconductors, challenged the physical picture of the superconducting mechanism in iron pnictides [5]. The absence of hole pockets even suggested the possibility for the different type of pairing mechanism [6]. Another striking feature in  $K_x\text{Fe}_{2-y}\text{Se}_2$  was the presence of the intrinsic nano to mesoscale phase separation between an insulating phase and a metallic/superconducting phase [7–10]. The insulating phase hosts antiferromagnetically,  $\sqrt{5} \times \sqrt{5}$  ordered iron vacancies, whereas the superconducting stripe-like phase is free of vacancies [7]. The theoretical study of

<sup>6</sup> Present address: Advanced Light Source, E O Lawrence Berkeley National Laboratory, Berkeley, CA 94720, USA

Huang *et al* [11] revealed that proximity effects of the two phases result in the Fermi surface deformation due to inter-layer hopping and, consequently, suppression of superconductivity. On the other hand, a large antiferromagnetic order protects the superconductivity against interlayer hopping, thus explaining relatively high  $T_c$  in  $K_x\text{Fe}_{2-y}\text{Se}_2$  [11]. However, the correlation between the two phases and its impact on superconductivity are still not fully understood.

Although the absolute values of resistivity are much smaller for the Ni-member of the  $K_x\text{M}_{2-y}\text{Se}_2$  ( $M =$  transition metal) series than for the iron member, this material does not exhibit superconductivity down to 0.3 K [12]. As opposed to  $K_x\text{Fe}_{2-y}\text{Se}_2$ , vacancy ordering has not been observed in the  $K_x\text{Ni}_{2-y}\text{Se}_2$  single crystal [13]. These materials, together with the Co- and Ni-doped  $K_x\text{Fe}_{2-y}\text{Se}_2$  single crystals, have very rich structural, magnetic and transport phase diagrams. This opens a possibility for fine tuning of their physical properties by varying the sample composition [14, 15]. First results obtained on  $K_x\text{Co}_{2-y}\text{Se}_2$  single crystal revealed the ferromagnetic ordering below  $T_c \sim 74$  K, as well as the absence of the superconducting phase [16].

Raman spectroscopy is a valuable tool not only for measuring vibrational spectra, but it also helps in the analysis of structural, electronic and magnetic properties, and phase transitions. There are several recent studies of the influence of the antiferromagnetic order, [17, 18] ferromagnetism, [19, 20] and magnetic fluctuations [21] on the Raman spectra.

In this paper the Raman scattering study of the  $K_x\text{Co}_{2-y}\text{Se}_2$  single crystal ( $x = 0.3$ ,  $y = 0.1$ ), together with the lattice dynamics calculations of  $\text{KCo}_2\text{Se}_2$ , is presented. The polarized Raman scattering measurements were performed in the temperature range from 20 K up to 300 K. The observation of only two Raman active modes when measuring from the (001)-oriented samples suggests that the  $K_x\text{Co}_{2-y}\text{Se}_2$  single crystal has no ordered vacancies. The temperature dependence of the energy and linewidth of the observed Raman modes reveals a clear fingerprint of the phase transition. A large linewidth of the  $B_{1g}$  mode and its Fano line shape indicate the importance of spin fluctuations.

The rest of the manuscript is organized as follows. Section 2 contains a brief description of the experimental and numerical methods, section 3 are the results, and section 4 contains a discussion of the phonon frequencies and linewidths and their temperature dependencies. Section 5 summarizes the results.

## 2. Experiment and numerical method

Single crystals of  $K_x\text{Co}_{2-y}\text{Se}_2$  were grown by the self-flux method, as described in [12]. The elemental analysis was performed using energy-dispersive x-ray spectroscopy (EDX) in a JEOL JSM-6500 scanning electron microscope. Raman scattering measurements were performed on freshly cleaved (001)-oriented samples with size up to  $3 \times 3 \times 1$  mm<sup>3</sup>, using a TriVista 557 Raman system equipped with a nitrogen-cooled CCD detector, in a backscattering micro-Raman configuration. The 514.5 nm line of an Ar<sup>+</sup>/Kr<sup>+</sup> ion gas laser was used as an excitation source. A microscope objective with  $50 \times$  magnification was used for focusing the laser beam. All

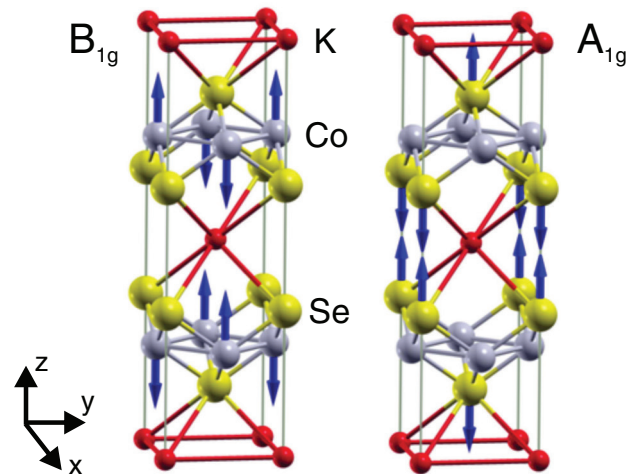


**Figure 1.** Unit cell of  $\text{KCo}_2\text{Se}_2$  single crystal, together with the displacement patterns of the  $A_{1g}$  and  $B_{1g}$  Raman modes.

measurements were carried out at low laser power, in order to minimize local heating of the sample. Low temperature measurements were performed using KONTI CryoVac continuous flow cryostat with 0.5 mm thick window. Spectra were corrected for the Bose factor.

The electronic structure of the ferromagnetic (FM) and paramagnetic (PM) phases is calculated within the density functional theory (DFT), and the phonon frequencies at the  $\Gamma$ -point are obtained within the density functional perturbation theory (DFPT) [22]. All calculations are performed using the QUANTUM ESPRESSO package [23]. We have used projector augmented-wave (PAW) pseudo-potentials with Perdew–Burke–Ernzerhof (PBE) exchange–correlation functional with nonlinear core correction and Gaussian smearing of 0.005 Ry. The electron wave-function and the density energy cutoffs are 40 Ry and 500 Ry, respectively. The Brillouin zone is sampled with a  $16 \times 16 \times 8$  Monkhorst–Pack  $k$ -space mesh. The phonon frequencies were calculated with relaxed unit cell parameters and, for comparison, with the unit cell size taken from the experiments and the relaxed positions of only Se atoms. The forces acting on individual atoms in the relaxed configuration were smaller than  $10^{-4}$  Ry/a.u. and the pressure smaller than 0.5 kbar.

## 3. Results

$\text{KCo}_2\text{Se}_2$  crystallizes in the tetragonal crystal structure of  $\text{ThCr}_2\text{Si}_2$ -type,  $I4/mmm$  space group, which is shown in figure 1. The experimental values of the unit cell parameters are  $a = 3.864(2)$  Å and  $c = 13.698(2)$  Å [24]. The potassium atoms are at  $2a$ : (0, 0, 0), Co atoms at  $4d$ :  $(0, \frac{1}{2}, \frac{1}{4})$ , and Se atoms at  $4e$ : (0, 0,  $z$ ) Wyckoff positions, with the experimental value  $z = 0.347$ .

The  $\text{KCo}_2\text{Se}_2$  single crystal consists of alternatively stacked K ions and CoSe layers, isostructural to the  $\text{KFe}_2\text{Se}_2$  [25]. Factor group analysis for the  $I4/mmm$  space group yields a normal mode distribution at the Brillouin-zone center, which is shown in table 1. According to the selection rules, when measuring from the (001)-plane of the sample, only two

**Table 1.** Atomic types with their Wyckoff positions and the contribution of the each site to the  $\Gamma$ -point phonons, the Raman tensors and the selection rules for the  $K_x\text{Co}_{2-y}\text{Se}_2$  single crystal ( $I4/mmm$  space group).

Atoms	Wyckoff positions	Irreducible representations
K	2a	$A_{2u} + E_u$
Co	4d	$A_{2u} + B_{1g} + E_g + E_u$
Se	4e	$A_{1g} + A_{2u} + E_g + E_u$
Raman tensors		
$\hat{R}_{A_{1g}} = \begin{pmatrix}  a \exp i\varphi_a & 0 & 0 \\ 0 &  a \exp i\varphi_a & 0 \\ 0 & 0 &  b \exp i\varphi_b \end{pmatrix}$		$\hat{R}_{B_{1g}} = \begin{pmatrix}  c \exp i\varphi_c & 0 & 0 \\ 0 & - c \exp i\varphi_c & 0 \\ 0 & 0 & 0 \end{pmatrix}$
$\hat{R}_{E_g} = \begin{pmatrix} 0 & 0 &  e \exp i\varphi_e \\ 0 & 0 & 0 \\  e \exp i\varphi_e & 0 & 0 \end{pmatrix}$		$\hat{R}_{E_g} = \begin{pmatrix} 0 & 0 & 0 \\ 0 & 0 &  f \exp i\varphi_f \\ 0 &  f \exp i\varphi_f & 0 \end{pmatrix}$
Activity and selection rules		
$\Gamma_{\text{Raman}} = A_{1g}(\alpha_{xx+yy}, \alpha_{zz}) + B_{1g}(\alpha_{xx-yy}) + 2E_g(\alpha_{xz}, \alpha_{yz})$		
$\Gamma_{IR} = 2A_{2u}(\mathbf{E}\ \mathbf{z}) + 2E_u(\mathbf{E}\ \mathbf{x}, \mathbf{E}\ \mathbf{y})$		
$\Gamma_{\text{acoustic}} = A_u + E_u$		

modes ( $A_{1g}$  and  $B_{1g}$ ) are expected to be observed in the Raman scattering experiment. Displacement patterns of the experimentally observable Raman modes are illustrated in figure 1. The  $A_{1g}$  ( $B_{1g}$ ) mode represents the vibrations of the Se (Co) ions along the  $c$ -axis, whereas the  $E_g$  modes (which are not observable for our scattering configuration) involve the vibration of both Co and Se ions within the (001)-plane.

Figure 2 shows polarized Raman scattering spectra of the  $K_x\text{Co}_{2-y}\text{Se}_2$  single crystal, measured from the (001)-plane of the sample at room temperature, in different sample orientations. Only two modes, at about 187 and 198  $\text{cm}^{-1}$ , are observed, which is in agreement with the selection rules for (001)-oriented samples. In some iron-chalcogenide compounds, the appearance of additional Raman active modes due to the iron vacancy ordering and, consequently, symmetry lowering, has been observed [8, 26]. The absence of additional phonon modes in figure 2 suggests that in  $K_x\text{Co}_{2-y}\text{Se}_2$  single crystals vacancy ordering does not occur in our samples.

Selection rules imply that the  $A_{1g}$  mode may be observed for any sample orientation, provided that the polarization vector of the incident light  $\mathbf{e}_i$  is parallel to the scattered light polarization vector  $\mathbf{e}_s$ , whereas it vanishes if these vectors are perpendicular. On the other hand, the intensity of the  $B_{1g}$  mode strongly depends on the sample orientation ( $I_{B_{1g}} \sim |c|^2 \cos^2(\theta + 2\beta)$ , where  $\theta = \angle(\mathbf{e}_i, \mathbf{e}_s)$  and  $\beta = \angle(\mathbf{e}_i, \mathbf{x})$  [8]). This implies that, in parallel polarization configuration ( $\theta = 0^\circ$ ), the intensity of the  $B_{1g}$  mode is maximal when the sample is oriented so that  $\mathbf{e}_i \parallel \mathbf{x}$ , gradually decreases with increasing  $\beta$  and finally vanishes for  $\beta = 45^\circ$ . In crossed polarization configuration ( $\theta = 90^\circ$ ),  $B_{1g}$  mode intensity decreases from its maximal value for  $\beta = 45^\circ$  to zero, which reaches when  $\beta = 0^\circ$ . From figure 2 it can be seen that the intensity of the Raman mode at about 187  $\text{cm}^{-1}$  coincides with theoretically predicted behavior for the  $B_{1g}$  mode; thereby, this phonon mode is assigned accordingly. The phonon mode at  $\sim 198 \text{ cm}^{-1}$ , which is present in Raman spectra only for the parallel polarization configuration ( $\theta = 0^\circ$ ) and whose intensity is independent on

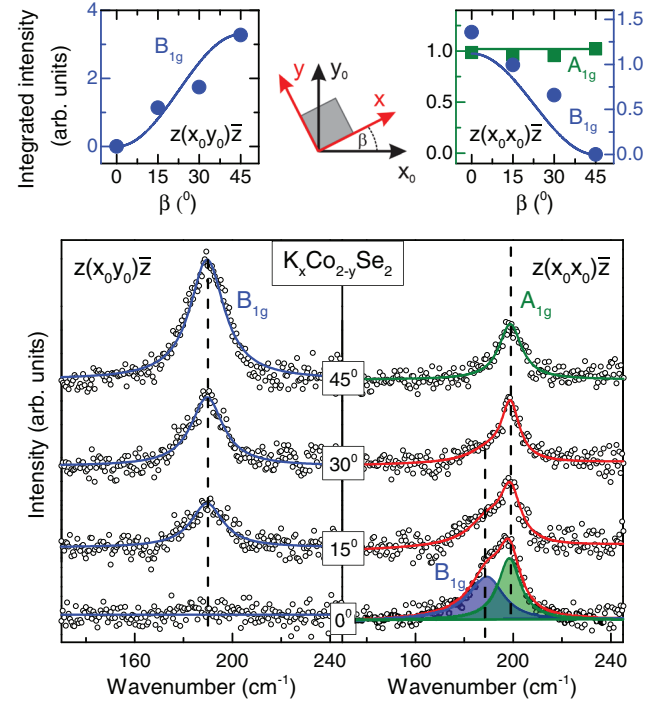


**Figure 2.** Upper panel: integrated intensity of the observed Raman modes as a function of the crystal orientation with respect to the laboratory axes  $\mathbf{x}_0$  and  $\mathbf{y}_0$ . In order to estimate the intensity of the modes, phonon at 198  $\text{cm}^{-1}$  was fitted with Lorentzian, whereas an asymmetric Raman mode appearing at 187  $\text{cm}^{-1}$  was fitted with Fano line shape. Lower panel: Raman scattering spectra of  $K_x\text{Co}_{2-y}\text{Se}_2$  single crystal measured at room temperature, in various sample orientations ( $\mathbf{x} = (100)$ ,  $\mathbf{y} = (010)$ ).

the sample orientation, can be assigned as the  $A_{1g}$  mode. The intensity ratio of the two Raman modes can be obtained from the spectrum measured in ( $\theta = 0^\circ, \beta = 0^\circ$ ) scattering geometry as  $I_{B_{1g}}/I_{A_{1g}} \approx 1.38$ . Having in mind that the  $A_{1g}$  mode intensity is given by [8]  $I_{A_{1g}} \sim |a|^2 \cos^2 \theta$ , the ratio of the appropriate Raman tensor components can be estimated as  $|c|/|a| \approx 1.17$ .

**Table 2.** Optimized lattice constants and internal coordinate  $z_{\text{Se}}$  in the FM and PM solution.

	$a$ (Å)	$c$ (Å)	$z_{\text{Se}}$
FM <sup>rel</sup>	3.893	13.269	0.350
PM <sup>rel</sup>	3.766	13.851	0.368
FM <sup>fixed</sup>	3.864	13.698	0.3486
PM <sup>fixed</sup>	3.864	13.698	0.3496
Exper.	3.864	13.698	0.347

Note: The next two rows give the relaxed  $z_{\text{Se}}$  when the unit cell size is taken from the experiment, and the last row contains the atomic positions from the experiment [24].

The experimentally determined frequencies are compared with those obtained with DFT numerical calculations. The experimental lattice constants [24] are shown in table 2, together with their values from the DFT calculation which relaxes or keeps fixed the unit cell size. The DFPT phonon frequencies obtained using the fully relaxed atomic positions in both FM and PM phases are given in table 3, with the corresponding values obtained with the fixed unit cell size and relaxed only fractional coordinate  $z_{\text{Se}}$  given in the parenthesis. The equilibrium atomic positions in the FM solution are given by  $a = 3.893$  Å,  $c = 13.269$  Å, and  $z_{\text{Se}} = 0.350$ . The corresponding phonon frequencies are  $199.5$  cm<sup>-1</sup> for  $A_{1g}$  mode and  $171.2$  cm<sup>-1</sup> for  $B_{1g}$  mode. When we enforce the PM solution, we obtain  $a = 3.766$  Å,  $c = 13.851$  Å, and  $z_{\text{Se}} = 0.368$ , and  $212.6$  cm<sup>-1</sup>,  $176.6$  cm<sup>-1</sup> for the frequencies of the  $A_{1g}$  and  $B_{1g}$  mode, respectively. These values agree rather well with the experimental data, and agree with recently published numerical results [27]<sup>7</sup>. They can be used to confirm the experimental assignment of the modes, but cannot resolve subtle changes of the phonon frequencies near the FM–PM transition. This level of discrepancy is expected for metallic materials with magnetic ordering since the DFT calculations neglect spin fluctuations, as discussed in some detail in the next section (see also [21]). A rather large difference between the calculated frequencies in the two phases is due to the relatively large change in the unit cell size. This difference between the unit cell sizes in the FM and PM phases is overestimated in the calculation which neglects spin fluctuations. For comparison, we also calculated the frequencies keeping the experimental values of the unit cell size, and relaxing just the coordinate  $z_{\text{Se}}$  of the Se atoms, which is often done in the case of iron based superconductors and related compounds [21]. This gives  $z_{\text{Se}} = 0.3486$  in the FM solution and  $z_{\text{Se}} = 0.3496$  in the PM solution, while the change in the phonon frequencies between the two solutions is much smaller, see table 3 and a discussion in section 4.

Polarized Raman scattering spectra of  $\text{K}_x\text{Co}_{2-y}\text{Se}_2$  single crystals, measured at various temperatures from the (001)-plane of the sample, are presented in figure 3. The orientation of the sample is chosen so that each of the observable modes appears in a different polarization configuration. A pronounced feature in the spectra is an asymmetric Fano profile of the  $B_{1g}$  mode, persisting down to low temperatures, as well as its large linewidth compared to isostructural  $\text{K}_x\text{Fe}_{2-y}\text{Se}_2$  [8, 28]. This feature should be mainly due to the spin

fluctuations influencing the  $B_{1g}$  vibrational mode which modulates the distances between the magnetic Co atoms. A detailed discussion of the frequency and linewidth temperature dependence is given in the next section.

## 4. Discussion

There are several factors that affect the phonon frequencies (energies) and linewidths, and their changes across the FM–PM transition. In general, the temperature dependence of the phonon frequency of the mode  $i$ ,  $\omega_i(T)$ , is influenced by thermal expansion and magnetostriction, anharmonicity effects, electron–phonon and magnetic exchange interaction (spin–phonon coupling) [29, 30]

$$\omega_i(T) - \omega_i(T_0) = \Delta\omega_i(T) = (\Delta\omega_i)_{\text{latt}} + (\Delta\omega_i)_{\text{anh}} + (\Delta\omega_i)_{\text{el-ph}} + (\Delta\omega_i)_{\text{sp-ph}}. \quad (1)$$

The first term is the frequency shift due to the change of the unit cell size caused by the thermal effects and magnetostriction.  $(\Delta\omega_i)_{\text{anh}}$  is the anharmonic frequency shift.  $(\Delta\omega_i)_{\text{el-ph}}$  appears due to the change in the electron–phonon interaction primarily influenced by changes in the electronic spectrum near the Fermi level, and  $(\Delta\omega_i)_{\text{sp-ph}}$  is the spin–phonon contribution caused by the modulation of exchange interaction by lattice vibrations.

In our case of  $\text{K}_x\text{Co}_{2-y}\text{Se}_2$ , for temperatures above  $T_c$ ,  $\omega_i(T)$  decreases and  $\Gamma_i(T)$  (full width at half-maximum, FWHM) increases with increasing temperature for  $A_{1g}$  and  $B_{1g}$  modes, similar as in the Raman spectra of many other materials. However, they show anomalous behavior near  $T_c$ , see figure 4. In the following, we analyze  $\omega_i(T)$  and  $\Gamma_i(T)$  more closely.

### 4.1. Phonon frequencies

The frequencies of the  $A_{1g}$  and  $B_{1g}$  modes change by less than 2 percent in the temperature range between 20 K and 250 K. The red solid lines in figures 4(a)–(c) represent the fits of the phonon energy temperature dependence (see below), following the frequencies of the two modes in the high-temperature PM phase. The red dotted line is the extrapolation to  $T = 0$ . For  $T > T_c$ , the temperature dependence of the frequency looks conventional for both modes: the frequency decreases with increasing temperature. This behavior is expected both due to the thermal expansion and the anharmonicity. These two effects can be standardly analyzed as follows.

The temperature dependent frequency of the vibrational mode  $i$  is given by

$$\omega_i(T) = \omega_{0,i} + \Delta_i(T), \quad (2)$$

where  $\omega_{0,i}$  denotes the temperature independent term and  $\Delta_i(T)$  can be decomposed as [19, 31, 32]

$$\Delta_i(T) = \Delta_i^V + \Delta_i^A. \quad (3)$$

$\Delta_i^V$  describes a change of the Raman mode energy as a consequence of the lattice thermal expansion and can be expressed with [31]

<sup>7</sup>There is typo in table 3 of [27] in the frequency of the  $B_{1g}$  mode.

**Table 3.** The experimental phonon energies measured at 20 K in the FM phase and the extrapolated value to 0 K from the PM phase (see the text).

Symmetry	Activity	Experiment FM (cm <sup>-1</sup> )	Experiment PM (cm <sup>-1</sup> )	Calculation FM (cm <sup>-1</sup> )	Calculation PM (cm <sup>-1</sup> )	Main atomic displacements
A <sub>1g</sub>	Raman	201.9	201.3	199.5 (193.2)	212.6 (193.1)	Se(z)
B <sub>1g</sub>	Raman	195.3	194.2	171.2 (172.7)	176.6 (168.1)	Co(z)
E <sub>g</sub> <sup>1</sup>	Raman			93.1 (100.7)	92.7 (99.0)	Co(xy), Se(xy)
E <sub>g</sub> <sup>2</sup>	Raman			237.9 (237.6)	257.2 (235.6)	Co(xy), Se(xy)
A <sub>2u</sub> <sup>1</sup>	IR			115.1 (99.0)	113.7 (102.9)	K(z), Se(-z)
A <sub>2u</sub> <sup>2</sup>	IR			246.7 (241.4)	250.9 (241.4)	Co(z), K(-z)
E <sub>u</sub> <sup>1</sup>	IR			97.9 (95.0)	100.1 (95.0)	K(xy)
E <sub>u</sub> <sup>2</sup>	IR			239.0 (229.7)	231.0 (229.9)	Co(xy), Se(-xy)

*Note:* The phonon frequencies at the  $\Gamma$  point are calculated with fully relaxed atomic positions. The frequencies obtained with only relaxed internal coordinate are given in parenthesis.

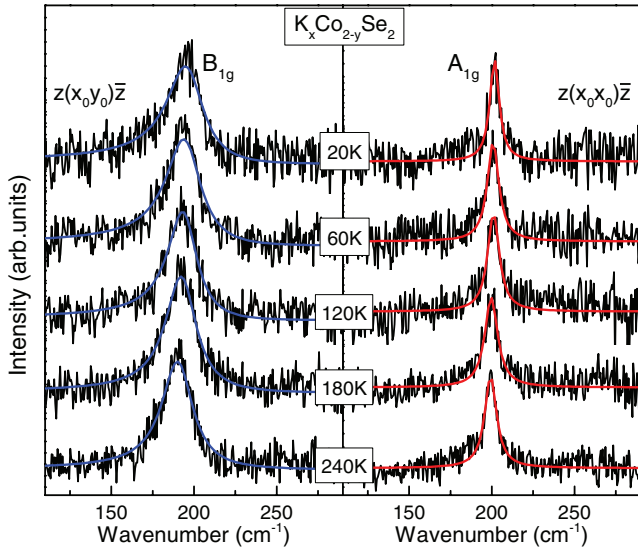


**Figure 3.** Temperature dependent Raman spectra of  $K_xCo_{2-y}Se_2$  single crystal in parallel (left panel) and crossed (right panel) polarization configuration ( $\mathbf{x}_0 = \frac{1}{\sqrt{2}}(1\ 1\ 0)$ ,  $\mathbf{y}_0 = \frac{1}{\sqrt{2}}(\bar{1}\ 1\ 0)$ ). The solid lines represent fits of the experimental spectra with the Lorentzian ( $A_{1g}$  mode) and the Fano profile ( $B_{1g}$  mode).

$$\Delta_i^V = \omega_{0,i} \left( e^{-3\gamma_i \int_0^T \alpha(T') dT'} - 1 \right), \quad (4)$$

where  $\gamma_i$  is the Grüneisen parameter of the Raman mode  $i$  and  $\alpha(T)$  is the thermal expansion coefficient of a considered single crystal.  $\Delta_i^A$  represents the anharmonic contribution to the Raman mode energy. If we assume, for simplicity, that anharmonic effects are described by three-phonon processes, this term is given by [31, 33]

$$\Delta_i^A = -C \left( 1 + \frac{2\lambda_{p-p,i}}{e^{\hbar\omega_{0,i}/2k_B T} - 1} \right), \quad (5)$$

where  $C$  is the anharmonic constant and  $\lambda_{p-p,i}$  is a fitting parameter which describes the phonon–phonon coupling, including the nonsymmetric phonon decay processes.

The relative importance of the thermal expansion and anharmonicity to frequency changes is, to the best of our knowledge, not yet firmly established for pnictides and

chalcogenides. In several cases [13, 17] the anharmonic formula, equation (5), is used for the  $\omega(T)$  fit. We follow here the arguments from [19, 28, 34] that  $\omega(T)$  is dominated by the thermal expansion. To the best of our knowledge, the thermal expansion coefficient  $\alpha(T)$  of the  $K_xCo_{2-y}Se_2$  single crystal is unknown. For estimating the lattice thermal expansion contribution to the phonon energy change, the coefficient  $\alpha(T)$  for FeSe, given in [35], is used. The best fit shown in our figure 4 is obtained with  $\omega_{0,A_{1g}} = 201.3\text{ cm}^{-1}$ ,  $\gamma_{A_{1g}} = 1.23$  and  $\omega_{0,B_{1g}} = 194.2\text{ cm}^{-1}$ ,  $\gamma_{B_{1g}} = 1.7$ .

There exists a shift in phonon frequencies as the temperature is lowered below  $T_c$ . This shift does not show clear discontinuity (as well as the corresponding shift in the linewidths) and no additional modes are registered in the Raman spectra, which suggest that the FM–PM transition is continuous, without structural changes. There are several causes of the sudden frequency change as the sample gets magnetized. It can change due to the magnetostriction, modulation of the magnetic exchange by lattice vibrations (spin–phonon coupling), and due to the changes in the electron–phonon interaction due to spin polarization and changes in the electronic spectrum.

The effect of spin–phonon interactions, caused by the modulation of magnetic exchange interaction by lattice vibrations, may be quantitatively examined within the framework developed in [29] for insulating magnets, and recently applied also to several itinerant ferromagnets [36–39]. In this model, the shift of the Raman mode energy due to the spin–phonon interaction is proportional to the spin–spin correlation function  $\langle S_i | S_j \rangle$  between nearest magnetic ions. This term should have the same temperature dependence as  $(M(T)/M_0)^2$ , where  $M(T)$  is the magnetization per magnetic ion at a temperature  $T$  and  $M_0$  is the saturation magnetization,

$$\Delta\omega(T) = \omega_{\text{exp}}(T) - \omega_{\text{fit}}(T) \propto \pm \left( \frac{M(T)}{M_0} \right)^2, \quad (6)$$

where  $\omega_{\text{fit}}(T)$  is the extrapolation from the high-temperature data. This model does not predict the sign of the phonon energy shift—softening or hardening. From the inset in figure 4(c) it can be seen that the  $B_{1g}$  mode energy renormalization scales well with the  $(M(T)/M_0)^2$  curve. However, the effect of the



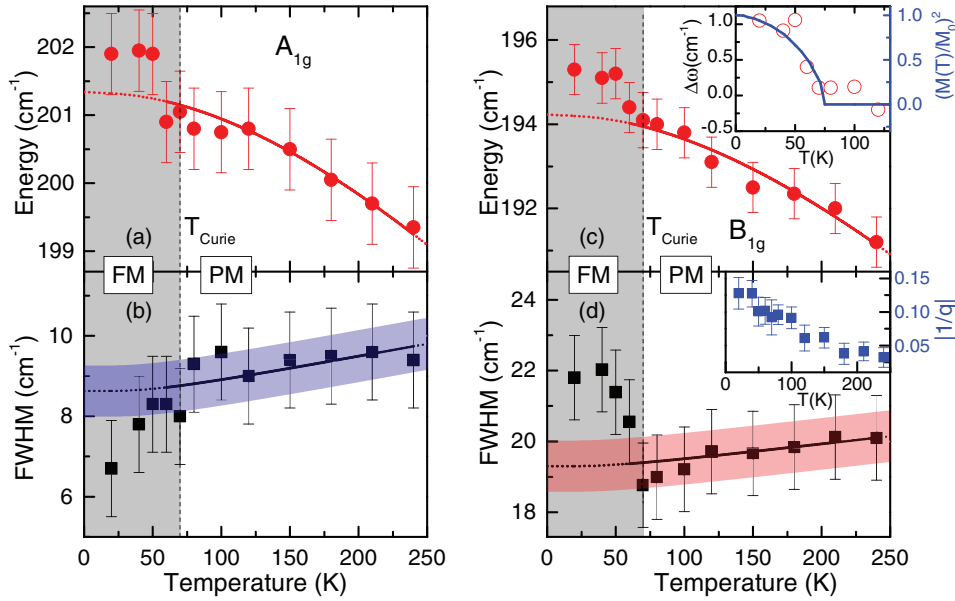


**Figure 4.** Temperature dependence of the energy and linewidth for the  $A_{1g}$  (a), (b) and  $B_{1g}$  (c), (d) Raman modes of the  $K_x\text{Co}_{2-y}\text{Se}_2$  single crystal. Solid lines are a theoretical fit (see the text) and the dotted lines are the extrapolation to the FM phase. Upper inset: temperature dependence of the  $B_{1g}$  mode frequency, compared with the  $(M(T)/M(0))^2$  curve. Lower inset: measure of the electron-mediated photon–phonon coupling ( $1/q$ ) of the  $B_{1g}$  mode as a function of temperature.

magnetostriction (change of the unit cell size due to the magnetization) cannot be excluded based just on this plot, especially since the  $A_{1g}$  mode corresponding to the vibrations of nonmagnetic Se ions also shows a similar shift in frequency.

The DFT calculations can give us some guidance for understanding of the changes of the phonon frequencies and linewidths, but one has to be aware of its limitations. The DFT calculations (see table 2) give a rather large magnetostriction, i.e. rather large change in the size of the unit cell between the FM and PM phases ( $a$  changes by 3.2% and  $c$  by 4.3%). This leads to very large changes in the phonon frequencies, see table 3. The calculated frequencies are lower in the FM phase, as opposed to the experimental data. This already points to the limitations of the DFT calculations, which is expected near the phase transition. A similar conclusion is also present in [21]. The DFT ignores spin fluctuations which often leads to quantitative discrepancy in various physical quantities [40] and, in some cases, even predicts wrong phases. In the case of  $K_x\text{Co}_{2-y}\text{Se}_2$ , the DFT calculations correctly predict the FM ground state, but the calculated magnetic moment  $m = 0.947 \mu_B$  is much larger than the experimental value  $m \approx 0.72 \mu_B$  [16]. This already shows the importance of correlations and quantum fluctuations which are neglected within the DFT. Strong correlation effects can be captured using screened hybrid functional [41] or within the dynamical mean field theory combined with DFT (LDA+DMFT) [42], which is beyond our present work.

Since the magnetostriction effects are overestimated in the DFT calculations with relaxed unit cell size, we repeated the DFT (DFPT) calculations keeping the experimental value for the unit cell size and relaxing only the fractional coordinate (positions of the Se atoms). This is often done in the literature on iron based superconductors and related compounds [21]. Our calculated frequencies are given in the parenthesis

in table 3. We see that the frequency changes between the two phases are small, in better agreement with the experiment.

#### 4.2. Phonon linewidths

The phonon linewidths of the  $A_{1g}$  and  $B_{1g}$  modes are very large,  $\Gamma_{i,A_{1g}} \sim 10 \text{ cm}^{-1}$  and  $\Gamma_{i,B_{1g}} \sim 20 \text{ cm}^{-1}$ , which implies the importance of disorder (impurities, nonstoichiometry, lattice imperfections) in measured samples. In general, the broadening of the phonon lines can be a consequence of the electron–phonon interaction, disorder, spin fluctuations and anharmonicity effects. The temperature dependence of the linewidth in the PM phase is, however, very weak, which indicates that the anharmonicity effects are small. The DFT calculation of the linewidth is usually based on the Allen’s formula, [43]  $\Gamma_{\mathbf{q},i} = \pi N(E_F) \lambda_{\mathbf{q},i} \omega_{\mathbf{q},i}^2$ . Here,  $N(E_F)$  is the density of states (DOS) at the Fermi level,  $\lambda_{\mathbf{q},i}$  is the electron–phonon coupling constant, and  $\omega_{\mathbf{q},i}^2$  is the phonon frequency of the mode  $i$  and wavevector  $\mathbf{q}$ . A straightforward implementation of Allen’s formula in the  $\mathbf{q} \rightarrow 0$  limit corresponding to the  $\Gamma$  point is, however, unjustified, as explained for example in [44, 45]. In addition, structural disorder and impurities break the conservation of the momentum, which means that phonons with finite wave vectors also contribute to the Raman scattering spectra. The standard DFT calculation for the Brillouin zone averaged electron–phonon coupling constant  $\lambda$  gives too small value to explain the large width of the Raman lines in pnictides and chalcogenides, [33] and several other metallic systems like  $\text{MgB}_2$  [44] and fullerides [46]. A correct estimate of the phonon linewidth can be obtained only by explicitly taking into account the disorder and electron scattering which enhances the electron–phonon interaction, [44, 46] which is beyond the standard DFT approach and scope of the present work.

The Raman mode linewidth is not directly affected by the lattice thermal expansion. Assuming that the three-phonon processes represent the leading temperature dependent term in the paramagnetic phase, full width at half-maximum,  $\Gamma_i(T)$ , is given by

$$\Gamma_i(T) = \Gamma_{0,i} \left( 1 + \frac{2\lambda_{p-p,i}}{e^{\hbar\omega_{0,i}/2k_B T} - 1} \right) + A_i. \quad (7)$$

The first term represents the anharmonicity induced effects, where  $\Gamma_{0,i}$  is the anharmonic constant. The second term  $A_i$  includes the contributions from other scattering channels, i.e. structural disorder and/or coupling of phonons with other elementary excitations, like particle-hole and spin excitations. These effects, typically, depend very weakly on temperature, but can become important near the phase transition. The best fit parameters are  $\lambda_{p-p,i} = 0.2$  for both modes,  $A_{A_{1g}} = 6.6 \text{ cm}^{-1}$  and  $A_{B_{1g}} = 17.3 \text{ cm}^{-1}$ . The value  $\Gamma_{0,i} = 2 \text{ cm}^{-1}$  is adopted from [28] for related compound  $\text{K}_x\text{Fe}_{2-y}\text{Se}_2$ , where the anharmonic effects dominate the temperature dependence. We see that  $\lambda_{p-p,i}$  assumes values much smaller than 1. Small and sometimes irregular changes in  $\Gamma_i(T)$  are also observed in other materials whose Raman spectra are considered to be dominated by spin fluctuations [21, 33]. Therefore, we believe that a simple separation of  $\Gamma_i(T)$  to the anharmonic and temperature independent term, which works well in many systems, is not appropriate for itinerant magnetic systems like  $\text{K}_x\text{Co}_{2-y}\text{Se}_2$ . We conclude that the spin fluctuations and electron-phonon coupling are likely to affect the linewidth even above  $T_c$ .

The electron-phonon interaction strength is proportional to the density of states at the Fermi level  $N(E_F)$ . Our DFT calculations for the DOS agree with those in [47]. The calculated DOS in the FM phase,  $N(E_F) = 3.69 \text{ eV}^{-1}$ , is smaller than,  $N(E_F) = 5.96 \text{ eV}^{-1}$ , in the PM phase. (Though, in reality, it is possible that the DOS significantly differs from the one given by the DFT calculations due to the spin fluctuations and disorder effects.) Therefore, one expects that the phonon line is narrower in the FM phase than in the PM phase. This is indeed the case for the  $A_{1g}$  mode, but the opposite is observed for the  $B_{1g}$  mode.

It is also interesting to note that the  $B_{1g}$  mode is much more asymmetric than the  $A_{1g}$  mode and almost twice broader. These two observations are in striking similarity with the Raman spectra in the quasi-one-dimensional superconductor  $\text{K}_2\text{Cr}_3\text{As}_3$  [21]. In this material the vibrational mode that modulates the distance between the magnetic Cr atoms also features large asymmetry and linewidth. In our case, the distances between the magnetic Co ions are modulated by the vibrations of the  $B_{1g}$  mode, see figure 1. This leads us to the conclusion that the anomalous features of the  $B_{1g}$  mode are the consequence of spin fluctuations coupled to the electronic structure via lattice vibrations (in addition to the magnetostriction and spin polarization, which change the electronic spectrum near the Fermi level and, therefore, affect the electron-phonon interaction for both modes). It should be noted that similar anomalous properties of  $B_{1g}$  phonon were experimentally observed in the cuprate high-temperature superconductor  $\text{YBa}_2\text{Cu}_3\text{O}_7$  [48, 49], and

explained as a consequence of the out-of-phase nature of this mode which couples to oxygen-oxygen in-plane charge fluctuations [50–52]. In the case of iron-based superconductors and related compounds, the chalcogen atoms and Fe (or Co) are not in the same plane and phonons of  $A_{1g}$  symmetry can also directly couple with the electrons. A satisfactory agreement of theory and Raman experiments remains to be established [53].

The asymmetric  $B_{1g}$  phonon line can be described by the Fano profile [21, 36, 54, 55]

$$I(\omega) = I_0 \frac{(\epsilon + q)^2}{1 + \epsilon^2}, \quad (8)$$

where  $\epsilon = 2(\omega - \omega_0)/\Gamma$ ,  $\omega_0$  is the bare phonon frequency,  $\Gamma$  is the linewidth.  $I_0$  is a constant and  $q$  is the Fano asymmetry parameter. It serves as a measure of a strength of the electron-phonon coupling: an increase in  $|1/q|$  indicates an increase in the electron-phonon interaction, more precisely, an increase in the electron-mediated photon-phonon coupling function [51, 53]. From the inset of figure 4(d) it can be seen that  $|1/q|$  increases as the temperature is lowered and reaches the highest values around  $T_c$ , when the spin fluctuations are the strongest. Spin fluctuations increase the electron-phonon scattering, similarly does the disorder. Technically, the electronic Green function acquires an imaginary component of the self energy due to the spin fluctuations, and this implies the increase in the damping term in the phonon self-energy, as explained in, e.g. [44]. This leads us to conclude that the spin fluctuations strongly enhance the electron-phonon interaction for the  $B_{1g}$  vibrational mode affecting its frequency and linewidth near  $T_c$ .

## 5. Conclusion

In summary, the Raman scattering study of the  $\text{K}_x\text{Co}_{2-y}\text{Se}_2$  ( $x = 0.3, y = 0.1$ ) single crystals and lattice dynamics calculations of the  $\text{KCo}_2\text{Se}_2$ , have been presented. Two out of four Raman active phonons are experimentally observed and assigned. The lack of any additional modes indicates the absence of vacancy ordering. The Raman spectra show sudden changes in the phonon energy and linewidth near the FM-PM phase transition. Above  $T_c$  the energy and linewidth temperature dependence of the  $A_{1g}$  and  $B_{1g}$  modes look conventional, as expected from the thermal expansion and anharmonicity effects. The linewidth, though, has very weak temperature dependence even above  $T_c$  which may be the consequence of the proximity of the phase transition and spin fluctuations. The  $B_{1g}$  vibrational mode has particularly large linewidth and features a Fano profile, which is likely the consequence of the magnetic exchange coupled to the vibrations of the Co atoms. Interestingly, the  $A_{1g}$  mode linewidth decreases below  $T_c$ , whereas the linewidth of the  $B_{1g}$  mode increases. The DFT calculations generally agree with the measured phonon frequencies. However, fine frequency differences in the two phases cannot be correctly predicted since the DFT calculations do not account for the spin fluctuation effects.

## Acknowledgments

We gratefully acknowledge discussions with R Hackl. This work was supported by the Serbian Ministry of Education, Science and Technological Development under Projects ON171032, III45018 and ON171017, by the European Commission under H2020 project VI-SEEM, Grant No. 675121, as well as by the DAAD through the bilateral Serbian-German project (PPP Serbien, grant-no. 56267076) ‘Interplay of Fe-vacancy ordering and spin fluctuations in iron-based high temperature superconductors’. Work at Brookhaven is supported by the US DOE under Contract No. DE-SC0012704 and in part by the Center for Emergent Superconductivity, an Energy Frontier Research Center funded by the US DOE, Office for Basic Energy Science (CP). Numerical simulations were run on the PARADOX supercomputing facility at the Scientific Computing Laboratory of the Institute of Physics Belgrade. MMR also acknowledges the support by the Deutsche Forschungsgemeinschaft through Transregio TRR 80 and Research Unit FOR 1346.

## References

- [1] Stewart G R 2011 *Rev. Mod. Phys.* **83** 1589–652
- [2] Wei B, Qing-Zhen H, Gen-Fu C, Green M A, Du-Ming W, Jun-Bao H and Yi-Ming Q 2011 *Chin. Phys. Lett.* **28** 086104
- [3] Liu R H *et al* 2011 *Europhys. Lett.* **94** 27008
- [4] Ma L, Ji G F, Dai J, Lu X R, Eom M J, Kim J S, Normand B and Yu W 2012 *Phys. Rev. Lett.* **109** 197002
- [5] Dagotto E 2013 *Rev. Mod. Phys.* **85** 849–67
- [6] Zhang Y M *et al* 2011 *Nat. Mater.* **10** 273–7
- [7] Li W *et al* 2012 *Nat. Phys.* **8** 126–30
- [8] Lazarević N, Abeykoon M, Stephens P W, Lei H, Bozin E S, Petrovic C and Popović Z V 2012 *Phys. Rev. B* **86** 054503
- [9] Ding X, Fang D, Wang Z, Yang H, Liu J, Deng Q, Ma G, Meng C, Hu Y and Wen H-H 2013 *Nat. Commun.* **4** 1897
- [10] Louca D, Park K, Li B, Neuefeind J and Yan J 2013 *Sci. Rep.* **3** 2047
- [11] Huang S-M, Mou C-Y and Lee T-K 2013 *Phys. Rev. B* **88** 174510
- [12] Lei H, Abeykoon M, Wang K, Bozin E S, Ryu H, Graf D, Warren J B and Petrovic C 2014 *J. Phys.: Condens. Matter* **26** 015701
- [13] Lazarević N, Radonjić M, Šćepanović M, Lei H, Tanasković D, Petrovic C and Popović Z V 2013 *Phys. Rev. B* **87** 144305
- [14] Ryu H, Wang K, Opačić M, Lazarević N, Warren J B, Popović Z V, Bozin E S and Petrovic C 2015 *Phys. Rev. B* **92** 174522
- [15] Ryu H, Abeykoon M, Wang K, Lei H, Lazarević N, Warren J B, Bozin E S, Popović Z V and Petrovic C 2015 *Phys. Rev. B* **91** 184503
- [16] Yang J, Chen B, Wang H, Mao Q, Imai M, Yoshimura K and Fang M 2013 *Phys. Rev. B* **88** 064406
- [17] Um Y J *et al* 2012 *Phys. Rev. B* **85** 064519
- [18] Popović Z V, Lazarević N, Bogdanović S, Radonjić M M, Tanasković D, Hu R, Lei H and Petrovic C 2014 *Solid State Commun.* **193** 51–5
- [19] Eiter H-M, Jaschke P, Hackl R, Bauer A, Gangl M and Pfleiderer C 2014 *Phys. Rev. B* **90** 024411
- [20] Kirillov D, Suzuki Y, Antognazza L, Char K, Bozovic I and Geballe T H 1995 *Phys. Rev. B* **51** 12825–8
- [21] Zhang W-L, Li H, Xia D, Liu H W, Shi Y-G, Luo J L, Hu J, Richard P and Ding H 2015 *Phys. Rev. B* **92** 060502
- [22] Baroni S, de Gironcoli S, Dal Corso A and Giannozzi P 2001 *Rev. Mod. Phys.* **73** 515–62
- [23] Gianozzi P *et al* 2009 *J. Phys.: Condens. Matter* **21** 395502
- [24] Huan G and Greenblatt M 1989 *J. Less-Common Met.* **156** 247–57
- [25] Guo J, Jin S, Wang G, Wang S, Zhu K, Zhou T, He M and Chen X 2010 *Phys. Rev. B* **82** 180520
- [26] Lazarević N, Lei H, Petrovic C and Popović Z V 2011 *Phys. Rev. B* **84** 214305
- [27] Wdowik U D, Jaglo G and Piekarczyk P 2015 *J. Phys.: Condens. Matter* **27** 415403
- [28] Opačić M, Lazarević N, Šćepanović M, Ryu H, Lei H, Petrovic C and Popović Z V 2015 *J. Phys.: Condens. Matter* **27** 485701
- [29] Granado E, García A, Sanjurjo J A, Rettori C, Torriani I, Prado F, Sánchez R D, Caneiro A and Oseroff S B 1999 *Phys. Rev. B* **60** 11879–82
- [30] Gupta R, Sood A K, Metcalf P and Honig J M 2002 *Phys. Rev. B* **65** 104430
- [31] Menéndez J and Cardona M 1984 *Phys. Rev. B* **29** 2051–9
- [32] Haro E, Balkanski M, Wallis R F and Wanser K H 1986 *Phys. Rev. B* **34** 5358–67
- [33] Rahlenbeck M, Sun G L, Sun D L, Lin C T, Keimer B and Ulrich C 2009 *Phys. Rev. B* **80** 064509
- [34] Gnezdilov V, Pashkevich Y G, Lemmens P, Wulferding D, Shevtsova T, Gusev A, Chareev D and Vasiliev A 2013 *Phys. Rev. B* **87** 144508
- [35] Böhmer A E, Hardy F, Eilers F, Ernst D, Adelman P, Schweiss P, Wolf T and Meingast C 2013 *Phys. Rev. B* **87** 180505
- [36] Kumar A, Chaudhary S, Pandya D K and Sharma S K 2014 *Phys. Rev. B* **90** 024302
- [37] Iliev M N, Abrashev M V, Litvinchuk A P, Hadjiev V G, Guo H and Gupta A 2007 *Phys. Rev. B* **75** 104118
- [38] Laverdière J, Jandl S, Mukhin A A, Ivanov V Y, Ivanov V G and Iliev M N 2006 *Phys. Rev. B* **73** 214301
- [39] Kumar D, Kumar S and Sathe V G 2014 *Solid State Commun.* **194** 59–64
- [40] Yin Z P, Haule K and Kotliar G 2011 *Nat. Mater.* **10** 932–5
- [41] Yin Z P, Kutepov A and Kotliar G 2013 *Phys. Rev. X* **3** 021011
- [42] Haule K, Shim J H and Kotliar G 2008 *Phys. Rev. Lett.* **100** 226402
- [43] Allen P B 1972 *Phys. Rev. B* **6** 2577–9
- [44] Cappelluti E 2006 *Phys. Rev. B* **73** 140505
- [45] Calandra M and Mauri F 2005 *Phys. Rev. B* **71** 064501
- [46] Aksenov V L and Kabanov V V 1998 *Phys. Rev. B* **57** 608–12
- [47] Bannikov V V, Shein I R and Ivanovskii A L 2012 *Phys. B: Condens. Matter* **407** 271–5
- [48] Ruf T, Thomsen C, Liu R and Cardona M 1988 *Phys. Rev. B* **38** 11985–7
- [49] Macfarlane R M, Rosen H and Seki H 1987 *Solid State Commun.* **63** 831–4
- [50] Barišić S, Kupčić I and Batistić I 1989 *Int. J. Mod. Phys. B* **03** 2051–63
- [51] Devereaux T P, Virosztek A and Zawadowski A 1995 *Phys. Rev. B* **51** 505–14
- [52] Kupčić I and Barišić S 2007 *Phys. Rev. B* **75** 094508
- [53] García-Martínez N A, Valenzuela B, Ciuchi S, Cappelluti E, Calderón M J and Bascones E 2013 *Phys. Rev. B* **88** 165106
- [54] Iliev M N, Jandl S, Popov V N, Litvinchuk A P, Cmaidalka J, Meng R L and Meen J 2005 *Phys. Rev. B* **71** 214305
- [55] Lazarević N, Popović Z V, Hu R and Petrovic C 2010 *Phys. Rev. B* **81** 144302

**Electronic structure of palladium in the presence of many-body effects**A. Östlin,<sup>1</sup> W. H. Appelt,<sup>1,2</sup> I. Di Marco,<sup>3</sup> W. Sun,<sup>3</sup> M. Radonjić,<sup>1,4</sup> M. Sekania,<sup>1,5</sup> L. Vitos,<sup>3,6,7</sup>  
O. Tjernberg,<sup>8</sup> and L. Chioncel<sup>1,2</sup><sup>1</sup>*Theoretical Physics III, Center for Electronic Correlations and Magnetism, Institute of Physics, University of Augsburg,  
D-86135 Augsburg, Germany*<sup>2</sup>*Augsburg Center for Innovative Technologies, University of Augsburg, D-86135 Augsburg, Germany*<sup>3</sup>*Department of Physics and Astronomy, Division of Materials Theory, Uppsala University, Box 516, SE-75120 Uppsala, Sweden*<sup>4</sup>*Scientific Computing Laboratory, Institute of Physics Belgrade, University of Belgrade, Pregrevica 118, 11080 Belgrade, Serbia*<sup>5</sup>*Andronikashvili Institute of Physics, Tamarashvili 6, 0177 Tbilisi, Georgia*<sup>6</sup>*Department of Materials Science and Engineering, Applied Materials Physics, KTH Royal Institute of Technology,  
SE-10044 Stockholm, Sweden*<sup>7</sup>*Research Institute for Solid State Physics and Optics, Wigner Research Center for Physics, P.O. Box 49, H-1525 Budapest, Hungary*<sup>8</sup>*Materials Physics, KTH Royal Institute of Technology, SE-16440 Kista, Sweden*

(Received 1 March 2016; published 25 April 2016)

Including on-site electronic interactions described by the multiorbital Hubbard model we study the correlation effects in the electronic structure of bulk palladium. We use a combined density functional and dynamical mean-field theory, LDA+DMFT, based on the fluctuation exchange approximation. The agreement between the experimentally determined and the theoretical lattice constant and bulk modulus is improved when correlation effects are included. It is found that correlations modify the Fermi surface around the neck at the  $L$  point while the Fermi surface tube structures show little correlation effects. At the same time we discuss the possibility of satellite formation in the high-energy binding region. Spectral functions obtained within the LDA+DMFT and  $GW$  methods are compared to discuss nonlocal correlation effects. For relatively weak local Coulomb interaction and Hund's exchange coupling the LDA+DMFT spectra show no major difference in comparison to  $GW$ .

DOI: [10.1103/PhysRevB.93.155152](https://doi.org/10.1103/PhysRevB.93.155152)**I. INTRODUCTION**

Transition metals have their density of states characterized by a partially filled narrow  $d$  band, superimposed on a broad free-electron-like  $sp$  band. The shape of the  $d$  band especially in the  $3d$  series is a consequence of the construction of the  $d$  orbitals, as they overlap only to a limited extent with orbitals on neighboring atoms and consequently the hopping integrals between  $d$  orbitals are small, as is the bandwidth. This points towards the importance of short-range strong Coulomb repulsion for the  $3d$  elements. An additional ingredient in the  $3d$  series is the appearance of magnetism. In a partially filled shell of a free atom the exchange interaction between electrons favors the parallel alignment of electron spins (Hund's rule). In solids, electrons of the extended states and orbitals experience the competition between the kinetic energy favoring no spin alignment and the exchange interaction favoring spin alignment. If the band is narrow the energy gain from the exchange interaction may win and the spin alignment is favored. In this sense, the occurrence of magnetism in the  $3d$  series is a consequence of the narrowness of the  $3d$  band. A quantitative theory to explain the electronic structure and hence the physical properties of  $3d$  elements has been consistently developed during the past decades in the form of the combined density functional theory (DFT) and dynamical mean-field theory (DMFT) [1–4], which is generally referred to as the LDA+DMFT method [4,5] (where LDA stands for local density approximation). In the LDA+DMFT scheme the LDA provides the *ab initio* material-dependent input (orbitals and hopping parameters), while the DMFT solves the many-body problem for the local interactions. Therefore, the LDA+DMFT approach is

able to compute, and even predict, properties of correlated materials. Theoretical results obtained with LDA+DMFT can be compared with experimental data obtained, for example, by photoemission spectroscopy (PES) [6,7]. In particular, this technique measures spectral functions, i.e., the imaginary part of the one-particle Green's function, and thus determines correlation-induced shifts of the spectral weight. Indeed, most experimental investigations on the electronic structure of the  $3d$  metal Ni rely on PES [8,9]. Braun *et al.* [10] demonstrated the importance of local correlations in Ni by exploiting the magnetic circular dichroism in bulk sensitive soft x-ray PES measurements. One of the dominant correlation effects observed in the PES data for Ni is the satellite peak situated at 6 eV below the Fermi level [11–13]. This feature is not captured by LDA, but it is well explained by LDA+DMFT [12]. LDA+DMFT also reproduces the correct width of the occupied  $3d$  bands and the exchange splitting [11,12,14].

As LDA+DMFT is very successful for  $3d$  elements, this motivates us to investigate the applicability of LDA+DMFT to  $4d$  transition-metal elements. Transition metals from the  $4d$  series have larger bandwidths compared to that of the  $3d$  elements and correspondingly larger kinetic energies, which will favor an itinerant bandlike picture over an atomiclike localized picture and somewhat weaker correlation effects. In our present study we focus on the  $4d$  metal palladium. Despite being in the same group as Ni in the periodic table, the physical properties of Pd are very different, so a theoretical study including local and nonlocal correlation effects is particularly desirable. The electronic structure of Pd has been widely studied, both from a fundamental physics points of view and in its industrial applications as catalysts and hydrogen storage. As a late  $4d$  transition-metal element, Pd is not far

from the ferromagnetic instability: it has a high density of states at the Fermi level and a large Stoner enhancement in the magnetic susceptibility [15]. On expansion (for a larger lattice constant) Pd turns ferromagnetic, as shown by DFT calculations [16]. Experimental studies involving PES have been used in the search for signatures of electronic correlations in Pd such as the existence of satellites in the spectral function [17,18]. Liebsch [19,20] investigated the satellite formation mechanism in detail using many-body methods, pointing out the importance of taking electron-hole and hole-hole scattering into account by ladderlike summations in the  $T$ -matrix formulation. Mårtensson and Johansson predicted a satellite in PES for Pd [21] at 8 eV binding energy, which is in good agreement with later experimental findings ( $\sim 8.5$  eV) by Chandesris *et al.* [17]. The method employed in Ref. [21] was semiempirical, using thermodynamic input data. In this study we discuss the satellite formation in Pd using *ab initio* self-consistent state-of-the-art calculations as well.

Complementary information can be obtained from the analysis of the Fermi surface. Features of the Fermi surface can be experimentally probed by photoemission spectroscopy and de Haas–van Alphen (dHvA) measurements. The so-called Kohn anomalies [22] may appear in the phonon dispersion relations of metals, arising from virtual scattering of conduction electrons from state  $\mathbf{k}$  to  $\mathbf{k}'$  connected by nesting vectors  $\mathbf{q}$ . The appearance of a Kohn anomaly in Pd, however, is still debated [23,24]. Therefore, the determination of possible Fermi-surface nesting in Pd remains of high interest.

Palladium is perhaps the best studied high-susceptibility paramagnet and played an important role in elucidating several aspects of the theory of spin fluctuations. Among the elements, Pd is traditionally taken as the best candidate for observing spin fluctuations because of its high electronic density of states and large Stoner enhancement in the magnetic susceptibility. Specific heat experiments [25] showed a reduction in the electronic specific heat coefficient of 7% in a magnetic field of about 10 T, suggesting that strong spin fluctuations do appear in Pd. The reduction of spin-fluctuation contributions to the electronic specific heat at high magnetic fields is well established theoretically by several works: Doniach and Engelsberg [26], Berk and Schrieffer [27], Béal-Monod and co-authors [28,29], and many others. In their classical works, the Crabtree group experimentally investigated the evidence of spin fluctuations in Pd by measuring the cyclotron effective masses and the amplitude of the dHvA effect as a function of the magnetic field [30,31]. These typical measurements provide in principle information about spin-fluctuation contributions to the conduction electron properties. While the former allows one to obtain information about the density of states at the Fermi level, which determines the electronic specific heat, the latter measures the difference in volume between the spin-up and spin-down Fermi surfaces, which determines the magnetization. The absence of significant field dependence of the cyclotron effective mass and the spin splitting factor [30,31] implies that the spin-fluctuation contributions to the electronic specific heat and static spin susceptibility  $\chi = M/H$  are not appreciably affected by applied fields up to 13 T. This is consistent with the theoretical estimations made by Brinkmann and Engelsberg [32] and Hertel *et al.* [33] that magnetic fields much larger than 13 T are required

to suppress the spin fluctuations in Pd. Highly accurate LDA calculations were performed to estimate the parameters entering in Moriya's spin-fluctuation theory [34]; in particular the Landau functional for Pd was used to connect critical fluctuations beyond the local density approximation with the band structure. The magnetic properties and dynamical fluctuations in Pd were discussed recently by Larson *et al.* [35]. It was pointed out [35] that the key parameter for the nontrivial properties of Pd is the mean-square amplitude of the spin fluctuations, which is a nonlocal quantity determined by the momentum-dependent spin susceptibility in a large part of the Brillouin zone, and therefore nonlocality is expected to play a significant role in the physical properties. It is one of the aims of this work to identify local and nonlocal correlation effects on the spectral function by comparing results obtained via LDA+DMFT and  $GW$  methods [36].

The results presented here include the electronic structure, the Fermi surface and nesting vectors of Pd, and the satellite formation in the high-binding-energy region of the density of states. Most of our results have been obtained within the full-potential linearized muffin-tin orbitals (FPLMTO) method implemented within the RSPT code [37], which has previously proven to be able to accurately determine ground-state quantities within LDA+DMFT for  $3d$  transition metals [38,39]. Self-consistent quasiparticle  $GW$  calculations have also been performed [40,41], which allows us to discuss the effect of nonlocal electronic correlations in Pd. The paper is organized as follows: Section I is an introduction. In Sec. II we present computational methods and details of the calculations. Section III A presents the total-energy data, from which we extract the optimal  $U$  and  $J$  values matching the experimental and the calculated equilibrium lattice parameters. We also present results concerning the onset of ferromagnetic long-range order upon lattice expansion. In Sec. III C the calculated spectral function of palladium is shown, and the relation to the photoemission satellite is discussed in detail. The effect of nonlocal correlations is discussed in Sec. III D.

## II. COMPUTATIONAL METHODS AND DETAILS

### A. The LDA+DMFT method

Correlation effects in the valence Pd  $4d$  orbitals were included via an on-site electron-electron interaction in the form  $\frac{1}{2} \sum_{i\{m,\sigma\}} U_{mm'm''m'''} c_{im\sigma}^\dagger c_{im'\sigma'}^\dagger c_{im''\sigma''} c_{im'''\sigma'''} c_{im'''\sigma'''} c_{im''\sigma''} c_{im'\sigma'} c_{im\sigma}$ . Here,  $c_{im\sigma}$  ( $c_{im\sigma}^\dagger$ ) annihilates (creates) an electron with spin  $\sigma$  on the orbital  $m$  at the lattice site  $i$ . The Coulomb matrix elements  $U_{mm'm''m'''}$  are expressed in the usual way [42] in terms of Slater integrals. Since specific correlation effects are already included in the local spin-density approximation (LSDA), so-called “double-counted” terms must be subtracted. To take this into account, we employed the interpolation double-counting scheme [43]. For the impurity solver a fluctuation exchange (FLEX) [44] type of approximation was used for the multiorbital case [45–47]. In contrast to the original formulation of FLEX [44], the spin-polarized  $T$ -matrix FLEX (SPTFLEX) is employed for the present calculations, which treats the particle-particle and the particle-hole channel differently [45–47]. While the particle-particle processes are important for the renormalization of the effective interaction [48], the particle-hole channel

describes the interaction of electrons with the spin fluctuations, which represents one of the most relevant correlation effects in Pd. In addition, the advantage of this computational scheme lies in the treatment of the Coulomb matrix elements in a full spin and orbital rotationally invariant form, relevant for realistic materials.

### B. The self-consistent quasiparticle $GW$ method

In recent years, first-principles calculations involving the  $GW$  approximation [36] have become more popular. In particular *self-consistent*  $GW$  formulations are promising because they can more accurately calculate quantities like band gaps as compared to “one-shot”  $GW$  approaches [41]. In these methods, the first step is to compute the band structure of the solid, usually within DFT-LDA. The density response function is then calculated by the random-phase approximation (RPA) and employed to evaluate the dielectric function and the screened Coulomb interaction  $W$ . The matrix elements of the self-energy are added as corrections to the LDA eigenvalues, and the effective potential is self-consistently updated. In spite of the simplified formalism of calculation, as compared to that of the full  $GW$  scheme, a good agreement with experiment for several materials has been obtained [41]. In this study we employed the quasiparticle self-consistent  $GW$  (QSGW) method [40,41]. Our main object of interest is the self-energy-corrected eigenvalue for band  $n$  and Bloch vector  $\mathbf{k}$ ,

$$E_{\mathbf{k}n} = \epsilon_{\mathbf{k}n} + Z_{\mathbf{k}n} \Delta \Sigma_{\mathbf{k}n}, \quad (1)$$

where the operator  $\Delta \Sigma_{\mathbf{k}n} = \langle \Psi_{\mathbf{k}n} | \Sigma(\mathbf{r}, \mathbf{r}', \epsilon_{\mathbf{k}n}) - V_{xc}(\mathbf{r}) | \Psi_{\mathbf{k}n} \rangle$ . The self-energy is given in terms of the Green’s function and the screened Coulomb interaction  $W$ :  $\Sigma(\mathbf{r}, \mathbf{r}', \omega) = \frac{i}{2\pi} \int d\omega' G(\mathbf{r}, \mathbf{r}', \omega - \omega') W(\mathbf{r}, \mathbf{r}', \omega') e^{-\delta\omega'}$ . From the slope of the real part one can obtain the renormalization factor

$$Z_{\mathbf{k}n} = \left[ 1 - \frac{\partial \text{Re} \Sigma_{\mathbf{k}n}(\omega)}{\partial \omega} \right]^{-1}. \quad (2)$$

In a direct comparison with the LDA+DMFT results,  $GW$  calculations reveal if significant nonlocal correlation effects occur in Pd.

### C. Technical details

The LDA+DMFT calculations were done using the FPLMTO code RSPT [37] as a base for the underlying density functional theory calculations. The RSPT calculations were based on the local-density approximation with the parametrization of Perdew and Wang [49] for the exchange-correlation functional. Three kinetic energy tails were used, with corresponding energies 0.3,  $-2.3$ , and  $-1.5$  Ry. Palladium is a face-centered-cubic metal, and the  $\mathbf{k}$ -mesh we used had the size  $16 \times 16 \times 16$  for the equations of state,  $24 \times 24 \times 24$  for the other calculations, and Fermi-Dirac smearing with  $T = 400$  K (the same temperature as was used for the imaginary-frequency Matsubara mesh). The muffin-tin radius was set to 2.45 Bohr atomic units (a.u.) and was kept constant throughout all unit-cell volumes. For the charge density and potential angular decomposition, inside the muffin-tin spheres, a maximum angular momentum  $l_{\max} = 8$  was set. The calculations included spin-orbit coupling

and scalar-relativistic terms within the muffin-tin spheres, unless otherwise noted. The SPTFLEX impurity solver was implemented in the Matsubara domain, and we used 2048 imaginary frequencies and an electronic temperature of 400 K. The analytic continuations of the self-energy from imaginary frequencies to the real energy axis in the complex plane were performed by Padé approximants [50].

The QSGW scheme used in this study is implemented into the LMSuite package [40,41], which is based on the full-potential linear muffin-tin orbitals code by M. Methfessel *et al.* [51]. The muffin-tin radius was chosen to be 2.63 a.u., and the integration of the Brillouin zone (BZ) was mapped with  $24 \times 24 \times 24$   $\mathbf{k}$ -points. For the  $GW$  calculation, we reduced the  $\mathbf{k}$ -points to  $6 \times 6 \times 6$  [41]. A double- $\kappa$  basis set with  $l_{\max} = 4$  was used, including the semicore  $4p$  states with local orbitals. This basis set allows for an accurate description of the high-lying conduction-band states. Spin-orbit coupling was included within the muffin-tin spheres.

We point out that both the RSPT and the QSGW methods employ the full-potential linearized muffin-tin orbital basis set, but using different implementations. As can be seen in Sec. III D, this causes no major differences between the RSPT and the QSGW LDA results.

## III. RESULTS AND DISCUSSION

### A. Equation of state

We begin our study by showing that LDA+DMFT can accurately determine the equilibrium lattice constant and bulk modulus, the two most important ground-state properties. The Coulomb and exchange parameters  $U$  and  $J$  used in the DMFT calculations are considered adjustable parameters in this study. In principle, they can be calculated from first principles too [52]. In this section we adjust the  $U$  and  $J$  values such that the calculated equation of state (EOS) energy-volume curve reproduces the experimental lattice constant (see Table I for a collection of experimental lattice constants from the literature).

In Fig. 1 (top), EOS curves for different values of  $U$  and  $J$  are presented. The experimental volume has been marked out. The equilibrium volume  $V_0$  and bulk modulus  $B_0$  for each of the curves can be seen in Table II. One

TABLE I. Experimental lattice constants  $a$  (and equivalent unit-cell volume) of palladium from various sources, as a function of temperature.

$T$ (K)	$a$ (Å)	$a$ (a.u.)	Volume (a.u. <sup>3</sup> )	Ref.
853	3.9184	7.4047	101.50	[53]
673	3.9088	7.3866	100.76	[53]
297	3.9049	7.3792	100.45	[54]
296	3.8904	7.3518	99.34	[53]
296	3.8902	7.3514	99.32	[53]
120	3.8830	7.3378	98.77	[53]
23	3.8907	7.3524	99.36	[54]
0 <sup>a</sup>	3.881	7.334	98.62	[55]
0 <sup>b</sup>	3.877	7.326	98.32	[55]

<sup>a</sup>Estimated from room temperature using linear thermal expansion coefficient; see Ref. [55].

<sup>b</sup>Corrected for zero-point anharmonic expansion; see Ref. [55].

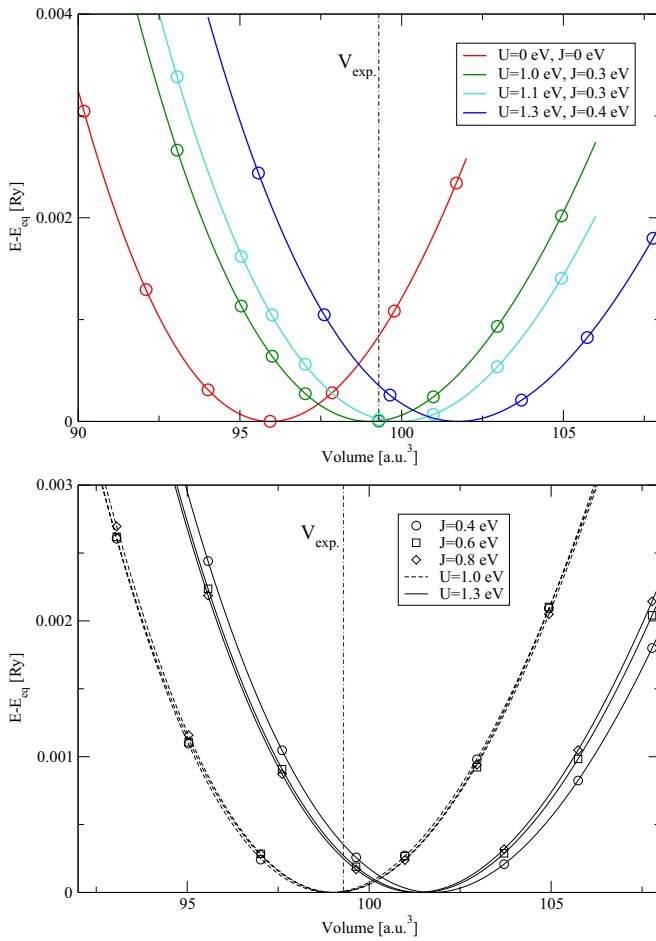


FIG. 1. Equation of state curves. Top: Effect of increasing  $U$ . LDA (red) compared to  $U = 1.0$  eV,  $J = 0.3$  eV (green);  $U = 1.1$  eV,  $J = 0.3$  eV (turquoise); and  $U = 1.3$  eV,  $J = 0.4$  eV (blue). Bottom: Effect of altering  $J$  while keeping  $U$  fixed, for  $U = 1.0$  eV (dashed line) and  $U = 1.3$  eV (solid line).

TABLE II. Equilibrium volumes  $V_0$  and bulk moduli  $B_0$  extracted from equation-of-state fitting function (Birch-Murnaghan), for different sets of  $U$  and  $J$  parameters. The experimental volume  $99.3$  a.u.<sup>3</sup> is taken from the room-temperature data of Ref. [53], which differs from the  $T = 0$  K data by  $<1\%$ . The experimental bulk modulus is  $189$  GPa [56].

$U$ (eV)	$J$ (eV)	$V_0$ (a.u. <sup>3</sup> )	$B_0$ (GPa)
0	0	95.94	226.6
1.0	0.3	99.02	190.6
	0.4	98.92	192.2
	0.6	99.03	192.2
	0.8	99.05	193.2
1.1	0.3	99.92	181.7
1.3	0.4	101.74	167.7
	0.6	101.42	171.9
	0.8	101.31	174.7
	3.0	0.3	127.91
	0.9	124.07	124.2

observes (Fig. 1, top) that  $U = J = 0$  eV (red curve), i.e., the LDA, underestimates the volume, which is commonly known. The generalized gradient approximation (GGA) to the exchange-correlation potential, as pointed out for Pd in Ref. [57] (data not shown here), overestimates the lattice constant and leads to a ferromagnetic ground state and is therefore unsuitable. As the value of  $U$  is increased, the computed lattice constant approaches the experimental value from below. For  $U = 1.0$  eV the calculated  $V_0$  and  $B_0$  for different exchange parameters  $J$  are given in Table II, and the values are closer to experiment than the LDA value. The effect of varying the exchange parameter  $J$  on the EOS can be observed in Fig. 1 (bottom, dashed lines). The equilibrium volumes are tabulated in Table II and give a standard deviation of  $0.05$  a.u.<sup>3</sup>, which is of the same order as the scattering in the data for room temperature (see  $T = 296$  K in Table I). At  $U = 1.1$  eV and  $J = 0.3$  eV,  $V_0$  is overestimated compared to the experimental value, while  $B_0$  is underestimated. Increasing  $U$  to  $1.3$  eV leads to an even larger  $V_0$  and a smaller  $B_0$ . Varying  $J$  at this value of  $U$  gives a standard deviation of  $0.18$  a.u.<sup>3</sup>, which is an order of magnitude larger than the standard deviation at  $U = 1.0$  eV. The effect of exchange  $J$  on the volume is larger for  $U = 1.3$  eV than for  $U = 1.0$  eV, but it is still below the experimentally observed thermal expansion (see Table I). The increase of  $J$  (for a fixed  $U = 1.3$  eV) decreases the equilibrium volume, which is opposite to the trend given by increasing  $U$ . However, this is a small effect and not relevant to this study. By increasing  $U$  even further to  $3$  eV, the same trend of increasing  $V_0$  and decreasing  $B_0$  is maintained (see Table II).

Based on the results presented in this section,  $U = 1.0$  eV and  $J = 0.3$  eV can be taken as a reasonable choice to reproduce the lattice constant and bulk modulus in our LDA+DMFT calculations.

## B. Ferromagnetic instability

It is known that palladium is on the verge of ferromagnetism, having a large density of states at the Fermi level  $D(E_F)$  leading to a large static susceptibility. An early theory that tried to explain the magnetic transition in itinerant electron systems was the Stoner model. According to this model, a magnetic state is favored over a nonmagnetic state when the criterion  $D(E_F)I \geq 1$  is fulfilled, where  $I$  is the Stoner parameter [58]. This criterion points to the possibility of inducing magnetic order by increasing  $D(E_F)$ . In some cases, this can be achieved by reducing the effective dimensionality of the system. To create magnetic order, attempts have been made to lower the dimensionality of Pd systems, e.g., by creating nanoparticles and nanowires [59–61] or thin films [62]. There are also density functional theory studies that indicate that bulk palladium turns ferromagnetic as the volume is expanded [16,63–65].

In Fig. 2 the magnetic moment in units of  $\mu_B$  is plotted as a function of lattice constant. For the LDA, within the scalar-relativistic approximation (red curve), a magnetic onset is brought about at a lattice constant of  $7.65$  a.u. This is about  $4\%$  larger than the experimental lattice constant, which is in accordance with previous studies, where the magnetic onset varies between a  $1\%$  and  $6\%$  increase of the lattice constant.

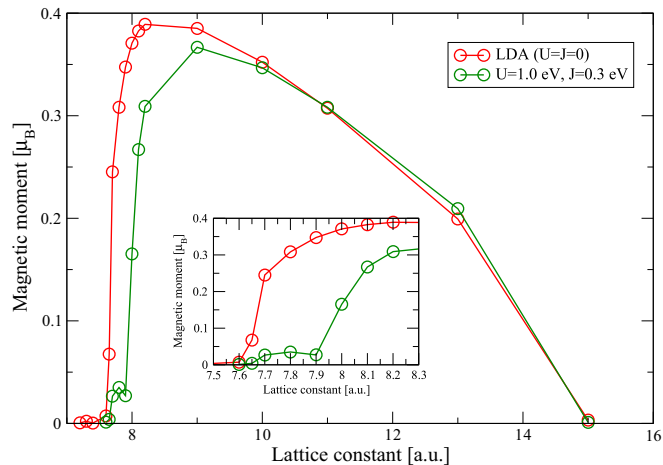


FIG. 2. Magnetic moment calculated as a function of volume, within the LDA (red circles) and within LDA+DMFT (green circles), for  $U = 1.0$  eV and  $J = 1.3$  eV. Relativistic effects were treated using the scalar-relativistic approximation.

Hong and Lee [65] point out that this variance could be due to the sensitivity of  $D(E_F)$  on the  $\mathbf{k}$ -point mesh and show that  $D(E_F)$  is difficult to fully converge even at dense mesh sizes. Note that the curve reaches a maximum (about  $0.4\mu_B$ ) and then decreases toward zero magnetic moment at large lattice constants. A full charge transfer to the  $d$  states has then been accomplished, leading to fully occupied  $d$  states with no net magnetic moment [16].

We next calculated the magnetic moment as a function of increasing lattice constant within the LDA+DMFT scheme, using the scalar-relativistic approximation, and setting  $U = 1.0$  eV and  $J = 0.3$  eV (Fig. 2, green curve). The magnetic transition is pushed further upwards in volume, compared to the scalar-relativistic LDA curve (red), giving a transition first into a “low-moment” and then into a “high-moment” state. We also note that the LDA+DMFT curve more or less coincides with the LDA curve at larger lattice constants. The system is then close to having a fully occupied  $d$  band, where correlation should have a negligible effect. Therefore, DMFT is able to capture some dynamical spin-fluctuation effects, and this could explain the suppression of the magnetic moment at those intermediate volumes, where the LDA still produces noticeable moments.

### C. Density of states and Fermi surface

#### 1. Spectral functions and the formation of satellite structure

The density of states (DOS) at the experimental lattice constant is presented in Fig. 3. Including electronic correlations, for increased values of the local Coulomb parameter  $U$ , in the higher-binding-energy region a satellite structure develops. We tuned  $J$  for fixed  $U$  and saw no significant change in DOS (not shown). Hence, the satellite position is mostly insensitive to the value of the exchange parameter  $J$ .

The quasiparticle weights  $Z = (1 - \partial \text{Re}[\Sigma(E)]/\partial E|_{E_F})^{-1}$  for the different  $U$ , shown in Fig. 3, are in the range  $Z = 0.975 - 0.916$  for  $U = 1 - 4$  eV. These correspond to effective mass ratios  $m^*/m_{\text{LDA}} = Z^{-1} = 1.03 - 1.09$ , where  $m_{\text{LDA}}$  is the LDA band mass. This should be compared

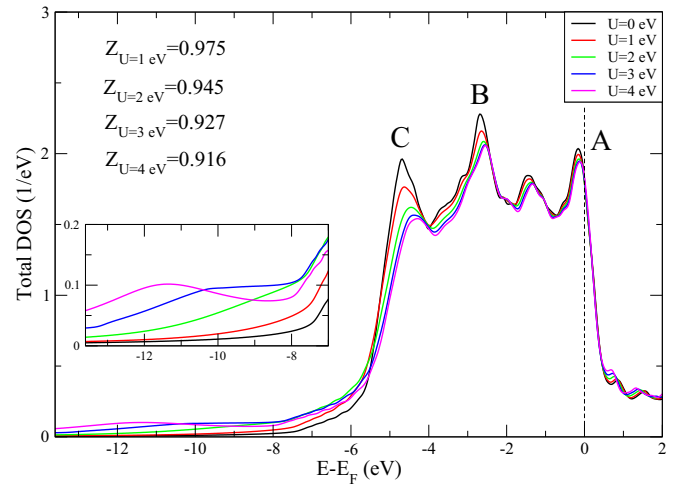


FIG. 3. Total density of states as a function of the Coulomb interaction  $U$ . Note that the peak closest to the Fermi level (marked by A) is pinned and that the lowest-lying peak (C) decreases in intensity while a satellite structure is formed for high binding energies (see inset). Corresponding quasiparticle weights  $Z = (1 - \partial \text{Re}[\Sigma(E)]/\partial E|_{E_F})^{-1}$  are given in the upper left corner.

with  $m_{\text{sp.heat}}^*/m_{\text{LDA}} = 1.66$ , where  $m_{\text{sp.heat}}^*$  is estimated from electronic specific heat measurements and  $m_{\text{LDA}}$  is taken from band-structure calculations [66,67], which is considerably larger than what we obtain in this study. It should be noted that the electron-phonon coupling  $\lambda_{e\text{-ph}}$  is not included in our self-energy, and previous theoretical studies have shown this quantity  $\lambda_{e\text{-ph}}$  to be in the range 0.35–0.41 [68,69]. Recent angle-resolved PES (ARPES) by Hayashi *et al.* [67] estimated the electron-phonon coupling to be  $\lambda_{e\text{-ph}} \approx 0.39$ , and the electron-electron and electron-paramagnon coupling to be  $\lambda_{e\text{-e}} + \lambda_{e\text{-para}} \approx 0.08$ , leading to an effective mass  $m_{\text{ARPES}}^*/m_{\text{LDA}} = 1 + \lambda_{\text{tot}} \approx 1.5$ . Using Hayashi *et al.*'s [67] value for  $\lambda_{e\text{-ph}}$ , together with our calculated self-energy, the effective mass is  $m^*/m_{\text{LDA}} = 1.42 - 1.48$ , for  $U = 1 - 4$  eV. This is in good agreement with Hayashi *et al.* [67], but still underestimates the value from specific heat measurements. It should be noted that our quasiparticle weights  $Z$  are averaged over the BZ, while Ref. [67] investigated specific paths in the BZ, being also a surface-sensitive study. The overall magnitude, however, is similar as this comparison shows.

Just below the Fermi level a dominant peak, with a relatively large value of the density of states, is situated with a maximum at about  $-0.15$  eV (marked by A) for all investigated  $U$  values. A second major peak (B) is situated in the middle of the valence band around  $-2.7$  eV at  $U = 0$  and is shifted to approximately  $-2.5$  eV as  $U$  is increased. The third major peak (C) is at the bottom of the  $d$  band near  $-4.7$  eV and is shifted towards  $-4.4$  eV as correlation is increased. The contributions of different bands to the peaks in the DOS can be inferred by studying the spectral function along high-symmetry lines in the BZ; see Fig. 4.

Concerning the high-energy binding region in the photoemission spectra, there exist discrepancies of the order of 0.5 eV between experiment and band-structure calculations, as pointed out by Kang *et al.* [70]. The LDA seems to overestimate the bandwidth of Pd as compared to the measured



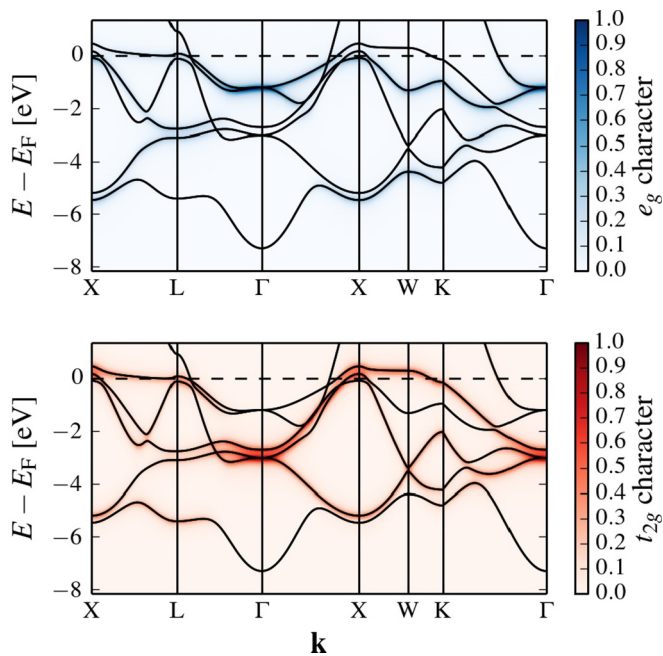


FIG. 4. LDA orbital-resolved spectral functions along high-symmetry lines in the BZ. Top:  $e_g$  symmetry. Bottom:  $t_{2g}$  symmetry.

PES bandwidth, and some experimental states are located closer to the Fermi level than the theoretical states [70–73]. It was proposed [70] that surface and correlation effects could modify the LDA band structure, explaining the discrepancies. It is not altogether clear how to separate these two effects from each other since both bulk and surface states will contribute to the PES, especially for low photon energies. Kang *et al.* [70] performed combined PES and LDA band-structure calculations for Pd, and their results indicate that the surface effects could indeed explain the bandwidth narrowing. However, they also ruled out many-body correlation effects since they found no trace of a satellite in the PES. The absence of the satellite might be caused by a missing  $4p$ - $4d$  photoabsorption threshold in Ref. [70], since the energy range (around 55 eV photon energy) does not seem to be investigated. The experimental photoemission studies in Refs. [17,18] scan this range and do indeed find a satellite. The  $4p$ - $4d$  photoabsorption process can be viewed as follows: A photon with energy at the  $4p$  core level will excite a core electron to the Fermi level. As the  $4p$  core hole is filled by a valence electron, the resulting valence hole will interact with the photoabsorbed electron and contribute to the satellite intensity. Note that the  $4p$ - $4d$  photoabsorption will affect the satellite intensity, but not its position [74]. The satellite position will be determined by the valence hole spectral function, which we access in our calculations. We cannot capture the contribution from the core levels on the spectra, and hence the satellite intensity which we obtain should not be directly compared with experiment. From comparison with Fig. 3 and the experimental satellite position 8.5 eV [17], the  $U$  value needed to reproduce the satellite position can be estimated to be between 2 and 3 eV. By including correlations we also get a shift of the B and C peaks to lower binding energy, in better agreement with experiment. The B peak position has been measured at  $-2.55$  eV [72],  $-2.4$  eV [18], and  $-2.5$  eV (estimated from

Ref. [70]), which indicates that the LDA positions this peak at too-high binding energy (about  $-2.7$  eV in this study) and that including correlations will improve the peak position in comparison with experiment. Here we emphasize that no attempt was made to model the surface states; instead only bulk calculations were performed. Note that matrix element effects were also not taken into account in this study.

As shown in Sec. III A  $U$  values above 1.0 eV overestimate the equilibrium lattice constant. Hence a different  $U$  value is required to match the experimental spectra than the one that reproduces the equilibrium volume. The same discrepancy was also encountered for Ni [38,75].

It is interesting to discuss the satellite formation in Pd, in comparison with Ni. The effect of electron correlations on energies of one-electron removal from a partially filled band is described in terms of interactions between three-body configurations, one hole plus one electron-hole pair, giving the rise to hole-hole and hole-electron scattering [19,20]. The effectiveness of these scattering processes depends not only on the strength of the screened on-site electron-electron interaction, but also on the occupation of orbitals involved in the scattering process. In particular on the number of empty  $d$  states, necessary for the creation of three-particle configurations, since no electron-hole pair can be added to a completely filled band, in the case of nickel where only the minority-spin band has a sizable number of empty states available, the creation of a majority-spin hole will be followed by scattering processes involving only opposite spin electron-hole pairs. The strength of the interaction for this channel is proportional to  $U$ , while the creation of a minority-spin hole will involve a scattering with parallel spin electron-hole pairs only of strength proportional to  $U - J$ . In Pd both spin channels are always symmetric (paramagnetic metal), while for Ni the exchange splitting redistributes holes in the  $d$  bands. Even for the reduced scattering amplitudes of electron-hole pairs, the  $T$ -matrix formalism generates a satellite structure, but due to the small satellite weight it is hardly discernible for valence-state spectroscopy.

## 2. Fermi surface

The Fermi surface of Pd was extensively studied within density functional theory formalism [66,76,77]. Here we present a detailed comparison of the Fermi surface obtained by different methods including correlation effects. In Fig. 5 (bottom left), we present a cut of the LDA Fermi surface in the  $k_x - k_y$  plane together with a projection of the three-dimensional Fermi surface sheets (Fig. 5, top left). The Fermi surface geometry contains the closed electron surface around the  $\Gamma$  point, and a set of hole ellipsoids at the  $X$  points. Open hole surfaces consists of cylinders, extending in the  $[100]$  and  $[010]$  directions (i.e., along the  $X$ - $W$ - $X$  paths) and intersecting in pairs at the symmetry points  $X$ ; see top right of Fig. 5. The open hole surfaces are particularly interesting as they are associated with the large effective masses and contribute substantially to the density of states near the Fermi level [77]. The Kohn anomaly [22], in the slope of the  $[\xi\xi 0]$  transverse acoustic branch of the Pd phonon dispersion, is attributed to Fermi surface nesting between these open hole cylinders (see Ref. [23] and references therein). Previous calculations also predicted the existence of small  $L$  pockets, which were

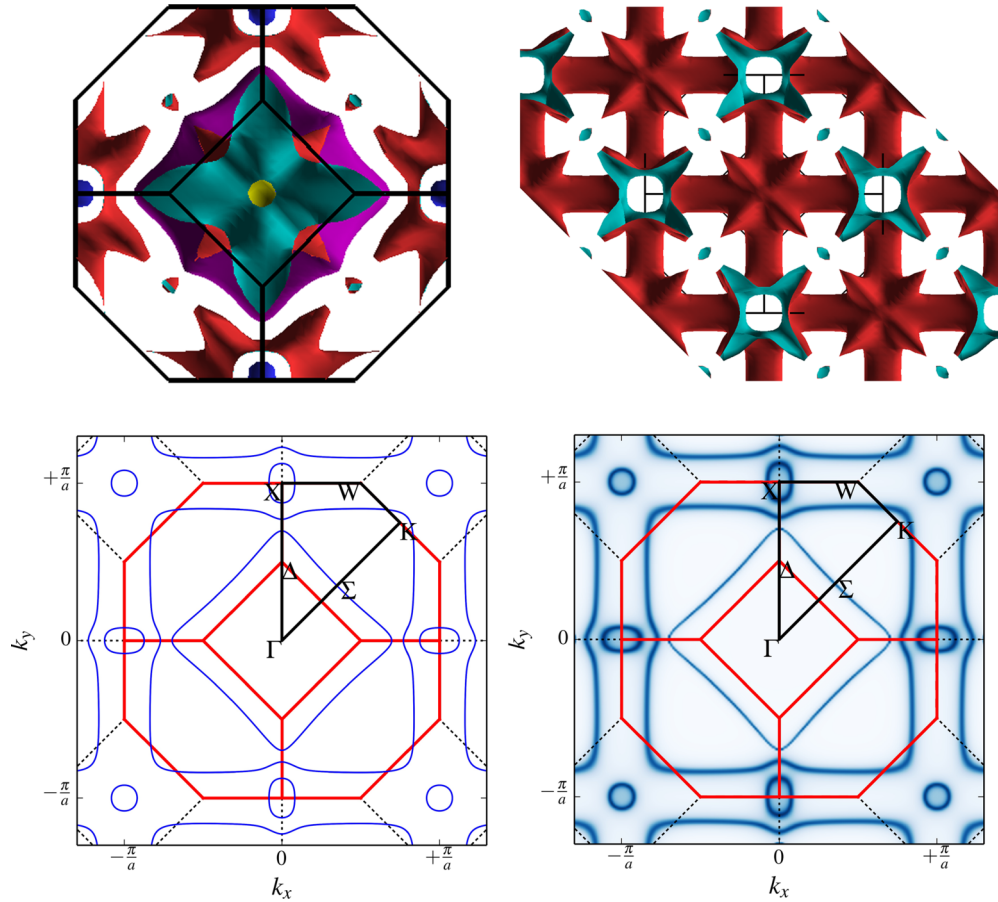


FIG. 5. Fermi surfaces. Top left: three-dimensional Fermi surface in the first BZ, projected on the  $k_x$ - $k_y$  plane. Note the  $X$  hole pockets centered at the square faces (blue, hole side; yellow, electron side), the  $L$  hole pockets centered at the hexagonal faces (red, hole side; turquoise, electron side), and the tube hole structures intersecting at the  $X$  points (red, hole side; turquoise, electron side). Also note that the  $L$  pockets only exist if spin-orbit terms are included. A large electron surface sheet is centered around the  $\Gamma$  point (purple). Top right: Hole tube structure as seen in the extended zone scheme. Bottom left: Cut at  $k_z = 0$  within the LDA. Bottom right: Cut at  $k_z = 0$  within the LDA+DMFT,  $U = 1.0$  eV and  $J = 0.3$  eV. The three-dimensional Fermi surface was created with the XCrysden software [78].

seen if spin-orbit coupling was taken into account [66,76]. These  $L$  pockets were later confirmed by magnetoacoustic measurements [79].

The orbital character of the Fermi surface sheets can be determined by investigation of the orbital-resolved spectral function; see Fig. 4. The tube structure (stemming mostly from the flat band between the  $W$  and the  $X$  symmetry points) has mostly  $t_{2g}$  character, which was pointed out already by Kanamori [80]. The Fermi surface obtained with LDA+DMFT is also presented in Fig. 5 (bottom right). There is no significant difference between the Fermi surfaces from LDA and LDA+DMFT. The diameters of the tube structures are only weakly affected. The Fermi-surface nesting vector, believed to be responsible for the Kohn anomaly in the phonon dispersion of Pd, is estimated to be  $\mathbf{q} = \frac{2\pi}{a}[0.30, 0.30, 0]$ , in close agreement with previous studies [23]. Therefore, the Kohn anomaly is already well captured at the level of the LDA [23].

#### D. Local and nonlocal correlation effects

In order to investigate the effect of nonlocal electron correlations on the electronic structure of Pd, calculations

employing the QSGW method were also performed. The band structure, the spectral functions, and the Fermi surfaces were calculated using the experimental volume.

In Fig. 6 (top left) the band structure along high-symmetry lines within the Brillouin zone is plotted. The bands within the LDA from RSPT (solid green lines) and from QSGW (dashed blue lines) coincide well. Turning on correlation effects, the bands are modified as compared to the LDA result. The QSGW (red dots) and the LDA+DMFT (blue energy scale) are nearly coinciding around the Fermi level, and differences are mainly visible at higher energies. Around the  $\Gamma$  point, for energies between  $-6$  eV and the Fermi level, the QSGW bands are shifted towards the Fermi level to a larger extent than the LDA+DMFT bands. For binding energies larger than 6 eV, the lowest band is shifted downwards in energy to a larger extent than the LDA+DMFT bands. The trends (upwards or downwards shifts in energy) are, however, the same for both methods, indicating that the  $U$  value used in LDA+DMFT ( $U = 1.0$  eV) is too small to reproduce the correct quasiparticle eigenvalue position. This was also found when LDA+DMFT spectral functions were compared with the experiment in Sec. III C.

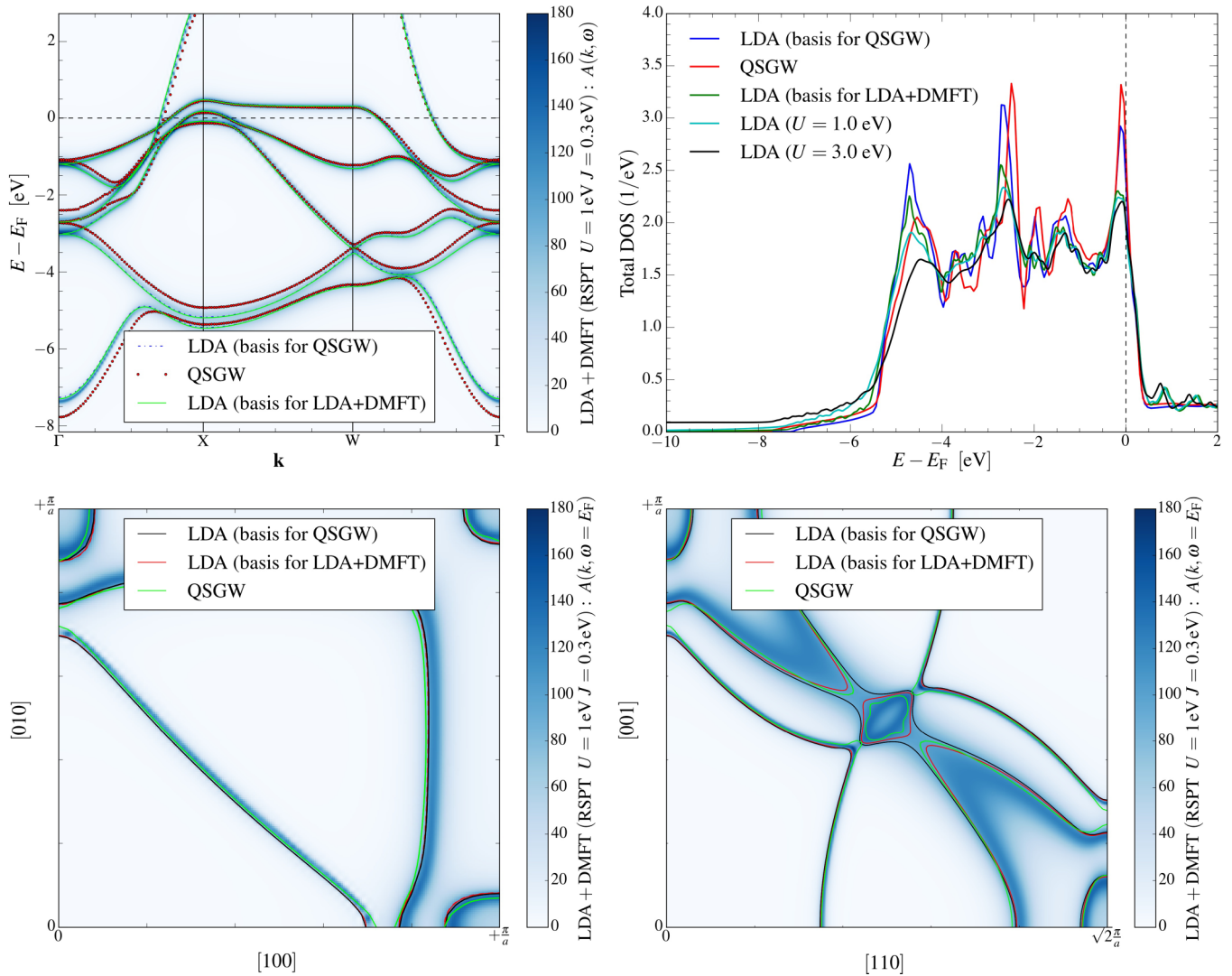


FIG. 6. Blue color map corresponds to LDA+DMFT,  $U = 1.0 \text{ eV}$ , and  $J = 0.3 \text{ eV}$ . Top left: Band structure along high-symmetry directions in the BZ. Top right: QSGW and LDA+DMFT DOS. Bottom left: Fermi surface cut in the  $k_x$ - $k_y$  plane. Bottom right: Fermi surface cut including the  $L$  point.

The density of states calculated within the QSGW method (red line) and within LDA (blue line) are also plotted in Fig. 6 (top right). The effect of correlations is most easily identified by inspecting the three main peaks in the DOS. In Fig. 6 (top right), we also show the LDA+DMFT  $\mathbf{k}$ -integrated spectral function. The spectral functions within LDA+DMFT are calculated along a horizontal complex contour at a distance  $\delta$  from the real axis, giving a broadening to the DOS. We performed LDA density of states calculations within RSPT along the real axis as well, and found excellent agreement with the LDA from QSGW (not shown). As correlations are turned on, similar trends in the three main peaks can be observed for the QSGW method as within the LDA+DMFT method. One main difference, however, is that LDA+DMFT can produce the high-energy satellite, while QSGW cannot. This can be attributed to the  $T$ -matrix ladder diagrams which are present in the LDA+DMFT self-energy, but not in the QSGW self-energy. There exist extensions of the  $GW$  formalism that allow for  $T$ -matrix diagrams (see Refs. [81,82]) that are not included in the present study.

The computed Fermi surface in a cut of the  $k_x$ - $k_y$  plane from both LDA+DMFT and QSGW is presented in Fig. 6 (bottom left). Both methods change the Fermi surface slightly. The topology of the sheets is unchanged, but the  $\mathbf{k}$ -space volume enclosed by the sheets shows some effect of correlations. The largest changes can be seen in the tube structure running along the  $X$ - $W$ - $X$  symmetry directions. In the case of LDA+DMFT (blue intensity scale) the tube radius is slightly reduced, while for QSGW (green line) the radius is slightly increased. A different cut in the BZ, including the  $L$  pocket, is shown in Fig. 6 (bottom right). QSGW and LDA+DMFT display similar trends in the change of the Fermi surface, mainly the beginning of a “neck” formation in the  $\Gamma$ - $L$  direction and a decreasing of the  $L$ -pocket diameter. Note that within the LDA solution used as a starting point for the QSGW, the  $L$  pocket and the “tongue” feature are connected along the  $X$ - $L$ - $X$  direction. We found by explicit calculation that this was attributed to the use of the tetrahedron  $\mathbf{k}$ -point integration method, which pushes the hole sheet slightly upwards in energy, creating the connection.

To conclude this section, we note that nonlocal effects captured by the QSGW method on the spectral functions come close to our LDA+DMFT data.

#### IV. CONCLUSION

Electron correlations are commonly assumed to affect the electronic structure of the  $3d$  elements to a larger degree than in the  $4d$  elements due, in part, to the difference in  $d$ -state bandwidth. By electronic structure calculations within a LDA+DMFT context, we could show that, even though the LDA can provide a reasonable description of the electronic structure of Pd, correlation effects give important contributions to ground-state and spectral properties. We could improve the equilibrium lattice constant and bulk modulus from that of the LDA, and on expansion of the lattice constant Pd was shown to be ferromagnetic with a magnetic moment suppressed by spin fluctuations. The spectral function calculated with LDA+DMFT supported a formation of a satellite in the high-energy binding region while at the same time improving the band positions in comparison with experiment. The spectral function and the Fermi surface showed no major difference between the LDA+DMFT and QSGW method, and in particular the nesting vector in the  $[\xi\xi 0]$  direction was only slightly changed from its LDA value.

We found that the different Coulomb interaction parameters are required in order to reproduce the experimental equilibrium lattice constant on the one hand and the PES satellite on the other hand. The obtained values, however, fall in the range 1.5–4 eV of the recent constraint RPA calculations of Ref. [52], where different degrees of screening are considered. A possible origin of the observed discrepancies might lie in the ignored nonlocal correlations or the frequency dependence of  $U$  [52,83].

Within the present LDA+DMFT calculations the spin-fluctuation effects were shown to influence the volume at which the magnetic transition occurs, pushing it to a higher value than the LDA one. These results suggests that spin fluctuations could be important also for the case of low-dimensional systems, like surfaces, nanoparticles, or epitaxial thin films of Pd.

Our study confirms the band narrowing and favors the satellite formation picture reported in some experimental studies of Pd [17]. Previously, the difference between the

PES and band-structure calculations has been attributed to surface effects [70], but our results indicate that correlations should be also taken into account. This goes along with the empirical arguments presented in the earlier studies [18,21]. The LDA+DMFT method should be able to probe the effect of correlations on the PES on an *ab initio* level, and further studies in conjunction with bulk and surface-sensitive PES should hopefully make it possible to disentangle surface and correlation effects from each other.

By performing *GW* calculations in combination with DMFT, the so-called *GW+DMFT* schema [83], nonlocal correlations and spin fluctuation can be captured on an equal footing, which turns out to be the next essential step for the realistic description of the physical properties of palladium. Particularly interesting in this context would be momentum-dependent susceptibilities that correctly address paramagnon physics, recently observed in the experimental studies of palladium [84].

#### ACKNOWLEDGMENTS

We gratefully acknowledge financial support from the Deutsche Forschungsgemeinschaft through the Research Unit FOR 1346. I.D.M. and W.S. acknowledge financial support from the Swedish Research Council (VR), the Swedish strategic research programme eSSSENCE, and the Knut and Alice Wallenberg foundation (KAW, Grants No. 2013.0020 and No. 2012.0031). M.R. also acknowledges support by the Ministry of Education, Science, and Technological Development of the Republic of Serbia under Projects No. ON171017 and No. III45018. M.S. acknowledges support by the Rustaveli National Science Foundation through Grant No. FR/265/6-100/14. L.V. acknowledges financial support from the Swedish Research Council and the Hungarian Scientific Research Fund (Research Projects OTKA No. 84078 and No. 109570). A.Ö. is also thankful for the financial support from the foundation of Axel Hultgren and from the Swedish Steel Producer's Association (Jernkontoret). We acknowledge computational resources provided by the Swedish National Infrastructure for Computing (SNIC) at the National Supercomputer Centre (NSC) in Linköping, Sweden.

- 
- [1] W. Metzner and D. Vollhardt, *Phys. Rev. Lett.* **62**, 324 (1989).
  - [2] A. Georges, G. Kotliar, W. Krauth, and M. J. Rozenberg, *Rev. Mod. Phys.* **68**, 13 (1996).
  - [3] G. Kotliar and D. Vollhardt, *Phys. Today* **57**, 53 (2004).
  - [4] G. Kotliar, S. Y. Savrasov, K. Haule, V. S. Oudovenko, O. Parcollet, and C. A. Marianetti, *Rev. Mod. Phys.* **78**, 865 (2006).
  - [5] K. Held, *Adv. Phys.* **56**, 829 (2007).
  - [6] J. Minar, H. Ebert, C. DeNadai, N. B. Brookes, F. Venturini, G. Ghiringhelli, L. Chioncel, M. I. Katsnelson, and A. I. Lichtenstein, *Phys. Rev. Lett.* **95**, 166401 (2005).
  - [7] J. Minar, *J. Phys.: Condens. Matter* **23**, 253201 (2011).
  - [8] P. Aebi, T. J. Kreutz, J. Osterwalder, R. Fasel, P. Schwaller, and L. Schlapbach, *Phys. Rev. Lett.* **76**, 1150 (1996).
  - [9] C. M. Schneider, U. Pracht, W. Kuch, A. Chassé, and J. Kirschner, *Phys. Rev. B* **54**, R15618 (1996).
  - [10] J. Braun, J. Minár, H. Ebert, A. Chainani, J. Miyawaki, Y. Takata, M. Taguchi, M. Oura, and S. Shin, *Phys. Rev. B* **85**, 165105 (2012).
  - [11] J. Sánchez-Barriga, J. Braun, J. Minár, I. Di Marco, A. Varykhalov, O. Rader, V. Boni, V. Bellini, F. Manghi, H. Ebert *et al.*, *Phys. Rev. B* **85**, 205109 (2012).
  - [12] A. I. Lichtenstein, M. I. Katsnelson, and G. Kotliar, *Phys. Rev. Lett.* **87**, 067205 (2001).

- [13] F. J. Himpsel, J. A. Knapp, and D. E. Eastman, *Phys. Rev. B* **19**, 2919 (1979).
- [14] A. Grechnev, I. Di Marco, M. I. Katsnelson, A. I. Lichtenstein, J. Wills, and O. Eriksson, *Phys. Rev. B* **76**, 035107 (2007).
- [15] G. Chouteau, R. Fourneaux, K. Gobrecht, and R. Tournier, *Phys. Rev. Lett.* **20**, 193 (1968).
- [16] V. L. Moruzzi and P. M. Marcus, *Phys. Rev. B* **39**, 471 (1989).
- [17] D. Chandesris, G. Krill, G. Maire, J. Lecante, and Y. Petroff, *Solid State Commun.* **37**, 187 (1981).
- [18] P. O. Nilsson, C. G. Larsson, and W. Eberhardt, *Phys. Rev. B* **24**, 1739 (1981).
- [19] A. Liebsch, *Phys. Rev. Lett.* **43**, 1431 (1979).
- [20] A. Liebsch, *Phys. Rev. B* **23**, 5203 (1981).
- [21] N. Maartensson and B. Johansson, *Phys. Rev. Lett.* **45**, 482 (1980).
- [22] W. Kohn, *Phys. Rev. Lett.* **2**, 393 (1959).
- [23] D. A. Stewart, *New J. Phys.* **10**, 043025 (2008).
- [24] Z.-L. Liu, J.-H. Yang, L.-C. Cai, F.-Q. Jing, and D. Alfè, *Phys. Rev. B* **83**, 144113 (2011).
- [25] T. Y. Hsiang, J. W. Reister, H. Weinstock, G. W. Crabtree, and J. J. Vuillemin, *Phys. Rev. Lett.* **47**, 523 (1981).
- [26] S. Doniach and S. Engelsberg, *Phys. Rev. Lett.* **17**, 750 (1966).
- [27] N. F. Berk and J. R. Schrieffer, *Phys. Rev. Lett.* **17**, 433 (1966).
- [28] M. T. Béal-Monod, S.-K. Ma, and D. R. Fredkin, *Phys. Rev. Lett.* **20**, 929 (1968).
- [29] M. T. Béal-Monod and J. M. Lawrence, *Phys. Rev. B* **21**, 5400 (1980).
- [30] W. Joss, L. N. Hall, G. W. Crabtree, and J. J. Vuillemin, *Phys. Rev. B* **30**, 5637 (1984).
- [31] W. Joss and G. W. Crabtree, *Phys. Rev. B* **30**, 5646 (1984).
- [32] W. F. Brinkman and S. Engelsberg, *Phys. Rev.* **169**, 417 (1968).
- [33] P. Hertel, J. Appel, and D. Fay, *Phys. Rev. B* **22**, 534 (1980).
- [34] T. Moriya, *Spin Fluctuations in Itinerant Electron Magnetism* (Springer, Berlin, 1985).
- [35] P. Larson, I. I. Mazin, and D. J. Singh, *Phys. Rev. B* **69**, 064429 (2004).
- [36] L. Hedin, *Phys. Rev.* **139**, A796 (1965).
- [37] J. M. Wills, M. Alouani, P. Andersson, A. Delin, O. Eriksson, and O. Grechnev, *Full-Potential Electronic Structure Method* (Springer-Verlag, Berlin, 2010).
- [38] I. Di Marco, J. Minár, S. Chadov, M. I. Katsnelson, H. Ebert, and A. I. Lichtenstein, *Phys. Rev. B* **79**, 115111 (2009).
- [39] O. Granas, I. di Marco, P. Thunström, L. Nordström, O. Eriksson, T. Björkman, and J. Wills, *Comput. Mater. Sci.* **55**, 295 (2012).
- [40] M. van Schilfhaarde, T. Kotani, and S. Faleev, *Phys. Rev. Lett.* **96**, 226402 (2006).
- [41] T. Kotani, M. van Schilfhaarde, and S. V. Faleev, *Phys. Rev. B* **76**, 165106 (2007).
- [42] M. Imada, A. Fujimori, and Y. Tokura, *Rev. Mod. Phys.* **70**, 1039 (1998).
- [43] A. G. Petukhov, I. I. Mazin, L. Chioncel, and A. I. Lichtenstein, *Phys. Rev. B* **67**, 153106 (2003).
- [44] N. E. Bickers and D. J. Scalapino, *Ann. Phys. (N.Y.)* **193**, 206 (1989).
- [45] A. I. Lichtenstein and M. I. Katsnelson, *Phys. Rev. B* **57**, 6884 (1998).
- [46] M. I. Katsnelson and A. I. Lichtenstein, *J. Phys.: Condens. Matter* **11**, 1037 (1999).
- [47] L. V. Pourovskii, M. I. Katsnelson, and A. I. Lichtenstein, *Phys. Rev. B* **72**, 115106 (2005).
- [48] V. Drchal, V. Janis, J. Kudrnovsky, V. S. Oudovenko, X. Dai, K. Haule, and G. Kotliar, *J. Phys.: Condens. Matter* **17**, 61 (2005).
- [49] J. P. Perdew and Y. Wang, *Phys. Rev. B* **45**, 13244 (1992).
- [50] H. J. Vidberg and J. W. Serene, *J. Low Temp. Phys.* **29**, 179 (1977).
- [51] M. Methfessel, M. van Schilfhaarde, and R. A. Casali, in *Electronic Structure and Physical Properties of Solids: The Uses of the LMTO Method*, edited by H. Dreyse (Springer-Verlag, Berlin, 2000).
- [52] E. Şaşıoğlu, C. Friedrich, and S. Blügel, *Phys. Rev. B* **83**, 121101 (2011).
- [53] A. P. Miiller and B. N. Brockhouse, *Can. J. Phys.* **49**, 704 (1971).
- [54] C. N. Rao and K. K. Rao, *Can. J. Phys.* **42**, 1336 (1964).
- [55] V. N. Staroverov, G. E. Scuseria, J. Tao, and J. P. Perdew, *Phys. Rev. B* **69**, 075102 (2004).
- [56] D. A. Young, *Phase Diagrams of the Elements* (University of California Press, Berkeley, CA, 1991).
- [57] S. S. Alexandre, M. Mattesini, J. M. Soler, and F. Yndurain, *Phys. Rev. Lett.* **96**, 079701 (2006).
- [58] P. Mohn, *Magnetism in the Solid State* (Springer-Verlag, Berlin, 2002).
- [59] B. Sampedro, P. Crespo, A. Hernando, R. Litrán, J. C. Sánchez López, C. López Cartes, A. Fernandez, J. Ramírez, J. González Calbet, and M. Vallet, *Phys. Rev. Lett.* **91**, 237203 (2003).
- [60] A. Delin, E. Tosatti, and R. Weht, *Phys. Rev. Lett.* **92**, 057201 (2004).
- [61] L. Vitos, B. Johansson, and J. Kollár, *Phys. Rev. B* **62**, R11957 (2000).
- [62] S. Sakuragi, T. Sakai, S. Urata, S. Aihara, A. Shinto, H. Kageshima, M. Sawada, H. Namatame, M. Taniguchi, and T. Sato, *Phys. Rev. B* **90**, 054411 (2014).
- [63] L. Fritsche, J. Noffke, and H. Eckardt, *J. Phys. F: Met. Phys.* **17**, 943 (1987).
- [64] H. Chen, N. E. Brener, and J. Callaway, *Phys. Rev. B* **40**, 1443 (1989).
- [65] S. C. Hong and J. I. Lee, *J. Korean Phys. Soc.* **52**, 1099 (2008).
- [66] O. K. Andersen, *Phys. Rev. B* **2**, 883 (1970).
- [67] H. Hayashi, K. Shimada, J. Jiang, H. Iwasawa, Y. Aiura, T. Oguchi, H. Namatame, and M. Taniguchi, *Phys. Rev. B* **87**, 035140 (2013).
- [68] S. Y. Savrasov and D. Y. Savrasov, *Phys. Rev. B* **54**, 16487 (1996).
- [69] F. J. Pinski, P. B. Allen, and W. H. Butler, *Phys. Rev. Lett.* **41**, 431 (1978).
- [70] J.-S. Kang, D. W. Hwang, C. G. Olson, S. J. Youn, K.-C. Kang, and B. I. Min, *Phys. Rev. B* **56**, 10605 (1997).
- [71] D. R. Lloyd, C. M. Quinn, and N. V. Richardson, *Surf. Sci.* **63**, 174 (1977).
- [72] F. J. Himpsel and D. E. Eastman, *Phys. Rev. B* **18**, 5236 (1978).
- [73] K. Yagi, K. Higashiyama, S. Yamazaki, H. Yanashima, H. Ohnuki, H. Fukutani, and H. Kato, *Surf. Sci.* **231**, 397 (1990).
- [74] S. Hüfner, *Photoelectron Spectroscopy, Principles and Applications* (Springer-Verlag, Berlin, 2003).
- [75] M. I. Katsnelson and A. I. Lichtenstein, *Eur. Phys. J. B* **30**, 9 (2002).
- [76] F. M. Mueller, A. J. Freeman, J. O. Dimmock, and A. M. Furdyna, *Phys. Rev. B* **1**, 4617 (1970).
- [77] D. H. Dye, S. A. Campbell, G. W. Crabtree, J. B. Ketterson, N. B. Sandesara, and J. J. Vuillemin, *Phys. Rev. B* **23**, 462 (1981).

- [78] A. Kokalj, *Comput. Mater. Sci.* **28**, 155 (2003).
- [79] C. R. Brown, J. P. Kalejs, F. D. Manchester, and J. M. Perz, *Phys. Rev. B* **6**, 4458 (1972).
- [80] J. Kanamori, *Prog. Theor. Phys.* **30**, 275 (1963).
- [81] V. P. Zhukov, E. V. Chulkov, and P. M. Echenique, *Phys. Rev. B* **72**, 155109 (2005).
- [82] P. Romaniello, F. Bechstedt, and L. Reining, *Phys. Rev. B* **85**, 155131 (2012).
- [83] P. Werner, M. Casula, T. Miyake, F. Aryasetiawan, A. J. Millis, and S. Biermann, *Nat. Phys.* **8**, 331 (2012).
- [84] R. Double, S. M. Hayden, P. Dai, H. A. Mook, J. R. Thompson, and C. D. Frost, *Phys. Rev. Lett.* **105**, 027207 (2010).

**Transmission through correlated  $\text{Cu}_n\text{CoCu}_n$  heterostructures**L. Chioncel,<sup>1,2</sup> C. Morari,<sup>3</sup> A. Östlin,<sup>4</sup> W. H. Appelt,<sup>1,2</sup> A. Droghetti,<sup>5</sup> M. M. Radonjić,<sup>2,6</sup> I. Rungger,<sup>7,\*</sup> L. Vitos,<sup>4</sup> U. Eckern,<sup>8</sup> and A. V. Postnikov<sup>9</sup><sup>1</sup>*Augsburg Center for Innovative Technologies, University of Augsburg, 86135 Augsburg, Germany*<sup>2</sup>*Theoretical Physics III, Center for Electronic Correlations and Magnetism, Institute of Physics, University of Augsburg, 86135 Augsburg, Germany*<sup>3</sup>*National Institute for Research and Development of Isotopic and Molecular Technologies, 65-103 Donath, 400293 Cluj Napoca, Romania*<sup>4</sup>*Department of Materials Science and Engineering, Applied Materials Physics, KTH Royal Institute of Technology, Stockholm 100 44, Sweden*<sup>5</sup>*Nano-Bio Spectroscopy Group and European Theoretical Spectroscopy Facility (ETSF), Universidad del Pais Vasco CFM CSIC-UPV/EHU-MPC and DIPC, Avenida Tolosa 72, 20018 San Sebastian, Spain*<sup>6</sup>*Scientific Computing Laboratory, Institute of Physics Belgrade, University of Belgrade, Pregrevica 118, 11080 Belgrade, Serbia*<sup>7</sup>*School of Physics and CRANN, Trinity College, Dublin 2, Ireland*<sup>8</sup>*Theoretical Physics II, Institute of Physics, University of Augsburg, 86135 Augsburg, Germany*<sup>9</sup>*LCP-A2MC, Institute Jean Barriol, University of Lorraine, 1 Boulevard Arago, 57078 Metz, France*

(Received 22 April 2015; published 24 August 2015)

We propose a method to compute the transmission through correlated heterostructures by combining density functional and many-body dynamical mean field theories. The heart of this combination consists in porting the many-body self-energy from an all electron basis into a pseudopotential localized atomic basis set. Using this combination we study the effects of local electronic interactions and finite temperatures on the transmission across the  $\text{Cu}_4\text{CoCu}_4$  metallic heterostructure. It is shown that as the electronic correlations are taken into account via a local but dynamic self-energy, the total transmission at the Fermi level gets reduced (predominantly in the minority-spin channel), whereby the spin polarization of the transmission increases. The latter is due to a more significant  $d$ -electron contribution, as compared to the noncorrelated case in which the transport is dominated by  $s$  and  $p$  electrons.

DOI: [10.1103/PhysRevB.92.054431](https://doi.org/10.1103/PhysRevB.92.054431)

PACS number(s): 75.10.-b

**I. INTRODUCTION**

The design of multilayered heterostructures composed of alternating magnetic and nonmagnetic metals offers large flexibility in tailoring spin-sensitive electron transport properties of devices in which the current flow is perpendicular to the planes. In the framework of ballistic transport, the spin-polarized conductance and the giant magnetoresistance effect (GMR) depend on the mismatch between the electronic bands of the concerned metals near the Fermi level [1,2]. In order to maximize the spin polarization of current and hence the GMR, heterostructures including half-metallic materials [3–5] seem to be the materials of choice. In practice, however, the spin polarization is never complete due to the presence of defects, and/or due to intrinsic limitations caused by spin contamination and spin-orbit coupling [5]. Owing to the technological relevance, considerable progress has been achieved in the computational description of multilayered heterostructures. In particular, the ballistic transport properties have been addressed by considering the Landauer-Büttiker formalism [6–9], where the conductance is determined by the electron transmission probability through the device region, which is placed between two semi-infinite electrodes. The transmission probability can be then computed with different electronic structure approaches, such as the tight-binding [10–13] or the first-principles density functional theory (DFT) ones [14–16]. Various implementations exist, based on transfer matrix

[17,18], layer-Korringa-Kohn-Rostoker (KKR) [19,20], or nonequilibrium Green's function (NEGF) [21] techniques.

In the context of first-principles calculations, it is known that, for systems with moderate to strong electron correlations, the electronic structure, calculated with the “conventional” DFT local density approximation (LDA) or its generalized gradient approximation (GGA) extension, is not accurate enough to account for the observed spectroscopic behavior. A more adequate description is provided within the dynamical mean field theory (DMFT) [22–24] built on the LDA framework [25–27]. Since many interesting magnetic materials fall into this category, the prediction of their electron transport properties, obtained by combining the Landauer-Büttiker formalism with DFT [21,28,29], is expected to equally suffer from an insufficient treatment of correlation effects, which would be captured by adding DMFT. However, the full incorporation of correlation effects at the DMFT level into the transport calculations is not straightforward, not only because of technical reasons, such as large system size and lack of corresponding algorithms, but also because of conceptual difficulties in the development of many-body solvers in the out-of-equilibrium regime [30]. Attempts to close this gap include the use of combined techniques, in which equilibrium-DMFT calculations are performed in order to obtain the Landauer conductance of atomic contacts made of transition metals [31,32], or model calculations [33,34].

Here we propose a two-step approach, in which the Landauer transmission probability is calculated within the SMEAGOL NEGF electron transport code [21,28,29], whereby the Hamiltonian is obtained from DFT [35]. The many-body corrections to the Green's function are evaluated using DMFT

\*Present address: National Physical Laboratory, Hampton Road, TW11 0LW, United Kingdom.

in an exact muffin-tin orbitals (EMTO) based package [36–38], which uses a screened KKR approach [39]. These corrections are then passed to SMEAGOL for the calculation of the transport properties.

This method is applied to investigate the linear-response transport through a prototypical Cu-Co-Cu heterostructure, thus accounting for strong electron correlation effects in the Co monolayer. The attention to this system is drawn by a significant density of states that develops in the Co layer in the vicinity of the Fermi level in one spin channel only (the minority-spin one), whereas the Cu layers contribute with states at higher binding energies only.

The article is organized as follows. We start with a general description of the transport problem in the presence of electronic correlations (Sec. II A). Then the computational details are outlined in Sec. II B, and the geometry of the system considered in our simulations is described in Sec. II C. Finally, Sec. III presents the main results, and Sec. IV summarizes and concludes. The appendices deal with the technical implementation and various tests.

## II. METHODS

### A. Transport properties in the presence of electronic correlations

The electronic transport through a device can be addressed using the Kubo approach, where the central quantity is the conductivity, and the electrical current is the result of the linear response of the system to an applied electric field [40]. Alternatively, in the Landauer-Büttiker formulation [6–9], the current flow through a device is considered as a transmission process across a finite-sized scattering region placed between two semi-infinite leads, connected at infinity to charge reservoirs. The quantity of interest is the conductance, which, within linear response, is given by

$$\mathcal{G} = \frac{e^2}{h} \frac{1}{\Omega_{\text{BZ}}} \sum_{\sigma=\uparrow,\downarrow} \int_{\text{BZ}} d\mathbf{k}_{\parallel} T_{\sigma}(\mathbf{k}_{\parallel}, E_F), \quad (1)$$

where  $-e$  is the electron charge,  $h$  the Planck constant, and  $e^2/h$  half the quantum of conductance.  $T_{\sigma}(\mathbf{k}_{\parallel}, E_F)$  is the spin-dependent transmission probability from one lead to the other for electrons at the Fermi energy and with the transverse wave vector  $\mathbf{k}_{\parallel}$  perpendicular to the current flow (here we assume that the two spin components do not mix). The integral over  $\mathbf{k}_{\parallel}$  goes over the Brillouin zone (BZ) perpendicular to the transport direction, and  $\Omega_{\text{BZ}}$  is the area of the BZ. In the case when the interaction between electrons involved in transport is completely neglected, the transmission for a given energy,  $E$ , of the incident electrons can be evaluated as [41]

$$T_{\sigma}(\mathbf{k}_{\parallel}, E) = \text{Tr}[\Gamma_L^{\sigma}(\mathbf{k}_{\parallel}, E) \mathbf{G}^{\sigma\dagger}(\mathbf{k}_{\parallel}, E) \Gamma_R^{\sigma}(\mathbf{k}_{\parallel}, E) \mathbf{G}^{\sigma}(\mathbf{k}_{\parallel}, E)], \quad (2)$$

where  $\mathbf{G}^{\sigma}(\mathbf{k}_{\parallel}, E)$  is the retarded Green's function of the scattering region coupled to the leads,

$$\mathbf{G}^{\sigma}(\mathbf{k}_{\parallel}, E) = [\epsilon^+ \mathbf{S}(\mathbf{k}_{\parallel}) - \mathbf{H}^{\sigma}(\mathbf{k}_{\parallel}) - \Sigma_L^{\sigma}(\mathbf{k}_{\parallel}, E) - \Sigma_R^{\sigma}(\mathbf{k}_{\parallel}, E)]^{-1}. \quad (3)$$

All terms presented are matrices  $[\mathbf{G}^{\sigma}(\mathbf{k}_{\parallel}, E)]_{\mu\nu}$ , labeled by the global indices  $\mu, \nu$  which run through the basis functions at all

atomic positions in the scattering region.  $\mathbf{S}(\mathbf{k}_{\parallel})$  represents the orbital overlap matrix, and the energy shift into the complex plane,  $\epsilon^+ = \lim_{\delta \rightarrow 0^+} (E + i\delta)$ , has been introduced to respect causality.  $\mathbf{H}^{\sigma}(\mathbf{k}_{\parallel})$  is the Hamiltonian of the scattering region for spin  $\sigma$ ; the right and left self-energies  $\Sigma_R^{\sigma}(\mathbf{k}_{\parallel}, E)$  and  $\Sigma_L^{\sigma}(\mathbf{k}_{\parallel}, E)$  describe the energy-, momentum-, and spin-dependent hybridization of the scattering region with the left and right leads, respectively [29]. Therefore,  $\mathbf{G}^{\sigma}(\mathbf{k}_{\parallel}, E)$  is formally the retarded Green's function associated to the effective, non-Hermitian Hamiltonian  $\mathbf{H}_{\text{eff}}^{\sigma}(\mathbf{k}_{\parallel}, E) = \mathbf{H}^{\sigma}(\mathbf{k}_{\parallel}) - \Sigma_L^{\sigma}(\mathbf{k}_{\parallel}, E) - \Sigma_R^{\sigma}(\mathbf{k}_{\parallel}, E)$ , in which the self-energies act as external energy-, momentum-, and spin-dependent potentials. In Eq. (2),  $\Gamma_{L(R)}^{\sigma}(\mathbf{k}_{\parallel}, E) = i[\Sigma_{L(R)}^{\sigma}(\mathbf{k}_{\parallel}, E) - \Sigma_{L(R)}^{\sigma\dagger}(\mathbf{k}_{\parallel}, E)]$  is the so-called left (right) broadening matrix that accounts for the hybridization-induced broadening of the single-particle energy levels of the scattering region. Importantly, for noninteracting electrons, it has been proved that the Landauer and the Kubo approaches are equivalent [42], so that the linear-response transport properties of a system can be computed with either formalism. During the last few years, the Landauer approach has been systematically applied in conjunction with DFT in order to perform calculations of the conductance of different classes of real nanodevices [43]. In this combination the DFT provides a single-particle theory in which the Kohn-Sham eigenstates are interpreted as single-particle excitations. Although this approach is only valid approximatively, DFT-based transport studies have provided insightful results concerning the role of the band structure in the electron transport process through layered heterostructures [1,2,44–46].

With the effect of the electron-electron interaction beyond the DFT explicitly considered, the retarded Green's function of Eq. (3) is replaced by the following one, carrying the subscript ‘‘MB’’ for ‘‘many-body’’:

$$\mathbf{G}_{\text{MB}}^{\sigma}(\mathbf{k}_{\parallel}, E) = [\epsilon^+ \mathbf{S}(\mathbf{k}_{\parallel}) - \mathbf{H}^{\sigma}(\mathbf{k}_{\parallel}) - \Sigma_L^{\sigma}(\mathbf{k}_{\parallel}, E) - \Sigma_R^{\sigma}(\mathbf{k}_{\parallel}, E) - \Sigma_{\text{MB}}^{\sigma}(\mathbf{k}_{\parallel}, E)]^{-1}. \quad (4)$$

Here,  $\Sigma_{\text{MB}}^{\sigma}(\mathbf{k}_{\parallel}, E)$  is the many-body self-energy defined through the Dyson equation  $\Sigma_{\text{MB}}^{\sigma}(\mathbf{k}_{\parallel}, E) = \mathbf{G}^{\sigma}(\mathbf{k}_{\parallel}, E)^{-1} - \mathbf{G}_{\text{MB}}^{\sigma}(\mathbf{k}_{\parallel}, E)^{-1}$  [40]. This accounts for all electron-electron interaction effects neglected in  $\mathbf{G}^{\sigma}(\mathbf{k}_{\parallel}, E)$ . The self-energy acts as a spin-, momentum-, and energy-dependent potential, whose imaginary part produces a broadening of the single-particle states due to finite electron-electron lifetime. In this work, the many-body self-energy is computed at the DMFT level, meaning that  $\Sigma_{\text{MB}}^{\sigma}(\mathbf{k}_{\parallel}, E)$  is approximated by a  $\mathbf{k}$ -independent quantity  $\Sigma_{\text{MB}}^{\sigma}(E)$ , i.e., a spatially local but energy-dependent potential. Then, as suggested by Jacob *et al.* [31,32], the conductance and the transmission probability are obtained within the Landauer approach by using Eqs. (1) and (2), where one replaces  $\mathbf{G}^{\sigma}(\mathbf{k}_{\parallel}, E)$  by  $\mathbf{G}_{\text{MB}}^{\sigma}(\mathbf{k}_{\parallel}, E)$ . This is an approximation, since it neglects vertex corrections due to in-scattering processes [47,48], which in general increase the conductivity. But we are not aware of any established method to compute those vertex corrections to linear-response transport within the considered framework. In our approach the Landauer transmission is calculated using the improved DMFT electronic structure, rather than the DFT one. Note that the DMFT provides the single-particle excitations of the



system, whereas the Kohn-Sham DFT eigenvalues formally do not reveal such quasiparticle states.

### B. DMFT-based computational approach

The transport calculations are performed according to the Green's function scheme presented above by using the DFT-based transport code SMEAGOL [21,28,29]. The many-body self-energy entering in Eq. (4) is calculated using the EMTO-DMFT method [36–38,49] within a screened KKR [39] approach. In both codes the Perdew-Burke-Ernzerhof (PBE) GGA [50] for the exchange-correlation density functional is used. Self-consistent DFT calculations are performed separately in SMEAGOL and in the EMTO code. The many-body self-energy is then evaluated after self-consistency in the EMTO code, and passed to the SMEAGOL Green's function to compute the transmission along Eq. (2). SMEAGOL imports the DFT Hamiltonian from the SIESTA code [35], which uses pseudopotentials and expands the wave functions of valence electrons over the basis of numerical atomic orbitals (NAOs). The EMTO code, in its turn, uses the muffin-tin construction; we present a detailed description of the projection of quantities such as the many-body self-energy from the EMTO basis set into the NAO basis set (SMEAGOL/SIESTA) in Sec. II E.

For the EMTO-DMFT calculations, the following multiorbital on-site interaction term is added to the GGA Hamiltonian in the EMTO basis:  $\frac{1}{2} \sum_{i\{m,\sigma\}} U_{mm'm''m'''} c_{im\sigma}^\dagger c_{im'\sigma'}^\dagger c_{im''\sigma''} c_{im'''\sigma'''}^\dagger$ . Here,  $c_{im\sigma}$  ( $c_{im\sigma}^\dagger$ ) destroys (creates) an electron with spin  $\sigma$  on orbital  $m$  at the site  $i$ . The Coulomb matrix elements  $U_{mm'm''m'''}$  are expressed in the standard way [51] in terms of three Kanamori parameters  $U$ ,  $U'$ , and  $J$ . Then, within DMFT the many-body system is mapped onto a multiorbital quantum impurity problem, which corresponds to a set of local degrees of freedom connected to a bath and obeys a self-consistently condition [23,24]. In the present work the impurity problem is solved with a spin-polarized  $T$ -matrix fluctuation exchange (SPTF) method [5,26,52]. This method was first proposed by Bickers and Scalapino [53] in the context of lattice models. In practice, it is a perturbative expansion of the self-energy in powers of  $U$ , with a resummation of a specific classes of diagrams, such as ring diagrams and ladder diagrams. The expansion remains reliable when the strength of interaction  $U$  is smaller than the bandwidth of the bath, which is fulfilled in the case of Cu-Co-Cu heterostructures and for the considered values of the Coulomb parameters. The impurity solver we use is multiorbital, fully rotationally invariant, and moreover computationally fast, since it involves matrix operations like inversions and multiplications. The perturbation theory can be performed either self-consistently, in terms of the fully dressed Green's function, or non-self-consistently, as was done in the initial implementations [49,54]. When the interaction is small with respect to the bandwidth, no appreciable difference exists between the non-self-consistent and self-consistent results [55,56]. Moreover, it was recently shown that bare series summations with noninteracting Green's functions converge to the correct physical self-energy at least for the two-dimensional Hubbard model [57]. This has to be distinguished from the DMFT self-consistency, which is employed in both cases. In the present calculation, we use nondressed Green's functions to perform these infinite summation of diagrams.

Moreover, we consider a different treatment of particle-hole (PH) and particle-particle (PP) channels. The particle-particle (PP) channel is described by the  $T$ -matrix approach [58] which yields renormalization of the effective interaction. This effective interaction is used explicitly in the particle-hole channel; details of this scheme can be found in Ref. [52]. The particle-particle contribution to the self-energy is combined with the Hartree-Fock and the second-order contributions [59]. The many-body self-energy is computed at Matsubara frequencies  $\omega_n = (2n + 1)\pi/\beta$ , where  $n = 0, 1, 2, \dots$  and  $\beta$  is the inverse temperature. The Padé [60] analytical continuation is employed to map the self-energies from the Matsubara frequencies onto real energies, as required in the transmission calculation. Note that since some parts of the correlation effects are already included in the GGA, the double counting of some terms has to be corrected. To this end, we start with the GGA electronic structure and replace the obtained  $\Sigma_{MB}^\sigma(E)$  by  $\Sigma_{MB}^\sigma(E) - \Sigma_{MB}^\sigma(0)$  in all equations of the GGA+DMFT method [61], the energy  $E$  here being relative to the Fermi energy. This is a common double-counting correction for treating metals; a more detailed description can be found in [62].

### C. Cu-Co-Cu heterostructure setup

The basis set used in the SIESTA and SMEAGOL calculations is of “double-zeta with polarization” (DZP) quality. In the “standard” SIESTA basis construction algorithm, there is an “energy shift” parameter which allows us to control the extent of basis functions on different atoms in a multielement system in a balanced way; in our case this parameter was taken to be 350 meV, resulting in basis functions extending to  $6.17 a_0$  (Cu  $4s$ ),  $3.39 a_0$  (Cu  $3d$ ), and  $6.31 a_0$  (Co  $4s$ ). For Co- $3d$  states, a smaller basis function localization was intentionally imposed, corresponding to the extension of  $4.61 a_0$ , where  $a_0$  is the Bohr radius. The basis functions are usually freely chosen and not subject to optimization; however, in view of their quite restricted number in SIESTA, it often makes sense to look at resulting ground-state properties of materials as a benchmark for the validity, or sufficiency, of a basis. With the above settings, the relaxed lattice parameters of pure constituents were found to be  $a = 3.65 \text{ \AA}$  (fcc Cu, 1% larger than the experimental value) and  $a = 2.52 \text{ \AA}$ ,  $c = 4.06 \text{ \AA}$  (hcp Co, both within 0.5% of experimental values). Moreover the magnetic moment per Co atom was  $1.65 \mu_B$  (equal to experiment).

In order to calculate the transport properties, semi-infinite leads are attached on both sides of the scattering region. We consider Cu(111)-cut leads, characterized by the ABCABC atomic plane repetition into the leads, i.e., along the transport direction henceforth referred to as  $z$ . It is assumed that the ABCABC layer sequence is smoothly continued throughout the scattering region, including the Co monolayer (see Fig. 1). To model the scattering region the sequence is repeated and the Co layer is considered to replace the Cu layer.

In SMEAGOL the Hamiltonian of the scattering region is matched to that of the leads at the boundary of the scattering region, thus implying that whatever perturbation is induced by a scatterer it has to be confined within the scattering region. In other words, the simulation cell needs to contain enough Cu layers on each side of the Co layer to “screen” it completely. We verified that using seven layers on each

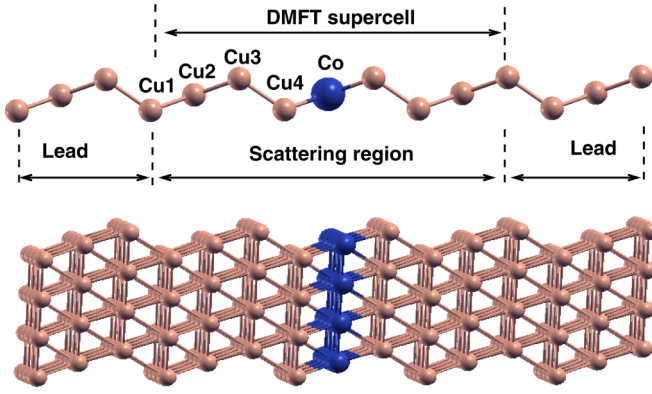


FIG. 1. (Color online) Schematic representation of the supercell used in calculations. The length of the cell and the distances between Cu1, Cu2, Cu3, Cu4, and Co are given in the text. The unit cell dimensions of the leads are kept at the relaxed bulk value 3.65 Å. The ABCABC sequence describes the lead periodicity along the 111 direction.

side provides a good agreement between the potential at the boundaries of our setup with the one from the periodic Cu leads calculation. The resulting cell geometry is shown in Fig. 1: the “Lead”+“Scattering region”+“Lead” composes the SMEAGOL cell, merging on its two ends with the unperturbed semi-infinite Cu electrodes. A restricted spatial relaxation within the scattering region was done by SIESTA, whereby the total thickness of this region varied in small steps, and the  $z$  positions of Cu2, Cu3, and Cu4 layers between the limiting Cu1 and the central Co layer were adjusted till the forces fell below 0.01 eV/Å. This resulted in interlayer distances of 2.119 Å (Cu1-Cu2 and Cu2-Cu3), 2.118 Å (Cu3-Cu4), and 2.104 Å (Cu4-Co). The length for the supercell along the  $z$  direction resulting from the minimization of the cell total energy was 31.619 Å. The relaxed structural parameters obtained within the GGA were then used in the GGA+DMFT calculation, and no additional structure relaxation was attempted at the GGA+DMFT level.

#### D. SIESTA and EMTO density of states

In order to demonstrate the reliability of both codes concerning the electronic structures, we present below the density of states for the heterostructure (Fig. 2). A rather good agreement is apparent.

#### E. Matrix elements of the self-energy in the NAO basis set

The matrix representation of the self-energy operator is determined by the chosen basis. Within the EMTO basis set it has the form  $\delta_{RR'} \sum_{LL'} \Sigma_{RL,RL'}^{\sigma}(z)$ . Here  $R$  and  $R'$  are site indices while the  $L$  symbol labels the orbital quantum numbers. To compute the transmission/conductance it is desirable to work within the SIESTA/SMEAGOL basis. We emphasize that the major part of calculation is done within the SIESTA+SMEAGOL package.

Since significant methodological differences exist between SIESTA and EMTO, in the following we discuss the methodology of data transfer between the two codes. We describe briefly the most significant differences. The former (SIESTA) imple-

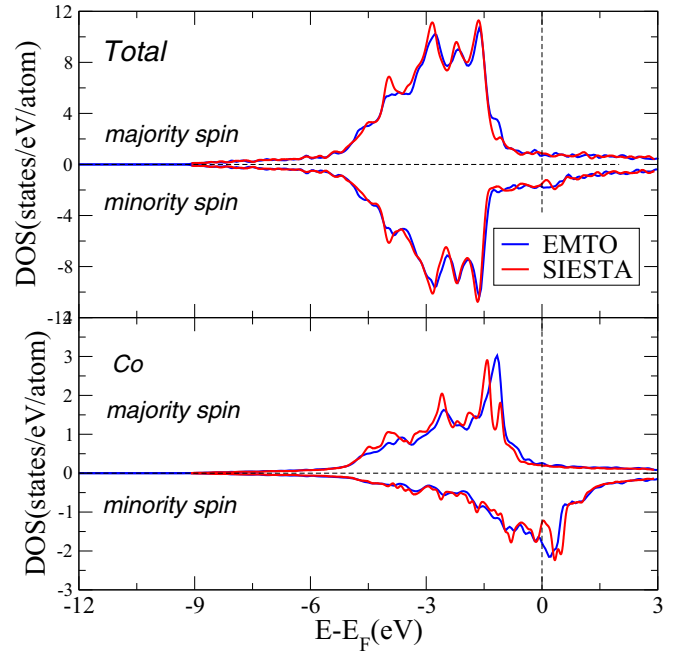


FIG. 2. (Color online) Total (unit cell) and Co density of states computed within the SIESTA and EMTO technique.

mentation uses norm-conserving pseudopotentials, whereas the latter (EMTO) uses an all-electron formulation. SIESTA uses no shape approximation with respect to the potential, whereas EMTO relies on the muffin-tin concept [36,38]. Basis functions in SIESTA are atom-centered numerical functions, whose angular parts are spherical harmonics, and radial parts are strictly confined numerical functions. A tradition finding its origins in quantum chemistry suggests that, in order to improve variational freedom of the basis set, more than one radial function is adopted into the basis for a given angular combination ( $l, m$ ), referred to as “multiple- $\zeta$ ” basis orbitals.

Even as SIESTA maintains flexibility in constructing the basis set out of different “zetas”, possibly including moreover “polarization orbitals” and allowing a variety of schemes to enforce confinement, we shall stick in the following to the case of just “double- $\zeta$ ”, i.e.,  $2 \times 5 = 10$  basis functions, provided to accurately describe the  $3d$  states on each cobalt atom. We shall fix some notation for further reference. The cumulate index of a basis function will be  $\mu \equiv \{I l m \zeta\}$ , where  $I$  indicates the atom carrying the basis function,  $\zeta$  numbers the “zeta”s ( $= 1$  or  $2$  in our case), and the  $(l, m)$  is the conventional angular momentum index. It should be noted, however, that SIESTA employs real combinations of “standard” spherical harmonics, so that the indices  $m = -2$  through  $2$  for  $l = 2$  correspond to  $xy$ ,  $yz$ ,  $3z^2 - r^2$ ,  $xz$ , and  $x^2 - y^2$   $d$ -functions, correspondingly. With the above notation, the  $i$ th eigenstate of the Kohn-Sham Hamiltonian will expand into the basis functions  $\phi_{\mu}$  as follows:

$$\Psi_i(\mathbf{r}) = \sum_{\mu} c_{\mu i} \phi_{\mu}(\mathbf{r} - \mathbf{R}_I), \quad (5)$$

and the variational principle yields the expansion coefficients [35]. Within the EMTO, the  $d$ -orbitals manifold is constructed using a basis set with real harmonics (physical orbitals representation), and the occupation matrix is obtained integrating

the complex contour Green's function (properly normalized path operator) in terms of the exact muffin-tin orbitals  $\Psi_{RL}(\epsilon, \mathbf{r})$  corresponding to the energy  $\epsilon$  [36–38]. On the other hand, in SIESTA the numerical basis set is not restricted to the physical orbitals and allows the definition of simple/double  $\zeta$  “atomic-like” representations. Enhancing the numerical atomic orbitals basis vectors does not affect the dimension of the vector spaces (in both cases the  $d$  subspace); however, it complicates the algebra for the transformation matrix. The transformation involves the double-zeta basis set,  $\phi_\mu$ , which for the  $L(l, m)$  manifold contains  $2(2l + 1)$  components split into the first  $(2l + 1)$ -single-zeta and the second  $(2l + 1)$ -double-zeta components. First we write the explicit form for the EMTO orbital in a vector form for the  $L(l = 2, m = 2l + 1)$  subspace  $|\Psi_{RL}(\epsilon, \mathbf{r})\rangle$ , and the corresponding SIESTA basis vector in the double- $\zeta$  basis,  $|\phi_{RL}(\mathbf{r})\rangle = (\phi^{1\zeta}(\mathbf{r}), \phi^{2\zeta}(\mathbf{r}))$ . The general transformation matrix  $V_{m_i, m_j}^{1\zeta, 2\zeta}(\epsilon)$  is defined as the inner products of  $\Psi_{R'L'}(\epsilon, \mathbf{r})$  with SIESTA's double- $\zeta$  basis, and takes the form of a dyadic product:

$$\begin{aligned} V_{m_i, m_j}^{1\zeta, 2\zeta}(\epsilon) &= \langle \Psi_{R'L'}(\epsilon, \mathbf{r}) | \otimes | \phi_{RL}(\mathbf{r}) \rangle = |\Psi_{RL}(\epsilon, \mathbf{r})\rangle^T | \phi_{RL}(\mathbf{r}) \rangle \\ &= \begin{pmatrix} V_{m_i, m_j}^{1\zeta}(\epsilon) \\ V_{m_i, m_j}^{2\zeta}(\epsilon) \end{pmatrix}. \end{aligned} \quad (6)$$

The definition Eq. (6) for the  $V$  matrix suggests the possibility of an explicit construction. However, a couple of obvious ambiguities may arise: (i) the transformation carries an energy dependence originating from the energy dependence of the EMTO orbitals [36–38], in contrast to the NAO basis set that is energy independent; (ii) normalization of the scattering path operator of EMTO is performed in a particular screened representation [36–38], a more involved procedure in comparison with the straight normalization of the NAO basis set.

Moreover, it is important to keep in mind that the closure relations that are typically used to build the matrix transformations are valid on the Hilbert space spanned by the eigenvectors of the Hamiltonian. These relations hold exactly for the numerical results of each code separately; nevertheless, the numerical results produced by different codes are not identical in the mathematical sense. Small differences between the observables computed with different codes may exist due to various factors—from unwanted numerical roundoff errors to incompleteness of the basis sets. This indicates that the closure relation for the Hilbert space of the EMTO will not be exact (in the mathematical sense) when used in the Hilbert space spanned by the eigenvectors of SIESTA. Consequently, we expect that the transformation matrix will fulfill the usual requirements (i.e., unitarity) only within numerical inaccuracies.

In view of these formal difficulties in obtaining a basis transformation to match a multiple scattering method with a Hamiltonian based scheme we propose an approach using the fact that expectation values should be independent of the specific representation. We apply this fundamental concept of quantum mechanics to the orbital occupation matrix (density matrix,  $n_{m_i, m_j}$ ) for the  $d$  manifold (i.e.,  $m_i, m_j = 1, \dots, 5$ ), and

TABLE I. Occupation matrix of Co- $d$  orbitals in the Cu-Co-Cu heterostructure.

		$m_i = xy$	$yz$	$z^2 - r^2$	$xz$	$x^2 - y^2$
$n_{m_i, m_i}^{EMTO}$	$\uparrow$	0.629	0.526	0.658	0.526	0.629
	$\downarrow$	0.922	0.925	0.908	0.925	0.922
$n_{m_i, m_i}^{SIESTA}$	$\uparrow$	0.639	0.485	0.784	0.485	0.639
	$\downarrow$	0.935	0.952	0.924	0.952	0.935

we look for a formally similar matrix transformation  $W$ :

$$(W_{m_j, m_i}^{1\zeta} \quad W_{m_j, m_i}^{2\zeta}) n_{m_i, m_j}^{EMTO} \begin{pmatrix} W_{m_i, m_j}^{1\zeta} \\ W_{m_i, m_j}^{2\zeta} \end{pmatrix} = n_{m_i, m_j}^{SIESTA}. \quad (7)$$

Equation (7) provides us with a system of equations to determine the matrix elements of  $W$  numerically. Indeed, by inspecting the diagonal elements of the occupation matrix for the  $xy$ ,  $yz$ ,  $z^2 - r^2$ ,  $xz$ , and  $x^2 - y^2$  orbitals respectively, we obtained the data shown in Table I. One should note that in the physical-EMTO basis the occupation matrix is diagonal. The corresponding SIESTA occupation matrix has nondiagonal elements that are about two orders of magnitude smaller than the diagonal ones.

While the symmetry and the qualitative trends in the occupations are the same, the exact numerical values are not. In other words, Eq. (7) is an approximative (numerical) relation; however, the resulting  $W$  matrix reflects the symmetry of  $n_{m_i, m_i}$ . The nonzero elements on the diagonal are close to 1 for the first- $\zeta$  block and take small imaginary values for the second- $\zeta$  one. The equations Eq. (B1) and (B4) provide explicit values.

Accordingly, given the matrix elements for the transformation matrix, the self-energy generated in the EMTO-basis set can be transferred to the double (multiple) zeta SIESTA basis set according to

$$\Sigma^{SIESTA} = W \Sigma^{EMTO} W^\dagger. \quad (8)$$

### III. RESULTS

In this section we discuss the changes in the electronic structure and in the conductance of a single Co layer sandwiched between semi-infinite Cu electrodes caused by the inclusion of the Coulomb interaction at the GGA+DMFT level. The chosen values for Coulomb and exchange parameters for the  $3d$ -Co orbitals are  $U = 3$  eV and  $J = 0.9$  eV, while no interaction beyond GGA is considered for the  $3d$ -Cu states either in the scattering region or in the leads. The values of  $U$  and  $J$  are sometimes used as fitting parameters, although it is possible, in principle, to compute the dynamic electron-electron interaction matrix elements with good accuracy [63]. The static limit of the energy-dependent screened Coulomb interaction leads to a  $U$  parameter in the energy range between 2 and 4 eV for all  $3d$  transition metals, depending on the definition of the correlated orbitals [64,65]. As the  $J$  parameter is not affected by screening it can be calculated directly within LSDA; it turns out to be about the same for all  $3d$  elements,  $J \approx 0.9$  eV [51]. The sensitivity of results to  $U$  and  $J$  will be briefly addressed towards the end of this section. As regards the

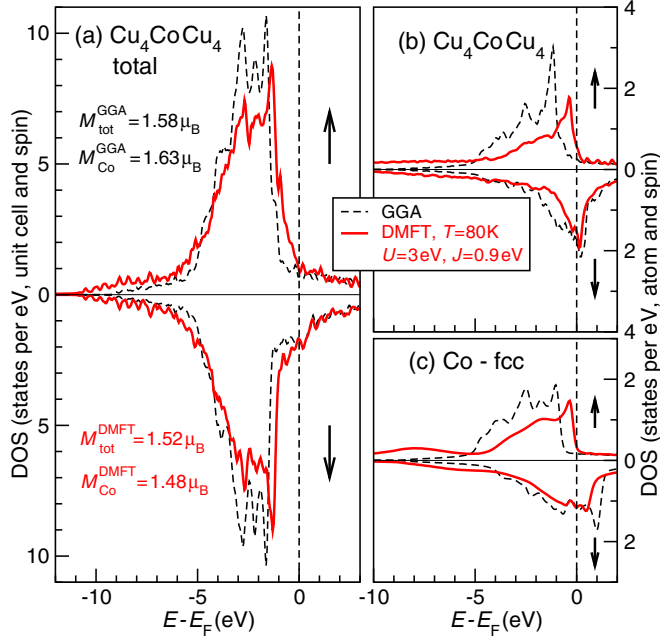


FIG. 3. (Color online) Densities of states calculated by EMTO in relaxed geometries. Dashed black lines: GGA results; solid red lines: GGA+DMFT results. (a) Total DOS per scattered region; (b) local DOS per central Co atom of the heterostructure; (c) local DOS per atomic sphere of the same size in pure fcc bulk cobalt. The values of total and local Co magnetic moments for the scattered region are indicated in (a).

temperature, two values  $T = 80$  K and  $200$  K are addressed. Smaller temperatures could be considered; however, this would strongly increase the computational efforts connected with the analytical continuation of the data onto the real axis.

### A. Electronic structure calculations

The total density of states (DOS) for the Cu-Co-Cu heterostructure is shown in Fig. 3(a). The Co contribution to the total DOS, attributed to the atomic sphere radius of  $2.69 a_0$ , is presented in Fig. 3(b). For comparison we plot in Fig. 3(c) the Co DOS in the bulk fcc structure, with the same atomic sphere radius.

We start with discussing the features of the electronic structure of bulk Co. For the majority-spin electrons, the GGA DOS [Fig. 3(c)] is fully occupied. In the minority-spin

channel, the Fermi level falls between two pronounced peaks at  $\sim E_F \pm 1$  eV. The orbital occupations are shown in Table II. According to the GGA results the majority spin-up channel has a nominal  $d$  occupation of 4.70 while for minority electrons the occupation amounts to 2.87. The  $s$  electrons carry a negligible polarization, while  $p$  electrons are slightly spin polarized with a sign opposite to the main  $d$  polarization which establishes a magnetic moment of  $1.74 \mu_B$ . As a consequence of the local Coulomb interactions parametrized by  $U$  and  $J$  within DMFT, the DOS distribution changes considerably. The overall broadening is strongly modified by the imaginary part of the self-energy. The top of the occupied  $d$  band in the majority spin channel is shifted closer to the Fermi level, and some redistribution of the spectral weight occurs. These changes do not noticeably affect the occupation of  $s$  orbitals; however, the magnetic moment, mostly due to  $d$  electrons, is significantly reduced from  $1.74 \mu_B$  to  $1.41 \mu_B$ .

Essentially the correlation effects are determined not only by the magnitude of the local Coulomb parameters ( $U, J$ ) but also by the orbital occupations. It was argued [66,67] that electronic interactions may lead to the creation of either a majority-spin or a minority-spin hole. As the majority-spin channel is essentially full, there is effectively no space for excitations just across the Fermi level. On the contrary, in the minority-spin channel one finds a high density of electrons which can be immediately excited, leaving back holes. Such an occupation asymmetry has consequences concerning possible interaction channels in the multiorbital Hubbard model: A majority-spin hole can only scatter with opposite-spin particles, which would cost an effective interaction  $U$ , while a minority-spin hole may also scatter with parallel-spin particles with the effective interaction  $U - J < U$  [68]. Therefore correlation effects are expected to manifest themselves differently for majority- and minority-spin electrons.

Many DOS features of Co in the heterostructure geometry [Fig. 3(b)] resemble those of bulk cobalt [Fig. 3(c)], the occupation numbers of which are also given in Table II. As expected, the spin polarization in  $s$  and  $p$  channels is very small; moreover it is opposite to the  $d$  electrons, yielding an overall magnetic moment of  $1.63 \mu_B$ . As compared to the GGA case for the central Co layer of the heterostructure, in GGA+DMFT the Co  $s$ - and  $p$ -electron spin polarization changes sign, and the  $d$ -electron spin splitting decreases. In the Cu-Co-Cu heterostructure geometry the Co- $d$  orbitals experience hybridization with the neighboring Cu- $d$  orbitals

TABLE II. Orbital occupations and magnetic moments for the Cu-Co-Cu heterostructure and bulk Co-fcc. The DMFT calculations have been performed for  $T = 200$  K,  $U = 3$  eV,  $J = 0.9$  eV.

Atom	$n^{\text{GGA}}$			$M^{\text{GGA}}$ ( $\mu_B$ )	$n^{\text{DMFT}}$			$M^{\text{DMFT}}$ ( $\mu_B$ )
	$s(\downarrow/\uparrow)$	$p(\downarrow/\uparrow)$	$d(\downarrow/\uparrow)$		$s(\downarrow/\uparrow)$	$p(\downarrow/\uparrow)$	$d(\downarrow/\uparrow)$	
Co bulk-fcc:								
Co:	(0.34/0.33)	(0.39/0.31)	(2.87/4.70)	1.74	(0.34/0.33)	(0.38/0.35)	(3.04/4.50)	1.41
Cu <sub>4</sub> CoCu <sub>4</sub> scattering region:								
Cu1-3:	(0.36/0.36)	(0.33/0.33)	(4.78/4.78)	0.00	(0.39/0.39)	(0.45/0.45)	(4.72/4.72)	0.00
Cu4:	(0.36/0.36)	(0.36/0.33)	(4.76/4.79)	0.00	(0.38/0.37)	(0.42/0.39)	(4.58/4.65)	0.02
Co:	(0.33/0.32)	(0.33/0.31)	(2.96/4.63)	1.63	(0.32/0.33)	(0.33/0.37)	(2.70/4.13)	1.48

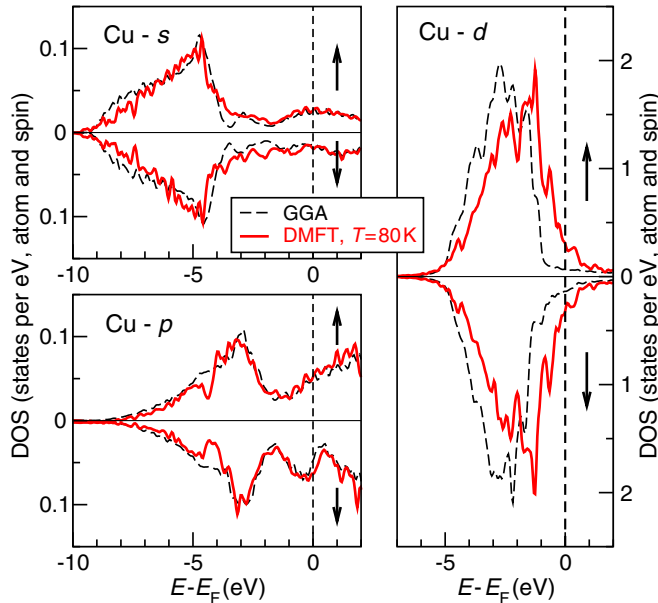


FIG. 4. (Color online) Orbital-resolved DOS for Cu4 in the  $\text{Cu}_4\text{CoCu}_4$  heterostructure computed within the GGA (black dashed line) and GGA+DMFT (red solid line) for  $U = 3$  eV and  $J = 0.9$  eV.

which leads to a change in the DOS of the Cu layer in the vicinity of the Co layer.

Figure 4 depicts the local DOS of the Cu atom closest to the Co monolayer (indicated Cu4 in Table II). Even as no on-site interaction terms have been added to the  $3d$ -Cu states, the Co self-energy has a large impact on the GGA-DMFT density of states. In fact, the  $3d$ -Cu4 states are strongly coupled with the correlated  $3d$ -Co states and are dragged towards the Fermi energy, thus increasing the hybridization with the  $4s$ - and  $4p$ -Cu4 states. In contrast, the three outmost (from Co) copper layers Cu3, Cu2, Cu1 have very similar orbital occupations which slightly differ from those of the Cu4. The inclusion of interaction in the spirit of DMFT has only a slight effect upon the orbital occupations within Cu3, Cu2, and Cu1 as compared to Cu4 (see Table II). Essentially the  $4s$ - and  $4p$ -Cu4 orbitals slightly increase in occupation, while  $3d$  orbitals are depleted accordingly. At the same time, the minority/majority spin contrast gets enhanced: from 4.76/4.79 in GGA to 4.58/4.65 in GGA+DMFT. This can be understood as the interaction may lead to a renormalization of the DFT orbitals splitting [69], a one-particle effect, or as a direct consequence of the behavior of the self-energy around the Fermi level from many-body correlations. The orbitals respond almost equally to the renormalization effects. The spectral weight transfer in the Co layer—a consequence of electron correlations—modifies slightly, through  $d$ - $d$  hybridization, the spin asymmetry in  $d$  holes of the closest copper layer inducing a magnetic moment.

We note that the temperature dependence of the DOS is negligible, and the effectiveness of electronic correlations is not significantly different in the heterostructure, as compared to the case of pure-Co fcc bulk.

These changes are typical for correlation effects in transition metals, where the self-energy near the Fermi level has Fermi-liquid character: for the imaginary part, we have

$-\text{Im}\Sigma_{MB,\alpha}^\sigma(E) \propto E^2$ , whereas the real part has negative slope,  $\partial\text{Re}\Sigma_{MB,\alpha}^\sigma(E)/\partial E < 0$ . Here  $E$  is the energy relative to the Fermi level, and  $\alpha$  numbers the three groups of  $d$  states in hexagonal symmetry,  $(z^2)$ ,  $(xz, yz)$ , and  $(x^2 - y^2, xy)$ . From the self-energy we can also evaluate the mass enhancement [40], which within DMFT amounts to

$$\left(\frac{m^*}{m_b}\right)_\alpha^\sigma = 1 - \frac{\partial}{\partial E} \text{Re} \Sigma_{MB}^{\sigma,\alpha}(E), \quad (9)$$

where  $m_b$  represents the band mass obtained within the GGA calculations.

The values are given in Table III, and we note that the enhancement factors for all orbitals are similar, in the range of 1.6–1.8, which indicates that the system is medium correlated.

## B. Transport properties

Turning to transport properties, we display in Fig. 5(a) the total and spin-resolved transmission probabilities computed with GGA and GGA+DMFT. The spin-resolved transmission probability,  $T_\sigma(E)$ , is obtained from the  $\mathbf{k}$ -dependent transmission, Eq. (2), by integrating over all  $\mathbf{k}_\parallel$  points, so that  $T_\sigma(E) = \frac{1}{\Omega_{\text{BZ}}} \int_{\text{BZ}} d\mathbf{k}_\parallel T_\sigma(\mathbf{k}_\parallel, E)$ . By inspecting Fig. 5(a) it can be seen that the overall transmission is a smooth function of energy, and has a rather large value of about  $0.5 e^2/h$  in both spin channels for most considered energies, which reflects the fact that we deal with an all-metal junction. The results for the transmission Fig. 5(a) can be related to the density of states results shown in Fig. 3 and Fig. 4. In GGA the transport is mainly dominated by the Cu- $4s$ ,  $-4p$  states, which are transmitted across the Co layer passing through the Co- $4s$  states, while the Co- $3d$  states do not contribute significantly to the transmission in this energy range. The Cu- $3d$  states contribute to the transmission only at energies below  $-1.5$  eV. Note that the GGA+DMFT transmission is always smaller than the GGA one. The black arrows in Fig. 5(a) indicate the energies at which a significant departure between the GGA+DMFT and the GGA transmission is observed. Specifically, the spin-down transmission drops at about 0.3 eV below the Fermi level, where the Co- $3d$  DOS is high in the DMFT results, while the GGA transmission stays rather constant. In contrast, the spin-up transmission shows a “bump” which extends over a region of about 2 eV around the Fermi level. The slight dip within this bump at about  $-0.5$  eV is at the same energy as the peak in the Co- $3d$  DOS, and represents a Fano-type reduction of transmission in such a metallic system due to interference of electrons in different conducting channels [31,32,70]. In our calculations this feature is a consequence of electronic correlations on the Co atom, which through the  $d$ - $d$  hybridization induce spin-polarization

TABLE III. Effective mass enhancements  $(m^*/m)^{\uparrow,\downarrow}$  for different bands of  $d$  symmetry, calculated according to Eq. (9) as a function of the Coulomb and the exchange parameter,  $U$  and  $J$ .

$U$ (eV)	$J$ (eV)	$xy_\downarrow$	$yz_\downarrow$	$z_\downarrow^2$	$xy_\uparrow$	$yz_\uparrow$	$z_\uparrow^2$
1	0.3	1.551	1.703	1.617	1.578	1.737	1.656
2	0.6	1.625	1.797	1.698	1.654	1.837	1.743
3	0.9	1.661	1.791	1.703	1.697	1.856	1.753

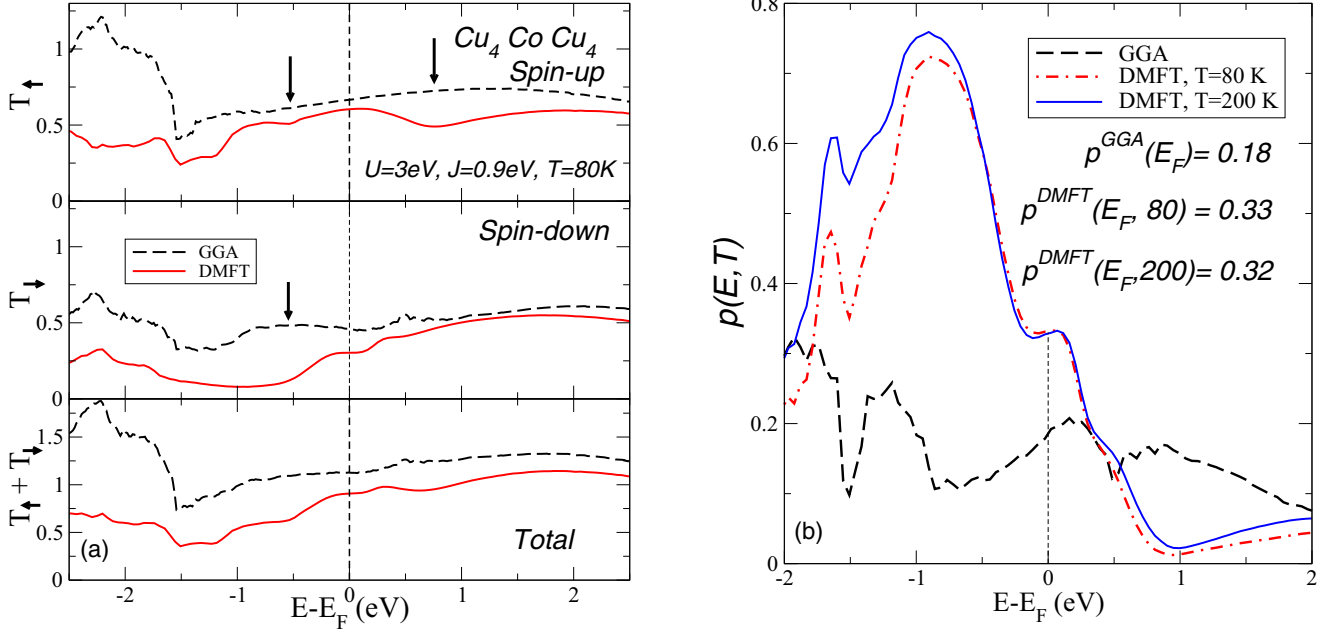


FIG. 5. (Color online) Left: Spin-resolved transmission: majority spins  $T_{\uparrow}$  (upper panel), minority spins  $T_{\downarrow}$  (middle panel), and total (lower panel). Black dashed/red solid lines are the GGA/GGA+DMFT results. Right: Transmission spin polarization around the Fermi energy obtained within the GGA (black dashed) and at finite temperatures  $T = 80 \text{ K}$  (red dot dashed),  $T = 200 \text{ K}$  (blue solid). The Coulomb and exchange parameters are  $U = 3 \text{ eV}$ ,  $J = 0.9 \text{ eV}$ .

of the  $3d$ -Cu4 states and simultaneously produce the shift in the DOS of Fig. 4. In general, we note that for such all-metal systems the relation between DOS and transmission is nontrivial, since interference effects can lead to enhanced transmission also for energies with low DOS; alternatively, for high DOS the increased number of pathways for electrons can lead to a decrease of transmission.

From a many-body perspective, the added self-energy contributes in dephasing the electrons during the flow through the scattering region, so that the Landauer transmission computed with the many-body Green's function is expected to be reduced in comparison with the DFT case. In principle, the opposite effect, namely the effective in-flow of electrons from the many-body self-energy “electrode” into the scattering region, would tend to increase the transmission. However, this in-flow process is not included in our calculations, as it is related to the vertex corrections [47].

The spin polarization of the transmission is computed according to the formula

$$p(E_F) = \frac{T_{\uparrow}(E_F) - T_{\downarrow}(E_F)}{T_{\uparrow}(E_F) + T_{\downarrow}(E_F)}, \quad (10)$$

for either DFT or DFT+DMFT, where  $T_{\sigma=\uparrow,\downarrow}$  is the transmission for the spin channel  $\sigma$ . The spin polarization in transmission obtained by GGA yields  $p^{\text{GGA}}(E_F) = 0.18$  [see also Fig. 5(b)], while the GGA+DMFT value reaches 0.33 at the Fermi level, and increases up to almost 0.8 at slightly lower energies. These results demonstrate that electronic correlations may be decisive and lead to an increase in the spin polarization of transmission. As seen in Fig. 5(b), the enhancement in the spin polarization with respect to the GGA result is essentially temperature independent in the energy range of  $E_F \pm 0.5 \text{ eV}$ .

Therefore we conclude that the enhanced spin contrast in transmission is a many-body effect rather than a temperature fluctuation effect.

Finally, we test how the results for the transmission depend on the strength of the local Coulomb interaction parameters  $U$  and  $J$ . The interaction matrix elements  $U_{mm'm''m'''}$  are usually parametrized using Slater integrals ( $F^k$ ) with  $k = 0, 2, 4$  [51]. Accordingly the Hubbard  $U$  parameter is constructed as a simple average over all possible pairs of correlated orbitals and is identified with the Slater integral  $U = F^0$ . The other Slater integrals  $F^2, F^4$  are fitted to the multiplet structure measured in x-ray photoemission [71]. An empiric relation has been introduced which connects the magnitude of the second- and fourth-order Slater integrals,  $F^4/F^2 \approx 0.625$  [72]. The Hund's exchange  $J$  is expressed in terms of  $F^2$  and  $F^4$  which for the  $d$  shell takes the form  $J = (F^2 + F^4)/14$  [73]; therefore the knowledge of the  $(U, J)$  pair allows us to compute all the matrix elements  $U_{mm'm''m'''}$ . In Fig. 6(a) we plot the transmission (computed at 200 K) keeping the ratio  $U/J = 1.0/0.3$  constant. While scaling the ratio  $\alpha \cdot U/J$  with  $\alpha = 1, 2, 3$  we observe a monotonic reduction of the transmission at the Fermi level. This result is expected, as the matrix elements of the interaction are scaled in magnitude. In the same time, larger mass enhancement factors are obtained as  $\alpha$  increases (see Table II). Consequently we may conclude that the heavier the electron is, the smaller is the transmission at the Fermi level. Within  $\pm 0.15 \text{ eV}$  of the Fermi level, a flat region in the transmission can be seen. Beyond these ranges, we note that below the Fermi level, down to  $-1 \text{ eV}$  from it, the transmission decreases almost indiscriminately for different values of  $(U, J)$ . In the positive energy range up to roughly  $+1 \text{ eV}$ , on the contrary, the transmission values differ, with larger  $(U, J)$  resulting in lower transmission.

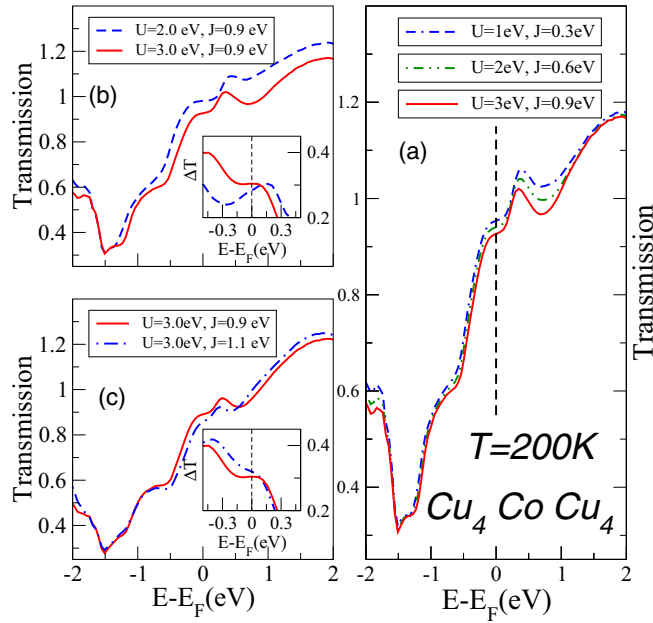


FIG. 6. (Color online) Transmission for different values of Coulomb parameters: (a) with a fixed ratio  $U/J$ , (b) fixed  $J$ , and (c) fixed  $U$ , at  $T = 200$  K.

In Fig. 6(b) we display the dependence on parameters differently keeping  $J = 0.9$  eV constant and varying  $U$ . We note that with higher  $U$ , the flat region centered at  $E_F$  shrinks a bit, which can be traced back to a stronger presence of  $d$  orbitals in the correlated transmission. The inset of Fig. 6(b) depicts the “contrast” or spin difference in transmission:  $\Delta T(E) = T_{\uparrow}(E) - T_{\downarrow}(E)$ . The spin contrast changes slope as  $U$  varies, from markedly positive  $d(\Delta T)/dE$  at  $E_F$  for  $U = 2$  eV to roughly zero for  $U = 3$  eV.

In Fig. 6(c), on the contrary, the  $U$  parameter is kept fixed to a “good” (yielding large flat region) value  $U = 3$  eV, and two different values are taken for the  $J$  parameter. On increasing  $J$ , the flat region around  $E_F$  gets further reduced. Simultaneously [as seen in the inset and contrary to the behavior depicted in Fig. 6(b)],  $\Delta T(E)$  acquires a negative slope. The change in the slope is potentially an interesting effect to be exploited in thermoelectric transport.

#### IV. CONCLUSION

We propose a method to compute the transmission probability by combining two different *ab initio* codes, EMTO and SIESTA/SMEAGOL. In order to transfer the many-body self-energy computed within the EMTO code into SIESTA/SMEAGOL, we use an approximately unitary transformation, which can be determined by requiring that the expectation value of the occupation matrix should be representation independent. The methodology is carried out numerically for the  $\text{Cu}_4\text{CoCu}_4$  heterostructure, and illustrated analytically for a two-orbital model (see Appendix A). Note that such a transformation is rather general and can be used for transferring quantities between two different implementations. Several tests confirm that the proposed method is robust and numerically stable.

Electronic structure calculations are performed using GGA and GGA+DMFT, assuming a local Coulomb interaction in the Co layer. We use a fully rotationally invariant Coulomb interaction on cobalt  $d$  orbitals. The effective mass enhancement ratio for all orbitals is in the range of 1.6 to 1.8, suggesting that we deal with medium correlated system. Concerning the density of states, the presence of Coulomb interactions leads to a shift of the majority-spin channel of Co- $d$  orbitals towards the Fermi level and to a redistribution of the spectral weights. In the minority-spin channel, the changes are less pronounced. This difference leads to different correlation effects for the majority- and minority-spin electrons. All these cause a decrease of the overall Co magnetic moment (with a predominant  $d$  character) from  $1.63 \mu_B$  (GGA) to  $1.48 \mu_B$  (GGA+DMFT). With this combination of methods we have studied the transmission as a function of temperature and Coulomb parameters, which reveals the metallic character of the system considered. Substantial differences in the conducting processes, related to the presence of local Coulomb interaction in the cobalt layer, are observed, due to changes in the electronic structure. Generally the transmission decreases with interaction, although the relation between changes in the electronic configuration and the transmission is highly nontrivial, due to interference effects. With electron correlations properly taken into account, the total transmission at the Fermi level drops by about 20%, whereas its spin polarization (spin contrast) increases by about 40%. These effects are entirely a consequence of the electronic correlation, since the transmission is practically temperature independent in the range of  $E_F \pm 0.5$  eV. This suggests that the enhanced spin contrast in transmission is predominantly a many-body effect. In order to quantify the spin polarization effects in the transmission, we study the transmission difference  $\Delta T(E)$ . This quantity clearly displays a strong dependence on the Coulomb parameters.

In conclusion, we have shown that electronic correlations may considerably affect the transmission and spin filter properties of heterostructures, even though the correlations would be classified only as “medium” when considering the effective mass enhancement. Hence results based on studies neglecting electronic correlations, which are numerous, must be interpreted with caution.

#### ACKNOWLEDGMENTS

The calculations were performed in the Data Center of NIRDIMT. Financial support offered by the Augsburg Center for Innovative Technologies and by the Deutsche Forschungsgemeinschaft (through TRR 80) is gratefully acknowledged. A.D. and I.R. acknowledge financial support from the European Union through the EU FP7 program through project 618082 ACMOL. M.R. also acknowledges support by the Ministry of Education, Science, and Technological Development of the Republic of Serbia under Projects No. ON171017 and No. III45018. A.Ö. would like to acknowledge financial support from the Axel Hultgren foundation and the Swedish steel producer’s association (Jernkontoret), and the hospitality received at the Center for Electronic Correlations and Magnetism, Institute of Physics, University of Augsburg, Germany. L.V. acknowledges support from the Swedish Research Council.

**APPENDIX A: EXAMPLE: A TWO-ORBITAL MODEL IN THE CUBIC SYMMETRY**

We consider a simplified case of a diagonal self-energy corresponding to a two-orbital model in the cubic symmetry. The self-energy and the ‘‘occupation’’ matrix can be written as

$$\Sigma^{EMTO}(z) = \begin{pmatrix} \Sigma_1 & 0 \\ 0 & \Sigma_2 \end{pmatrix}; \quad n^{EMTO} = \begin{pmatrix} n_1 & 0 \\ 0 & n_2 \end{pmatrix}. \quad (\text{A1})$$

In such a case all inner products of the type  $\langle \Psi_{m_i}(\epsilon, \mathbf{r}) | \phi_{m_j}^{\zeta_1}(\mathbf{r}) \rangle$  are zero unless  $m_i = m_j$ , such that the transformation matrix has a generic form:

$$W_{m_i, m_i}^{1\zeta, 2\zeta}(\epsilon) = \begin{pmatrix} W_{11}^{1\zeta} & 0 \\ 0 & W_{22}^{1\zeta} \\ W_{11}^{2\zeta} & 0 \\ 0 & W_{22}^{2\zeta} \end{pmatrix}. \quad (\text{A2})$$

Rewriting Eq. (7),

$$\begin{pmatrix} W_{11}^{1\zeta} & 0 \\ 0 & W_{22}^{1\zeta} \\ W_{11}^{2\zeta} & 0 \\ 0 & W_{22}^{2\zeta} \end{pmatrix} \cdot \begin{pmatrix} n_1 & 0 \\ 0 & n_2 \end{pmatrix} \cdot \begin{pmatrix} W_{11}^{1\zeta} & 0 & W_{11}^{2\zeta} & 0 \\ 0 & W_{22}^{1\zeta} & 0 & W_{22}^{2\zeta} \end{pmatrix} = \begin{pmatrix} \tilde{n}_1^{1\zeta} & 0 & 0 & 0 \\ 0 & \tilde{n}_2^{1\zeta} & 0 & 0 \\ 0 & 0 & \tilde{n}_1^{2\zeta} & 0 \\ 0 & 0 & 0 & \tilde{n}_2^{2\zeta} \end{pmatrix}, \quad (\text{A3})$$

one finds

$$W_{m_i, m_i}^{1\zeta, 2\zeta}(\epsilon) = \begin{pmatrix} \frac{\sqrt{\tilde{n}_1^{1\zeta}}}{\sqrt{n_1}} & 0 \\ 0 & \frac{\sqrt{\tilde{n}_2^{1\zeta}}}{\sqrt{n_2}} \\ \frac{\sqrt{\tilde{n}_1^{2\zeta}}}{\sqrt{n_1}} & 0 \\ 0 & \frac{\sqrt{\tilde{n}_2^{2\zeta}}}{\sqrt{n_2}} \end{pmatrix}, \quad (\text{A4})$$

and accordingly the self-energy in the NAO basis set has the form

$$\Sigma = \begin{pmatrix} \Sigma_1 \frac{\tilde{n}_1^{1\zeta}}{n_1} & 0 & \Sigma_1 \frac{\sqrt{\tilde{n}_1^{1\zeta} \tilde{n}_1^{2\zeta}}}{n_1} & 0 \\ 0 & \Sigma_2 \frac{\tilde{n}_2^{1\zeta}}{n_2} & 0 & \Sigma_2 \frac{\sqrt{\tilde{n}_2^{1\zeta} \tilde{n}_2^{2\zeta}}}{n_2} \\ \Sigma_1 \frac{\sqrt{\tilde{n}_1^{1\zeta} \tilde{n}_1^{2\zeta}}}{n_1} & 0 & \Sigma_1 \frac{\tilde{n}_1^{2\zeta}}{n_1} & 0 \\ 0 & \Sigma_2 \frac{\sqrt{\tilde{n}_2^{1\zeta} \tilde{n}_2^{2\zeta}}}{n_2} & 0 & \Sigma_2 \frac{\tilde{n}_2^{2\zeta}}{n_2} \end{pmatrix} = \begin{pmatrix} \boxed{\Sigma^{1\zeta, 1\zeta}} & \boxed{\Sigma^{1\zeta, 2\zeta}} \\ \boxed{\Sigma^{2\zeta, 1\zeta}} & \boxed{\Sigma^{2\zeta, 2\zeta}} \end{pmatrix} \quad (\text{A5})$$

in which every  $\Sigma^{i\zeta, j\zeta}$  is a  $2 \times 2$  block-diagonal matrix. There are a couple of conclusions to be drawn from the above simplified example: (i) as a consequence of the reduced weight in the second  $\zeta$  occupation (at least 10 times smaller than in the single  $\zeta$ ), the magnitude of the matrix elements of the self-energy in the NAO basis set follow the relation  $\Sigma^{1\zeta, 1\zeta} > \Sigma^{1\zeta, 2\zeta} > \Sigma^{2\zeta, 2\zeta}$ ; (ii) the existence of only-diagonal orbital occupations does not imply the existence of a unitary transformation, except for the case of numerical identical values for the occupation matrices in both basis. These observations do not change when the symmetry is lower than cubic and nonzero matrix elements on the nondiagonal of the occupation matrix appear.



**APPENDIX B: TRANSFORMATION MATRIX FOR THE Co- $d$  MANIFOLD IN THE Cu-Co-Cu HETEROSTRUCTURE**

This section provides the spin-resolved matrix elements,  $W_{\sigma=\uparrow,\downarrow}$ , used in the calculation.

$$W_{\uparrow} = \begin{pmatrix} 1.024 & 0 & 0 & 0 & 0 \\ 0 & 0.987 & 0 & 0 & 0 \\ 0 & 0 & 1.096 & 0 & 0 \\ 0 & 0 & 0 & 0.985 & 0 \\ 0.178i & 0 & 0 & 0 & 1.024 \\ 0 & 0.218i & 0 & 0 & 0 \\ 0 & 0 & 0 & 0 & 0 \\ 0 & 0 & 0 & 0.218i & 0 \\ 0 & 0 & 0 & 0 & 0.178i \end{pmatrix}. \quad (\text{B1})$$

The orthogonality can be checked using the following relations:

$$W_{\uparrow}^{\dagger} W_{\uparrow} = \begin{pmatrix} 1.016 & 0 & 0 & 0 & 0 \\ 0 & 0.922 & 0 & 0 & 0 \\ 0 & 0 & 1.202 & 0 & 0 \\ 0 & 0 & 0 & 0.922 & 0 \\ 0 & 0 & 0 & 0 & 1.016 \end{pmatrix} \quad (\text{B2})$$

and

$$W_{\uparrow} W_{\uparrow}^{\dagger} = \begin{pmatrix} 1.048 & 0 & 0 & 0 & 0 & 0.182i & 0 & 0 & 0 & 0 \\ 0 & 0.970 & 0 & 0 & 0 & 0 & 0.215i & 0 & 0 & 0 \\ 0 & 0 & 1.202 & 0 & 0 & 0 & 0 & 0 & 0 & 0 \\ 0 & 0 & 0 & 0.970 & 0 & 0 & 0 & 0 & 0.215i & 0 \\ 0 & 0 & 0 & 0 & 1.047 & 0 & 0 & 0 & 0 & 0.182i \\ 0.182i & 0 & 0 & 0 & 0 & -0.032 & 0 & 0 & 0 & 0 \\ 0 & 0.215i & 0 & 0 & 0 & 0 & -0.048 & 0 & 0 & 0 \\ 0 & 0 & 0 & 0 & 0 & 0 & 0 & 0 & 0 & 0 \\ 0 & 0 & 0 & 0.215i & 0 & 0 & 0 & 0 & -0.048 & 0 \\ 0 & 0 & 0 & 0 & 0.183i & 0 & 0 & 0 & 0 & -0.032 \end{pmatrix}. \quad (\text{B3})$$

The corresponding transformation matrix for spin-down component reads

$$W_{\downarrow} = \begin{pmatrix} 0.960 & 0 & 0 & -0.007 & 0 \\ 0 & 0.9572 & 0 & 0 & -0.007 \\ 0 & 0 & 0.967 & 0 & 0 \\ -0.007 & 0 & 0 & 0.957 & 0 \\ 0 & -0.007 & 0 & 0 & 0.960 \\ 0.304 & 0 & 0 & -0.002 & 0 \\ 0 & 0.337 & 0 & 0 & -0.002 \\ 0 & 0 & 0.287 & 0 & 0 \\ -0.002 & 0 & 0 & 0.337 & 0 \\ 0 & -0.002 & 0 & 0 & 0.304 \end{pmatrix}, \quad (\text{B4})$$

$$W_{\downarrow}^{\dagger} W_{\downarrow} = \begin{pmatrix} 1.014 & 0 & 0 & -0.015 & 0 \\ 0 & 1.029 & 0 & 0 & -0.015 \\ 0 & 0 & 1.017 & 0 & 0 \\ -0.015 & 0 & 0 & 1.029 & 0 \\ 0 & -0.015 & 0 & 0 & 1.014 \end{pmatrix}, \quad (\text{B5})$$

$$W_{\downarrow} W_{\downarrow}^{\dagger} = \begin{pmatrix} 0.922 & 0 & 0 & -0.014 & 0 & 0.292 & 0 & 0 & 0 & 0 \\ 0 & 0.916 & 0 & 0 & -0.014 & 0 & 0.322 & 0 & 0 & 0 \\ 0 & 0 & 0.935 & 0 & 0 & 0 & 0 & 0.278 & 0 & 0 \\ -0.014 & 0 & 0 & 0.916 & 0 & 0 & 0 & 0 & 0.322 & 0 \\ 0 & -0.014 & 0 & 0 & 0.922 & 0 & 0 & 0 & 0 & 0.292 \\ 0.292 & 0 & 0 & 0 & 0 & 0.092 & 0 & 0 & 0 & 0 \\ 0 & 0.325 & 0 & 0 & 0 & 0 & 0.114 & 0 & 0 & 0 \\ 0 & 0 & 0.278 & 0 & 0 & 0 & 0 & 0.083 & 0 & 0 \\ 0 & 0 & 0 & 0.325 & 0 & 0 & 0 & 0 & 0.114 & 0 \\ 0 & 0 & 0 & 0 & 0.292 & 0 & 0 & 0 & 0 & 0.092 \end{pmatrix}. \quad (\text{B6})$$

## APPENDIX C: ASSESSMENT OF ACCURACY

In order to test the effect of the numerical inaccuracies occurring in the transformation matrix on the final results, we compute the total transmission by using a simplified model for the transformation matrix:

$$W_{\text{Model}}^{1\zeta, 2\zeta} = \begin{pmatrix} W^{1\zeta} \\ W^{2\zeta} \end{pmatrix}, \quad (\text{C1})$$

where  $W^{1\zeta} = \alpha I$  and  $W^{2\zeta} = \beta I$ , where  $I$  is the unity matrix. The results for  $\alpha = 0.9, \beta = 0.1$ ;  $\alpha = 0.5, \beta = 0.5$ ; and  $\alpha = 0.1, \beta = 0.9$ , respectively are given in Fig. 7. It can be clearly seen that even for such a crude approximation, the results for the first model (i.e., with a significant weight of the self-energy on the first zeta orbital) differ with only a few percent over large energy domains. For the occupied states, large values for  $\Sigma^{1\zeta}$  provide already a good approximation for the transformation.

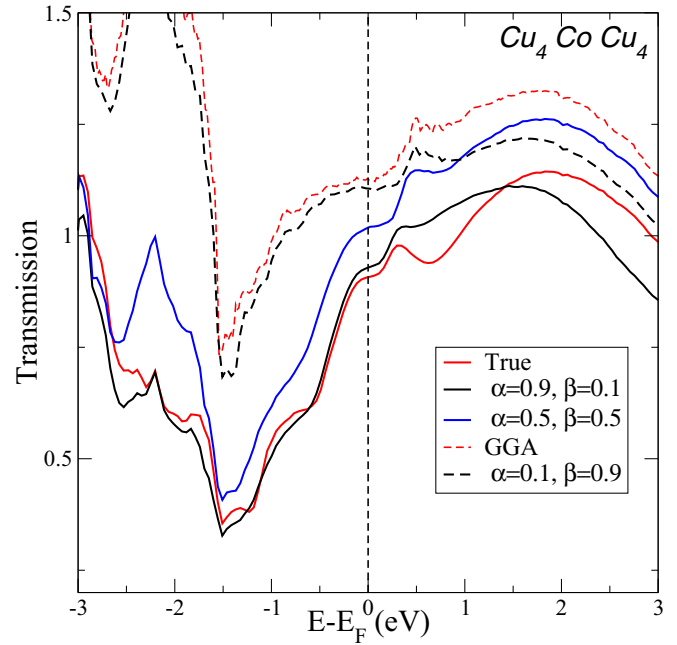


FIG. 7. (Color online) Comparison between the transmission functions obtained for different model forms of  $W^{1\zeta, 2\zeta}$ .

- [1] K. M. Schep, P. J. Kelly, and G. E. W. Bauer, *Phys. Rev. Lett.* **74**, 586 (1995).
- [2] K. M. Schep, P. J. Kelly, and G. E. W. Bauer, *Phys. Rev. B* **57**, 8907 (1998).
- [3] R. A. de Groot, F. M. Mueller, P. G. van Engen, and K. H. J. Buschow, *Phys. Rev. Lett.* **50**, 2024 (1983).
- [4] I. Zutic, J. Fabian, and S. D. Sarma, *Rev. Mod. Phys.* **76**, 323 (2004).
- [5] M. I. Katsnelson, V. Y. Irkhin, L. Chioncel, A. I. Lichtenstein, and R. A. de Groot, *Rev. Mod. Phys.* **80**, 315 (2008).
- [6] R. Landauer, *IBM J. Res. Develop.* **1**, 223 (1957).
- [7] R. Landauer, *IBM J. Res. Develop.* **32**, 306 (1988).
- [8] M. Büttiker, *Phys. Rev. Lett.* **57**, 1761 (1986).
- [9] M. Büttiker, *IBM J. Res. Develop.* **32**, 317 (1988).
- [10] S. Sanvito, C. J. Lambert, J. H. Jefferson, and A. M. Bratkovsky, *Phys. Rev. B* **59**, 11936 (1999).
- [11] J. Mathon, A. Umerski, and M. Villeret, *Phys. Rev. B* **55**, 14378 (1997).
- [12] E. Y. Tsymlal and D. G. Pettifor, *Phys. Rev. B* **64**, 212401 (2001).
- [13] P. S. Krstić, X.-G. Zhang, and W. H. Butler, *Phys. Rev. B* **66**, 205319 (2002).
- [14] P. Hohenberg and W. Kohn, *Phys. Rev.* **136**, B864 (1964).
- [15] W. Kohn and L. J. Sham, *Phys. Rev.* **140**, A1133 (1965).
- [16] W. Kohn, *Rev. Mod. Phys.* **71**, 1253 (1999).
- [17] D. Wortmann, H. Ishida, and S. Blügel, *Phys. Rev. B* **65**, 165103 (2002).
- [18] D. Wortmann, H. Ishida, and S. Blügel, *Phys. Rev. B* **66**, 075113 (2002).
- [19] M. D. Stiles and D. R. Hamann, *Phys. Rev. B* **38**, 2021 (1988).
- [20] J. M. MacLaren, X.-G. Zhang, W. H. Butler, and X. Wang, *Phys. Rev. B* **59**, 5470 (1999).
- [21] A. R. Rocha, V. M. García-Suárez, S. Bailey, C. Lambert, J. Ferrer, and S. Sanvito, *Phys. Rev. B* **73**, 085414 (2006).
- [22] W. Metzner and D. Vollhardt, *Phys. Rev. Lett.* **62**, 324 (1989).
- [23] A. Georges, G. Kotliar, W. Krauth, and M. J. Rozenberg, *Rev. Mod. Phys.* **68**, 13 (1996).
- [24] G. Kotliar and D. Vollhardt, *Phys. Today* **57**(3), 53 (2004).
- [25] V. I. Anisimov, A. I. Poteryaev, M. A. Korotin, A. O. Anokhin, and G. Kotliar, *J. Phys.: Condens. Matter* **9**, 7359 (1997).
- [26] A. I. Lichtenstein and M. I. Katsnelson, *Phys. Rev. B* **57**, 6884 (1998).
- [27] E. Koch, G. Sangiovanni, and O. Gunnarsson, *Phys. Rev. B* **78**, 115102 (2008).
- [28] A. R. Rocha, V. M. García Suárez, S. Bailey, C. Lambert, J. Ferrer, and S. Sanvito, *Nat. Mater.* **4**, 335 (2005).
- [29] I. Rungger and S. Sanvito, *Phys. Rev. B* **78**, 035407 (2008).
- [30] H. Aoki, N. Tsuji, M. Eckstein, M. Kollar, T. Oka, and P. Werner, *Rev. Mod. Phys.* **86**, 779 (2014).
- [31] D. Jacob, K. Haule, and G. Kotliar, *Phys. Rev. Lett.* **103**, 016803 (2009).
- [32] D. Jacob and G. Kotliar, *Phys. Rev. B* **82**, 085423 (2010).
- [33] A. Valli, G. Sangiovanni, O. Gunnarsson, A. Toschi, and K. Held, *Phys. Rev. Lett.* **104**, 246402 (2010).
- [34] A. Valli, G. Sangiovanni, A. Toschi, and K. Held, *Phys. Rev. B* **86**, 115418 (2012).
- [35] J. M. Soler, E. Artacho, J. D. Gale, A. García, J. Junquera, and P. Ordejón, *J. Phys.: Condens. Matter* **14**, 2745 (2002).
- [36] O. K. Andersen and T. Saha-Dasgupta, *Phys. Rev. B* **62**, R16219 (2000).

- [37] L. Vitos, H. L. Skriver, B. Johansson, and J. Kollár, *Comput. Mater. Sci.* **18**, 24 (2000).
- [38] L. Vitos, *Phys. Rev. B* **64**, 014107 (2001).
- [39] P. Weinberger, *Electron Scattering Theory for Ordered and Disordered Matter* (Clarendon Press, Oxford, 1990).
- [40] G. D. Mahan, *Many-Particle Physics* (Plenum Press, New York, 1990).
- [41] S. Datta, *Electronic Transport in Mesoscopic Systems*, Vol. 3 of Cambridge Studies in Semiconductor Physics and Microelectronic Engineering (Cambridge University Press, New York, 1995).
- [42] D. S. Fisher and P. A. Lee, *Phys. Rev. B* **23**, 6851 (1981).
- [43] J. Taylor, H. Guo, and J. Wang, *Phys. Rev. B* **63**, 245407 (2001).
- [44] W. H. Butler, X.-G. Zhang, T. C. Schulthess, and J. M. MacLaren, *Phys. Rev. B* **63**, 054416 (2001).
- [45] I. Rungger, O. Mryasov, and S. Sanvito, *Phys. Rev. B* **79**, 094414 (2009).
- [46] N. M. Caffrey, T. Archer, I. Rungger, and S. Sanvito, *Phys. Rev. Lett.* **109**, 226803 (2012).
- [47] A. Oguri, *J. Phys. Soc. Jpn.* **70**, 2666 (2001).
- [48] Y. Meir and N. S. Wingreen, *Phys. Rev. Lett.* **68**, 2512 (1992).
- [49] L. Chioncel, L. Vitos, I. A. Abrikosov, J. Kollár, M. I. Katsnelson, and A. I. Lichtenstein, *Phys. Rev. B* **67**, 235106 (2003).
- [50] J. P. Perdew, K. Burke, and M. Ernzerhof, *Phys. Rev. Lett.* **77**, 3865 (1996).
- [51] M. Imada, A. Fujimori, and Y. Tokura, *Rev. Mod. Phys.* **70**, 1039 (1998).
- [52] M. I. Katsnelson and A. I. Lichtenstein, *Eur. Phys. J. B* **30**, 9 (2002).
- [53] N. E. Bickers and D. J. Scalapino, *Ann. Phys. (N.Y.)* **193**, 206 (1989).
- [54] J. Minár, L. Chioncel, A. Perlov, H. Ebert, M. I. Katsnelson, and A. I. Lichtenstein, *Phys. Rev. B* **72**, 045125 (2005).
- [55] V. Drchal, V. Janiš, J. Kudrnovský, V. S. Oudovenko, X. Dai, K. Haule, and G. Kotliar, *J. Phys.: Condens. Matter* **17**, 61 (2005).
- [56] G. Kotliar, S. Y. Savrasov, K. Haule, V. S. Oudovenko, O. Parcollet, and C. A. Marianetti, *Rev. Mod. Phys.* **78**, 865 (2006).
- [57] E. Kozik, M. Ferrero, and A. Georges, *Phys. Rev. Lett.* **114**, 156402 (2015).
- [58] V. M. Galitski, *Zh. Eksp. Teor. Fiz.* **34**, 1011 (1958) [*Sov. Phys. JETP* **7**, 698 (1958)].
- [59] M. I. Katsnelson and A. I. Lichtenstein, *J. Phys.: Condens. Matter* **11**, 1037 (1999).
- [60] H. J. Vidberg and J. W. Serene, *J. Low Temp. Phys.* **29**, 179 (1977).
- [61] A. I. Lichtenstein, M. I. Katsnelson, and G. Kotliar, *Phys. Rev. Lett.* **87**, 067205 (2001).
- [62] A. G. Petukhov, I. I. Mazin, L. Chioncel, and A. I. Lichtenstein, *Phys. Rev. B* **67**, 153106 (2003).
- [63] F. Aryasetiawan, M. Imada, A. Georges, G. Kotliar, S. Biermann, and A. I. Lichtenstein, *Phys. Rev. B* **70**, 195104 (2004).
- [64] I. V. Solovyev and M. Imada, *Phys. Rev. B* **71**, 045103 (2005).
- [65] T. Miyake and F. Aryasetiawan, *Phys. Rev. B* **77**, 085122 (2008).
- [66] S. Monastera, F. Manghi, C. A. Rozzi, C. Arcangeli, E. Wetli, H.-J. Neff, T. Greber, and J. Osterwalder, *Phys. Rev. Lett.* **88**, 236402 (2002).
- [67] A. Grechnev, I. Di Marco, M. I. Katsnelson, A. I. Lichtenstein, J. Wills, and O. Eriksson, *Phys. Rev. B* **76**, 035107 (2007).
- [68] F. Manghi, V. Bellini, J. Osterwalder, T. J. Kreutz, P. Aebi, and C. Arcangeli, *Phys. Rev. B* **59**, R10409 (1999).
- [69] N. Parragh, G. Sangiovanni, P. Hansmann, S. Hummel, K. Held, and A. Toschi, *Phys. Rev. B* **88**, 195116 (2013).
- [70] M. R. Calvo, J. Fernandez-Rossier, J. J. Palacios, D. Jacob, D. Natelson, and C. Untiedt, *Nature (London)* **458**, 1150 (2009).
- [71] V. I. Anisimov and O. Gunnarsson, *Phys. Rev. B* **43**, 7570 (1991).
- [72] F. M. F. de Groot, J. C. Fuggle, B. T. Thole, and G. A. Sawatzky, *Phys. Rev. B* **42**, 5459 (1990).
- [73] V. I. Anisimov, I. V. Solovyev, M. A. Korotin, M. T. Czyżyk, and G. A. Sawatzky, *Phys. Rev. B* **48**, 16929 (1993).

## Lattice dynamics of $\text{BaFe}_2\text{X}_3$ ( $X = \text{S}, \text{Se}$ ) compounds

Z. V. Popović, M. Šćepanović, N. Lazarević, and M. Opačić

*Center for Solid State Physics and New Materials, Institute of Physics Belgrade, University of Belgrade, Pregrevica 118, 11080 Belgrade, Serbia*

M. M. Radonjić

*Scientific Computing Laboratory, Institute of Physics Belgrade, University of Belgrade, Pregrevica 118, 11080 Belgrade, Serbia, and Center for Electronic Correlations and Magnetism, Theoretical Physics III, Institute of Physics, University of Augsburg, D-86135 Augsburg, Germany*

D. Tanasković

*Scientific Computing Laboratory, Institute of Physics Belgrade, University of Belgrade, Pregrevica 118, 11080 Belgrade, Serbia*

Hechang Lei (雷和畅)\* and C. Petrovic

*Condensed Matter Physics and Materials Science Department, Brookhaven National Laboratory, Upton, New York 11973-5000, USA*

(Received 20 May 2014; revised manuscript received 31 December 2014; published 27 February 2015)

We present the Raman scattering spectra of the  $\text{BaFe}_2\text{X}_3$  ( $X = \text{S}, \text{Se}$ ) compounds in a temperature range between 20 and 400 K. Although the crystal structures of these two compounds are both orthorhombic and very similar, they are not isostructural. The unit cell of  $\text{BaFe}_2\text{S}_3$  ( $\text{BaFe}_2\text{Se}_3$ ) is base-centered  $Cmcm$  (primitive  $Pnma$ ), giving 18 (36) modes to be observed in the Raman scattering experiment. We have detected almost all Raman active modes, predicted by factor group analysis, which can be observed from the cleavage planes of these compounds. Assignment of the observed Raman modes of  $\text{BaFe}_2\text{S}(\text{Se})_3$  is supported by the lattice dynamics calculations. The antiferromagnetic long-range spin ordering in  $\text{BaFe}_2\text{Se}_3$  below  $T_N = 255$  K leaves a fingerprint both in the  $A_{1g}$  and  $B_{3g}$  phonon mode linewidth and energy.

DOI: [10.1103/PhysRevB.91.064303](https://doi.org/10.1103/PhysRevB.91.064303)

PACS number(s): 78.30.-j, 63.20.D-, 75.50.-y, 74.70.Xa

### I. INTRODUCTION

Iron-based compounds are one of the top research fields in condensed matter physics [1]. These materials are not only superconducting [2] but also form low-dimensional magnetic structures—spin chains, spin ladders, or spin dimers [3], similar to the cases of cuprates [4] or vanadates [5]. Properties of iron-based selenide superconductors and other low-dimensional magnetic phases of iron-chalcogenides are reviewed in Ref. [6].

$\text{BaFe}_2\text{S}_3$  and  $\text{BaFe}_2\text{Se}_3$  belong to the family of the iron-based  $S = 2$  two-leg spin-ladder compounds. The crystal structure of these materials can be described as alternate stacking of Fe-S(Se) layers and Ba cations along the crystallographic  $a$  axis ( $b$  axis). In the Fe-S(Se) plane, only one-dimensional (1D) double chains of edge-shared  $[\text{FeS}(\text{Se})_4]$  tetrahedra propagate along the  $a$  axis ( $b$  axis), as shown in Fig. 1. Although the crystal structures of the  $\text{BaFe}_2\text{S}_3$  and  $\text{BaFe}_2\text{Se}_3$  are isomorphic, they are not isostructural.  $\text{BaFe}_2\text{S}_3$  crystallizes in a base-centered orthorhombic structure with  $Cmcm$  space group [7]. The unit cell of  $\text{BaFe}_2\text{Se}_3$  is also orthorhombic but primitive of the  $Pmna$  space group. The main crystal structure difference of these compounds is an alternation of the Fe-Fe distances in  $\text{BaFe}_2\text{Se}_3$  along the chain direction which does not exist in  $\text{BaFe}_2\text{S}_3$ , where all distances between Fe atoms along the chain direction are the same;

see Figs. 1(b) and 1(c). This difference probably leads to the diverse magnetic properties of these two compounds at low temperatures.

$\text{BaFe}_2\text{S}_3$  is a quasi-one-dimensional semiconductor. The magnetic susceptibility of  $\text{BaFe}_2\text{S}_3$ , measured at 100 Oe, showed the divergence of the field-cooled susceptibility and zero-field-cooled susceptibility with the cusp at 25 K (freezing temperature) [8], indicating the presence of short-range magnetic correlations and spin-glass-like behavior below 25 K. On the basis of these observations Gönen *et al.* [8] proposed that each  $[\text{Fe}_2\text{S}_3]^{2-}$  chain possess strong intrachain antiferromagnetic coupling of Fe ions that is mediated through the sulfide ions. The combination of antiferromagnetic coupling, additional crystal field splitting due to neighboring Fe atoms, and direct Fe-Fe interactions presumably give rise to  $S = 0$  ground states in this compound [8].

$\text{BaFe}_2\text{Se}_3$  is an insulator down to the lowest measured temperature with a long-range antiferromagnetic (AFM) order with  $T_N$  around 255 K and short-range AFM order at higher temperatures [9–12]. It was shown that a dominant order involves  $2 \times 2$  blocks of ferromagnetically aligned four iron spins, whereas these blocks order antiferromagnetically in the same manner as the block AFM  $\sqrt{5} \times \sqrt{5}$  state of the iron vacancy ordered  $\text{A}_2\text{Fe}_4\text{Se}_5$  [13–15].

To the best of our knowledge there are no data about the phonon properties of these compounds. In this paper we have measured polarized Raman scattering spectra of  $\text{BaFe}_2\text{X}_3$  ( $X = \text{S}, \text{Se}$ ) in the temperature range between 20 and 400 K. We have observed the Raman active optical phonons, which are assigned using polarized measurements and the lattice dynamical calculations. At temperatures below

\*Present address: Department of Physics, Renmin University of China, 59 Zhongguancun Street, Haidian District, Beijing 100872, China.

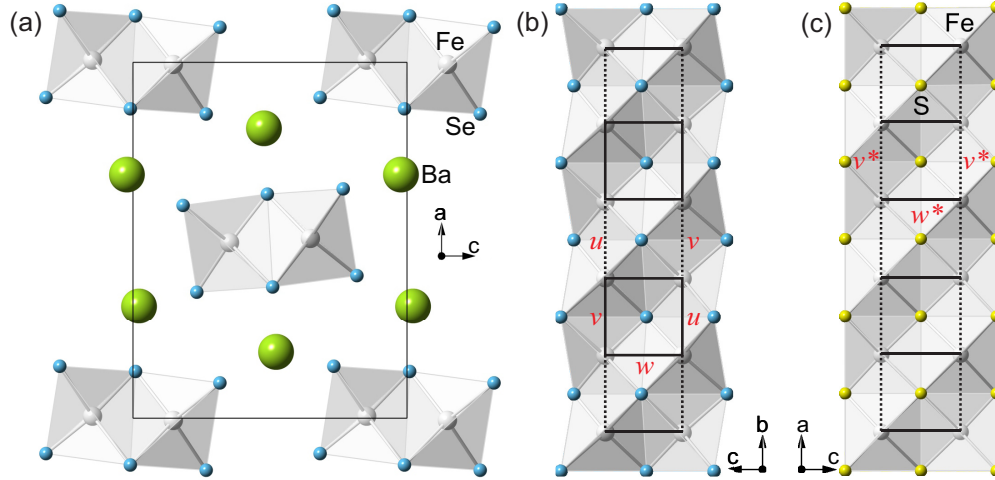


FIG. 1. (Color online) Schematic representation of the  $\text{BaFe}_2X_3$  ( $X = \text{S}, \text{Se}$ ) crystal structure. (a) Projection of the  $\text{BaFe}_2\text{Se}_3$  crystal structure in the  $(ac)$  plane. (b) The double chain of Fe-Se tetrahedra connected via common edges along the  $b$  axis. (c) The Fe-S double chain in the  $(010)$  projection.  $w, u, v$  represents Fe-Fe distances of ladder rungs ( $w = 0.2697$  nm;  $w^* = 0.2698$  nm) and legs ( $u = 0.2688$  nm,  $v = 0.2720$  nm;  $v^* = 0.2643$  nm). Note that in the case of  $\text{BaFe}_2\text{S}_3$  the Fe atoms form an “ideal” ladder (all Fe-Fe distances along the ladder legs are equivalent, which is not the case in  $\text{BaFe}_2\text{Se}_3$ ).

$T_N = 255$  K in  $\text{BaFe}_2\text{Se}_3$  the Raman modes shows an abrupt change of energy and linewidth due to the antiferromagnetic spin ordering.

## II. EXPERIMENT AND NUMERICAL METHOD

Single crystals of  $\text{BaFe}_2X_3$  ( $X = \text{S}, \text{Se}$ ) were grown using self-flux method with nominal composition  $\text{Ba:Fe:X} = 1:2:3$ . Details were described in Ref. [16]. Raman scattering measurements were performed on  $(110)$ (sulfide) [ $(100)$  (selenide)]-oriented samples in the backscattering micro-Raman configuration. Low-temperature measurements were performed using KONTI CryoVac continuous flow cryostat coupled with JY T64000 and TriVista 557 Raman systems. The 514.5-nm line of an  $\text{Ar}^+/\text{Kr}^+$  mixed gas laser was used as excitation source. The Raman scattering measurements at higher temperatures were done using a LINKAM THMS600 heating stage.

We calculated phonon energies of the nonmagnetic  $\text{BaFe}_2\text{S}(\text{Se})_3$  single crystals at the center of the Brillouin zone. Calculations were performed within the theory of linear response using the density functional perturbation theory (DFPT) [17] as implemented in the QUANTUM ESPRESSO package [18]. In the first step, we obtained the electronic structure by applying the pseudopotentials based on the projected augmented waves method with the Perdew-Burke-Ernzerhof exchange-correlation functional and nonlinear core correction. Used energy cutoffs for the wave functions and electron densities were 80 (64) Ry and 960 (782) Ry for  $\text{BaFe}_2\text{S}(\text{Se})_3$ , respectively. We have carried out the calculation with experimental values of the  $\text{BaFe}_2\text{S}(\text{Se})_3$  unit cell parameters  $a = 0.87835$  nm,  $b = 1.1219$  nm,  $c = 0.5286$  nm [7] ( $a = 1.18834$  nm,  $b = 0.54141$  nm,  $c = 0.91409$  nm [11]), and the relaxed fractional coordinates; see Table I. Relaxation was applied to place atoms in their equilibrium positions in respect to used pseudopotentials (all forces acting on every atom were smaller than  $10^{-4}$  Ry/a.u.). The difference between experimental and relaxed coordinates is less than 3% for almost

all atom coordinates, except for the  $x$  direction of the Ba atoms in  $\text{BaFe}_2\text{Se}_3$ , which is 6%. Reduction of the  $x$  coordinate of Ba atoms by relaxation leads to an increase of the distance between the Ba layers. The Brillouin zone was sampled with  $8 \times 8 \times 8$  Monkhorst-Pack  $\mathbf{k}$ -space mesh. Calculated  $\Gamma$  point phonon energies of the  $\text{BaFe}_2\text{S}_3$  and  $\text{BaFe}_2\text{Se}_3$  are listed in Tables II and Table IV, respectively.

The DFPT calculation of the phonon-mode energies is performed assuming the paramagnetic solution and the comparison of energies is performed with the experimental results at room temperature. The paramagnetic density functional theory (DFT) solution is metallic, whereas  $\text{BaFe}_2\text{Se}_3$  is AFM insulator at low temperatures. Therefore, we have performed also the spin-polarized DFT calculations, assuming AFM ordering of  $2 \times 2$  ferromagnetic iron blocks [10–12]. We find the AFM solution and opening of the gap at the Fermi level in agreement with earlier DFT calculations by Saparov *et al.* [10]. Accordingly, we attempted to calculate the phonon

TABLE I. Experimental and relaxed (in square brackets) fractional coordinates of  $\text{BaFe}_2\text{S}_3$  (Ref. [7]) and  $\text{BaFe}_2\text{Se}_3$  (Ref. [11]) crystal structures.

Atom	Site	$x$	$y$	$z$
<b><math>\text{BaFe}_2\text{S}_3</math></b>				
Ba	(4c)	0.50 [0.50]	0.1859 [0.1817]	0.25 [0.25]
Fe	(8e)	0.3464 [0.3553]	0.50 [0.50]	0.00 [0.00]
S1	(4c)	0.50 [0.50]	0.6147 [0.6051]	0.25 [0.25]
S2	(8g)	0.2074 [0.2108]	0.3768 [0.3945]	0.25 [0.25]
<b><math>\text{BaFe}_2\text{Se}_3</math></b>				
Ba	(4c)	0.186 [0.175]	0.25 [0.25]	0.518 [0.513]
Fe	(8d)	0.493 [0.490]	0.002 [−0.001]	0.353 [0.358]
Se1	(4c)	0.355 [0.366]	0.25 [0.25]	0.233 [0.230]
Se2	(4c)	0.630 [0.613]	0.25 [0.25]	0.491 [0.485]
Se3	(4c)	0.402 [0.415]	0.25 [0.25]	0.818 [0.809]

TABLE II. Calculated and experimentally observed values of Raman active phonon mode energies (in cm<sup>-1</sup>) of BaFe<sub>2</sub>S<sub>3</sub> single crystal.

Symmetry	Calculation		Experiment		Activity	Symmetry	Calculation		Experiment		Activity
	relax. (unrelax.)		300 K	100 K			relax. (unrelax.)	300 K	100 K		
A <sub>g</sub> <sup>1</sup>	42.3 (51.2)			39	(xx,yy,zz)	B <sub>1g</sub> <sup>1</sup>	16.7 (63)				(xy)
A <sub>g</sub> <sup>2</sup>	154.2 (156)			157	(xx,yy,zz)	B <sub>1g</sub> <sup>2</sup>	55.1 (81.8)	44	48		(xy)
A <sub>g</sub> <sup>3</sup>	201.9 (167.4)	152	165		(xx,yy,zz)	B <sub>1g</sub> <sup>3</sup>	138.8 (153.1)	127	133		(xy)
A <sub>g</sub> <sup>4</sup>	366.9 (294.8)	295	301		(xx,yy,zz)	B <sub>1g</sub> <sup>4</sup>	243.5 (221.9)	203	214		(xy)
A <sub>g</sub> <sup>5</sup>	385.8 (307.1)	365	372		(xx,yy,zz)	B <sub>1g</sub> <sup>5</sup>	337.8 (241.6)		332(?)		(xy)
						B <sub>1g</sub> <sup>6</sup>	400.2 (330)	374	381		(xy)
B <sub>2g</sub> <sup>1</sup>	107.8 (113.7)	107	109		(xz)	B <sub>3g</sub> <sup>1</sup>	55.1 (66.8)				(yz)
B <sub>2g</sub> <sup>2</sup>	224.1 (180.8)	181	193		(xz)	B <sub>3g</sub> <sup>2</sup>	201.1 (171.1)	181	193		(yz)
B <sub>2g</sub> <sup>3</sup>	347.8 (283.6)				(xz)	B <sub>3g</sub> <sup>3</sup>	311.2 (308.7)	297	307		(yz)
						B <sub>3g</sub> <sup>4</sup>	369.3 (351.7)				(yz)

energies in the spin-polarized case. However, having now 48 atoms in the unit cell, this calculation turned out to be computationally too demanding. Furthermore, we do not believe that such a calculations would gives us in this case important new insights since the number of phonon modes becomes  $2 \times 72 - 1 = 143$  (one mode is degenerate), and it is not likely that small splitting of the modes could be compared with the experiments. Also, the phonon frequencies are not particularly sensitive on the precise form of the density of states near the Fermi level (or gap opening) if the overall spectral function remains similar. Therefore, we believe that the usage of the nonmagnetic DFT is a reasonable method for identification of vibrational modes and comparison with the experimental data.

### III. RESULTS AND DISCUSSION

#### A. BaFe<sub>2</sub>S<sub>3</sub>

The BaFe<sub>2</sub>S<sub>3</sub> crystal symmetry is orthorhombic, space group *Cmcm* and  $Z = 4$  [7]. The site symmetries of atoms in *Cmcm* space group are  $C_{2v}^y$  (Ba, S1),  $C_2^x$  (Fe), and  $C_s^{xy}$  (S2). Factor group analysis yields

$$(C_{2v}^y): \Gamma = A_g + B_{1g} + B_{3g} + B_{1u} + B_{2u} + B_{3u},$$

$$(C_2^x): \Gamma = A_g + 2B_{1g} + 2B_{2g} + B_{3g} \\ + A_u + 2B_{1u} + 2B_{2u} + B_{3u}.$$

$$(C_s^{xy}): \Gamma = 2A_g + 2B_{1g} + B_{2g} + B_{3g} + A_u \\ + B_{1u} + 2B_{2u} + 2B_{3u}.$$

Summarizing these representations and subtracting the acoustic ( $B_{1u} + B_{2u} + B_{3u}$ ) and silent ( $2A_u$ ) modes, we obtained the following irreducible representations of BaFe<sub>2</sub>S<sub>3</sub> vibrational modes:

$$\Gamma_{\text{BaFe}_2\text{S}_3}^{\text{optical}} = 5A_g(xx,yy,zz) + 6B_{1g}(xy) + 3B_{2g}(xz) \\ + 4B_{3g}(yz) + 4B_{1u}(E \parallel z) + 5B_{2u}(E \parallel y) \\ + 4B_{3u}(E \parallel x).$$

Thus 18 Raman and 13 infrared active modes are expected to be observed in the BaFe<sub>2</sub>S<sub>3</sub> infrared and Raman spectra. Because

our BaFe<sub>2</sub>S<sub>3</sub> single-crystal samples have (110) orientation, we were able to observe all symmetry modes in the Raman scattering experiment.

The polarized Raman spectra of BaFe<sub>2</sub>S<sub>3</sub>, measured from the (110) plane at 100 K, are given in Fig. 2. Five  $A_g$  symmetry modes at about 39, 157, 165, 301, and 373 cm<sup>-1</sup> (100 K) are clearly observed for the  $x'(zz)\bar{x}'$  polarization configuration ( $x' = [110]$ ,  $y' = [1\bar{1}0]$ ,  $z = [001]$ ). For parallel polarization along the  $y'$  axis, the  $A_g$  and  $B_{1g}$  symmetry modes may be observed. By comparison ( $y'y'$ ) with ( $zz$ ) polarized spectrum we assigned the modes at 48, 133, 214, 332, and 381 cm<sup>-1</sup> as the  $B_{1g}$  ones. The intensity of the 332 cm<sup>-1</sup> mode is at a level of noise. Because of that, assignment of this mode as  $B_{1g}^5$  should be taken as tentative.

For the  $x'(y'z)\bar{x}'$  polarization configuration both the  $B_{2g}$  and the  $B_{3g}$  symmetry modes can be observed. Because we cannot distinguish the  $B_{2g}$  and  $B_{3g}$  by selection rules from the (110) plane, the assignment of these modes was done with help of the lattice dynamics calculation; see Table II. Features between 40 and 100 cm<sup>-1</sup> come after subtracting of nitrogen

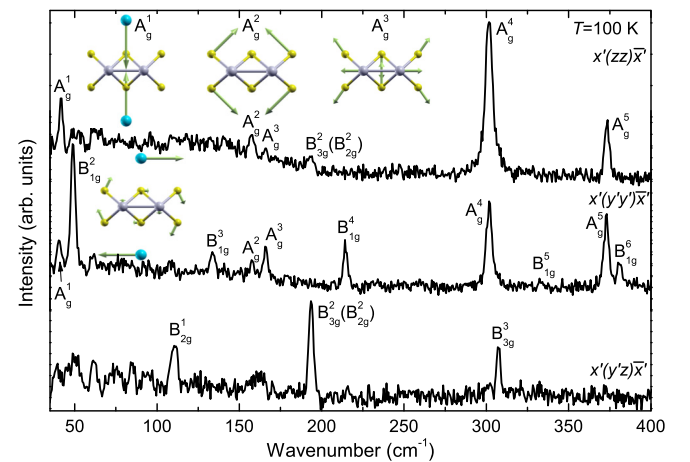


FIG. 2. (Color online) The polarized Raman scattering spectra of BaFe<sub>2</sub>S<sub>3</sub> single crystal measured at 100 K. Insets are the normal modes of the  $A_g^1$ ,  $A_g^2$ ,  $A_g^3$ , and  $B_{1g}^1$  vibrations.  $x' = [110]$ ,  $y' = [1\bar{1}0]$ , and  $z = [001]$ .

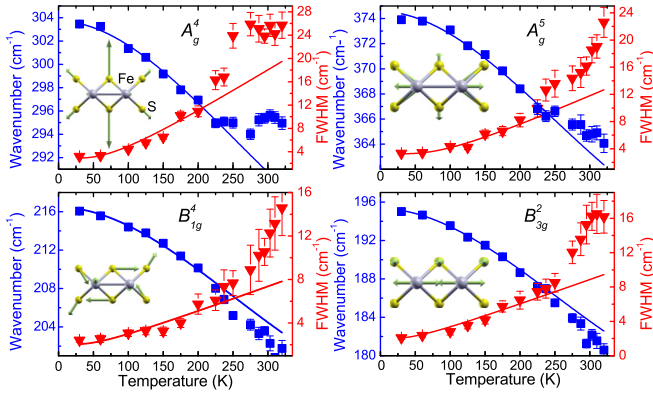


FIG. 3. (Color online) Experimental values (symbols) and calculated temperature dependence (solid lines) of the  $\text{BaFe}_2\text{S}_3$  Raman mode energies and broadenings. Insets represent the normal modes of the  $A_g^4$ ,  $A_g^5$ ,  $B_{1g}^4$ , and  $B_{3g}^2$  vibrations.

vibration modes. Bump at about  $160 \text{ cm}^{-1}$  is a leakage of  $A_g^2$  and  $A_g^3$  modes from parallel polarization.

The normal modes of some of  $A_g$ ,  $B_{1g}$ , and  $B_{3g}$  vibrations, obtained by the lattice dynamics calculations, are given as insets in Figs. 2 and 3. According to these representations the lowest energy  $A_g^1$  mode ( $39 \text{ cm}^{-1}$ ) originates from the Ba atom vibrations along the  $y$  axis, and the  $A_g^2$  mode ( $157 \text{ cm}^{-1}$ ) represents dominantly S atom vibrations, which tend to elongate  $[\text{Fe}_2\text{S}_3]^{2-}$  chains along the  $y$  axis. The  $A_g^3$  mode originates from both the sulfur and the iron atom vibrations, which tend to stretch ladders along the  $x$  axis. The  $A_g^4$  mode (Fig. 3) is sulfur atoms breathing vibrations, and the  $A_g^5$  symmetry mode represents the S and Fe atom vibrations with the opposite tendency. The Fe atoms vibrate in opposite directions along the  $x$  axis, elongating the ladder, together with S atom vibrations, which tend to compress ladder structure.

Temperature dependence of the  $A_g^4$ ,  $A_g^5$ ,  $B_{1g}^4$ , and  $B_{3g}^2$  mode energy and linewidth are given in Fig. 3.

In general, temperature dependance of Raman mode energy can be described with [19]

$$\omega(T) = \omega_0 + \Delta(T), \quad (1)$$

where  $\omega_0$  is temperature-independent contribution to the energy of the phonon mode, whereas  $\Delta(T)$  can be decomposed in

$$\Delta(T) = \Delta^V + \Delta^A. \quad (2)$$

The first term in Eq. (2) represents change of phonon energy due to the thermal expansion of the crystal lattice, and is given by [20]

$$\Delta^V = -\omega_0 \gamma \frac{\Delta V(T)}{V_0}, \quad (3)$$

where  $\gamma$  is the Grüneisen parameter of a given mode.

The second term in Eq. (2) is a contribution to the Raman mode energy from phonon-phonon scattering. By taking into account only three-phonon processes,

$$\Delta^A = -C \left( 1 + \frac{4\lambda_{\text{ph-ph}}}{e^{\hbar\omega_0/2k_B T} - 1} \right). \quad (4)$$

TABLE III. The best fit parameters of  $\text{BaFe}_2\text{S}_3$  and  $\text{BaFe}_2\text{Se}_3$ .

Mode symmetry	$\omega_0(\text{cm}^{-1})$	$\gamma$	$\Gamma_0(\text{cm}^{-1})$	$\lambda$
<b>BaFe<sub>2</sub>S<sub>3</sub></b>				
$A_g^4$	303.7(2)	3.7(2)	2.9(2)	2.8(5)
$A_g^5$	374.6(2)	2.6(2)	3.3(2)	1.9(3)
$B_{1g}^4$	216.5(2)	4.8(2)	2.0(3)	0.9(3)
$B_{3g}^2$	195.3(1)	5.2(2)	2.0(3)	1.0(1)
<b>BaFe<sub>2</sub>Se<sub>3</sub></b>				
$A_g^8$	200.0(1)	1.6(2)	2.3(1)	0.4(1)
$A_g^9$	272.6(2)	1.4(1)	2.3(1)	0.6(1)
$A_g^{10}$	288.1(3)	1.8(2)	5.2(1)	0.3(1)
$A_g^{11}$	297.1(4)	1.4(2)	5.6(2)	0.4(1)

$C$  and  $\lambda_{\text{ph-ph}}$  are the anharmonic constant and phonon-phonon interaction constant, respectively.

Temperature dependence of Raman mode linewidth is caused only by phonon anharmonicity:

$$\Gamma(T) = \Gamma_0 \left( 1 + \frac{2\lambda_{\text{ph-ph}}}{e^{\hbar\omega_0/2k_B T} - 1} \right), \quad (5)$$

where  $\Gamma_0$  is the anharmonic constant.

Parameter  $C$  is connected with  $\omega_0$  and  $\Gamma_0$  via relation [19]

$$C = \frac{\Gamma_0^2}{2\omega_0}. \quad (6)$$

$\omega_0$  and  $\Gamma_0$  can be determined by extrapolation of the corresponding experimental data to 0 K. With these parameters known, we can fit the phonon mode linewidth, using Eq. (5), to obtain  $\lambda_{\text{ph-ph}}$ . Then, by determining parameter  $C$  via Eq. (6), Raman mode energy can be properly fitted, with  $\gamma$  as the only unknown parameter. Using data from Ref. [12] for the temperature change of the lattice constants of  $\text{BaFe}_2\text{Se}_3$  one can perform the corresponding analysis of the Raman mode energies' temperature dependence.

The best-fit parameters are collected in Table III. Because the  $\Gamma_0$  is very small in comparison to  $\omega_0$ , for all modes of both compounds (Table III), according to Eq. (6) the  $C$  anharmonic parameter becomes very small. Thus, contribution to the Raman mode energy from the phonon-phonon interaction can be neglected. In fact, a change of Raman mode energy with temperature is properly described only with the thermal expansion term  $\Delta^V$ , Eq. (3).

The most intriguing finding in Fig. 3 is a dramatic change of slope of the  $A_g^4$  mode linewidth (energy) temperature dependence at about 275 K. Because a hump in the inverse molar magnetic susceptibility [8] and a change of slope of the electrical resistivity [21] temperature dependence are observed in  $\text{BaFe}_2\text{S}_3$  at about the same temperature we concluded that the deviation from anharmonic behavior for  $A_g^4$  mode could be related to spin and charge. In fact, many of iron-based spin-ladder materials have the 3D-antiferromagnetic phase transition at about 260 K. We believe that in the case of  $\text{BaFe}_2\text{S}_3$  the antiferromagnetic ordering of spins within the ladder legs changes from short-range to the long-range state, without 3D antiferromagnetic spin ordering (the Néel state) of the whole crystal. This transition is followed with change

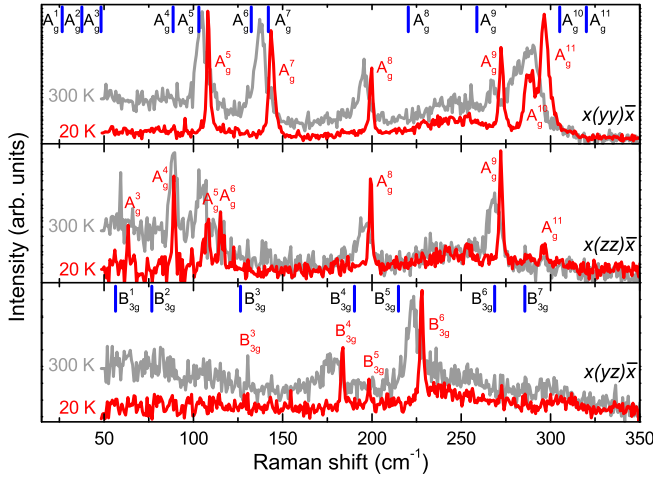


FIG. 4. (Color online) The  $x(yy)\bar{x}$ ,  $x(zz)\bar{x}$ , and  $x(yz)\bar{x}$  polarized Raman scattering spectra of BaFe<sub>2</sub>Se<sub>3</sub> single crystals measured at room temperature and at 20 K. Vertical bars are calculated values of the  $A_g$  and the  $B_{3g}$  symmetry Raman active vibrations.

of the electronic structure, which could explain the abrupt increase of the resistivity at this temperature [21]. A lack of the BaFe<sub>2</sub>Se<sub>3</sub> low-temperature crystallographic and transport properties measurements did not allow a more detailed study of a possible origin of the phonon energy and linewidth deviation from the anharmonic picture at about 275 K.

### B. BaFe<sub>2</sub>Se<sub>3</sub>

The BaFe<sub>2</sub>Se<sub>3</sub> unit cell consists of four formula units comprising of 24 atoms. The site symmetries of atoms in

$Pnma$  space group are  $C_s^{xz}$  (Ba, Se1, Se2, Se3) and  $C_1$  (Fe). Factor group analysis yields

$$(C_s^{xz}): \Gamma = 2A_g + 1B_{1g} + 2B_{2g} + 1B_{3g} \\ + A_u + 2B_{1u} + 1B_{2u} + 2B_{3u},$$

$$(C_1): \Gamma = 3A_g + 3B_{1g} + 3B_{2g} + 3B_{3g} \\ + 3B_{1u} + 3B_{2u} + 3B_{3u}.$$

Summarizing these representations and subtracting the acoustic ( $B_{1u} + B_{2u} + B_{3u}$ ) and silent ( $4A_u$ ) modes, we obtained the following irreducible representations of BaFe<sub>2</sub>Se<sub>3</sub> vibrational modes:

$$\Gamma_{\text{BaFe}_2\text{Se}_3}^{\text{optical}} = 11A_g + 7B_{1g} + 11B_{2g} + 7B_{3g} \\ + 11B_{1u} + 7B_{2u} + 11B_{3u}$$

Thus 36 Raman and 29 infrared active modes are expected to be observed in the BaFe<sub>2</sub>Se<sub>3</sub> vibrational spectra. Because the BaFe<sub>2</sub>Se<sub>3</sub> single crystals have the (100) orientation (the crystallographic  $a$  axis is perpendicular to the plane of the single crystal), we were able to access only the  $A_g$  and the  $B_{3g}$  symmetry modes in the Raman scattering experiment.

The polarized Raman spectra of BaFe<sub>2</sub>Se<sub>3</sub>, measured from (100) plane at room temperature and 20 K, for the parallel and crossed polarization configurations, are given in Fig. 4. The spectra measured for parallel polarization configurations consist of the  $A_g$  symmetry modes. Six modes at about 108, 143.5, 200, 272, 288.7, and 296.5 cm<sup>-1</sup> (20 K) are clearly observed for the  $x(yy)\bar{x}$  polarization configuration and three additional modes are observed at about 63.4, 89, and 115 cm<sup>-1</sup> for the  $x(zz)\bar{x}$  polarization configuration. For the  $x(yz)\bar{x}$  polarization configuration, three Raman active  $B_{3g}$  symmetry

TABLE IV. Calculated and experimentally observed values of Raman active phonon mode energies (in cm<sup>-1</sup>) of BaFe<sub>2</sub>Se<sub>3</sub> single crystal.

Symmetry	Calc.	Experiment		Activity	Symmetry	Calc.	Experiment		Activity
		300 K	20 K				300 K	20 K	
$A_g^1$	26.5			(xx, yy, zz)	$B_{2g}^1$	25.8			(xz)
$A_g^2$	37.5			(xx, yy, zz)	$B_{2g}^2$	48.0			(xz)
$A_g^3$	48.3	59	63.4	(xx, yy, zz)	$B_{2g}^3$	68.7			(xz)
$A_g^4$	88.6	88	89	(xx, yy, zz)	$B_{2g}^4$	88.8			(xz)
$A_g^5$	103.0	104.3	108	(xx, yy, zz)	$B_{2g}^5$	100.4			(xz)
$A_g^6$	132.4	111	115	(xx, yy, zz)	$B_{2g}^6$	138.2			(xz)
$A_g^7$	142.0	137	143	(xx, yy, zz)	$B_{2g}^7$	144.5			(xz)
$A_g^8$	220.4	195.6	200	(xx, yy, zz)	$B_{2g}^8$	212.9			(xz)
$A_g^9$	258.8	267	272	(xx, yy, zz)	$B_{2g}^9$	261.7			(xz)
$A_g^{10}$	305.2	280	288.7	(xx, yy, zz)	$B_{2g}^{10}$	303.9			(xz)
$A_g^{11}$	320.2	290	296.5	(xx, yy, zz)	$B_{2g}^{11}$	321.5			(xz)
$B_{1g}^1$	56.4			(xy)	$B_{3g}^1$	56.4			(yz)
$B_{1g}^2$	72.8			(xy)	$B_{3g}^2$	76.7			(yz)
$B_{1g}^3$	126.2			(xy)	$B_{3g}^3$	126.4			(yz)
$B_{1g}^4$	191.4			(xy)	$B_{3g}^4$	190.2	177	183.8	(yz)
$B_{1g}^5$	210.5			(xy)	$B_{3g}^5$	214.9		198	(yz)
$B_{1g}^6$	267.1			(xy)	$B_{3g}^6$	268.8	222.8	228	(yz)
$B_{1g}^7$	285.2			(xy)	$B_{3g}^7$	285.7			(yz)



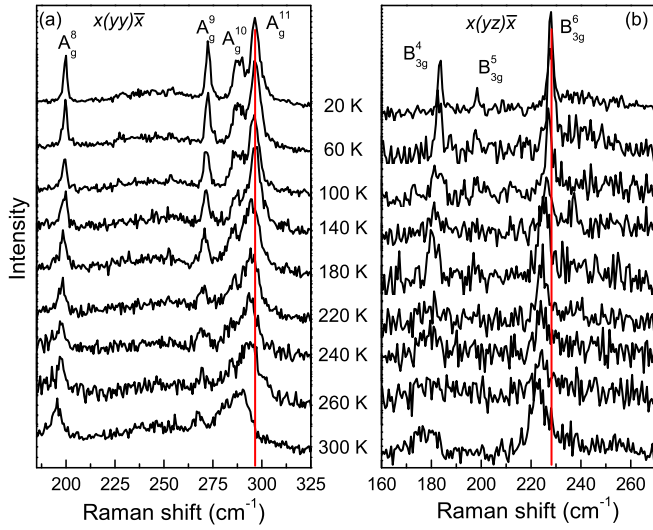


FIG. 5. (Color online) The polarized Raman spectra of  $\text{BaFe}_2\text{Se}_3$  single crystals measured at various temperatures. (a)  $x(yy)\bar{x}$  polarization configuration; (b)  $x(yz)\bar{x}$  polarization configuration.

modes at 183.8, 198, and 228  $\text{cm}^{-1}$  (20 K) are observed. Vertical bars in Fig. 4 denote the calculated energies of the  $A_g$  and  $B_{3g}$  symmetry modes, which are in rather good agreement with experimentally observed ones. The results of the lattice dynamics calculations, together with the experimental data, are summarized in Table IV.

According to the lattice dynamics calculations the lowest energy  $A_g^1$  mode is dominated by Ba atom vibrations along the  $\langle 101 \rangle$  directions and the  $A_g^2$  mode represents vibrations of Fe and Se atoms which tend to rotate  $[\text{Fe}_2\text{Se}_3]^{2-}$  chains around of the  $b$  axis. The  $A_g^3$  mode involves all atom vibrations, which tend to stretch crystal structure along the  $\langle 101 \rangle$  directions, whereas the  $A_g^4$  mode originates from Se atom vibrations along the  $c$  axis and the Fe atom vibrations along the  $\langle 101 \rangle$  directions. The  $A_g^5$  mode represents vibration of Fe and Se atoms, which leads to  $[\text{Fe}_2\text{Se}_3]^{2-}$ -chain compression along the  $c$  axis. The  $A_g^6$  mode originates from Se and Fe atom vibrations which stretch  $[\text{Fe}_2\text{Se}_3]^{2-}$  chains along the  $c$  axis. Finally, the  $A_g^7$  mode originates from Fe atom vibrations toward each other along the chain direction together with vibrations of the Se atoms along the  $c$  axis. The normal coordinates of the  $A_g^8$ ,  $A_g^9$ ,  $A_g^{10}$ , and  $A_g^{11}$  modes are given as insets in Fig. 6. As can be seen from Fig. 6 the  $A_g^8$  mode originates dominantly from Se atom stretching vibrations, whereas the  $A_g^9$ ,  $A_g^{10}$ , and  $A_g^{11}$  modes represent vibrations of both the Se and Fe atoms. In fact, the  $A_g^9$  mode represents mostly Se atom vibrations along the  $c$  axis, and the  $A_g^{10}$  mode consists of Fe and Se vibrations along the  $c$  axis, which tend to elongate ladder structure along the  $b$  axis. Finally, the  $A_g^{11}$  mode represents the Fe atom vibrations toward each other along the chain axis, together with Se atom vibrations perpendicular to the chain direction.

By lowering the temperature, the lattice parameters of  $\text{BaFe}_2\text{Se}_3$  decrease continuously without the crystal symmetry change around the magnetic ordering temperature [11,12]  $T_N = 255$  K. Consequently we should expect the Raman mode hardening, without any abrupt change. Contrary to

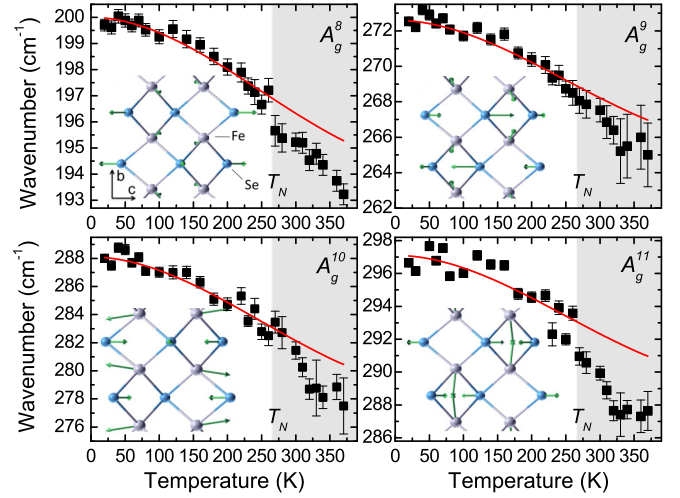


FIG. 6. (Color online) Experimental values (symbols) and calculated temperature dependence (solid lines) of  $\text{BaFe}_2\text{Se}_3$  Raman mode energies. The best-fit parameters, for the temperature range below  $T_N$ , are given in Table III. Insets represent normal modes of the  $A_g^8$ ,  $A_g^9$ ,  $A_g^{10}$ , and  $A_g^{11}$  vibrations.

expectations, the  $A_g$  and  $B_{3g}$  modes (see Figs. 5, 6, and 7) sharply increase their energies below the phase transition temperature  $T_N$ , as shown in details in Fig. 6. Because a significant local lattice distortion (Fe atom displacement along

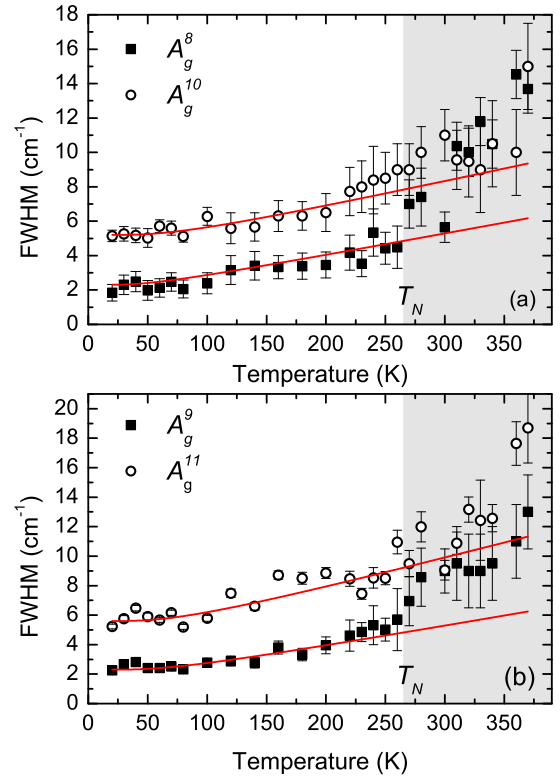


FIG. 7. (Color online) Linewidth vs temperature dependence of (a)  $A_g^8$  and  $A_g^{10}$  modes and (b)  $A_g^9$  and  $A_g^{11}$  modes of  $\text{BaFe}_2\text{Se}_3$ . Solid lines are calculated using Eq. (5). The best-fit parameters for a temperature range below  $T_N$  are given in Table III.

the  $b$  axis is as large as approximately 0.001 nm) [11,12] exists, driven by the magnetic order, we concluded that spin-phonon (magnetoelastic) coupling is responsible for Raman mode energy and linewidth change in the antiferromagnetic phase. In fact, the existence of local displacements in the Fe atoms at  $T_N$  have a significant impact on the electronic structure due to rearrangement of electrons near the Fermi level [11] and consequently the change in the phonon energy and broadening. Raman mode linewidth change at about  $T_N$  is clearly observed as deviation from the usual anharmonicity temperature dependence (solid lines in Fig. 7) for all modes presented in Fig. 6.

#### IV. CONCLUSION

We have measured the polarized Raman scattering spectra of the  $\text{BaFe}_2\text{S}_3$  and  $\text{BaFe}_2\text{Se}_3$  single crystals in a temperature range between 20 and 400 K. Almost all Raman-active modes predicted by factor-group analysis to be observed from the cleavage planes of  $\text{BaFe}_2\text{S}_3$  (110) and  $\text{BaFe}_2\text{Se}_3$  (100) single crystals are experimentally detected and assigned.

Energies of these modes are in rather good agreement with the lattice dynamics calculations. The  $\text{BaFe}_2\text{Se}_3$  Raman modes linewidth and energy change substantially at temperatures below  $T_N = 255$  K, where this compound becomes antiferromagnetically long-range ordered.

#### ACKNOWLEDGMENTS

This work was supported by the Ministry of Education, Science, and Technological Development of Republic of Serbia under Projects ON171032, ON171017, and III45018. Work at Brookhaven was supported by the Center for Emergent Superconductivity, an energy frontier research center funded by the US Department of Energy, Office for Basic Energy Science (H.L. and C.P.). Numerical simulations were run on the PARADOX supercomputing facility at the Scientific Computing Laboratory of the Institute of Physics Belgrade, supported in part by the Ministry of Education, Science, and Technological Development of Republic of Serbia under Project ON171017. M.M.R. acknowledges the Support by the Deutsche Forschungsgemeinschaft through Transregio TRR 80 and Research Unit FOR 1346.

- 
- [1] C. King and D. A. Pendlebury, Web of knowledge research fronts 2013: 100 top-ranked specialties in the sciences and social sciences, <http://sciencewatch.com/sites/sw/files/sw-article/media/research-fronts-2013.pdf>
- [2] Y. Kamihara, T. Watanabe, M. Hirano, and H. Hosono, *J. Am. Chem. Soc.* **130**, 3296 (2008).
- [3] Z. V. Popović, M. Šćepanović, N. Lazarević, M. M. Radonjić, D. Tanasković, H. Lei, and C. Petrovic, *Phys. Rev. B* **89**, 014301 (2014).
- [4] Z. V. Popović, M. J. Konstantinović, V. A. Ivanov, O. P. Khuong, R. Gajić, A. Vietkin, and V. V. Moshchalkov, *Phys. Rev. B* **62**, 4963 (2000).
- [5] M. J. Konstantinović, Z. V. Popović, M. Isobe, and Y. Ueda, *Phys. Rev. B* **61**, 15185 (2000).
- [6] E. Dagotto, *Rev. Mod. Phys.* **85**, 849 (2013).
- [7] H. Hong and H. Steinfink, *J. Solid State Chem.* **5**, 93 (1972).
- [8] Z. S. Gönen, P. Fournier, V. Smolyaninova, R. Greene, F. M. Araujo-Moreira, and B. Eichhorn, *Chem. Mater.* **12**, 3331 (2000).
- [9] H. Lei, H. Ryu, A. I. Frenkel, and C. Petrovic, *Phys. Rev. B* **84**, 214511 (2011).
- [10] B. Saporov, S. Calder, B. Sipos, H. Cao, S. Chi, D. J. Singh, A. D. Christianson, M. D. Lumsden, and A. S. Sefat, *Phys. Rev. B* **84**, 245132 (2011).
- [11] J. M. Caron, J. R. Neilson, D. C. Miller, A. Llobet, and T. M. McQueen, *Phys. Rev. B* **84**, 180409 (2011).
- [12] Y. Nambu, K. Ohgushi, S. Suzuki, F. Du, M. Avdeev, Y. Uwatoko, K. Munakata, H. Fukazawa, S. Chi, Y. Ueda, and T. J. Sato, *Phys. Rev. B* **85**, 064413 (2012).
- [13] F. Ye, S. Chi, W. Bao, X. F. Wang, J. J. Ying, X. H. Chen, H. D. Wang, C. H. Dong, and M. Fang, *Phys. Rev. Lett.* **107**, 137003 (2011).
- [14] N. Lazarević, M. Abeykoon, P. W. Stephens, H. Lei, E. S. Bozin, C. Petrovic, and Z. V. Popović, *Phys. Rev. B* **86**, 054503 (2012).
- [15] N. Lazarević, H. Lei, C. Petrovic, and Z. V. Popović, *Phys. Rev. B* **84**, 214305 (2011).
- [16] H. Lei, H. Ryu, V. Ivanovski, J. B. Warren, A. I. Frenkel, B. Cekic, W.-G. Yin, and C. Petrovic, *Phys. Rev. B* **86**, 195133 (2012).
- [17] S. Baroni, S. de Gironcoli, A. Dal Corso, and P. Giannozzi, *Rev. Mod. Phys.* **73**, 515 (2001).
- [18] P. Giannozzi, S. Baroni, N. Bonini, M. Calandra, R. Car, C. Cavazzoni, D. Ceresoli, G. L. Chiarotti, M. Cococcioni, I. Dabo, A. D. Corso, S. de Gironcoli, S. Fabris, G. Fratesi, R. Gebauer, U. Gerstmann, C. Gougoussis, A. Kokalj, M. Lazzeri, L. Martin-Samos, N. Marzari, F. Mauri, R. Mazzarello, S. Paolini, A. Pasquarello, L. Paulatto, C. Sbraccia, S. Scandolo, G. Sclauzero, A. P. Seitsonen, A. Smogunov, P. Umari, and R. M. Wentzcovitch, *J. Phys.: Condens. Matter* **21**, 395502 (2009).
- [19] H.-M. Eiter, P. Jaschke, R. Hackl, A. Bauer, M. Gangl, and C. Pfeleiderer, *Phys. Rev. B* **90**, 024411 (2014).
- [20] V. Gnezdilov, Y. Pashkevich, P. Lemmens, A. Gusev, K. Lamonova, T. Shevtsova, I. Vitebskiy, O. Afanasiev, S. Gnatchenko, V. Tsurkan, J. Deisenhofer, and A. Loidl, *Phys. Rev. B* **83**, 245127 (2011).
- [21] W. Reiff, I. Grey, A. Fan, Z. Eliezer, and H. Steinfink, *J. Solid State Chem.* **13**, 32 (1975).

# Far-infrared spectroscopic study of CeO<sub>2</sub> nanocrystals

Z. V. Popović · M. Grujić-Brojčin · N. Paunović ·  
M. M. Radonjić · V. D. Araújo · M. I. B. Bernardi ·  
M. M. de Lima · A. Cantarero

Received: 20 August 2014 / Accepted: 5 January 2015  
© Springer Science+Business Media Dordrecht 2015

**Abstract** We present the far-infrared reflectivity spectra of 5 nm-sized pure and copper-doped Ce<sub>1-x</sub>Cu<sub>x</sub>O<sub>2-y</sub> ( $x = 0; 0.01$  and  $0.10$ ) nanocrystals measured at room temperature in the 50–650 cm<sup>-1</sup> spectral range. Reflectivity spectra were analyzed using the factorized form of the dielectric function, which includes the phonon and the free carriers contribution. Four oscillators with TO energies of approximately 135, 280, 370, and 490 cm<sup>-1</sup> were included in the fitting procedure. These oscillators represent local maxima of the CeO<sub>2</sub> phonon density of states, which is also calculated using the density functional theory. The lowest energy oscillator represents TA(L)/TA(X) phonon states, which become infrared-active E<sub>u</sub> modes at the L and X points of the

Brillouin zone (BZ). The second oscillator originates from TO(Γ) phonon states. The oscillator at ~400 cm<sup>-1</sup> originates from Raman mode phonon states, which at the L point of BZ also becomes infrared-active E<sub>u</sub> mode. The last oscillator describes phonons with dominantly LO(Γ) infrared mode character. The appearance of phonon density of states related oscillators, instead of single F<sub>2u</sub> infrared-active mode in the far-infrared reflectivity spectra, is a consequence of the nanosized dimension of the CeO<sub>2</sub> particles. The best fit spectra are obtained using the generalized Bruggeman model for inhomogeneous media, which takes into account the nanocrystal volume fraction and the pore shape.

**Keywords** Nano ceria · Far-infrared spectroscopy · Phonon density of states · Bruggeman model · Nanoparticle characterization

Z. V. Popović (✉) · M. Grujić-Brojčin · N. Paunović  
Center for Solid State Physics and New Materials,  
Institute of Physics, University of Belgrade, Pregrevica  
118, 11080 Belgrade, Serbia  
e-mail: zoran.popovic@ipb.ac.rs

M. M. Radonjić  
Scientific Computing Laboratory, Institute of Physics  
Belgrade, University of Belgrade, Pregrevica 118,  
11080 Belgrade, Serbia

V. D. Araújo · M. I. B. Bernardi  
Instituto de Física, Universidade de São Paulo-USP,  
São Carlos, SP 13560-970, Brazil

M. M. de Lima · A. Cantarero  
Instituto de Ciencia de Los Materiales, Universidad de  
Valencia, 46071 Valencia, Spain

## Introduction

There are plenty of nanoscopic, microscopic, and other techniques that are used to study nanosized materials and structures (Popović et al. 2011). Among them, the most frequently used spectroscopic techniques are vibrational (phonon) spectroscopy techniques, such as Raman (R) and infrared (IR). The use of these techniques for nanostructure characterization is discussed in Popović et al. (2011), Grujić-Brojčin et al. (2005), and Cantarero (2013).

Ultrafine ceria powders represent an important material for solid oxide fuel cells or catalytic applications, which are attributed to  $\text{CeO}_2$  remarkable oxygen-storage capability, i.e., the ability to undergo rapid redox cycles by releasing and storing oxygen (Popović et al. 2012).

In a nanocrystal, the phonons are confined in space, and all the phonons over the entire Brillouin zone (BZ) will contribute to the first-order vibrational spectra. The weight of the off-center phonons increases as the crystal size decreases, and the phonon dispersion causes a mode shape change and the frequency shift. The influence of all these effects on the  $\text{CeO}_2$  Raman mode intensity, line shape, and energy were discussed in Popović et al. (2011) and Cantarero (2013).

Infrared spectroscopy is widely used in the 400–4,000  $\text{cm}^{-1}$  spectral range to characterize un-wished residuals during the synthesis of  $\text{CeO}_2$  nanoparticles (Orel 1999). To the best of our knowledge there are no study regarding infrared-active lattice vibrations in ceria nanocrystals. In this paper, we have measured room-temperature far-infrared reflectivity spectra of the pure and copper-doped  $\text{Ce}_{1-x}\text{Cu}_x\text{O}_{2-y}$  ( $x = 0, 0.01$  and  $0.10$ ) nanocrystals in the 50–650  $\text{cm}^{-1}$  spectral range. In order to assign the obtained features we performed lattice dynamics calculation of  $\text{CeO}_2$ . Reflectivity spectra were analyzed using the factorized form of the dielectric function, which includes several oscillators and the free carriers contribution to the dielectric function. The oscillators represent the phonon density of states (PDOS)-related IR active modes. The best fit spectra are obtained using the generalized Bruggeman model for inhomogeneous media, which takes into account the volume fraction of nanopowder and the pore shape.

## Experiment and numerical method

Ceria samples were prepared in one step by the polymeric precursor method (Araújo et al. 2013). The sizes of nanocrystals obtained by Raman scattering technique are about 5 nm. Specific surface area of the samples (BET-method) were estimated from the  $\text{N}_2$ -adsorption/desorption isotherms, at liquid nitrogen temperature, using a Micromeritics ASAP 2000 analyzer. The infrared reflectivity measurements were carried out at room temperature with a BOMEM DA-8

Fourier-transform IR spectrometer. A deuterated triglycine sulfate (DTGS) pyroelectric detector was used to cover the wave number region from 50 to 650  $\text{cm}^{-1}$ . Spectra were collected with 2  $\text{cm}^{-1}$  resolution, with 1,000 interferometer scans added for each spectrum.

In order to interpret the experimental data, we have performed density functional theory calculations implemented within the QUANTUM ESPRESSO package (Giannozzi et al. 2009). We have used the ultrasoft pseudopotentials with PBE exchange–correlation functional with  $4f^1, 5s^2, 5p^6, 5d^1, 6s^2$  valence electrons of cerium and  $2s^2, 2p^4$  valence electrons of oxygen. The energy cutoffs for the wave functions and the electron densities were 60 and 900 Ry, determined to ensure stable convergence. We have sampled the BZ with a  $32 \times 32 \times 32$  Monkhorst–Pack  $\mathbf{k}$ -space mesh.

The phonon frequencies are calculated within density functional perturbation theory (Baroni et al. 2001), over the BZ sampled with  $8 \times 8 \times 8$  Monkhorst–Pack  $\mathbf{q}$ -point mesh. We have calculated the PDOS using that mesh, and the phonon dispersion curves are obtained from interpolation along the chosen path.

## Results and discussion

Cerium dioxide crystallizes in the fluorite-type cubic crystal structure (Fig. 1), space group  $Fm\bar{3}m$  (no. 225), in which Ce is located in (4a) (0,0,0), surrounded by eight oxygen atoms located at (8c) (1/4, 1/4, 1/4) Wyckoff positions. This structure has one infrared ( $F_{2u}$ ) and one Raman ( $F_{2g}$ ) active mode, each of them being triple degenerated. The normal modes of these vibrations are sketched in Fig. 1. The  $F_{2u}$  mode represents vibrations of both the Ce and O atoms in opposite directions, whereas  $F_{2g}$  mode originates from the stretching vibrations of only oxygen atoms around Ce. In the  $\text{CeO}_2$  single crystals and polycrystalline samples, the infrared and Raman active modes appear at 283/596  $\text{cm}^{-1}$  ( $\omega_{\text{TO}}/\omega_{\text{LO}}$ ) (Marabelli and Wachter 1987; Santha et al. 2004) and 465  $\text{cm}^{-1}$  (R) (Kourouklis et al. 1988; Weber et al. 1993; Nakajima et al. 1994), respectively. In our less than 5 nm  $\text{CeO}_{2-y}$  nanocrystals (Popović et al. 2012) the Raman mode is centered at about 456  $\text{cm}^{-1}$ .

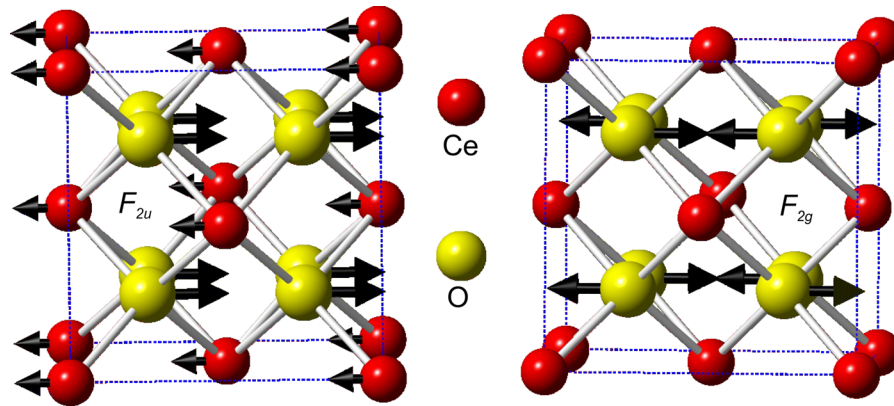


**Fig. 1** The normal modes of the infrared ( $F_{2u}$ ) and Raman ( $F_{2g}$ ) active lattice vibrations of  $\text{CeO}_2$  (Color online)

Because our nano  $\text{CeO}_2$  samples are inhomogeneous (they consist of  $\text{CeO}_2$  nanoparticles and air pores) we have applied the effective medium approximation (EMA) method to calculate infrared reflectivity of inhomogeneous media, taking into account the macroscopic volume fractions and local microstructural geometry (Grujić-Brojčin et al. 2005; Gonzalez et al. 1997; Spanier and Herman 2000; Bruggeman 1935). Two widely used effective medium theories are the Maxwell–Garnett theory (Maxwell–Garnett 1904) and the Bruggeman theory (Bruggeman 1935). In both theories the effective dielectric constant does not depend explicitly on the size of the grains or inclusions occurring inside the medium. Maxwell–Garnett approximation treats the effective medium as consisting of a matrix in which are embedded inclusions of a specific shape, where the fraction of the inclusions is very small ( $<0.15$ ), so that the inclusions are spatially separated and can be treated as a perturbation (Spanier and Herman 2000; Saarinen et al. 2003; Gehr et al. 1997). The other widely used approximation is the Bruggeman’s, which has no such limitations, and can be used for entire range of fraction values from 0 to 1. That was the reason why we used Bruggeman approach for analysis of infrared reflectivity spectra of inhomogeneous  $\text{CeO}_2$  nanocrystals.

As nanophase  $\text{CeO}_2$  is a porous material with a relatively large specific surface (see Table 1), the porosity of the nanopowder is included in modeling its dielectric function. The best agreement between calculated and experimental results is obtained by the generalized Bruggeman EMA (B-EMA), which introduces the effect of pore shape using the adjustable depolarization factor  $L$  for ellipsoidal voids ( $L = 1/3$

for spherical cavities and  $1/3 < L < 1$  for prolate spheroidal cavities).

Similar to the B-EMA, in the generalized Bruggeman model (Grujić-Brojčin et al. 2005, 2006; Spanier and Herman 2000), porous nanopowder with effective dielectric function  $\epsilon_{\text{eff}}$  is assumed to be an inhomogeneous media composed of nanopowder ( $\epsilon_{\text{nano}}$ ) and air ( $\epsilon_{\text{air}} = 1$ ) with volume fractions  $f_{\text{nano}}$  and  $f_{\text{air}}$ , respectively. The basic Bruggeman model is modified to include the influence of porosity:

$$\left( \frac{\epsilon_{\text{nano}} - \epsilon_{\text{eff}}}{\epsilon_{\text{eff}} + L(\epsilon_{\text{nano}} - \epsilon_{\text{eff}})} \right) f_{\text{nano}} + \left( \frac{\epsilon_{\text{air}} - \epsilon_{\text{eff}}}{\epsilon_{\text{eff}} + L(\epsilon_{\text{air}} - \epsilon_{\text{eff}})} \right) f_{\text{air}} = 0 \tag{1}$$

Generally, a decrease of nanopowder volume fraction results in a decrease of reflectivity and broadening of the IR features, due to the greater air fraction in the powder. Also, the decrease of depolarization factor  $L$ , from prolate spheroidal voids ( $L = 1$ ) to spherical pores ( $L = 1/3$ ), leads to the increase in the reflectivity, with characteristic IR features becoming more pronounced (Grujić-Brojčin et al. 2005).

Since the analysis of the far IR reflectivity spectrum of ceria nanopowders has revealed a presence of a plasmon mode, it was necessary to include both contributions of the phonon and the plasmon (free carrier contribution) to the dielectric function. Therefore, the factorized form of dielectric function has been decomposed into a sum of two independent terms (Gonzalez et al. 1997; Grujić-Brojčin et al. 2006; Gervais 1983):

**Table 1** The characteristic TO and LO phonon frequencies ( $\omega$ ) and damping factors ( $\gamma$ ) (all given in  $\text{cm}^{-1}$ ) of  $\text{Ce}_{1-x}\text{Cu}_x\text{O}_{2-y}$  nano- and poly-crystals, used in the fitting procedure together with the corresponding plasmon parameters for pure, 1, and 10 % Cu-doped  $\text{CeO}_2$  samples

Parameters	0 % Cu	1 % Cu	10 % Cu	10 nm nano	Polycrystal
$\omega_{\text{TO}}$ ( $\gamma_{\text{TO}}$ )	135 (190)	137 (220)	137 (300)	130 (132)	135 (130)
$\omega_{\text{LO}}$ ( $\gamma_{\text{LO}}$ )	155 (95)	147 (180)	147 (180)	160 (188)	161 (187)
$\omega_{\text{TO}}$ ( $\gamma_{\text{TO}}$ )	282 (37)	280 (28)	280 (25)	273 (57)	272 (25)
$\omega_{\text{LO}}$ ( $\gamma_{\text{LO}}$ )	375 (180)	380 (165)	385 (180)	280 (108)	416 (137)
$\omega_{\text{TO}}$ ( $\gamma_{\text{TO}}$ )	370 (100)	360 (95)	370 (140)	448 (159)	–
$\omega_{\text{LO}}$ ( $\gamma_{\text{LO}}$ )	407 (100)	407 (150)	407 (120)	468 (105)	–
$\omega_{\text{TO}}$ ( $\gamma_{\text{TO}}$ )	490 (180)	480 (140)	485 (180)	493 (113)	428 (157)
$\omega_{\text{LO}}$ ( $\gamma_{\text{LO}}$ )	580 (10)	580 (60)	585 (40)	585 (385)	587 (47)
$\omega_{\text{TO}}$ ( $\gamma_{\text{TO}}$ )	–	–	–	333 (67)	–
$\omega_{\text{LO}}$ ( $\gamma_{\text{LO}}$ )	–	–	–	350 (88)	–
$\omega_p$ ( $\gamma_p$ )	390 (400)	385 (580)	320 (550)	100 (50)	–
$f_{\text{nano}}$	0.80	0.83	0.86		
Pore shape $L$	0.74	0.70	0.70		
Specific surface area $S_{\text{BET}}$ ( $\text{m}^2/\text{g}$ )	40	40	44		
Average pore diameter (nm)	10.8	12.4	9.1		

The fitting parameters from Bruggeman model (powder volume fraction  $f_{\text{nano}}$  and the pore shape  $L$ ) together with the specific surface area and pore diameter values are listed for each nanopowder sample

$$\varepsilon(\omega) = \varepsilon_{\infty} \left[ \prod_{j=1}^n \frac{\omega_{\text{LO},j}^2 - \omega^2 + i\omega\gamma_{\text{LO},j}}{\omega_{\text{TO},j}^2 - \omega^2 + i\omega\gamma_{\text{TO},j}} - \frac{\omega_p^2}{\omega(\omega - i\gamma_p)} \right] \quad (2)$$

where  $\omega_{\text{LO},j}$  and  $\omega_{\text{TO},j}$  are longitudinal and transverse frequencies of the  $j$ th oscillator,  $\gamma_{\text{LO},j}$  and  $\gamma_{\text{TO},j}$  are their corresponding dampings,  $\omega_p$  ( $\gamma_p$ ) is the plasma frequency (damping), and  $\varepsilon_{\infty}$  is the high-frequency dielectric constant.

Figure 2a shows the PDOS of  $\text{CeO}_2$ . This PDOS is in complete agreement with previously published ones (Marabelli and Wachter 1987; Nakajima et al. 1994; Gürel and Eryigit 2006; Buckeridge et al. 2013).

The  $\text{CeO}_2$  IR reflectivity spectra of polycrystalline sample (Santha et al. 2004) and 10-nm particle size undoped  $\text{CeO}_2$  nanocrystal are given in Fig. 2b, c, respectively. These spectra are fitted using dielectric function model, Eq. (2), with parameters given in Table 1. In the case of the polycrystalline sample three oscillators are used to obtain a rather good agreement with experimental data. The lowest energy oscillator with TO energy of  $135 \text{ cm}^{-1}$  represents phonon states from the X and L point of BZ. Other two oscillators represent  $F_{2u}$  mode. Appearance of two instead of one IR active mode in this spectral range is related to the anharmonicity (Santha et al. 2004). In the case of the

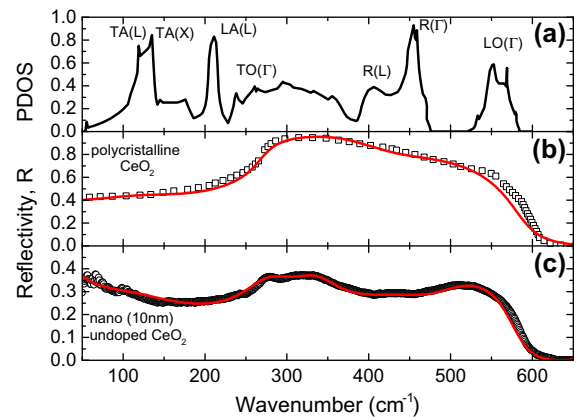


**Fig. 2** **a** The phonon density of states of  $\text{CeO}_2$ . **b** The IR reflectivity spectra of polycrystalline  $\text{CeO}_2$  sample (Santha et al. 2004); **c** nanocrystalline undoped  $\text{CeO}_2$  sample (particle size  $\sim 10 \text{ nm}$ ). Solid lines represent the calculated reflectivity spectra obtained by the fitting procedure based on Eq. (2), with the parameters given in Table 1 (Color online)

nanosized sample (Fig. 2c) five oscillators are included in the fitting procedure, as well as, plasma term (see Table 1). Origin of these oscillators will be discussed later.

The influence of nanopowder volume fraction and the pore shape on the IR reflectivity spectra is analyzed in Fig. 3a–c, which show the IR reflectivity spectra

calculated with the generalized B-EMA, with the variation of powder volume fraction  $f_{\text{nano}}$  and fixed value of depolarization factor (pore shape factor)  $L = 0.33, 0.75,$  and  $0.90,$  respectively. The spectra are calculated with the set of parameters corresponding to the pure  $\text{CeO}_2$  sample, listed in the Table 1 (0 % Cu), whereas  $f_{\text{nano}}$  is varied from 0.5 (50 % of  $\text{CeO}_2$  powder in porous sample) to 1 (nonporous powder). The pore shape factor  $L = 0.33$  defines ideally spherical pores and for given TO/LO parameters, the best volume fraction fit corresponds to values of  $f_{\text{nano}}$  between 50 and 60 % of powder content in the sample (Fig. 3a).

The pore shape factor  $L = 0.75$  defines pores with elongated structure, as indicated in Fig. 3b. For given TO/LO parameters (Table 1) the best volume fraction fit corresponds to values of  $f_{\text{nano}}$  around 80 % of powder content in the sample. In Fig. 3c the variation of powder volume fraction  $f_{\text{nano}}$  with depolarization factor  $L = 0.90$  is shown. The pore shape factor  $L = 0.90$  corresponds to extremely elongated pores.

For given TO/LO parameters (Table 1) the best volume fraction fit corresponds to values of  $f_{\text{nano}}$  between 80 and 90 % of powder content in the sample.

The pore shape variation is analyzed in Fig. 3d–f. In Fig. 3d the calculated spectrum for powder volume fraction  $f_{\text{nano}} = 1,$  i.e., nonporous powder is shown together with experimental IR reflectivity of the pure  $\text{CeO}_2$  sample. The spectrum is calculated with the set of parameters corresponding to the pure  $\text{CeO}_2$  sample, listed in Table 1 (0 % Cu), whereas the pore shape factor ( $L$ ) variation has no influence in this calculation. Figure 3e, f show the IR reflectivity spectra calculated with the generalized Bruggeman EMA with powder volume fraction of 80 % and 50 %. The pore shape factor varied from  $L = 0.3$ – $0.9.$  It may be noticed that in both cases, the intensity of the reflectivity is getting lower with the increase in pore shape factor. For given TO/LO parameters (Table 1) the best pore shape fit is obtained for values of  $L$  from 0.7 to 0.8 (Fig. 3e), corresponding to the area of elongated pores. These

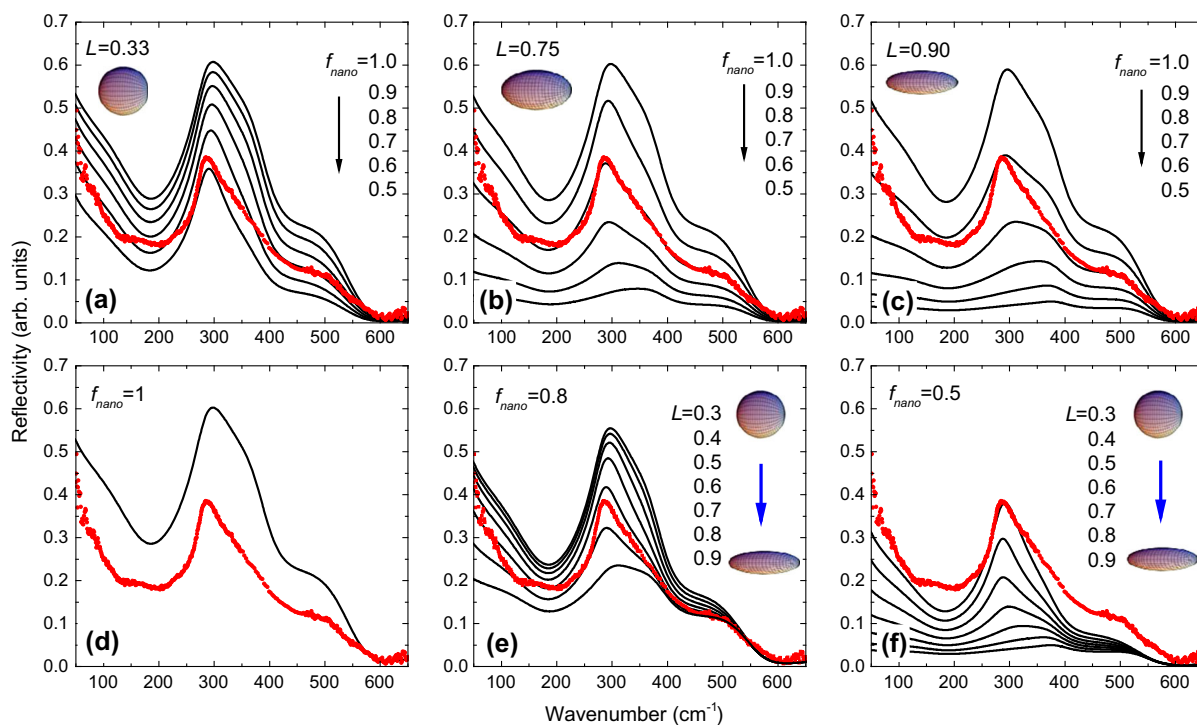


**Fig. 3** The IR reflectivity spectra calculated with the generalized B-EMA. **a** The volume fraction of nanopowder is in the range from 0.5 to 1.0 and the pore shape factor  $L = 0.33$  (spherical shape of pores); **b** pore shape factor  $L = 0.75$  (elongated pore structure); **c** pore shape factor  $L = 0.90$  (extremely elongated pore structure); **d** the IR reflectivity spectra calculated with the generalized B-EMA with the volume

fraction of the nanopowder  $f_{\text{nano}} = 1$  (nonporous powder); **e** fixed volume fraction of nanopowder ( $f_{\text{nano}} = 0.8$ ) with pore shape factor varying from 0.3 to 0.9; **f** fixed volume fraction of nanopowder ( $f_{\text{nano}} = 0.5$ ) with pore shape factor varying from 0.3 to 0.9. Experimental IR reflectivity spectrum (red curve) of pure  $\text{CeO}_2$  sample (0 % Cu) is given for comparison (Color online)

results correspond to those shown in Fig. 3b. Finally, in Fig. 3f the best pore shape fit is obtained for values of  $L$  around 0.3, corresponding to ideally spherical pores.

By analyzing the results shown in Fig. 3, we came to the following conclusions:

- (i) Bruggeman EMA model can be used to fit the experimental reflectivity spectra of inhomogeneous nanomaterials, in our case  $\text{CeO}_2$  nanocrystals.
- (ii) The B-EMA model parameters that best describe the experimental  $\text{CeO}_2$  reflectivity spectra are close to  $f_{\text{nano}} = 0.8$  and  $L = 0.75$ . (see Fig. 3b). Refinement of these parameters for samples under investigation gives values shown in Table 1.
- (iii) The very good agreement between the calculated and the experimental spectra illustrated in Fig. 4 suggests that the use of more specific model, which may include the pore shape distribution, instead of the B-EMA general and simple model, is not necessary.

In Fig. 4 experimental IR reflectivity spectra of 5 nm-sized pure, 1, and 10 % Cu-doped  $\text{CeO}_2$  samples are shown, together with the corresponding spectra calculated with the generalized B-EMA. Fitting parameters for these spectra are listed in Table 1. As can be seen from Table 1, four oscillators with TO energies of approximately 135, 280, 370, and 490  $\text{cm}^{-1}$  were included in the fitting procedure, Eq. (2), for 5 nm-sized  $\text{CeO}_2$  samples. These

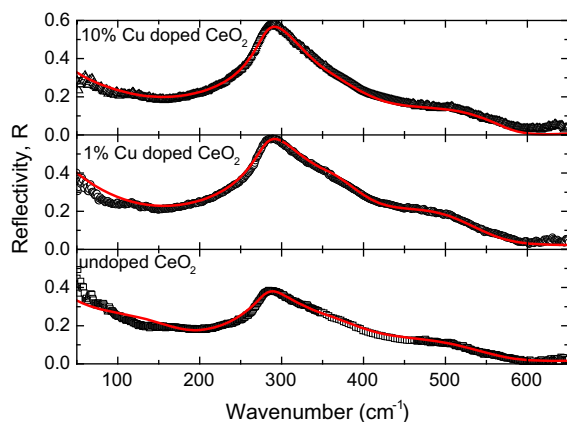


**Fig. 4** Experimental IR reflectivity spectra of pure, 1, and 10 % Cu-doped  $\text{CeO}_2$  samples, with the corresponding spectra obtained by the fitting procedure based on Eq. (2) and the generalized B-EMA, Eq. (1). Parameters are given in Table 1

oscillators represent local maxima of the PDOS. The lowest energy oscillator represents TA(L)/TA(X) phonon states, which become IR-active  $E_u$  modes (Buckeridge et al. 2013) at the L and X points of BZ. The second oscillator originates from TO( $\Gamma$ ) phonon states. The oscillator at  $\sim 400 \text{ cm}^{-1}$  originates from Raman mode phonon states which at the L point of BZ also becomes IR-active  $E_u$  mode (Buckeridge et al. 2013). The last oscillator describes phonons with dominantly LO( $\Gamma$ ) IR mode character. The appearance of PDOS-related oscillators, instead of single  $F_{2u}$  IR-active mode in the far-infrared reflectivity spectra, is a consequence of the nanosized dimension of the particles, as mentioned earlier. Besides that, the oscillator energies appear at lower energies than the maxima of PDOS. This is also related to the particle size. In fact, in nanocerium the unit cell dimensions abruptly increase by particle size reduction (Tsunekawa et al. 2000; Wu et al. 2004). Consequently, the PDOS softens with the particle size lowering due to an increase in the internal strain, as it was discussed in Buckeridge et al. (2013).

A small variation in the frequencies of TO (LO) modes of the pure and doped samples is noticed, whereas the damping parameters are clearly affected by the variation between pure and doped samples. Plasmon modes are registered in all samples, with significant plasma frequency decrease and damping parameter increase with Cu doping. The values of parameters used in the generalized Bruggeman EMA are varied with doping: similar porosity has been estimated in all studied samples. Namely, the volume fraction parameter is estimated from  $f_{\text{nano}} = 0.80$  in pure  $\text{CeO}_2$  (which means 80 % of  $\text{CeO}_2$  fraction in a porous sample) to 0.86 in 10 % Cu-doped  $\text{CeO}_2$  sample. The depolarization factor  $L$ , defining pore shape is estimated as 0.74 in pure  $\text{CeO}_2$  sample and slightly lower (0.70) in doped samples, therefore describing pores filled with the air as very elongated. Comparing these with textural measurement results, we find that in the 10 % Cu-doped sample, the reduction of  $L$  and an increase in volume fraction is correlated with a decrease of pore diameter and an increase in specific surface area (see Table 1).

## Conclusion

We have measured the unpolarized far-infrared reflectivity spectra of the  $\text{CeO}_2$  nanocrystals at room



temperature. Reflectivity spectra were analyzed using the factorized form of the dielectric function, which includes the phonon and plasmon contribution to the dielectric function. The best fit spectra are obtained using the generalized Bruggeman model for inhomogeneous media, which takes into account the volume fraction of CeO<sub>2</sub> nanocrystal and the air pore shape.

**Acknowledgments** This work was supported by the Serbian Ministry of Education, Science and Technological Development under Projects ON171032, ON171017 and III45018, the Spain–Serbia bilateral Project AIB2010SE-00160, the Spanish Grant MAT2012-33483, and the Brazilian governmental research funding agencies FAPESP, CAPES, and CNPq.

## References

- Araújo VD, de Lima MM Jr, Cantarero M, Bernardi MIB, Bellido JDA, Assaf EM, Balzer R, Probst LFD, Fajardo HV (2013) Catalytic oxidation of *n*-hexane promoted by Ce<sub>1-x</sub>Cu<sub>x</sub>O<sub>2</sub> catalysts prepared by one-step polymeric precursor method. *Mater Chem Phys* 142:677–681
- Baroni S, de Gironcoli S, Dal Corso A, Giannozzi P (2001) Phonons and related crystal properties from density-functional perturbation theory. *Rev Mod Phys* 73:515–562
- Bruggeman DAG (1935) Berechnung verschiedener physikalischer Konstanten von heterogenen Substanzen. I. Dielektrizitätskonstanten und Leitfähigkeiten der Mischkörper aus isotropen Substanzen. *Ann Phys* 24:636–664
- Buckeridge J, Scanlon DO, Walsh A, Catlow CRA, Sokol AA (2013) Dynamical response and instability in ceria under lattice expansion. *Phys Rev B* 87(21):214304
- Cantarero A (2013) Review on Raman scattering in semiconductor nanowires: I. Theory. *J Nanophotonics* 7(1):071598
- Gehr RJ, Fischer GL, Boyd RW (1997) Nonlinear-optical response of porous-glass-based composite materials. *J Opt Soc Am B* 14(9):2310–2314
- Gervais F (1983) High-temperature infrared reflectivity spectroscopy by scanning interferometry. In: Button KJ (ed) *Infrared and millimeter waves*. Academic Press, New York, pp 279–339
- Giannozzi P, Baroni S, Bonini N, Calandra M, Car R, Cavazzoni C, Ceresoli D, Chiarotti GL, Cococcioni M, Dabo I, Corso AD, de Gironcoli S, Fabris S, Fratesi G, Gebauer R, Gerstmann U, Gougoussis C, Kokalj A, Lazzeri M, Martin-Samos L, Marzari N, Mauri F, Mazzarello R, Paolini S, Pasquarello A, Paulatto L, Sbraccia C, Scandolo S, Sclauzero G, Seitsonen AP, Smogunov A, Umari P, Wentzcovitch RM (2009) QUANTUM ESPRESSO: a modular and open-source software project for quantum simulations of materials. *J Phys* 21(39):395502
- Gonzalez RJ, Zallen R, Berger H (1997) Infrared reflectivity and lattice fundamentals in anatase TiO<sub>2</sub>. *Phys Rev B* 55(11):7014–7017
- Grujić-Brojčin M, Šćepanović MJ, Dohčević-Mitrović ZD, Hinić I, Matović B, Stanišić G, Popović ZV (2005) Infrared study of laser synthesized anatase TiO<sub>2</sub> nanopowders. *J Phys D* 38(9):1415–1420
- Grujić-Brojčin M, Šćepanović MJ, Dohčević-Mitrović ZD, Popović ZV (2006) Infrared study of nonstoichiometric anatase TiO<sub>2</sub> nanopowders. *Sci Sinter* 38:183
- Gürel T, Eryiğit R (2006) Ab initio pressure-dependent vibrational and dielectric properties of CeO<sub>2</sub>. *Phys Rev B* 74(1):014302
- Kourouklis GA, Jayaraman A, Espinosa GP (1988) High-pressure Raman study of CeO<sub>2</sub> to 35 GPa and pressure-induced phase transformation from the fluorite structure. *Phys Rev B* 37(8):4250–4253
- Marabelli F, Wachter P (1987) Covalent insulator 2: optical reflectivity measurements. *Phys Rev B* 36(2):1234–1238
- Maxwell-Garnett JC (1904) Colours in metal glasses and in metallic films. *Philos Trans R Soc Lond, Ser.4* 203:385–420
- Nakajima A, Yoshihara A, Ishigame M (1994) Defect-induced Raman spectra in doped CeO<sub>2</sub>. *Phys Rev B* 50(18):13297–13307
- Orel Z (1999) Characterization of cerium dioxide dip-coated films by spectroscopic technique. *Internet J Vib Spec Vol 3*, Edition 4, Section 6 ([www.ijvs.com](http://www.ijvs.com)). Accessed 20 June 2013
- Popović ZV, Dohčević-Mitrović Z, Šćepanović M, Grujić-Brojčin M, Aškračić S (2011) Raman scattering on nanomaterials and nanostructures. *Ann Phys* 523(1–2):62–74
- Popović ZV, Dohčević-Mitrović ZD, Paunović N, Radović M (2012) Evidence of charge delocalization in Ce<sub>1-x</sub>Fe<sub>2+(3+)</sub>O<sub>2-y</sub> nanocrystals ( $x = 0, 0.06, 0.12$ ). *Phys Rev B* 85:014302
- Saariinen JJ, Vartiainen EM, Peiponen KE (2003) On tailoring of nonlinear spectral properties of nanocomposites having Maxwell Garnett or Bruggeman structure. *Opt Rev* 10(2):111–115
- Santha NI, Sebastian MT, Mohanan P, Alford NM, Sarma K, Pullar RC, Kamba S, Pashkin A, Samukhina P, Petzelt J (2004) Effect of doping on the dielectric properties of cerium oxide in the microwave and far-infrared frequency range. *J Am Ceram Soc* 87(7):1233–1237
- Spanier JE, Herman IP (2000) Use of hybrid phenomenological and statistical effective-medium theories of dielectric functions to model the infrared reflectance of porous SiC films. *Phys Rev B* 61(15):10437–10450
- Tsunekawa S, Ishikawa K, Li ZQ, Kawazoe Y, Kasuya A (2000) Origin of anomalous lattice expansion in oxide nanoparticles. *Phys Rev Lett* 85(16):3440–3443
- Weber WH, Hass KC, McBride JR (1993) Raman study of CeO<sub>2</sub>: second-order scattering, lattice dynamics, and particle-size effects. *Phys Rev B* 48(1):178–185
- Wu L, Wiesmann HJ, Moodenbaugh AR, Klie RF, Zhu Y, Welch DO, Suenaga M (2004) Oxidation state and lattice expansion of CeO<sub>2-x</sub> nanoparticles as a function of particle size. *Phys Rev B* 69(12):125415

7-11th October 2019  
Belgrade, Serbia



<http://www.sfkm.ac.rs/>

# The 20th Symposium on Condensed Matter Physics

---

## BOOK OF ABSTRACTS

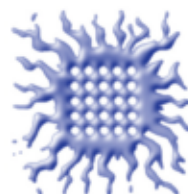
---



University of Belgrade,  
Faculty of Physics



Institute of Physics Belgrade



Vinca Institute  
of Nuclear Sciences



Serbian Academy  
of Sciences and Arts



Ministry of Education, Science and  
Technological Development,  
Republic of Serbia

## Conference Chair

Cedomir Petrovic, *Brookhaven National Laboratory, USA*

Željko Šljivančanin, *Vinča Institute of Nuclear Sciences Serbia*

## Organizing Committee

Jelena Pešić, *Institute of Physics Belgrade*

Andrijana Šolajić, *Institute of Physics Belgrade*

Petar Mali, *Faculty of Sciences, University of Novi Sad*

Jelena Pajović, *Faculty of Physics, University of Belgrade, Serbia*

Srđan Stavrčić, *Vinča Institute of Nuclear Sciences*

Svetislav Mijatović, *Faculty of Physics, University of Belgrade, Serbia*

Božidar Nikolić, *Faculty of Physics, University of Belgrade, Serbia – chair*

## Organized by

Institute of Physics Belgrade

Faculty of Physics, University of Belgrade

Vinča Institute of Nuclear Sciences

Serbian Academy of Sciences and Arts

## Program Committee

Ivan Božović, *Brookhaven National Laboratory, USA*

Vladimir Dobrosavljević, *Florida State University, USA*

Milan Damnjanović, *Faculty of Physics, University of Belgrade, Serbia*

Vladimir Djoković, *Vinča Institute, University of Belgrade, Serbia*

Gyula Eres, *Oak Ridge National Laboratory, USA*

Laszló Forró, *Ecole Polytechnique Fédérale de Lausanne, Switzerland*

Radoš Gajić, *Institute of Physics Belgrade, University of Belgrade, Serbia*

Igor Herbut, *Simon Fraser University, Canada*

Zoran Ikonić, *University of Leeds, UK*

Ivanka Milošević, *Faculty of Physics, University of Belgrade, Serbia*

Branislav Nikolić, *University of Delaware, USA*

Cedomir Petrovic, *Brookhaven National Laboratory, USA*

Dragana Popović, *National High Magnetic Field Laboratory USA*

Zoran S. Popović, *Vinča Institute, University of Belgrade, Serbia*

Zoran V. Popović, *Institute of Physics, University of Belgrade, Serbia*

Zoran Radović, *Faculty of Physics, University of Belgrade, Serbia*

Miljko Satarić, *Faculty of Technical Sciences, University of Novi Sad, Serbia*

Vojislav Stamenković, *Argonne National Laboratory, USA*

Željko Šljivančanin, *Vinča Institute, University of Belgrade, Serbia*

Bosiljka Tadić, *Jožef Štefan Institute, Slovenia*

Milan Tadić, *School of Electrical Engineering, University of Belgrade, Serbia*

Darko Tanasković, *Institute of Physics, University of Belgrade, Serbia*

# Superconducting Nature of Elemental Bismuth Under Pressure

Miloš M. Radonjić<sup>a</sup>, Rustem Khasanov<sup>b</sup>, Liviu Chioncel<sup>c</sup> and Alex Amato<sup>b</sup>

<sup>a</sup>Scientific Computing Laboratory, Center for the Study of Complex Systems, Institute of Physics Belgrade, University of Belgrade, Pregrevica 118, 11080 Belgrade, Serbia

<sup>b</sup>Laboratory for Muon Spin Spectroscopy, Paul Scherrer Institute, CH-5232 Villigen, Switzerland

<sup>c</sup>Augsburg Center for Innovative Technologies, and Center for Electronic Correlations and Magnetism, Theoretical Physics III, Institute of Physics, University of Augsburg, D-86135 Augsburg, Germany

**Abstract.** Elemental bismuth has a very rich pressure-dependent phase diagram. At room temperature, it undergoes a series of structural transitions. Upon cooling all phases become superconducting, but the superconducting nature between phases is very different. We report the superconductivity in the Bi-II phase of elemental bismuth (transition temperature  $T_c \simeq 3.94$  K at  $p \simeq 2.80$  GPa). It was studied experimentally by means of muon-spin rotation as well as theoretically using the Eliashberg theory in combination with Density Functional calculations. Experiments reveal that Bi-II is the type-I superconductor with the zero temperature thermodynamic critical field  $B_c(0) = 32.07(2)$  mT. The Eliashberg theory provides an excellent agreement with the experimental critical temperature and magnetic field and the estimated value for the strong coupling parameter  $T_c/\omega_{\text{In}}$  suggests that Bi-II is an intermediately-coupled superconductor. We also address the superconducting nature of Bi-I phase. We report the negligible electron-phonon interaction and possible signatures of exciton-mediated superconductivity.

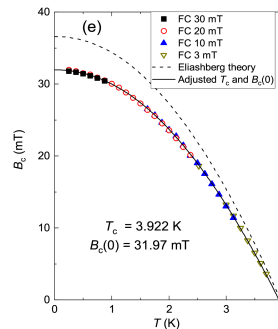


**FIGURE 1.** The temperature dependence of the thermodynamical critical field  $B_c$  for Bi-II phase obtained in  $\mu$ SR experiments and within the framework of *ab-initio* Eliashberg calculations using Density Functional Theory.

## REFERENCES

1. R. Khasanov, M. M. Radonjić, H. Luetkens, E. Morenzoni, G. Simutis, S. Schoenecker, W. H. Appelt, A. Östlin, L. Chioncel, and A. Amato, *Phys. Rev. B* **99**, 174506 (2019).

# Lattice dynamics and phonon anomalies in FeS

A. Baum<sup>a,b</sup>, A. Milosavljević<sup>c</sup>, N. Lazarević<sup>c</sup>, M.M. Radonjić<sup>d</sup>, B. Nikolić<sup>e</sup>, M. Mitschek<sup>a,b</sup>, Z. Inanloo Maranloo<sup>a</sup>, M. Šćepanović<sup>c</sup>, M. Grujić – Brojčin<sup>c</sup>, N. Stojilović<sup>f</sup>, M. Opel<sup>a</sup>, Aifeng Wang<sup>g</sup>, C. Petrović<sup>g</sup>, Z.V. Popović<sup>c,h</sup> and R. Hackl<sup>a</sup>

<sup>a</sup>Walther Meissner Institut, Bayerische Akademie der Wissenschaften, 85748 Garching, Germany

<sup>b</sup>Fakultät für Physik E23, Technische Universität München, 85748 Garching, Germany

<sup>c</sup>Center for Solid State Physics and New Materials, Institute of Physics Belgrade, University of Belgrade, Pregrevica 118, 11080 Belgrade, Serbia

<sup>d</sup>Scientific Computing Laboratory, Center for the Study of Complex Systems, Institute of Physics Belgrade, University of Belgrade, Pregrevica 118, 11080 Belgrade, Serbia

<sup>e</sup>Faculty of Physics, University of Belgrade, Studentski trg 12, Belgrade, Serbia

<sup>f</sup>Department of Physics and Astronomy, University of Wisconsin Oshkosh, Oshkosh, Wisconsin 54901, USA

<sup>g</sup>Condensed Matter Physics and Materials Science Department, Brookhaven National Laboratory, Upton, New York 11973-5000, USA

<sup>h</sup>Serbian Academy of Sciences and Arts, Knez Mihailova 35, 11000 Belgrade, Serbia

**Abstract.** Crystal structure, magnetic ordering and nematic phase are closely interrelated in the iron-based superconductors. Although isostructural and isoelectronic, properties of 11 chalcogenides, FeSe, FeTe and FeS, differ significantly. Whereas FeSe undergoes a nematic and structural phase transition at 90 K, together with superconductivity below 9 K, and no traces of long-range magnetic ordering, FeTe is not superconducting but exhibits magnetostructural phase transition at temperature of 67 K. The last member of the family, FeS, have a superconducting transition at 5 K, and remains tetragonal down to lowest temperatures.

Here, we present results of Raman scattering experiment on tetragonal FeS, and analysis of vibrational properties close to potential instabilities [1]. Besides  $A_{1g}$  and  $B_{1g}$  modes assignment, which is in a good agreement with DFT calculations, third peak within a gap of calculated phonon density of states can be identified as a result of second order scattering process. Both, selection rules for two-phonon processes, based on modified group projector technique and energy are in a good agreement with the experiment. A fourth mode, close to  $A_{1g}$  could originate from either defect-induced scattering or second order scattering as well. The temperature dependence of all four modes is governed by the contraction of the lattice, with anomalies at 50 K and below 20 K. The anomaly observed at 20 K has a correspondence with previously reported results of short-range magnetic ordering. The presence of two-phonon scattering indicates strong phonon-phonon scattering, which is likely to originate from an electron-phonon interaction being enhanced in comparison to other pnictides and chalcogenides.

## REFERENCES

1. A. Baum, A. Milosavljević, N. Lazarević, M. M. Radonjić, B. Nikolić, M. Mitschek, Z. I. Maranloo, M. Šćepanović, M. Grujić-Brojčin, N. Stojilović, M. Opel, A. Wang, C. Petrović, Z.V. Popović, and R. Hackl, Phonon anomalies in FeS, *Phys.Rev.B* **97**, 054306 (2018).

## O 57: Frontiers of Electronic-Structure Theory: Focus on the Interface Challenge VI (joint session O/DS/ CPP/TT)

Time: Wednesday 15:00–17:45

Location: H9

O 57.1 Wed 15:00 H9

**First-principles quantum transport simulations including strong correlation effects** — ●ANDREA DROGHETTI<sup>1</sup>, WILHELM APPELT<sup>2</sup>, LIVIU CHIONCEL<sup>2</sup>, MILOS RADONJIĆ<sup>3</sup>, ENRIQUE MUÑOZ<sup>4</sup>, STEFAN KIRCHNER<sup>5</sup>, DAVID JACOB<sup>1</sup>, DIETER VOLLHARDT<sup>2</sup>, ANGEL RUBIO<sup>6</sup>, and IVAN RUNGGER<sup>7</sup> — <sup>1</sup>University of the Basque Country (Spain) — <sup>2</sup>University of Augsburg (Germany) — <sup>3</sup>University of Belgrade (Serbia) — <sup>4</sup>Pontificia Universidad Católica de Chile — <sup>5</sup>Zhejiang University (China) — <sup>6</sup>Max Planck Institute for the Structure and Dynamics of Matter (Germany) — <sup>7</sup>National Physical Laboratory (UK)

When magnetic molecules are brought into contact with metals the electron-electron interaction leads to the appearance of the correlated Kondo state. In this talk we will present the results of first-principles calculations for the electronic structure and the linear-response conductance of radical molecules adsorbed on metallic surfaces in the Kondo regime [Phys. Rev. B 95, 085131 (2017), Nanoscale 10, 17738 (2018)]. In particular we will outline the methodological approach as implemented in the Smeagol electron transport code and we will benchmark the results against experiments. The method relies in the first place on the combination of Density Functional Theory with the Green's functions technique. We will explain how a molecular device is projected onto an effective Anderson impurity problem, which is then solved either by continuum time quantum Monte Carlo or numerical renormalization group. Finally, we will describe some work-in-progress aimed at computing transport properties beyond linear-response.

O 57.2 Wed 15:15 H9

**Density functional theory for transport through correlated systems** — ●STEFAN KURTH — Univ. of the Basque Country UPV/EHU, San Sebastian, Spain — IKERBASQUE, Basque Foundation for Science, Bilbao, Spain — Donostia International Physics Center DIPC, San Sebastian, Spain

A recently proposed density functional formalism to describe electronic transport through correlated systems in the steady state uses both the density on the junction and the steady current as basic variables. The corresponding Kohn-Sham system features two exchange-correlation (xc) potentials, a local xc potential and an xc contribution to the bias, which are universal functionals of the basic variables.

A recent parametrization of the xc potentials for the single-impurity Anderson model correctly incorporates both the Kondo and Coulomb blockade regimes. It allows for calculation of currents and differential conductances at arbitrary bias and temperature at negligible numerical cost but with the accuracy of sophisticated renormalization group methods. A time-local version of this functional is used to study the Anderson model under the influence of both DC and AC biases. We observe interaction-induced shifts of the photon-assisted conductance peaks, suppression of the Kondo plateau at zero temperature and lifting of Coulomb blockade at finite temperature.

O 57.3 Wed 15:30 H9

**Exact factorization of the many-electron wave function** — ●CAMILLA PELLEGRINI<sup>1</sup>, ANTONIO SANNA<sup>1</sup>, and EBERHARD K. U. GROSS<sup>1,2</sup> — <sup>1</sup>Max Planck Institute of Microstructure Physics, Weinberg 2, 06120 Halle, Germany — <sup>2</sup>Fritz Haber Center for Molecular Dynamics, Institute of Chemistry, The Hebrew University of Jerusalem, Jerusalem 91904, Israel

The exact factorization approach [1], originally developed for a system of electrons and nuclei, is extended to a system of electrons only. This allows for a two-particle Schrödinger equation, which uniquely defines the exact effective interaction between two electrons in the medium. This interaction differs from the effective interaction,  $W$ , used in many-body Green's function techniques. In particular, it is spin-dependent. We illustrate the formalism for the simplest case of exchange interactions only.

[1] A. Abedi, N.T. Maitra, E.K.U. Gross, PRL 105, 123002 (2010).

O 57.4 Wed 15:45 H9

**Many-body spectral functions from steady state density functional theory** — ●DAVID JACOB<sup>1,2</sup> and STEFAN KURTH<sup>1,2,3</sup> — <sup>1</sup>Dpto. de Física de Materiales, Universidad del País Vasco UPV/EHU, San

Sebastián, Spain — <sup>2</sup>IKERBASQUE, Basque Foundation for Science, Bilbao, Spain — <sup>3</sup>DIPC, San Sebastián, Spain

We present a scheme to extract the true many-body spectral function of an interacting many-electron system from an equilibrium density functional theory (DFT) calculation [1]. To this end we devise an ideal STM-like setup and employ the recently proposed steady-state DFT formalism (i-DFT) which allows to calculate the steady current through a nanoscopic region coupled to two biased electrodes [2]. In our setup one of the electrodes serves as a probe ("STM tip"). In the ideal STM limit of vanishing coupling to the tip, the system to be probed is in quasi-equilibrium with the "substrate" and the normalized differential conductance yields the exact equilibrium many-body spectral function. Moreover, from the i-DFT equations we derive an exact relationship which expresses the interacting spectral function in terms of the Kohn-Sham one. Making use of i-DFT xc functionals that capture Coulomb blockade as well as Kondo physics, the method yields spectral functions for Anderson impurity models in good agreement with NRG calculations. It is thus possible to calculate spectral functions of interacting many-electron systems at the cost of an equilibrium DFT calculation.

**References:** [1] D. Jacob and S. Kurth, Nano Lett. **18**, 2086 (2018) [2] G. Stefanucci and S. Kurth, Nano Lett. **15**, 8020 (2015)

O 57.5 Wed 16:00 H9

**Magnetic phase transitions induced by pressure and magnetic field: the case of antiferromagnetic USb<sub>2</sub>** — ●LEONID SANDRATSKII — Max Planck Institute of Microstructure Physics, Halle, Germany

Fascinating phenomena observed under applied pressure and magnetic field are currently attracting much research attention. Recent experiments have shown that application of the pressure or magnetic field to the USb<sub>2</sub> compound induce the transformations of the ground-state antiferromagnetic (AFM) up-down-down-up structure to, respectively, ferromagnetic (FM) or ferrimagnetic configurations. Remarkably, the magnetic critical temperature of the FM state, induced by pressure, is more than two times smaller than the Neel temperature of the ground state. We performed density-functional theory (DFT) and DFT+U studies to reveal the origin of the unusual magnetic ground-state of the system and the driving mechanisms of the phase transitions. We investigate both the magnetic anisotropy properties and the parameters of the interatomic exchange interactions. To study pressure-induced effects we carry out calculations for reduced volume and demonstrate that the AFM-FM phase transformation indeed takes place but depends crucially on the peculiar features of the magnetic anisotropy. We also explain why the magnetic field that couples directly to the magnetic moments of atoms leads to the phase transition to the ferrimagnetic state whereas the pressure that does not couple directly to magnetic moments results in the FM structure.

O 57.6 Wed 16:15 H9

**Charge localization at a weakly coupled molecule-metal system studied by linear expansion  $\Delta$ -self-consistent field density-functional theory ( $\Delta$ SCF-DFT)** — ●HADI H. AREFI<sup>1,2</sup>, DANIEL CORKEN<sup>3</sup>, REINHARD MAURER<sup>3</sup>, F. STEFAN TAUTZ<sup>1,2</sup>, and CHRISTIAN WAGNER<sup>1,2</sup> — <sup>1</sup>Peter Grünberg Institut (PGI-3), Forschungszentrum Jülich, Germany — <sup>2</sup>JARA-Fundamentals of Future Information Technology — <sup>3</sup>Department of Chemistry, University of Warwick, Coventry, United Kingdom

Predicting the charge arrangements at the interface between molecules and metals represents a formidable challenge for semi-local approximations to Density Functional Theory (DFT). This could become even more critical when molecules are only weakly coupled to the metal. Single-molecular devices based on such weak coupling have recently been created by molecular manipulation with a scanning probe microscope (SPM), where a single PTCDA (perylene-tetracarboxylic dihydride) molecule was placed in a free-standing upright configuration either on a SPM tip [1] or on a pedestal of two adatoms on the Ag(111) surface [2]. There are indications that the mechanism stabilizing these unexpected configurations is linked to an integer charge transfer creating a singly occupied molecular orbital. We use the  $\Delta$ SCF-DFT method [3] to confine charge on the LUMO of the PTCDA and study

TT 49.7 Wed 15:00 Poster D

**Superconductivity in doped tungsten oxide: a first principles description** — ●ANTONIO SANNA<sup>1</sup>, CAMILLA PELLEGRINI<sup>1</sup>, and HENNING GLAWE<sup>2</sup> — <sup>1</sup>Max Planck Institute of microstructure physics, Halle (Saale), Germany — <sup>2</sup>Max Planck Institute for the structure and dynamics of matter, Hamburg, Germany

Tungsten Oxide ( $\text{WO}_3$ ), its bronzes ( $\text{M}_x\text{WO}_3$ ), oxygen vacant ( $\text{WO}_{3-x}$ ) and fluorine doped ( $\text{WO}_{3-x}\text{F}_x$ ) are a family of crystals showing a large variety of electronic properties, including superconductivity. Most measurements report a consistent scenario of low  $T_c$ , although there have been some reports on possible high- $T_c$  low dimensional and metastable superconductivity in sodium doped surfaces, at the  $\text{W}/\text{WO}_3$  interface and upon H doping. We attempt a characterization of superconductivity in doped  $\text{WO}_3$  by *ab initio* methods, focusing on the two key questions:

- Are the stable low temperature superconducting phases driven by conventional electron phonon pairing? or, like in  $\text{BaBiO}_3$ , conventional approaches fail and the correct pairing mechanism is still an open problem.

- Can electron phonon coupling, in any geometry and doping regime, provide enough coupling strength to lead to high- $T_c$ ?

TT 49.8 Wed 15:00 Poster D

**Effects of self-consistency in mean-field theories of disordered systems: Superconductor Insulator Transition** — ●MATTHIAS STOSIEK and FERDINAND EVERS — Institute of Theoretical Physics, University of Regensburg, Germany

Our general interest is in aspects of self-consistency with respect to disorder in the mean-field treatment of disordered interacting systems. The example we here consider is the Superconductor Insulator Transition (SIT), where the superconducting gap is calculated in the presence of short-range disorder. Our focus is on disordered films with conventional s-wave pairing that we study numerically employing the negative-U Hubbard model within the standard Bogoliubov-deGennes approximation. The general question that we would like to address concerns the auto-correlation function of the pairing amplitude: Does it qualitatively change if full self-consistency is accounted for? Our research might have significant impact on the understanding of the SIT, if extra correlations appear due to the self-consistency condition that turn out sufficiently long-ranged. Such correlation effects are ignored in major analytical theories. To study the long-range behavior of the order parameter correlations, the treatment of large system sizes is necessary. Due to the self-consistency requirement, the relevant sizes (e.g.  $10^6$  sites) are numerically very expensive to achieve. For this reason, we have developed a parallelized code based on the Kernel Polynomial Method. We present data that indicates the existence of very long ranged (power-law) correlations that may indeed change the critical behavior in a significant way.

TT 49.9 Wed 15:00 Poster D

**Dynamics of nanostructured superconductors in curl-free vectorpotentials** — ●BJÖRN NIEDZIELSKI and JAMAL BERAKDAR — Martin-Luther-Universität Halle-Wittenberg, Insitut für Physik, Germany

In the theory of macroscopic quantum materials, like superconductors, the electromagnetic vectorpotential plays a crucial role. We show for nanoscopically structured superconductors how vectorpotentials with zero curl can be used to manipulate the state of such a system. It is demonstrated how a relation between flux quantization and the Aharonov-Bohm effect can be used to drive and control superconducting tunneling devices in a non-invasive way.

TT 49.10 Wed 15:00 Poster D

**Spin effects in a superconductor in proximity to an antiferromagnetic insulator** — AKASHDEEP KAMRA<sup>1</sup>, ●ALI REZAEI<sup>2</sup>, and WOLFGANG BELZIG<sup>2</sup> — <sup>1</sup>Center for Quantum Spintronics, Department of Physics, NTNU, Norway — <sup>2</sup>Department of Physics, University of Konstanz, Germany

Inspired by recent feats in exchange coupling antiferromagnets to an adjacent material, we demonstrate the possibility of employing them for inducing spin-splitting in a superconductor, thereby avoiding the parasitic effects of ferromagnets employed to this end. We derive the Gor'kov equation for the matrix Green's function in the superconducting layer, considering a microscopic model for its disordered interface with a two-sublattice magnetic insulator. We find that an antiferromagnetic insulator with effectively uncompensated interface induces a

large, disorder-resistant spin-splitting in the adjacent superconductor, thereby addressing the feasibility of a wide range of devices involving spin-split superconductors. In addition, we find contributions to the self-energy stemming from the interfacial disorder. Within our model, these mimic impurity and spin-flip scattering, while another breaks the symmetries in particle-hole and spin spaces. The latter contribution, however, vanishes in the quasi-classical approximation and thus, does not significantly affect the superconducting state. Our results illustrate the potential of antiferromagnets for superconducting spintronics avoiding stray fields usually accompanying ferromagnets.

[1] Akashdeep Kamra, Ali Rezaei, Wolfgang Belzig, arXiv:1806.10356 (2018); accepted in PRL

TT 49.11 Wed 15:00 Poster D

**Phonon anomalies in FeS** — ●LEANDER PEIS<sup>1,2</sup>, ANDREAS BAUM<sup>1,2</sup>, ANA MILOSAVLJEVIĆ<sup>3</sup>, NENAD LAZAREVIĆ<sup>3</sup>, MILOŠ M. RADONJIĆ<sup>3</sup>, BOŽIDAR NIKOLIĆ<sup>4</sup>, MERLIN MITSCHKE<sup>1,2</sup>, ZAHRA INANLOO MARANLOO<sup>1</sup>, MAJA ŠČEPANOVIĆ<sup>3</sup>, MIRJANA GRUJIĆ-BROJČIN<sup>3</sup>, NENAD STOJILLOVIĆ<sup>3,5</sup>, MATTHIAS OPEL<sup>1</sup>, AIFENG WANG<sup>6</sup>, CEDOMIR PETROVIĆ<sup>6</sup>, ZORAN V. POPOVIĆ<sup>3,7</sup>, and RUDI HACKL<sup>1</sup> — <sup>1</sup>Walther-Meissner-Institut, 85748 Garching, Germany — <sup>2</sup>Fakultät für Physik, Technische Universität München, 85748 Garching, Germany — <sup>3</sup>Institute of Physics Belgrade, 11080 Belgrade, Serbia — <sup>4</sup>Faculty of Physics, University of Belgrade, Belgrade, Serbia — <sup>5</sup>Department of Physics and Astronomy, University of Wisconsin Oshkosh, Oshkosh, WI 54901, USA — <sup>6</sup>Condensed Matter Physics and Materials Science Department, Brookhaven National Laboratory, Upton, NY 11973, USA — <sup>7</sup>Serbian Academy of Sciences and Arts, 11000 Belgrade, Serbia

Tetragonal FeS is studied using Raman spectroscopy. We identify the  $A_{1g}$  and  $B_{1g}$  phonon modes, a second order scattering process, and contributions from potentially defect-induced scattering. The temperature dependence between 300 and 20 K of all observed phonon energies is governed by the lattice contraction. The increase in energy of all modes below 20 K may indicate short range magnetic order. Lattice-dynamical simulations and a symmetry analysis for potential overtones are in good agreement with the experiments. The two-phonon excitation observed in a gap between the optical branches presumably becomes observable due to significant electron-phonon interaction.

TT 49.12 Wed 15:00 Poster D

**Microscopic phase diagram of LaFeAsO single crystals under pressure: A Mössbauer study** — ●PHILIPP MATERNE<sup>1</sup>, WENLI BI<sup>2,1</sup>, JIYONG ZHAO<sup>1</sup>, MICHAEL YU HU<sup>1</sup>, RHEA KAPPENBERGER<sup>3,4</sup>, SABINE WURMEHL<sup>3,4</sup>, SAICHARAN ASWARTHAM<sup>3</sup>, BERND BÜCHNER<sup>3,4</sup>, and ESEN ERCAN ALP<sup>1</sup> — <sup>1</sup>Argonne National Laboratory, Lemont, IL 60439, USA — <sup>2</sup>Department of Geology, University of Illinois at Urbana-Champaign, Urbana, Illinois 61801, USA — <sup>3</sup>Leibniz Institute for Solid State and Materials Research (IFW) Dresden, D-01069, Germany — <sup>4</sup>Institute of Solid State and Materials Physics, TU Dresden, D-01069 Dresden, Germany

We investigated a LaFeAsO single crystal by means of synchrotron Mössbauer spectroscopy under pressure up to 7.5 GPa and down to 13 K and provide a microscopic phase diagram. A continuous suppression of the magnetic hyperfine field with increasing pressure was found and it completely vanishes at  $\sim 7.5$  GPa which is in contrast to the behaviour in polycrystalline samples where the magnetic order vanishes at  $\sim 20$  GPa. We discuss the sample dependence of the magnetic order among different single and polycrystalline samples and its relationship to the structural parameters.

[1] P. Materne *et al.*, Phys. Rev. B. **98**, 174510 (2018)

TT 49.13 Wed 15:00 Poster D

**Observation of a highly ordered vortex lattice in LiFeAs** — ●SVEN HOFFMANN<sup>1</sup>, CHRISTIAN SALAZAR<sup>1</sup>, PAVLO KHANENKO<sup>1</sup>, DANNY BAUMANN<sup>1</sup>, RONNY SCHLEGEL<sup>1</sup>, SAICHARAN ASWARTHAM<sup>1</sup>, I. MOROZOV<sup>2</sup>, BERND BÜCHNER<sup>1</sup>, and CHRISTIAN HESS<sup>1</sup> — <sup>1</sup>IFW Dresden, Helmholtzstraße 20, D-01069 Dresden — <sup>2</sup>MSU, Leninskiye Gory 1, R-119991 Moscow

Unlike other Fe-based superconductors, LiFeAs is a stoichiometric superconductor, showing no trace of nematic order, charge ordering or magnetic ordering and no Fermi surface nesting, while still maintaining a fairly high transition temperature. To gain additional information about the order parameter in this material we performed low temperature scanning tunneling microscopy and spectroscopy measurements. Differential conductance maps revealed a highly ordered vortex lattice, even at high magnetic fields. These findings contradict previous

Physics, Karlsruhe, Germany

IrTe<sub>2</sub> is distinguished by a structural phase transition whose origin is not understood up to the present day [1]. We grew crystals using the self-flux method starting from the reagents iridium and tellurium and got specimen with varying amounts of IrTe<sub>2</sub> and Ir<sub>3</sub>Te<sub>8</sub>, analyzed by x-ray powder diffraction. We studied the transition near T = 280 K in magnetization measurements down to T = 1.8 K probing also for superconductivity, which was reported for intercalated samples [2]. Results indicate that the structural transition happens over an extended range in temperature and superconductivity is absent in our samples.

Ir<sub>3</sub>Te<sub>8</sub> is not studied to such an extent as IrTe<sub>2</sub>. In previous publications a structural phase transition is reported [3]. We characterized the transition by performing magnetization measurements and X-ray diffraction.

[1] G. L. Pascut et al., PRL **112**, 086402 (2014)

[2] J. J. Yang et al., PRL **108**, 116402 (2012)

[3] L. Li et al., PRB **87** (2013).

TT 78.56 Thu 15:00 Poster D

**Angle-Resolved Photoemission Spectroscopy of rare earth LaSb<sub>2</sub>** — MATTEO MICHARDI<sup>1</sup>, FABIAN ARNOLD<sup>1</sup>, G. SHWETHA<sup>2</sup>, V. KANCHANA<sup>2</sup>, VAITHEESWARAN GANAPATHY<sup>3</sup>, KARL FREDERIK FAERCH FISHER<sup>1</sup>, AXEL SVANE<sup>1</sup>, MARCO BIANCHI<sup>1</sup>, BO BRUMMERSTEDT IVERSEN<sup>1</sup>, and PHILIP HOFMANN<sup>1</sup> — <sup>1</sup>Aarhus University, Denmark — <sup>2</sup>IIT-Hyderabad, India — <sup>3</sup>University of Hyderabad, India

Several rare earth dantimonides have been found to exhibit intriguing electronic properties such as anisotropic linear and non-saturating magnetoresistance. Among these materials, LaSb<sub>2</sub> is not only considered for application in magnetoresistive devices but it is also found to be superconducting at low temperatures and it is investigated as candidate material to host charge density wave phases. Despite the several studies on its transport properties, the electronic structure of LaSb<sub>2</sub> is still largely unknown. Here we present an angle-resolved photoemission spectroscopy and ab-initio calculation study of LaSb<sub>2</sub>(001). The observed band structure is found to be in good agreement with theoretical predictions. Our results reveal that LaSb<sub>2</sub> is a semimetal with a strongly nested two-dimensional Fermi surface. The low energy spectrum is characterized by four massive hole pockets and by four shallow, strongly directional, electron pockets that exhibit Dirac-like dispersion. We speculate on the possibility that this peculiar electronic structure drives the magnetoresistance to its quantum limit, explaining its unconventional behavior.

TT 78.57 Thu 15:00 Poster D

**Ground state properties of MnB<sub>4</sub>** — JAN LENNART WINTER<sup>1</sup>, NICO STEINKI<sup>1</sup>, DIRK SCHULZE GRACHTRUP<sup>1</sup>, DIRK MENZEL<sup>1</sup>, STEFAN SÜLLOW<sup>1</sup>, ARNO KNAPPSCHNEIDER<sup>2</sup>, and BARBARA ALBERT<sup>2</sup> — <sup>1</sup>Institut für Physik der Kondensierten Materie, TU Braunschweig, Germany — <sup>2</sup>Eduard-Zintl-Institut für Anorganische und Physikalische Chemie, TU Darmstadt, Germany

Recently, single crystalline MnB<sub>4</sub> was synthesized for the first time, yielding microscale crystals with dimensions of the order of 200 μm [1]. Based on band structure calculations, it was argued that the material is semiconducting as result of a Peierls distortion. Conversely, in a study of polycrystalline material it was concluded that the material is a weakly ferromagnetic metal [2].

To establish if MnB<sub>4</sub> is a semiconductor we have carried out single crystal four point resistivity measurements. For this purpose a setup for measuring microscale samples was developed and characterized. Qualitatively, we find semiconducting behavior (increasing resistivity for decreasing temperature), although a band gap could not be derived because of a non-linear Arrhenius plot. Our data are consistent with MnB<sub>4</sub> being a pseudogap/small gap material as proposed in [1]. A pronounced sample dependence of the transport properties points to the presence of impurity states. For the single crystals no ferromagnetic signatures could be obtained, suggesting an extrinsic cause of it in polycrystalline material.

[1] A. Knappschneider et al., Angew. Chem. **126**, 1710 (2014)

[2] H. Gou et al., PRB **89**, 064108 (2014)

TT 78.58 Thu 15:00 Poster D

**Scaling of the Optical Conductivity in the Transition from Thermal to Many-Body Localized Phases** — ROBIN STEINIGEWEG<sup>1</sup>, JACEK HERBRYCH<sup>2</sup>, FRANK POLLMANN<sup>3</sup>, and WOLFRAM BRENIĞ<sup>4</sup> — <sup>1</sup>University of Osnabrück — <sup>2</sup>CCQCN and University of Crete — <sup>3</sup>MPIPKS Dresden — <sup>4</sup>Technical University Braunschweig

We study the frequency dependence of the optical conductivity  $\text{Re } \sigma(\omega)$  of the Heisenberg spin-1/2 chain in the transition from thermal to many-body localized phases induced by the strength of a spatially random magnetic field. Using the method of dynamical quantum typicality, we calculate the real-time dynamics of the spin-current autocorrelation function and obtain the Fourier transform  $\text{Re } \sigma(\omega)$  in high frequency resolution and for system sizes  $L$  much larger than  $L \sim 14$  accessible to standard exact-diagonalization approaches. We unveil that the low-frequency behavior of  $\text{Re } \sigma(\omega)$  is well described by  $\text{Re } \sigma(\omega) \approx \sigma_{\text{dc}} + a |\omega|^\alpha$ , with  $\alpha \approx 1$  in a wide range of the thermal phase and up to the many-body localized phase. We particularly detail the decrease of  $\sigma_{\text{dc}}$  as a function of increasing disorder for strong exchange anisotropies. We further find that the temperature dependence of  $\sigma_{\text{dc}}$  is consistent with the existence of a mobility edge.

TT 78.59 Thu 15:00 Poster D

**Non-Equilibrium transport study in strongly correlated hetero structures** — MILOŠ RADONJIC<sup>1,2</sup>, IVAN RUNGGER<sup>3</sup>, and LIVIU CHIONCEL<sup>1</sup> — <sup>1</sup>Center for Electronic Correlations and Magnetism, TP III, Institute of Physics, University of Augsburg, D-86135 Augsburg, Germany — <sup>2</sup>Scientific Computing Laboratory, Institute of Physics Belgrade, University of Belgrade, Pregrevica 118, 11080 Belgrade, Serbia — <sup>3</sup>Mathematics and Modelling, National Physical Laboratory, Hampton Rd, Teddington, Middlesex, UK, TW11 0LW

The effects of local electronic interactions and finite temperatures upon the non-equilibrium transport properties across the metallic heterostructure Cu<sub>4</sub>CoCu<sub>4</sub> are studied. Results are obtained by combining DFT and equilibrium DMFT solver on one side, and DFT and non-equilibrium steady state impurity solver based on second order perturbation in Hubbard interaction  $U$ , on the other side. Results of these two methods are compared for the transmission. It is shown that local, but dynamical electronic correlations reduce the total transmission at the Fermi level, and also increase the spin polarization. The multi-orbital non-equilibrium steady state impurity solver is formulated in the Keldysh Green's function formalism and allows us an access to all non-equilibrium quantities, such as non-equilibrium steady state current.

TT 78.60 Thu 15:00 Poster D

**Self-consistent Born approach to strongly correlated electron systems in non-equilibrium** — GERHARD DORN — TU Graz, Austria

The self-consistent Born master equation method is apt to describe the non-equilibrium behaviour of strongly correlated electron systems which are weakly coupled to non-interacting leads.

The poster compares the self-consistent Born approach with different other methods, like Born Markov master equation or Cluster Perturbation Theory (CPT), and shows the improvements according to correct representation of the Coulomb blockade or of the lead induced level broadening.

TT 78.61 Thu 15:00 Poster D

**Boundary-driven dissipative quantum chains in large external fields** — ZALA LENARCIC<sup>1</sup> and TOMAZ PROSEN<sup>2</sup> — <sup>1</sup>Institute for theoretical physics, University of Cologne, D-50937, Germany — <sup>2</sup>Faculty for mathematics and physics, University of Ljubljana, SI-1000 Ljubljana, Slovenia

We treat the nonequilibrium transport as a consequence of a combined driving: from a pseudo-force, originating in the bias in Markovian processes at the system's boundaries, and from a real force due to an external field gradient  $g$ . For strong field gradients a systematic perturbation theory of the steady state current and slowest decay modes of the density matrix can be formulated for a general inhomogeneous XXZ spin 1/2 chain. From the explicit asymptotic expression for the current it is clear that by combining both drivings arbitrarily large current rectification can be achieved under  $g \rightarrow -g$  in the presence of interaction. Moreover, via tailored field profiles one can obtain further control over the strength of stationary current.

[1] Z. Lenarčič and T. Prosen, PRE **91**, 030103(R) (2015).

TT 78.62 Thu 15:00 Poster D

**Combining ab initio wavefunction methods with dynamical mean-field theory: A feasibility study with NiO** — DANIL TOLOUI-MANTADAKIS, MARC HOEPPNER, THEODOROS TSATSOUKIS, ANDREAS GRUENEIS, and PHILIPP HANSMANN — Max Planck Institute for Solid State Research, Stuttgart, Germany



## TT 47: Correlated Electrons: Other Materials

Time: Wednesday 10:30–13:00

Location: H21

TT 47.1 Wed 10:30 H21

**Phonon renormalization in LaCoO<sub>3</sub> by inelastic neutron and x-ray scattering** — ●MAXIMILIAN KAUTH<sup>1</sup>, FRANK WEBER<sup>1</sup>, and JOHN-PAUL CASTELLAN<sup>1,2</sup> — <sup>1</sup>Institut für Festkörperphysik, Karlsruhe Institut für Technologie — <sup>2</sup>Laboratoire Léon Brillouin, CEA Saclay

LaCoO<sub>3</sub> exhibits two broad magnetic-electric transitions, a diamagnetic to paramagnetic spin-state transition at  $T_{SS} \approx 100$  K and a metal-insulator transition at  $T_{MI} \approx 500$  K. The spin transitions on heating are proposed to be as follows [1]: from a homogeneous LS state to a mixed Low-Spin/High-Spin (LS/HS) state with strong spin-charge fluctuations at  $T=T_{SS}$  and, subsequently, into a homogeneous HS state at  $T=T_{MI}$ . The lattice participates in the state mixture by expansion of CoO<sub>6</sub> octahedra around the HS sites, while the ones around LS sites have a reduced size [2]. The originally proposed static order [2] has not been observed experimentally and, hence, the ordering is expected to be dynamic and short-ranged. We investigated the lattice dynamical properties of LaCoO<sub>3</sub> using inelastic neutron scattering. Based on detailed ab-initio lattice dynamical calculations (performed in our institute), we aim for a comprehensive understanding of lattice dynamics in LaCoO<sub>3</sub>. The above discussed crossovers and spin state order should be reflected in the lattice degrees of freedom via quasi elastic scattering and phonon renormalization effects.

[1] M. Karolak et al., PRL **115**, 046401 (2015)[2] J. B. Goodenough, J. Phys. Chem. Solids **6**, 287 (1958)

TT 47.2 Wed 10:45 H21

**Excitonic transition in (Pr,Ca)CoO<sub>3</sub> family** — ●JAN KUNEŠ and PAVEL AUGUSTINSKÝ — Institute of Physics, AS CR, Prague

The members of  $(\text{Pr}_{1-y}\text{Y}_y)_{1-x}\text{Ca}_x\text{CoO}_3$  family exhibit a continuous phase transition accompanied by disappearance of the fluctuating moment of Co and increase of resistivity by several decades. Most intriguing feature of the low temperature phase is breaking of the time reversal symmetry without presence of ordered atomic moments. We will argue that the experimental observations are explained by condensation of atomic size excitons, which gives rise to ordered magnetic multipoles. We will present model calculations performed with dynamical-mean field theory, which demonstrate general features of the excitonic condensation. In addition, we will present results of material specific LDA+U calculations which uncover the excitonic order in  $\text{Pr}_{0.5}\text{YCa}_{0.5}\text{CoO}_3$  and explain its low temperature behavior.

[1] J. Kuneš, P. Augustinský, PRB **90**, 235112 (2014).

TT 47.3 Wed 11:00 H21

**Theoretical study of spin-state transition in LaCoO<sub>3</sub> using LDA+MLFT** — ●EVGENY GORELOV<sup>1</sup>, IGOR KRIVENKO<sup>2</sup>, MICHAEL KAROLAK<sup>3</sup>, and ALEXANDER LICHTENSTEIN<sup>1,2</sup> — <sup>1</sup>European XFEL GmbH Albert-Einstein-Ring 19, 22761 Hamburg, Germany — <sup>2</sup>University of Hamburg, Jungiusstrasse 9, 20355 Hamburg, Germany — <sup>3</sup>University of Würzburg, Sanderring 2, 97070 Würzburg, Germany

LaCoO<sub>3</sub> demonstrates variety of phase transitions due to competing interactions governing its electronic structure, including metal-to-insulator transition around  $T \approx 500$  K and gradual spin-state transition around  $T \approx 80$ –120 K. In this work we focus on spin-state transition, and use theoretical approach of M. Haverkort, taking into account transition metal ion and its octahedral oxygen surrounding [1]. This approach allow us to calculate the resonant Co  $L_{2,3}$  X-ray absorption spectra (XAS), using ab-initio calculated model parameters, i.e. nearest neighbors hopping matrix. The calculations are performed for experimental crystal structures for different temperatures in the range of 5–600 K [2]. In our calculations we include Co  $3d$  orbitals with full Coulomb vertex, and five ligand orbitals, constructed from  $2p$  orbitals of O atoms, forming the octahedra around Co ion. We discuss changes in the XAS spectra induced by thermal expansion of the lattice, as well as caused by change of electron temperature.

[1] M. W. Haverkort, M. Zwierzycki, and O. K. Andersen, PRB **85**, 165113 (2012)[2] P. G. Radaelli and S.-W. Cheong, PRB **66**, 094408 (2002)

TT 47.4 Wed 11:15 H21

**Construction of effective low-energy interactions for three-orbital cuprate models with electronic correlation** —

●CORNELIA HILLE<sup>1</sup>, XIAODONG CAO<sup>2</sup>, CARSTEN HONERKAMP<sup>3</sup>, PHILIPP HANSMANN<sup>2</sup>, and SABINE ANDERGASSEN<sup>1</sup> — <sup>1</sup>Institut für Theoretische Physik, Universität Tübingen, Tübingen, Germany — <sup>2</sup>Max Planck Institute for Solid State research, Stuttgart, Germany — <sup>3</sup>Institute for Solid State Theory, RWTH Aachen, Aachen, Germany

Real materials typically have involved bandstructures and a many-body solution of the full Hamiltonian is not feasible. To identify the most relevant degrees of freedom we often start from ab initio single particle (e.g. DFT, Hartree Fock, GW) calculations and integrate out states of high energy remaining with a low-energy effective Hamiltonian. For basically all transition metal oxides this procedure leads to the question if and how to include oxygen 2p states explicitly. We present effective low-energy interactions for three-orbital cuprate models calculated in a cRPA framework. We find effective copper d-state interactions which are strongly dynamically screened by transitions involving the oxygen 2p states.

TT 47.5 Wed 11:30 H21

**Self-consistent GW+EDMFT simulation of SrVO<sub>3</sub> - Hubbard vs. plasmon physics** — ●LEWIN BOEHNKE<sup>1</sup>, FREDRIK NILSSON<sup>2</sup>, FERDI ARYASETIWAN<sup>2</sup>, and PHILIPP WERNER<sup>1</sup> — <sup>1</sup>University of Fribourg, Switzerland — <sup>2</sup>Lund University, Sweden

SrVO<sub>3</sub> has been considered a prototypical strongly correlated metal for more than a decade. Its (inverse) photoemission spectra [1] show a characteristic three peak structure close to the Fermi level.

We develop a multi-orbital GW+extended dynamical mean-field theory [2,3] framework, applying approximations of increasing rigor to orbital subsets of increasing degree of correlation with the goal of unbiased finite temperature ab-initio calculations of materials classes with relevant local and non-local many-body correlations.

We use a suitable continuous time quantum Monte Carlo impurity solver (CT-Hyb) [4] to deal with the frequency dependence of the effective impurity interaction and a tailored Matsubara frequency implementation of the GW-algorithm to solve self consistency cycle.

For SrVO<sub>3</sub> we find that the screening from nonlocal Coulomb interactions substantially reduces the effective local interaction, suppressing the Hubbard bands. At the same time, plasmon satellites are formed that are consistent with experimental observations. [1]

[1] K. Morikawa, T. Mizokawa, K. Kobayashi, A. Fujimori, H. Eisaki, S. Uchida, F. Iga, and Y. Nishihara, PRB **52**, 13711 (1995)[2] S. Biermann, F. Aryasetiawan, and A. Georges, PRL **90**, 086402 (2003)[3] T. Ayral, S. Biermann, and P. Werner, PRB **87**, 125149 (2013)[4] E. Gull, *et al.* RMP **83**, 349 (2011)

## 15 min. break

TT 47.6 Wed 12:00 H21

**The electronic structure of palladium in the presence of many-body effects** — ●ANDREAS ÖSTLIN<sup>1,2</sup>, WILHELM APPELT<sup>3,1</sup>, IGOR DI MARCO<sup>4</sup>, WEIWEI SUN<sup>4</sup>, MILOS RADONJIC<sup>1</sup>, MICHAEL SEKANIA<sup>1</sup>, LEVENTE VITOS<sup>2,4,5</sup>, and LIVIU CHIONCEL<sup>3,1</sup> — <sup>1</sup>Theoretical Physics III, Center for Electronic Correlations and Magnetism, Institute of Physics, University of Augsburg, D-86135 Augsburg, Germany — <sup>2</sup>Department of Materials Science and Engineering, Applied Materials Physics, KTH Royal Institute of Technology, SE-10044 Stockholm, Sweden — <sup>3</sup>Augsburg Center for Innovative Technologies, University of Augsburg, D-86135 Augsburg, Germany — <sup>4</sup>Department of Physics and Astronomy, Division of Materials Theory, Uppsala University, Box 516, SE-75120 Uppsala, Sweden — <sup>5</sup>Research Institute for Solid State Physics and Optics, Hungarian Academy of Sciences, P.O. Box 49, H-1525 Budapest, Hungary

Including on-site electronic interactions described by the multi-orbital Hubbard model we study the correlation effects in the electronic structure of bulk palladium within the framework of combined density functional and dynamical mean field theory, DFT+DMFT, using the fluctuation exchange approximation. The agreement between the experimentally determined and the theoretical lattice constant and bulk modulus is improved when correlation effects are included. At the same time we discuss the possibility of satellite formation in the high energy binding region. Investigation of non-local correlation effects

within the *GW* method is also performed.

TT 47.7 Wed 12:15 H21

**Phase separation in  $Y_{0.63}Ca_{0.37}TiO_3$**  — •THOMAS KOETHE<sup>1</sup>, BERNHARD ZIMMER<sup>1</sup>, RAPHAEL GERMAN<sup>1</sup>, ALEXEI BARINOV<sup>2</sup>, ALEXANDER KOMAREK<sup>1,3</sup>, FULVIO PARMIGIANI<sup>2</sup>, MARKUS BRADEN<sup>1</sup>, and PAUL VAN LOOSDRECHT<sup>1</sup> — <sup>1</sup>III. Physikalisches Institut, Universität zu Köln — <sup>2</sup>Elettra Sincrotrone, Trieste (Italy) — <sup>3</sup>Max-Planck-Institut für Chemische Physik fester Stoffe, Dresden

We have investigated the domain structure and Raman response of  $Y_{0.63}Ca_{0.37}TiO_3$  single crystals which show a clear metal-to-insulator transition at ca. 170 K, with a wide hysteresis in the resistivity ranging down to ca. 50 K. We observe by use of a conventional optical microscope the appearance of two distinct regions at temperatures below ca. 200 K, with a characteristic length scale of order of 10  $\mu m$ . By means of Raman spectroscopy we can identify the regions to correspond to the metallic and insulating domains, and follow the evolution of the domains as function of temperature down to 5 K. Preliminary results of spacially resolved PES confirm the presence of electronically distinct regions on the  $\mu m$  scale at low temperature.

TT 47.8 Wed 12:30 H21

**Breathing Mode Distortion and Magnetic Order in Rare-Earth Nickelates  $RNiO_3$**  — •ALEXANDER HAMPEL and CLAUDE EDERER — Materials Theory, ETH Zürich, Switzerland

Rare-earth nickelate perovskites display a rich and not yet fully understood phase diagram, where all  $RNiO_3$  compounds with  $R$  from Sm to Lu undergo a non-magnetic metal-insulator transition (MIT). This transition is connected to a lattice distortion, which can be described as breathing mode of the oxygen octahedra surrounding the Ni cations. Between 100-250 K the  $RNiO_3$  compounds undergo a magnetic transition to an antiferromagnetic (AFM) state, with a wave-

vector  $k = [\frac{1}{4} \frac{1}{4} \frac{1}{4}]$  relative to the underlying simple cubic perovskite structure.

Here, we use density functional theory and its extensions (DFT+ $U$ , DFT+DMFT) together with distortion mode analysis to explore the interplay between lattice distortions, magnetic order, and the strength of the local Coulomb interaction  $U$  in rare earth nickelates. Our results show a strong dependency of the breathing mode amplitude on the magnetic order, with a much larger breathing mode obtained for the AFM state compared to the ferromagnetic case. Furthermore, we demonstrate that DFT+ $U$  is able to capture the correct trends of the lattice distortions across the nickelate series.

TT 47.9 Wed 12:45 H21

**Metal-insulator transition in 2D antiferromagnet  $FePS_3$  upon applied pressure** — •MATTHEW JOHN COAK<sup>1</sup>, CHARLES ROBERT SEBASTIAN HAINES<sup>1,2</sup>, and SIDDARTH SHANKAR SAXENA<sup>1</sup> — <sup>1</sup>CamCool Laboratory, University of Cambridge — <sup>2</sup>CamCool Research Ltd, UK

$FePS_3$  belongs to a rich family of structurally and magnetically quasi-two-dimensional compounds, with a magnetic ground state in which spins are ordered as ferromagnetic chains coupled antiferromagnetically. At ambient pressure, it is an insulator with a direct gap of approximately 0.5 eV and a room temperature resistivity of approximately 104  $\Omega cm$ .

We present the results of resistivity measurements under pressures up to 110 kbar for this material. The insulating phase is suppressed at a pressure in the range 40-70 kbar giving way to a new metallic phase. Interesting intermediate behaviour is seen at pressures around the transition as the gap closes. At high pressure, the resistivity develops linear temperature dependence with an upturn in resistivity which may indicate a low temperature phase transition or impurity scattering.

# APS March Meeting 2016

Baltimore, Maryland

<http://www.aps.org/meetings/march/index.cfm>

**2:54PM C21.00003 Study of magnetic and magnetocaloric properties of monoclinic and triclinic spin chain  $\text{CoV}_2\text{O}_6$** , MOUMITA NANDI, PRABHAT MANDAL, Saha Institute of Nuclear Physics, 1/AF Bidhannagar Kolkata, India — We have investigated magnetic and magnetocaloric properties of both monoclinic and triclinic phases of  $\text{CoV}_2\text{O}_6$  from magnetization and heat capacity measurements. Conventional and inverse magnetocaloric effects have been observed in both phases of  $\text{CoV}_2\text{O}_6$ . For a field change from 0 to 7 T, maximum values of magnetic entropy change and adiabatic temperature change reach  $11.8 \text{ J kg}^{-1} \text{ K}^{-1}$  and 9.5 K respectively for monoclinic  $\text{CoV}_2\text{O}_6$  while the corresponding values reach  $12.1 \text{ J kg}^{-1} \text{ K}^{-1}$  and 13.1 K for triclinic  $\text{CoV}_2\text{O}_6$ . Particularly for triclinic  $\text{CoV}_2\text{O}_6$ , the magnetocaloric parameters are quite large in low or moderate field range. Apart from this, we have constructed magnetic phase diagram of monoclinic  $\text{CoV}_2\text{O}_6$  where field-induced complex magnetic phases appear below a certain critical temperature 6 K when external magnetic field is applied along crystallographic easy axis.

**3:06PM C21.00004 Entanglement properties of the bond alternating Heisenberg chain with general integer spins**, SHOHEI MIYAKOSHI, Chiba Univ, SATOSHI NISHIMOTO, IFW Dresden, TU Dresden, YUKINORI OTHA, Chiba Univ — Symmetry protected topological (SPT) phases are a gapped phase under a given symmetry. Unless any symmetries that protect the SPT phases are broken, the SPT phases can be distinguished from each other. Recently, it was pointed out that the entanglement spectrum of the many-body state characterizes such SPT phases. In particular, the degeneracy of the entanglement spectrum reflects the corresponding symmetries and edge states of the system. Motivated by recent studies of the SPT phases, we study the bond-alternating Heisenberg model with general integer spins and clarify the entanglement properties of the ground state using the density matrix renormalization group method. In particular, this model has the intermediate phase at  $S > 1$  due to the bond alternation. The entanglement properties of this phase in the case of  $S > 2$  have not been studied sufficiently because of the numerical difficulties under an extremely small spin-gap situation. We studied the case of  $S = 1, 2, 3$  using the antiperiodic boundary condition. Under the antiperiodic boundary condition, we found that the doubly degenerate spectra which characterize the intermediate phase can be observed in the entanglement spectrum. We will also discuss the effect of the single-ion uniaxial anisotropy.

**3:18PM C21.00005 Finite temperature dynamics of spin-1/2 chains with symmetry breaking interactions<sup>1</sup>**, SALVATORE R. MANMANA, ALEXANDER C. TIEGEL, THOMAS PRUSCHKE, Institute for Theoretical Physics, University of Goettingen, ANDREAS HONECKER, LPTM, Université de Cergy-Pontoise — I will discuss recent developments for flexible matrix product state (MPS) approaches to calculate finite-temperature spectral functions of low-dimensional strongly correlated quantum systems. The main focus will be on a Liouvillean formulation. The resulting algorithm does not specifically depend on the MPS formulation, but is applicable for any wave function based approach which can provide a purification of the density matrix, opening the way for further developments of numerical methods. Based on MPS results for various spin chains, in particular systems with Dzyaloshinskii-Moriya interactions caused by spin-orbit coupling and dimerized chains, I will discuss how symmetry breaking interactions change the nature of the finite-temperature dynamic spin structure factor obtained in ESR and neutron scattering experiments.

<sup>1</sup>We acknowledge funding by the Helmholtz Virtual Institute "New States of Matter and Their Excitations".

**3:30PM C21.00006 Magnetic Spin Relaxation Probed with Sweep Speed Dependent Coercivity<sup>1</sup>**, THOMAS GREDIG, MATTHEW BYRNE, Department of Physics and Astronomy, California State University Long Beach — The magnetic spin relaxation of finite-length iron chains has been investigated in iron phthalocyanine thin films by means of sweep speed dependence on magnetic coercivity. The Fe(II) ions are embedded in a carbon matrix and molecules self-assemble during vacuum sublimation, so that the Fe(II) cores form well-separated chains of 1.3 nm and tunable chain lengths within the polycrystalline thin film. The average length of the chains is controlled through deposition variables and ranges from 30 nm to 300 nm. The coercivity strongly increases with chain length in this regime. This may be an interesting experimental realization of a low-dimensional finite-sized Ising model. The coercivity dependence on chain length and sweep speed is described with an Ising model based on Glauber dynamics.

<sup>1</sup>Research support from NSF under grant DMR 0847552.

**3:42PM C21.00007 ANISOTROPIC PHASE DIAGRAM OF THE FRUSTRATED SPIN CHAIN  $\beta\text{-TeVO}_4$** , F. WEICKERT, M JAIME, N HARRISON, B. L. SCOTT, Los Alamos Natl Lab, A. LEITMAE, L. HEINMAA, R STERN, O JANSON, NICPB Tallinn, Estonia, H. BERGER, EPFL, Lausanne, Switzerland, H ROSNER, MPI CPFS, Dresden, Germany, A. A. TSIRLIN, Augsburg University, Germany — We will present experimental as well as theoretical data on  $\beta\text{-TeVO}_4$  a candidate for the  $J_1\text{-}J_2$  chain model with ferromagnetic  $J_1 \sim 18 \text{ K}$  and antiferromagnetic  $J_2 \sim 48 \text{ K}$  coupling constants. The  $T - H$  magnetic phase diagram is revealed by measurements of the magnetization, specific heat, magnetostriction, and thermal expansion on oriented single crystals at temperatures between 0.5 K and 50 K and in magnetic fields up to 50 T. The high field data were taken in a capacitor bank-driven pulsed magnet at NHMFL - LANL and complemented with measurements in a superconducting magnet. Our comprehensive study allows for the first time a detailed mapping of the phase diagram in both directions,  $H \parallel ab$  and  $H \parallel c$ . We find clear evidence for 5 different phases including full polarization of the magnetic moments above 23 T that is only weakly dependent on the crystal orientation. Surprisingly, the phase boundary at the saturation field splits into two distinct lines below 5 K. The magnetic phases occurring at fields below 10 T show significant magnetic anisotropy between  $H \parallel ab$  and  $H \parallel c$ . The nature of the different phases and regions in  $\beta\text{-TeVO}_4$  is still far from being understood, but our results will stimulate further research on this interesting model compound.

**3:54PM C21.00008 Unusual features of magnetism in transition-metal-doped phthalocyanines  $\text{C}_{32}\text{H}_{16}\text{N}_8\text{TM}$  (TM = Mn, Fe, Co, Ni, Cu)**, ZHENGJUN WANG, MOHINDAR S. SEEHRA, Department of Physics and Astronomy, West Virginia University — Transition-metal-doped phthalocyanines (TMPc), semiconductors with potential optoelectronic applications [1], are planar molecules with the TM atom at the center bound to four N atoms and forming a linear chain along the monoclinic b-axis. Because of this symmetry, the ground states of TMPc often violate the Hund's rules; e.g. the  $S = 3/2$  state for  $d^5 \text{ Mn(II)}$  in  $\beta\text{-MnPc}$ ,  $S = 1/2$  state for the  $d^7 \text{ Co(II)}$  in  $\beta\text{-CoPc}$ , and  $S=0$  for  $\text{Ni(II)}$  in  $\text{NiPc}$ . The magnetic properties of TMPc are also affected by the stack angle  $\delta$  between the orientation of the molecular plane and the b-axis,  $\delta$  being  $65(45)$  for  $\alpha$  ( $\beta$ ) phase [2]. For  $\beta\text{-CoPc}$ , our  $M$  vs.  $T$  data fits well with the Bonner-Fisher model for  $S = 1/2$  AFM Heisenberg linear chain [3] yielding the  $\text{Co}^{2+}\text{-Co}^{2+}$  exchange constant  $J/k_B = -1.5 \text{ K}$ . For  $\beta\text{-MnPc}$ , a long-presumed ferromagnet with  $T_C \approx 9 \text{ K}$  [4], our magnetic studies show it to be an Ising chain magnet with Arrhenius magnetic relaxation governed by  $J/k_B = 2.6 \text{ K}$  and the zero-field splitting  $D/k_B = 8.3 \text{ K}$ . In  $\beta\text{-MnPc}$ , the absence of  $\lambda$ -type peak in specific heat and no peaks in ac susceptibilities near the quoted  $T_C \approx 9 \text{ K}$  confirms the absence of long range order (LRO). Instead we argue that LRO is absent in  $\beta\text{-MnPc}$  as  $D \gg J$  makes the spins in a chain parallel but canted with respect to spins in neighboring chains. [1]G. Mattioli et al, Phys. Rev. Lett. 101, 126805 (2008); [2]Z. Wang et al, IEEE Trans. Mag. 51, 2700104(2015); [3]J. Bonner & M. Fisher, Phys. Rev. 135, A640 (1964); [4]Y. Taguchi et al, J. Magn. Magn. Mater. 301, 1229 (2007).

means of the Constrained RPA method (157 elements).

TT 71.13 Wed 15:00 Poster B

**Multi-spin multi-channel Kondo box problem** — ●MIREK HÄNSEL, ANDREJ SCHWABE, and MICHAEL POTTHOFF — Institut für Theoretische Physik, Universität Hamburg

In a quantum box, where one or several quantum spins are coupled by a weak antiferromagnetic local exchange  $J$  to a system of non-interacting conduction electrons, the standard Kondo effect is cut by the finite system size. The residual finite-size Kondo effect can be described by perturbation theory in  $J$ . We show that the effective low-energy physics is given by a central-spin model where typically each impurity spin couples to the spin of a completely delocalized conduction-electron eigenstate at the Fermi edge. Different screening channels are given for the case of orthogonal eigenstates. We discuss the general case of several spins and several channels by analyzing various geometries, e.g., one-dimensional chains and two-dimensional lattices with different boundary conditions, and different geometrical setups of the impurity spins. The couplings in the effective central-spin model and the resulting magnetic structure are calculated as functions of the conduction-electron density and the geometry.

TT 71.14 Wed 15:00 Poster B

**Towards a Matrix Product State based description of steady-state non-equilibrium physics in 1D correlated quantum systems using Lindblad driving** — ●FRAUKE SCHWARZ<sup>1</sup>, IRENEUSZ WEYMANN<sup>2</sup>, JAN VON DELFT<sup>1</sup>, and ANDREAS WEICHELBAUM<sup>1</sup> — <sup>1</sup>Physics Department, Arnold Sommerfeld Center for Theoretical Physics and Center for NanoScience, Ludwig-Maximilians-Universität, Munich, Germany — <sup>2</sup>Faculty of Physics, Adam Mickiewicz University, Poznań, Poland

The Kondo effect in quantum impurity models in equilibrium is well-understood by means of the Numerical Renormalization Group (NRG). To extend the description of Kondo physics to situations of steady state non-equilibrium, we want to combine the ideas of NRG with the Lindblad approach to open quantum systems. For this purpose, we introduce additional reservoirs described by Lindblad terms in the Liouville equation which restore the continuum properties of the discretized leads that are coupled to the impurity. This enables us to define the temperature and the chemical potential for each lead independently. To reduce the dimensionality of the problem we employ the stochastic quantum trajectory approach to solve the underlying Lindblad equation.

Several ideas on how to define adequate Lindblad operators will be presented together with their implications for the calculation of the quantum trajectories based on Matrix Product States.

TT 71.15 Wed 15:00 Poster B

**Temperature dependent properties in the infinite-dimensional Hubbard model with a magnetic field** — ●MARKUS DUTSCHKE<sup>1</sup>, LIVIU CHIONCEL<sup>1,2</sup>, and JUNYA OTSUKI<sup>3</sup> — <sup>1</sup>Theoretical Physics III, Center for Electronic Correlations and Magnetism, Institute of Physics, University of Augsburg, D-86135 Augsburg, Germany — <sup>2</sup>Augsburg Center for Innovative Technologies, University of Augsburg, D-86135 Augsburg, Germany — <sup>3</sup>Department of Physics, Tohoku University, Sendai 980-8578, Japan

We investigate the temperature and field dependence of the spectral function, the effective mass enhancement and the magnetisation of the infinite-dimensional Hubbard model in a magnetic field. We compare results for different interaction strengths at half-filling, near half-filling and quarter-filling. These are achieved by using dynamical mean-field theory (DMFT) with a continuous-time quantum monte carlo (CT-QMC) impurity solver and are compared with some NRG results.

TT 71.16 Wed 15:00 Poster B

**Influence of strong disorder on incoherent transport near the Mott transition: Statistical DMFT approach** — ●MILOŠ RADONJIC<sup>1,2</sup>, DARKO TANASKOVIC<sup>2</sup>, and VLADIMIR DOBROSLAVJEVIC<sup>3</sup> — <sup>1</sup>Center for Electronic Correlations and Magnetism, Theoretical Physics III, Institute of Physics, University of Augsburg, D-86135 Augsburg, Germany — <sup>2</sup>Scientific Computing Laboratory, Institute of Physics Belgrade, University of Belgrade, Pregrevica 118, 11080 Belgrade, Serbia — <sup>3</sup>Department of Physics and National High Magnetic Field Laboratory, Florida State University, Tallahassee, Florida 32306, USA

We present the study of disordered half-filled Hubbard model within

the Statistical dynamical mean field theory, which is a unique theoretical method reliable and controllable in a wide temperature, disorder and interaction range. We have successfully applied this method, for the first time, on the finite size cubic lattice, at finite temperature.

The results show that the finite size effects are negligible already on the lattice with  $6*6*6$  sites (except at the lowest temperatures, deep in the Fermi liquid regime). Also we confirmed that disorder is strongly screened on the metallic side of the Mott MIT and that inelastic scattering is dominant outside of the Fermi liquid region. We defined a local resistivity and proposed a resistor network method for calculating lattice dc resistivity. Two types of sites can be identified: strongly correlated - with the local occupation close to 1, and weakly correlated - away from local half-filling. Strongly correlated sites are responsible for strong, non-monotonic temperature dependence of the resistivity.

TT 71.17 Wed 15:00 Poster B

**Electronic correlations and spin-orbit coupling in  $d^4$  osmates** — ●VLADISLAV POKORNÝ<sup>1</sup> and JAN KUNES<sup>2</sup> — <sup>1</sup>Center for Electronic Correlations and Magnetism, Institute of Physics, University of Augsburg, Germany — <sup>2</sup>Institute of Physics, Academy of Sciences of the Czech Republic, Prague, Czech Republic

We employ the combination of the density functional theory and the dynamical mean-field theory to investigate the electronic correlations in heavy transition metal compounds with partially filled  $t_{2g}$  levels such as  $d^4$  osmates which were prepared recently. Using the hybridization-expansion, continuous-time quantum Monte Carlo impurity solver we study the combined influence of electron correlations and spin-orbit coupling effects on the the electronic and magnetic structure of these systems.

TT 71.18 Wed 15:00 Poster B

**NMR on the quantum critical ferromagnet  $\text{YbNi}_4\text{P}_2$ : Evidence for a large basal plane local anisotropy** — ●RAJIB SARKAR<sup>1</sup>, MARCO GÜNTHER<sup>1</sup>, CORNELIUS KRELLNER<sup>3</sup>, MICHAEL BAENITZ<sup>2</sup>, CHRISTOPH GEIBEL<sup>2</sup>, and HANS-HENNING KLAUSS<sup>1</sup> — <sup>1</sup>IFP, TU Dresden, D-01069 Dresden, Germany — <sup>2</sup>MPI-CPFS, D-01187 Dresden, Germany — <sup>3</sup>Goethe University Frankfurt, D-60438 Frankfurt am Main, Germany

In the last 10 years there was growing evidence both from theoretical work and experimental observations that a ferromagnetic (FM) quantum critical point (QCP) cannot exist in a pure system, because the transition becomes first order before reaching the QCP. Therefore the recent report of clear evidence for a FM-QCP in the heavy fermion compound  $\text{YbNi}_4\text{P}_2$  attracted considerable attention. While the Bravais lattice of this compound is tetragonal, resulting in isotropic in-plane macroscopic magnetic properties, the local symmetry on the Yb site (and on the P-site) is lower, orthorhombic. Therefore some in-plane anisotropy of local magnetic properties is expected, which could however not yet been studied because of the absence of related effects on macroscopic properties. We performed <sup>31</sup>P NMR investigations on a grain aligned polycrystalline sample of  $\text{YbNi}_4\text{P}_2$ . We observed three structures in the NMR spectra, which present quite different T-dependence of the respective Knight shifts. An analysis of these results provides a clear evidence for strong local in-plane anisotropy of the Yb-moment due to the orthorhombic crystal electric field. Implication for the magnetic ordered state shall be discussed.

TT 71.19 Wed 15:00 Poster B

**Single crystal growth of the heavy fermion compounds  $\text{YbRh}_2\text{Si}_2$  and  $\text{YbNi}_4\text{P}_2$**  — ●CONSTANTIN BUTZKE, KRISTIN KLIEMT, and CORNELIUS KRELLNER — Physikalisches Institut, Goethe Universität Frankfurt, 60438 Frankfurt am Main, Germany

Heavy fermion systems are model systems to unravel the exciting physics around quantum-phase transitions. Studying these emergent phenomena necessitates the preparation of large and high-quality single crystals. We report on the optimization of the single crystal growth for two Yb-based quantum critical materials,  $\text{YbRh}_2\text{Si}_2$  and  $\text{YbNi}_4\text{P}_2$ . The prototype heavy-fermion system  $\text{YbRh}_2\text{Si}_2$  is situated extremely close to an unconventional antiferromagnetic (AF) quantum critical point (QCP). The AF ordering ( $T_N = 70$  mK) can be further lowered by chemically induced negative pressure using Ir-substitution. The QCP is reached for an Ir-substitution of  $x \approx 0.1$  in  $\text{Yb}(\text{Rh}_{1-x}\text{Ir}_x)_2\text{Si}_2$  [1]. Here, we report on the optimization of the crystal growth of the substitution series as well as of the unsubstituted compound. We also report on our attempts to determine the melting point of  $\text{YbRh}_2\text{Si}_2$  and present a phase analysis of the molten compound. In the heavy fermion metal,  $\text{YbNi}_4\text{P}_2$ , a ferromagnetic (FM) transition